



HAL
open science

A comprehensive study of balloon-borne stratospheric aerosol composition : formed by asian emissions, volcanic eruptions, and wildfires

Hazel Vernier

► **To cite this version:**

Hazel Vernier. A comprehensive study of balloon-borne stratospheric aerosol composition : formed by asian emissions, volcanic eruptions, and wildfires. Other. Université d'Orléans, 2023. English. NNT : 2023ORLE1040 . tel-04511607

HAL Id: tel-04511607

<https://theses.hal.science/tel-04511607>

Submitted on 19 Mar 2024

HAL is a multi-disciplinary open access archive for the deposit and dissemination of scientific research documents, whether they are published or not. The documents may come from teaching and research institutions in France or abroad, or from public or private research centers.

L'archive ouverte pluridisciplinaire **HAL**, est destinée au dépôt et à la diffusion de documents scientifiques de niveau recherche, publiés ou non, émanant des établissements d'enseignement et de recherche français ou étrangers, des laboratoires publics ou privés.

UNIVERSITÉ D'ORLÉANS
ÉCOLE DOCTORALE: ÉNERGIE MATÉRIAUX SCIENCES
DE LA TERRE ET DE L'UNIVERS
LABORATOIRE DE PHYSIQUE ET DE CHIMIE DE
L'ENVIRONNEMENT ET DE L'ESPACE

THÈSE présentée par :

Hazel Vernier

Soutenue le 19 Octobre 2023

pour obtenir le titre de : Docteur de l'Université d'Orléans

Discipline/ Spécialité : Science de l'Univers

A Comprehensive Study of Balloon-borne Stratospheric Aerosol
Composition formed by Asian Emissions, Volcanic Eruptions,
and Wildfires

THÈSE dirigée par :

Mr BERTHET Gwenaël

Chargé de Recherche - HDR, LPC2E

RAPPORTEURS :

Mr BEKKI Slimane

Directeur de recherche, LATMOS

Mr SAVARINO Joël

Directeur de recherche, IGE

JURY :

Mr GUIMBAUD Christophe

Professeur Université d'Orléans - Président du jury

Mr SMITH Bill

Professeur d'université, Wisconsin-Madison

Mr BEGUE Nelson

Maître de conf., Université de la Réunion

Mr BERTHET Gwenaël

Chargé de Recherche - HDR, LPC2E

Mr BEKKI Slimane

Directeur de recherche, LATMOS


Mr SAVARINO Joël

Directeur de recherche, IGE

INVITÉ :

Mr RASTOGI Neeraj

Professeur, PRL, Inde



Acknowledgements

I begin this expression of gratitude by acknowledging the abundant blessings bestowed upon me by the divine presence in my life. Without the guidance and grace of God, none of what I have achieved would have been possible. As I lay confined to a hospital bed, paralyzed by a brain hemorrhage at the tender age of 15, I believed it signified the end of my academic aspirations. Yet, in His boundless mercy, God revealed to me the profound truth that "In every unprecedented circumstance, and in every turmoil, there lies a great miracle of God."

The journey of writing this dissertation has been a remarkable odyssey, spanning three continents and six countries. It has been a tapestry woven with diverse experiences, from traversing forests and chasing payloads in Brazil, to soaring above verdant pastures in the countryside of France. It has also been a period of tremendous intellectual growth, nurtured by the enriching learning environments at LPC2E, CNRS, Orleans-France, IPMET, Bauru-Brazil, NIA-Hampton, USA, and PRL-India. The completion of this dissertation would not have been conceivable, nor would it have been as enjoyable, without the unwavering support of my friends, colleagues, and mentors from these esteemed institutions.

To my mentors, I extend my deepest gratitude. First and foremost, my supervisor Gwenael Berthet at LPC2E deserves my heartfelt appreciation for welcoming me into his research group. Gwenael has granted me the freedom to explore intellectual realms, gently guiding me back to the path when necessary. Throughout my tenure, his support and encouragement have contributed to an immensely rewarding graduate school experience, allowing me the autonomy to pursue my work and partake in various conferences. I am also indebted to other mentors at LPC2E who have profoundly influenced my academic journey.

Additionally, I express my gratitude to the members of my committee for their keen interest in my work. Every result presented in this thesis has been achieved with the assistance and collaboration of fellow lab mates and colleagues. I extend special thanks to Neeraj Rastogi and Harish Gadhavi for their trust in my analytical abilities, offering me an opportunity to rekindle my career after a prolonged hiatus. Without their initial support, I would not have ascended this far on the ladder of success. I am grateful for the enlightening and comfortable environment they provided me at PRL, as well as the freedom to conduct my research unhindered within their lab.

I extend my thanks to all the participants in the various field campaigns whose contributions to data collection have shaped this thesis.

The unwavering support and love of my family and friends have been instrumental in my accomplishments. A heartfelt appreciation goes to my husband, Jean-Paul Vernier, for introducing me to the world of Atmospheric sciences and satellite observations. For his constant support, guidance, and love throughout my academic journey. To my sons, Emmanuel, Edwin, and Eric, I express my gratitude for their timely help, love, and understanding. To my precious daughter, Ann, who became a motherly figure to Eric during my extended absences, I am profoundly grateful. Indeed, I consider myself blessed to be their mother. And to Jack, our one-year-old Great Pyrenees, thank you for providing companionship during the late nights and early mornings when everyone else was lost in slumber, chasing their dreams.

I extend my gratitude to Marge, and Barry Green, Thennia, and James Tucker for their faithful friendship, kindness, and generosity. A special thank you goes to Steve Benson for his invaluable help and dedication to the LaTeX version of my thesis. Each of you is a blessing in my life.

Lastly, I wish to express my gratitude to my parents. To my late father, P.N Vasudevan, whose spiritual presence continues to guide me from beyond, I am forever grateful. And to my mother, Eru Vasudevan, who has been my unwavering support and strength since the passing of my father, I extend my deepest appreciation for her constant prayers, support, and guidance across the vast expanse of the seven seas.

Contents

List of figures	v
List of tables	x
1 Aerosols and their global transport	7
1.1 Introduction	8
1.1.1 Vertical structure of the Earth's Atmosphere	8
1.2 General Circulation	9
1.2.1 The discovery of a footprint	9
1.2.2 The Brewer-Dobson Circulation	9
1.2.3 A wave-driven mechanism	10
1.2.4 Transport in the upper troposphere lower Stratosphere	11
1.2.5 Need for troposphere stratosphere differentiation	11
1.2.6 The tropical Tropopause layer (TTL)	11
1.3 Vertical Transport in the TTL	11
1.3.1 Radiative heating	12
1.3.2 Convective overshoot	12
1.4 The Earth's radiation budget	13
1.4.1 Global Earth radiation budget	13
1.4.2 Radiative impacts after a volcanic eruption.	14
2 Stratospheric aerosols- Observations, processes, and climatic impact	19
2.1 General introduction on aerosols	20
2.2 Stratospheric Aerosol Discovery	20
2.3 Processes controlling the stratospheric layer: overview	20
2.4 The Junge Layer	22
2.5 Microphysical properties	22
2.5.1 Nucleation	22
2.5.2 Coagulation and Condensation	22
2.5.3 Evaporation and Sedimentation	23
2.6 Sources of Stratospheric aerosols	23
2.6.1 Sulfate aerosols	23
2.6.2 Carbon oxysulfide	23
2.6.3 Sulfur Dioxide	24
2.6.4 Dimethyl sulfur, carbon disulfide,, and hydrogen sulfide	24
2.7 Sulfur balance and flux	25
2.8 Volcanic eruptions	25
2.9 Other sources of aerosols	27
2.9.1 Smoke aerosols from wildfires	27
2.9.2 Asian Summer Monsoon Transport	27
2.9.3 The ATAL	28
2.9.4 Chemical composition of the ATAL and stratospheric aerosols	29

3	Exploring the ionic composition of the Asian tropopause aerosol layer using medium-duration balloon flights	35
3.1	Introduction	36
3.1.1	Why is the ATAL an important research criterion?	36
3.1.2	What is the ATAL comprised of	36
3.2	Balloon flights, instrumentation, and chemical analysis	37
3.2.1	Rationale for the experiment	37
3.2.2	Zero-pressure balloon experiment	37
3.2.3	Balloon-borne aerosol impactor	37
3.3	Balloon flights, instrumentation, and chemical analysis	38
3.3.1	Rationale for the experiment	38
3.3.2	Balloon-borne aerosol impactor	38
3.3.3	IC analysis of major ions in aerosol samples	39
3.3.4	Results of the IC analysis	39
3.4	Presence of ice clouds during flight ZF2	41
3.4.1	Nitrate particles in-cloud	42
3.4.2	NAT particles	42
3.4.3	In-cloud calcium and its Implication	44
3.5	The influence of Canadian wildfire plumes during the winter flight	44
3.6	Convective influence	45
3.7	Nitrite measurements	45
3.8	Comparison with GEOS-Chem simulations	46
3.9	Conclusions	47
4	An ocean of stratospheric aerosols after the Hunga Tonga Hunga-Ha'apai Volcanic eruption	57
4.1	Introduction	58
4.2	Modest injection of Sulfur Dioxide and the large resulting AOD	58
4.3	BraVo campaign	59
4.4	Materials and methods	61
4.4.1	Radio-Controlled balloon system:	61
4.4.2	Lightweight aerosol sampler	62
4.4.3	Ion Chromatography Analysis	63
4.4.4	Method to derive mass from POPC	64
4.5	Results	64
4.6	GEOS-Chem simulation and conclusion.	66
5	Impacts of wildfires and volcanic eruptions on stratospheric aerosol over the Northern Hemisphere- The REAS project	71
5.1	Introduction	72
5.2	Major events before the REAS Campaign	72
5.2.1	The volcanic eruption of La Soufriere	72
5.2.2	The 2021 Northern Hemisphere wildfires	73
5.3	REAS project	75
5.3.1	Balloon flights	75
5.3.2	Instruments used during REAS	76
5.4	Offline chemical analysis during REAS	77
5.4.1	Ion Chromatography	77
5.4.2	Orbitrap Q-Exactive, high-resolution mass spectrometry	77
5.5	Microphysical properties of volcanic aerosol and smoke during REAS	78
5.6	Chemical composition during REAS	79
5.7	Combined IC and Orbitrap analysis during the Jan 18th flight	82
5.7.1	Flight description	82
5.7.2	Results of the ORBITRAP analysis	83
5.7.3	Results of IC analysis	85
5.8	Discussion and Conclusion	87

List of Figures

1.1	Thermal structure of the atmosphere showing the different layers with increasing altitude. The dashed line indicates the tropical tropopause layer (TTL). (From Figure 1-19, p. 20 in Lutgens and Tarbuck’s <i>The Atmosphere</i> , 2001).	8
1.2	Brewer-Dobson circulation. Vertical ascent in the tropics in cumulonimbus clouds relayed by a slow ascent on a large scale. Transport to mid-latitudes in the middle stratosphere induced by planetary waves acting as a pump in tropical regions The TTL has been added in red.(Holton et al., 1995)	10
1.3	Schematic of cloud processes (left) and zonal mean circulation (right). Arrows denote circulation, the dashed line indicates a clear sky level of net zero radiative heating (LZRH). Black solid lines denote isentropes in K. Letters are associated with transport processes. (Fueglistaler et al., 2009).	12
1.4	The above figure portrays the troposphere-stratosphere transport. On the left convection carries air up to 13-14 km. In the center, the radiative heating amplifies by the presence of cirrus clouds and lifts the air to the tropopause’s cold point, supplemented by the slow ascent in the clear sky The average transport time of the boundary layer is indicated in red. (Corti et al., 2005).	13
1.5	Diagrams of the annual land mean energy balance (Units: $W m^{-2}$) over East Asia under (a) all sky and (b) clear-sky conditions for the present-day climate. The uncertainty ranges are also given in parentheses. (Qiuyan Wang1 et al., 2022).	16
1.6	The Figure provides an updated summary of the major climate impacts resulting from a large-magnitude volcanic eruption and the processes that lead to them. These impacts are highlighted in blue, while the relevant processes are in bold. The methods used to study the effects of volcanic eruptions on climate, such as observations, proxy reconstructions, and modeling, are described in italic text. Key research questions that remain unanswered are presented in boxes (Marshall et al., 2022).	17
2.1	(Adapted from Thornberry et al., 2021) shows the processes contributing to the formation, transport, and removal of stratospheric aerosols.	21
2.2	A view of Earth from space, visualizing the stratospheric aerosol layer (Junge Layer in red) Credit: Timothy Marvel, NASA/SSAI, Hampton, Va.	22
2.3	Integrated backscatter coefficient of at 694.3 nm measured by lidar in Garmish (Germany) from 1 km above the tropopause to the moment of layering. The position at the time of the main eruptions is indicated by arrows (http:// www. Imkifu.kit.edu/331.php).	24
2.4	Sheng et al. [2015] presented a global balance of atmospheric sulfur (above), where solid arrows indicate net surface emission fluxes, tropopause, sinks, physicochemical sources, and microphysical transformations in Gg of sulfur per year. Dotted arrows indicate the flow in one direction and provide details of microphysical and chemical conversions. Boxes represent tanks of compounds expressed in Gigagrams of sulfur. Red data are from the SOCOL-ARE model, black data from SPARC (2006), green data from the GOCART model, and orange data from Chin and Davis [1995]. Finally, blue data represent measurements from SAGE II	26

2.5	Profile showing an enhanced aerosol layer due to the fire, originating from the plume. at 42.94°N and 103.8°E. (a) The given tropopause height by the SAGE III data set is represented by the dotted line. (b) CLaMS CO map at 400 K on 3 September 2017. (c) IASI CO map, integrated over 12 h at 85.18 hPa, 18 d before the SAGE III profile measurement in (a). Superimposed: every fifth of the 1000 18 d TRACZILLA kinematic back-trajectories initialized at the geographical position and altitude of the fire plume peak in (a).	28
2.6	(a) Schematic of the transport processes indicating the formation and dissipation dynamics of the ATAL during the ASM (Q He et al., 2021). (b) CO mixing ratio (ppbv) at 100 hPa, in addition to the interception of the tropopause at 100 hPa pressure surface, and the easterly and westerly jets (Pan et al., 2016).	30
3.1	(a) Schematic diagram of the zero-pressure flight (ZP) concept. (b) Picture of the science payload, impactor preparation, and balloon flight launch. (c) Time–height curves of the GPS altitudes of the three zero-pressure flights during summer 2017, in comparison with that of winter 2018, launched from TIFR-BF, Hyderabad, India.	40
3.2	Schematic of the balloon-borne impactor used for sampling aerosols. Stages S1, S2, S3, & S4 collect aerosol particles of sizes greater than and between 2 μm to 0.05 μm in descending order.	41
3.3	Time series of the altitude, temperature, and relative humidity profiles of the samples inside the foam box during the ZF2 flight.	42
3.4	(a) Results from the analysis of inorganic aerosol for the aerosol ionic composition of the filters collected (i) on the ground (ii) during ZF2, (iii) during ZF3 in summer 2017, and (iv) during ZFW in winter 2018. (b) The percentage distribution of individual ions. S-1 to S-4 indicate the four stages of the impactor. The size cutoffs are > 2, 0.5, 0.15, and 0.05 microm for S-1, S-2, S-3, and S-4, respectively.	43
3.5	Cirrus cloud layer properties using CALIOP L2V4.2 Cloud Layer product for August 15th, 2017 between 17.12°N and 17.92°N corresponding to the profiles shown in Fig.1.4. Depolarization ratio versus color ratio plot for these layers which indicates the presence of aspherical large particles consistent with the properties of sub-visible cirrus clouds (mean AOD $\sim 0.03 \pm 0.02$).	44
3.6	(a) COBALD in situ scattering ratio (SR) and color index (CI) profiles and (b) CALIOP satellite SR and volume depolarization profiles co-located in time and space (within 20 km and 1 h, respectively) on 15 August at 19:00 UT. (c) Time series along ZF2 of SRs at 940 and 470 nm from COBALD as well as the GPS altitude and measured pressure from the iMet radiosonde.	50
3.7	Zonal mean aerosol extinction at 1020 nm derived from the SAGE III/ISS V051 data products between September 2017 and February 2018. Ice clouds in the troposphere have been removed using a threshold of color ratio (521nm/1020nm) below 2 (Vernier et al., 2015). An increase in aerosol extinction between 10–50°N and 13–21 km is observed from September 2017 to the end of 2017 due to the Pacific Northwest Canadian PyroCbs which injected smoke in the Upper Troposphere and Lower Stratosphere in August 2017. A residual of the smoke plume is still detected up to February 2018. The white rings show the location of the balloon flight at the bottom of the aged smoke plume.	51
3.8	Back trajectories initialized from ZF2 (15/08) and ZF3 (21/08) measurements between 150 and 70 hPa. Black dots along the trajectories are the position of convective systems intersecting air masses sampled during the balloon flight.	52
3.9	The two sets of six panels show the respective GEOS-Chem model-simulated carbon monoxide (CO, ppbv), sulfate (SO_4^{2-} , ng m^{-3} at STP), nitrate (NO_3^- , ng m^{-3} at STP), ammonium (NH_4^+ , ng m^{-3} at STP), black carbon (BC, ng m^{-3} at STP), and dust (Ca_2^+ , ng m^{-3} at STP) concentrations averaged over 100–150 hPa at 22:00UTC on 15 August 2017 (top six panels) and 21 August 2017 (bottom six panels). Standard temperature and pressure are 298 K and 1013.25 hPa, respectively. Arrows denote the wind direction, and the white circle indicates the sampling location in Hyderabad, India.	54

3.10	BTime series of simulated 3-hourly CO, SO ₄ ²⁻ , and NO ₃ ⁻ concentrations averaged over 100–150 hPa at Hyderabad during the ZF2 and ZF3 flights on 15 and 21 August 2017. Also shown are concentrations of NO ₃ due to lightning NO _x emissions (NO ₃ ⁻ , LNO _x). See the text for details.	55
3.11	GEOS-Chem model-simulated NO ₃ ⁻ , CO, and SO ₄ ²⁻ concentrations (at STP) extracted along the trajectory lines during flights ZF2 and ZF3 (as shown in Fig. 1.5).	55
4.1	GloSSAC time series zonal mean [60N-60S] Stratospheric Aerosol Optical Depth (SAOD) was calculated with a combination of satellite observations above the tropopause (left). Scatter plot (right) of volcanic SO ₂ and semi-annual mean SAOD from the date of each eruption [the first two letters of each volcanic eruption are annotated]. El: El Chinchon, Pi: Mt Pinatubo, Ka: Kasatochi, Sa: Sarychev, Na: Nabro, Ca: Calbuco, Ra: Raikoke, HTHH: Hunga Tonga Hunga Ha’apai.	59
4.2	Payloads used for the campaign.	60
4.3	(bottom right) world map showing the location of the BraVo campaign in Brazil. (Top right) Ground-based lidar observations Scattering Ratio (SR) at 532 nm from Bauru in August 2022.(Top left) Latitudinal cross-section of the mean SR at 532 nm between 23 May and 2 June 2022 showing the HTHH volcanic plume (in red).	62
4.4	Aerosol concentration profiles for aerosol radius greater than 13 size bins between 0.15µm and 5µm derived from the Particle Plus Optical Particle Counter	63
4.5	Preparation of the aerosol sampler flight (left). Zoom on the radio-controlled valve used to reduce the ascent inside the HTHH plume on 08/12.	64
4.6	(left) Trajectory of the radio-controlled balloon flight showing GPS altitude with respect to time, and temperature. (right) Aerosol concentration profiles from POPC show that the sampling was done within the HTHH plume	65
4.7	(a,b) CHEM lightweight balloon-borne filter sampler.(c,d) filter holders bearing filters.	65
4.8	(a,b) Loading and unloading of filters in the Laminar air flow chamber. (c) Aerosol extraction. (d) Analysis of extracts using Dionex ion chromatograph instrument.	66
4.9	The aerosol concentration profile was measured using POPC on August 12th, and on August 18th, the ionic mass concentration was determined through flow rate and IC analysis (right). Aerosol samples were collected on PTFE filters at three distinct positions, enabling the differentiation of aerosols in the boundary layer (Pos #2), the free troposphere (Pos #3), and within the HTHH aerosol layer (Pos #4). The error bars for each species were calculated based on the standard deviation obtained from three repetitions of the IC analysis	67
4.10	Aerosol concentration profiles for selected sizes (0.3 µm to 10 µm) from three flights (08/07, 08/12, and 08/20) in the POPC, along with the corresponding volumetric size distribution between 19-21 km and 21-24 km (dark orange represents the overlapping distribution of the two layers).	68
4.11	(top) Latitudinal cross-section of sulfate concentration in STP in August 2022 derived from GEOS-Chem simulation and (bottom) associated mean sulfate concentration profile within ±2.5° latitudes and ±10° longitudes from Bauru, Brazil.	69
5.1	Zonal mean cross-section of Scattering Ratio (SR) from CALIOP level 1 V4.01 between 01-16 April 2021 (a), 01-16 May 2021 (b), 01-16 October 2021(c) and 01-16 November 2021 (d). White lines are zonal mean isentropic surfaces, and the tropopause altitude is shown in orange. Data 3 km below the tropopause are discarded for possible contamination by cirrus cloud). Depolarization values > 5% are used to remove clouds (Vernier et al., 2009). Adapted from Dumelie et al.(2023).	73
5.2	displays three different pieces of information. (4a) is a composite image in red, green, and blue (RGB) showing a pyrocumulonimbus cloud on October 4th. (4b) is a graph showing the total attenuated backscatter at 532nm measured by CALIPSO, which indicates the presence of a plume in Europe. Lastly, (4c) is a HYSPLIT back-trajectory associated with the OMPS Aerosol index that was measured on October 4th. Dumelie et al., 2023.	74

5.3	. (a) Model display of Aircore. (b) Schematic showing the working principle of Aircore. Aircore is a gas collector system that rely on a balloon flight to store air gases into a long coil which is further empty on the ground and pass through a gas analyzer to derive gases concentration such as CO, CO ₂ and CH ₄	76
5.4	(Left) image of the 3-stage particle sampler. (Right) Schematic of their flow within the MPS-3 Particle sampler.	77
5.5	(Left) photo of the orbitrap instrument and (right) schematic of desorption technique used for extracting organic matters from the filters.	78
5.6	OMPS time series of daily mean aerosol extinction at 675nm between January 2020 and November 2022 above the 38°N – 60°N/10°W – 20°E area corresponding to the major part of Europe (Top). Zoom of OMPS extinction time series from June 2021 to February 2022 (Bottom left) for the same area. Vertical profiles of aerosol extinction from the SAGEIII/ISS instrument (Bottom right).	79
5.7	Aerosol concentration profiles for sizes greater than 0.15 μm obtained with the Particle Plus Optical Particle Counter (POPC) and the Printed Optical Particle Spectrometer (POPS) during 6 balloon flights of the REAS campaign between November 2021 and January 2022 and corresponding Scattering Ratio at 940 nm for 3 flights of the COBALD instrument coincident with POPC on 11/24/2021, 12/02/2021 and 01/17/2022. (Dumelie et al., 2023). 80	80
5.8	(Left panel) Particle size concentration measurements from POPC. (Middle) COBALD backscattering ratio at 940 and 470 nm. (Right) results of the IC analysis using the aerosol impactor: in stage 1 ($r > 1.4 \mu\text{m}$) and stage 2 ($0.2 \mu\text{m} < r < 0.05 \mu\text{m}$). The major difference observed between the two samples is in stage 3 ($r \leq 0.05 \mu\text{m}$)	82
5.9	(Left panel) Particle size concentration measurements from POPC. (Middle) temperature, ozone, and CO profiles from M20 radiosonde and Electrochemical concentration cell (ECC) and Aircore. (Right) flow rate at different positions of the aerosol sampler corresponding to sampling altitudes	83
5.10	Venn diagram showing common chemical formulas detected in samples 2–5 AF	84
5.11	The distribution of carbon numbers for filters 2-5. As seen in the figure the number of carbon chains increase with altitude	85
5.12	(Left). Particle concentration for 9 size radii between 0.15 μm and 0.4 μm measured by the Particle plus Optical Counter (POPC) on a balloon flight on January 18, 2022, from Reims. (Right) results of the ionic composition of aerosol samples collected on the ground and in the UTLS using the balloon-borne impactor and the aerosol sampler.	86

List of Tables

4.1	Balloon flights from Bauru (-22.36, -49.03), Brazil during the BraVo campaign.	61
5.1	List of balloon flights launched throughout the REAS campaign showing associated details on flight altitude, duration, and payloads used (Dumelie et al., 2023).	75
5.2	Showing the aerosol sampling altitude and time using the balloon-borne impactor and the lightweight aerosol sampler	80

Hazel Vernier

Une étude approfondie de la composition des aérosols stratosphériques par ballons : aperçu des émissions asiatiques, des éruptions volcaniques et des incendies de forêt.

Les aérosols atmosphériques ont un impact significatif sur la physique et la chimie de l'atmosphère en interagissant avec les rayonnements solaires et IR et en participant à de multiples réactions chimiques. Ils jouent également un rôle crucial en tant que noyaux pour la formation de gouttelettes de nuages et de cristaux de glace. Les aérosols d'origine humaine ont un effet de refroidissement qui contraste avec l'effet de réchauffement des gaz à effet de serre, comme le souligne le rapport du GIEC de 2013. Caractériser les propriétés optiques, microphysiques et chimiques des aérosols permet de mieux comprendre leur origine, leur histoire et leurs implications potentielles pour l'environnement et la santé humaine. La stratosphère, une composante importante du système climatique de la Terre, a subi des changements notables en raison de la pollution atmosphérique, de l'appauvrissement de la couche d'ozone et des altérations de la circulation, ce qui pose des défis à la recherche. Cette thèse analyse les effets des éruptions volcaniques, des émissions anthropiques en Asie et des émissions de feux de forêt sur la composition chimique de la couche d'aérosols stratosphériques, en se concentrant spécifiquement sur les impacts sur la population d'aérosols au cours de trois campagnes de terrain : Batal, Bravo et REAS. Des collecteurs d'aérosols embarqués sous ballons, des compteurs optiques de particules et d'autres instruments ont été utilisés pour explorer les propriétés chimiques, microphysiques et optiques de différentes couches d'aérosols. Les résultats ont été comparés aux données satellitaires afin de faire la lumière sur les sources des aérosols et leur mécanisme d'évolution. L'analyse des masses d'air et les simulations de modèles ont permis de mieux comprendre le transport et la distribution de ces aérosols

Mots-clés: Aérosols stratosphériques, incendies de forêt, éruptions volcaniques.

A Comprehensive Study of Balloon-borne Stratospheric Aerosol Composition formed by Asian Emissions, Volcanic Eruptions, and Wildfires

Atmospheric aerosols have a significant impact on the physics and chemistry of the atmosphere by interacting with solar and IR radiations and by participating in multiple chemical reactions. They also play a crucial role as nuclei for cloud droplet and ice crystal formation. Understanding the characteristics of aerosol optical, physical, and chemical properties provides insights into their origin, history, and potential implications for the environment and human health. The stratosphere, an important component of Earth's climate system, has undergone notable changes due to atmospheric pollution, ozone depletion, and circulation alterations, posing research challenges. This Ph.D. thesis analyzes the effects of volcanic eruptions, anthropogenic emissions in Asia, and wildfire emissions on the chemical composition of the stratospheric aerosol layer, specifically focusing on the alterations in aerosol population during three field campaigns: Batal, BraVo, and REAS. Balloon-borne aerosol collectors, optical particle counters, and other instruments were used to explore the chemical, physical, and optical properties of different aerosol layers. The results were compared with satellite data to illuminate the source and evolution. The analysis of air masses and model simulations provided insights into the transport and distribution of these aerosols.

Keywords: stratospheric aerosols, wildfires, volcanic eruptions.



3 Av. de la Recherche Scientifique,
45071 Orléans, France



Introduction

The stratosphere is a key component of the Earth's climate system that has undergone significant changes over the past decades. The abrupt climate shift has indeed generated numerous challenges in research activities in the field of Earth and Atmospheric sciences lately. Processes like atmospheric pollution, ozone depletion, and alterations in the Brewer-Dobson circulation are some of the crucial attributes of the entire climate affecting the radiative budget and atmospheric circulation. In order to predict the evolution of our climate, it is essential to understand the dynamic, chemical, and radiative coupling between the stratosphere and troposphere among many other processes. Researchers have been exploring the transport of trace chemical species, natural and anthropogenic between the stratosphere and the troposphere. The anthropogenic constituents transported upward into the stratosphere from the troposphere initiate most of the ozone depletion chemistry. On the contrary, the downward transfer from the stratosphere not only involves the main removal mechanisms for many stratospheric species, including those responsible for ozone depletion but also characterizes a significant input of ozone and other reactive species into the tropical chemical system.

A key constituent of the stratosphere is an aerosol layer that is largely enhanced after major volcanic eruptions but also maintained in their absence through the transport of sulfur-based aerosol precursors (Kremser et al., 2018). Over the past decade, it was found that the stratospheric aerosol layer is also influenced by anthropogenic emissions in Asia resulting in the formation of the Asian Tropopause Aerosol Layer (ATAL, Vernier et al., 2011). In addition, extreme wildfires can influence the stratosphere through the direct injection of smoke via PyroCbs (fire-induced storm) followed by their ascent through radiative heating. Due to the large variety of sources in the stratosphere, its composition is uncertain but crucial to predict its radiative, climate, and chemical impacts. This PhD dissertation focuses on assessing the composition of stratospheric aerosols using offline analysis of samples collected in the stratosphere.

Dissertation outline and science questions

In order to have a better understanding of the stratospheric aerosol sources, transportation mechanisms, and lifetime, followed by their climatic impact, it is essential to explore stratospheric aerosol chemical composition. New techniques for aerosol sampling and subsequent analysis must be developed. Further, there is a need to derive the relationship between sources and aerosol properties on a local scale before understanding their global impact.

Chapter 3¹ describes an extensive analysis of the ATAL aerosols in India during the summer monsoon and in the winter using a balloon-borne aerosol impactor system with offline Ion Chromatography (IC) analysis. The chapter sheds light on the concept of the balloon experiment with the impactor system and compares satellite data and the chemistry model with balloon observations. Moreover, the origin of air masses to understand the convective transport and distribution of aerosols on a regional scale will be emphasized therefore, the first goal of this dissertation is to:

1. Study the physical, chemical, and optical properties of aerosols using a unique and valuable strategy involving balloon-borne measurements over the upper troposphere/lower troposphere (UTLS) region, in India

In Chapter 4² we investigate the impact of the Hunga-Tonga undersea eruption on the stratospheric aerosol population using Balloon measurements, Satellite data, and model simulations. Indeed, the stratospheric aerosol layer has witnessed large perturbations in the last couple of years. From extreme wildfires in North America and Australia to medium-size volcanic eruptions like Ambae, in July 2018, Raikoke, in 2019, and finally the Hunga-Tonga Ha'apai in January 2022. Reported as the largest marine

¹This study, titled "Exploring the inorganic composition of the Asian Tropopause aerosol layer using medium duration balloon flights" (Vernier, H., Rastogi, N., Liu, H., Pandit, A. K., Bedka, K., Patel, A., Ratnam, M. V., Kumar, B. S., Zhang, B., Gadhavi, H., Wienhold, F., Berthet, G., and Vernier, J.-P, 2022, is published in *Atmos. Chem. Phys.*, <https://doi.org/10.5194/acp-22-12675-2022>, 2022.

²This study, titled "An ocean of stratospheric aerosols after the Hunga Tonga Hunga Ha'apai volcanic eruption" by Hazel Vernier, Demilson Quintão, Bruno Biazon, Eduardo Landulfo, Giovanni Souza, Benoit Grosseil, Neeraj Rastogi, Amanda, V. Dos Santos, Fabio J. S. Lopes, Alex C. PMendes, José A. da Matta, Maria F. Andrade, Neeraj Rastogi, Rohit Meena, Hongyu Liu, Suvarna Fadnavis, Maria P. P. M. Jorge, Damaris K. Pinheiro, Maheesh Kovolakam, Akhil Raj, Rohit Meena, Gwenaél Berthet and Jean-Paul Vernier, submitted to *Nature*.

eruption ever recorded, researchers used Microwave Limb Sounder (MLS) satellite data to reveal that this volcano injected the equivalent of 10% of the total stratospheric water vapor content (100 Tg) into the stratosphere. Cloud Aerosol Lidar and Infrared Pathfinder Satellite Observation (CALIPSO) and lidar measurements revealed the existence of a volcanic plume between 20-25 km. Balloon measurements and Radio sounding of the Aerosols of Volcanic Origin (BRAVO) campaign was mounted in Brazil, to study the consequence of a marine eruption on the stratospheric aerosol layer. Particle size information derived from balloon-borne optical counters showed the presence of aerosols with a size diameter $< 1.2 \mu\text{m}$ and their subsequent sedimentation. As a consequence, increased OH radicals from water vapor were reported to further reduce the SO_2 lifetime by 50%. The chapter will focus on analyzing the inorganic composition of the plume using analytical techniques described in the previous chapters. The results obtained therein are compared with satellite data and climate chemistry model simulations to validate the results. Processes involved in the vertical distribution of the volcanic plume are investigated using satellite data and ground-based lidar measurements.

In addition, the results of ion chromatographic analysis of samples collected within the plume using a lightweight aerosol sampler will be used to understand the aerosol chemistry within the plume. Moreover, this chapter will help strengthen the understanding of the primary source of sulfate aerosols whether volcanically derived or as a consequence of the oceanic source of dimethylamine.

Finally, this chapter of the dissertation will fulfill the second goal of this dissertation:

2. To investigate the impact of a marine eruption on stratospheric aerosol chemistry and differentiate the same from those of terrestrial eruptions and wildfires using balloon measurements, and satellite data validations.

Extreme wildfires have been identified as new sources of carbonaceous aerosols in the stratospheric aerosol population. In order to study the impacts of wildfires on stratospheric aerosol loading in the northern hemisphere, the Rapid Experiments for Sudden Aerosol Injection in the Stratosphere (REAS) campaign was mounted. In chapter 4³ an extensive study on the organic and inorganic composition of stratospheric aerosols to unveil the signature of a mixed plume of volcano and wildfire using a lightweight aerosol sampler will be discussed. This chapter will focus on the efficient analytical techniques in sample analysis by high-resolution mass spectrometry (Orbitrap Q-Exactive Thermo scientific), in addition to ion chromatography, using the sampling strategy described in Chapter 3 for deriving the organic and inorganic components present at 3 different layers from the troposphere to the stratosphere (20 km). Satellite data in comparison with in situ measurements will enable the distinction of the plume signature from an aged volcanic activity from that of a wildfire event thereby fulfilling the third objective of this dissertation:

3. Compare and validate satellite observations with balloon measurements to characterize organic matter and volcanic components present through the troposphere-stratosphere region.

³This study, titled "Impacts of wildfires, and volcanic eruptions on stratospheric aerosols over the Northern hemisphere-The REAS project" (Vernier, H., Rastogi, N., Berthet, G., Liu, H., Zhang, B., Wienhold, F., and Vernier, J.-P) is in preparation for submission to ACP

Résumé en Français de l'introduction et des objectives de la thèse

La stratosphère est une partie cruciale du système climatique terrestre qui a connu des changements importants au cours des dernières décennies. Ces changements ont posé des défis à la recherche en sciences de la Terre et de l'atmosphère. Des facteurs tels que la pollution atmosphérique, l'appauvrissement de la couche d'ozone et les modifications de la circulation de Brewer-Dobson ont des implications importantes pour le climat, affectant le bilan radiatif et la circulation atmosphérique. Pour prédire avec précision l'évolution du climat, il est essentiel de comprendre les interactions dynamiques, chimiques et radiatives entre la stratosphère et la troposphère les processus associés. Les chercheurs ont étudié le transport d'espèces chimiques à l'état de traces, naturelles et anthropiques, entre la stratosphère et la troposphère. Les substances anthropiques transportées dans la stratosphère à partir de la troposphère jouent un rôle important dans la chimie de l'appauvrissement de la couche d'ozone. Inversement, les substances transférées de la stratosphère à la troposphère contribuent à l'élimination de nombreuses espèces stratosphériques, y compris celles impliquées dans l'appauvrissement de la couche d'ozone. De plus, ce transfert vers le bas introduit des quantités importantes d'ozone et d'autres espèces réactives dans le système chimique tropical. La stratosphère contient une couche d'aérosols qui est principalement renforcée après des éruptions volcaniques majeures. Cependant, elle est également influencée par le transport d'espèces précurseurs d'aérosols à base de soufre en l'absence d'activité volcanique. Ces dernières années, on a découvert que les émissions anthropiques en Asie contribuent à la formation d'une couche asiatique d'aérosols vers la tropopause nommée l'ATAL. De plus, les feux de forêt extrêmes peuvent avoir un impact sur la stratosphère en injectant de la fumée directement à travers les PyroCbs (tempêtes induites par les feux de forêt) et en les soulevant par la suite par chauffage radiatif. La composition de la couche d'aérosols stratosphériques est incertaine mais essentielle pour prédire ses effets radiatifs, climatiques et chimiques. Cette thèse vise à améliorer notre compréhension des aérosols stratosphériques en étudiant leurs sources, leurs mécanismes de transport, leur durée de vie et leur impact climatique. Pour ce faire, de nouvelles techniques d'échantillonnage et d'analyse des aérosols ont été explorées pendant plusieurs campagnes de mesures. En outre, il est crucial d'établir le lien entre les sources d'aérosols et leurs propriétés à l'échelle locale avant de comprendre leur influence mondiale. En abordant ces questions scientifiques, la recherche cherche à fournir des informations précieuses sur la composition chimique des aérosols stratosphériques et leurs implications pour le climat. Le chapitre 3 de la thèse se concentre sur une analyse approfondie des aérosols dans la couche d'aérosols de tropopause asiatique (ATAL) au-dessus de l'Inde pendant la mousson d'été et les saisons hivernales. L'étude utilise un système d'impaction d'aérosols transporté sous ballon combiné à une analyse par chromatographie ionique (CI) en laboratoire. Le chapitre met en évidence l'expérience en ballon et le système d'impaction, en comparant les observations avec des données satellitaires et un modèle chimique. En outre, le chapitre vise à fournir une compréhension de l'origine des masses d'air, en mettant l'accent sur le transport convectif et la distribution régionale des aérosols. L'objectif principal de ce chapitre est d'étudier les propriétés physiques, chimiques et optiques des aérosols dans la région de la haute troposphère / basse stratosphère (UTLS) au-dessus de l'Inde. De plus, l'origine des masses d'air pour comprendre le transport convectif et la distribution des aérosols à l'échelle régionale sera étudiée. Le premier objectif de cette thèse est :

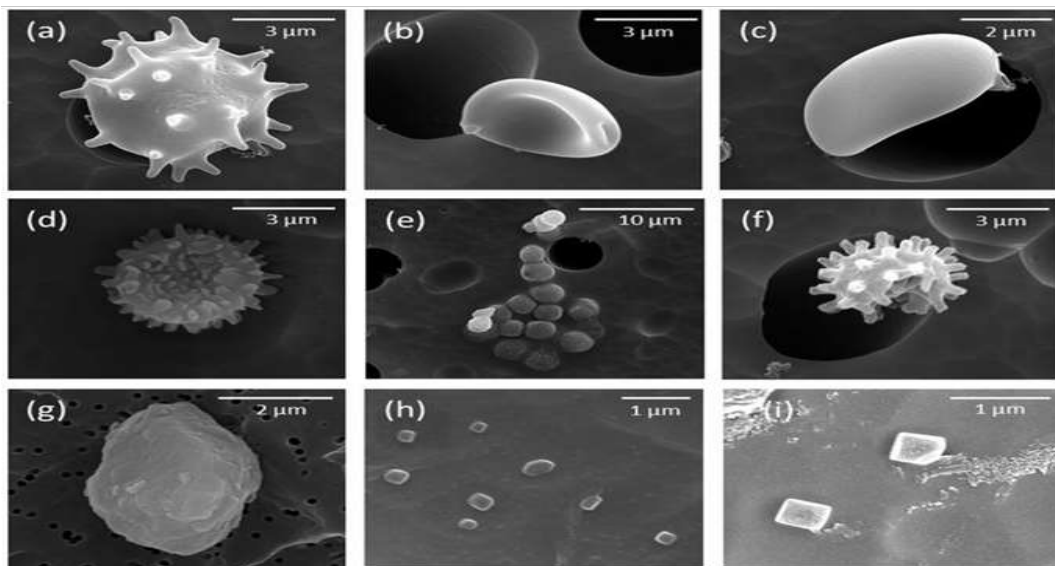
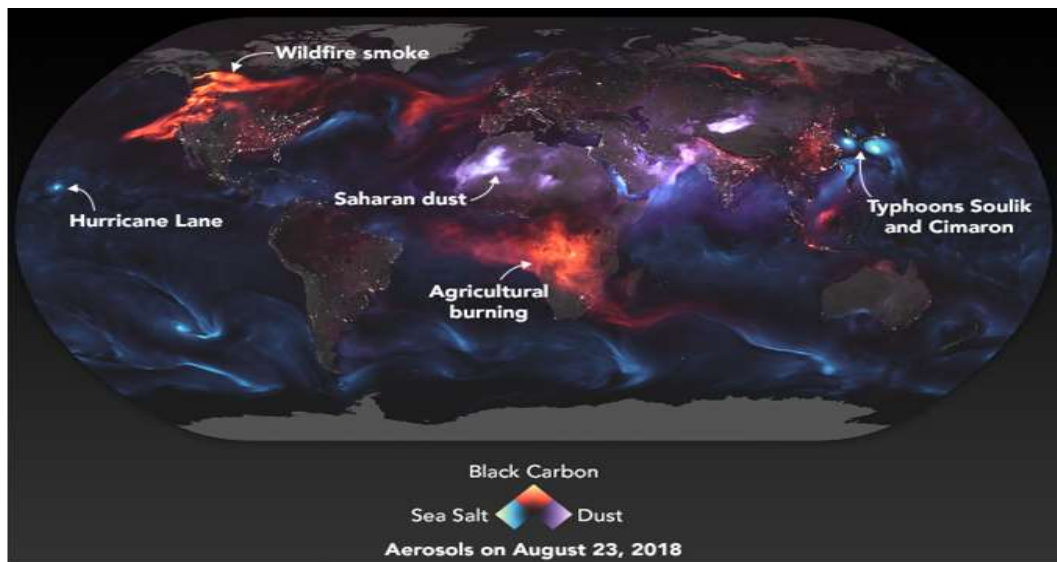
1. d'étudier les propriétés physiques, chimiques et optiques des aérosols à l'aide d'une stratégie impliquant des mesures sous ballons dans la haute troposphère / basse troposphère (UTLS), en Inde.

Le chapitre 4 de la thèse se concentre sur l'étude de l'impact de l'éruption sous-marine Hunga-Tonga sur la population d'aérosols stratosphériques. L'étude utilise des mesures de ballons, des données satellitaires et des simulations numériques. L'éruption probablement la plus grande éruption sous-marine jamais enregistrée, injectant une quantité importante de vapeur d'eau dans la stratosphère. Cette thèse décrit les résultats des mesures sous ballons effectuées lors de la campagne des aérosols d'origine volcanique au Brésil (BRAVO). Ces mesures fournissent des informations sur la taille des particules et la sédimentation des aérosols dans le panache. La présence accrue de radicaux OH provenant de la vapeur d'eau réduirait la durée de vie du SO₂ de 50%. Ce chapitre se concentre sur l'analyse de la composition inorganique du panache volcanique à l'aide des techniques analytiques décrites dans les chapitres précédents. Les résultats sont comparés aux données satellitaires et aux simulations de modèles de chimie-climat pour valider les résultats. Le chapitre étudie également les processus impliqués dans la distribution verticale du panache volcanique à l'aide de données satellitaires et de mesures lidar au sol. De plus,

l'analyse chromatographique ionique des échantillons prélevés dans le panache à l'aide d'un échantillonneur d'aérosol léger sous ballon météorologique aide à mieux comprendre la chimie des aérosols dans le panache. Le chapitre 4 de la thèse se concentre sur l'étude des feux de forêt extrêmes en tant que nouvelles sources d'aérosols carbonés dans la population d'aérosols stratosphériques. Pour étudier les impacts des feux de forêt sur la charge d'aérosols stratosphériques dans l'hémisphère Nord, la campagne REAS (Rapid Experiments for Sudden Aerosol Injection in the Stratosphere) a été menée. Ce chapitre traite d'une étude approfondie sur la composition organique et inorganique des aérosols stratosphériques afin d'identifier les signatures d'aérosols résultant d'une combinaison d'activité volcanique et de feux de forêt. Un échantillonneur d'aérosols léger est utilisé pour prélever des échantillons à différentes couches allant de la troposphère à la stratosphère (jusqu'à 20 km). Des techniques analytiques comprenant la spectrométrie de masse à haute résolution (Orbitrap Q-Exactive Thermo scientific) et la chromatographie ionique, sont utilisées pour l'analyse des échantillons. Le chapitre se concentre sur la comparaison des données satellitaires avec des mesures in situ pour distinguer la signature du panache provenant d'une activité volcanique ancienne de celle d'un incendie de forêt. Cette comparaison et validation d'observations satellitaires avec des mesures en ballon vise à caractériser la matière organique et les composants volcaniques présents dans toute la région troposphère-stratosphère.

Chapter 1

Aerosols and their global transport



1.1 Introduction

Almost seven decades now climate change debates continue to trigger unrest among the scientific community. Much of this is associated with the changing weather patterns on account of anthropogenic and natural emissions that make it to the atmosphere where they can alter the Earth's climate. Greenhouse gases such as CO_2 and CH_4 thereby interfere with the Earth's radiation budget. Among the main culprits responsible for this climate-related unrest is also the aerosol population (anthropogenic and natural) in the atmosphere which tends to affect the weather by absorbing /scattering solar radiation and eventually the cloud and rainfall phenomenon. The direct and indirect effects of aerosols on the earth's radiative balance and cloud distribution remain significant sources of uncertainty for climate models (IPCC AR5). An accurate study of aerosols is essential to understand the impact on climate and predict air pollution episodes. This chapter will cover the structure of the Earth's atmosphere and dynamics focusing in the upper troposphere and lower stratosphere (UTLS)

It will also present general information on aerosol optical properties followed by their climate-related impact.

1.1.1 Vertical structure of the Earth's Atmosphere

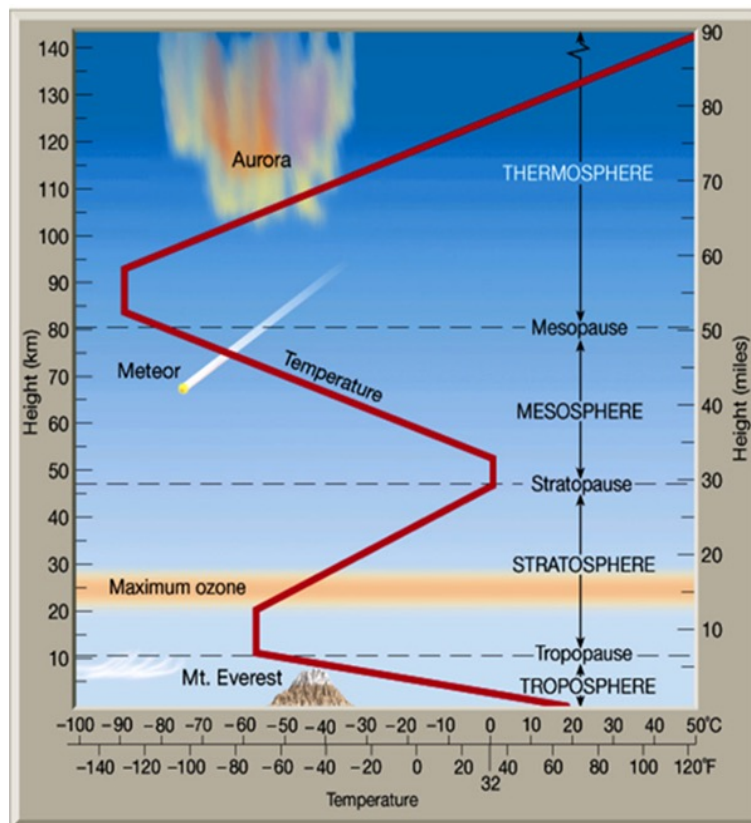


Figure 1.1: Thermal structure of the atmosphere showing the different layers with increasing altitude. The dashed line indicates the tropical tropopause layer (TTL). (From Figure 1-19, p. 20 in Lutgens and Tarbuck's *The Atmosphere*, 2001).

The Earth's atmosphere is comprised of five major layers and several secondary layers on account of the temperature structure (Fig. 1.1). The layers are the troposphere, stratosphere, mesosphere, thermosphere, and exosphere in ascending order.

Troposphere: The lowest layer is identified as the troposphere where the temperature decreases with altitude. Tropopause, a layer uppermost to the troposphere varies from low to high latitudes. Extending at 16 km in the tropics, 13 km at mid-latitudes, and 8 km in high latitudes, with its

height lower in the poles and higher at the equator. All weather processes occur in this layer of the atmosphere. It contains 99% of water vapor and aerosols (tiny solid or liquid particles suspended in air). Here the temperature decreases with altitude since tropospheric heat is generated by the energy transfer from the Earth's surface

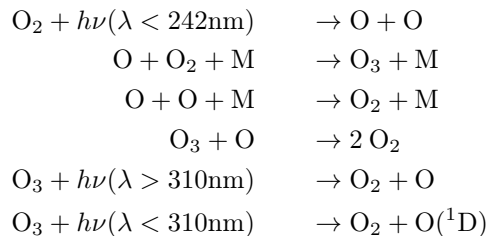
Stratosphere: Situated approximately between 12 and 50 km is the stratosphere. The layer is stratified with the denser, cooler air below the warmer, lighter air. This leads to an increase in temperature with height. 90% of the ozone is believed to reside here, making it a home for the same. The associated UV absorption in this layer is responsible for warmer temperatures with increasing altitudes. The stratosphere contains a key constituent of the climate system, the stratospheric aerosol layer. Largely enhanced after major volcanic eruptions and moderately influenced by medium eruptions, extreme wildfires, and Asian pollution.

Mesosphere: The layer above the stratosphere is called the mesosphere. The temperature decreases to a very low value at the mesopause estimated at around 85 km. This layer is known for the occurrence of polar stratospheric clouds, auroral activities, solar proton events, and mesospheric showers. Gravity waves create great momentum for mesospheric circulation. The remaining atmospheric layers shown in Fig. 1.1 aren't relevant to this work and will not be covered.

1.2 General Circulation

1.2.1 The discovery of a footprint

Ozone (O_3) production mainly occurs in the tropical stratosphere where the oxygen molecules O_2 are separated into oxygen atoms (O), which undergo a reaction with other O_2 molecules forming O_3 . However, much of O_3 is detected outside of its natural tropical stratospheric region at higher latitudes as a result of slow atmospheric circulation displacing O_3 from its production zone to mid and polar latitudes.



In the 50s, the first measurements of water vapor and helium in the lower stratosphere above England led to the development of a theory on the general circulation in which the tropics played a fundamental role. Indeed, the scarcity of water vapor in the stratosphere was compatible with the circulation patterns of the time when the stratosphere and troposphere were seen as two decoupled and independent complementary regions. These observations suggested the existence of a general circulation in which air entered the stratosphere through tropical regions where the temperature prevailing at the tropopause led to it being dried up by condensation before entering the stratosphere (Brewer, 1949). This circulation also permitted us to explain the high ozone values observed at mid-latitudes with an instrument called "Dobson". Thus, it was given the name of Brewer-Dobson Circulation (BDC).

1.2.2 The Brewer-Dobson Circulation

The BDC model consists of three main parts. The first part is the ascending tropical movement of air, the second is the poleward transport into the stratosphere, and the third is the descending motion in both mid-stratosphere and polar latitudes. Air enters the stratosphere through tropical regions in the circulation of BDC. The first step of this transport is associated with convection and the formation of convective clouds called "cumulonimbus" transporting air from the ground to a neutral buoyancy level of around 14 km (Holton et al., 1995). This convection depends on solar heating at ground level and

the static stability of the air. In an unstable atmosphere, the air continues its ascent to higher altitudes thanks to the latent heat released by condensation when saturation is reached. The second step of the ascent above 14 km is fueled by large-scale mechanisms related to the propagation of planetary waves in the stratosphere (fig.1.2.2).

The differences in time scales associated with vertical transport in the troposphere and tropical stratosphere imply intrigue between these two regions. Indeed, in tropospheric convective systems, it corresponds to time scales of a few hours while it takes several months for a parcel of air to rise in the stratosphere in the BDC. These differences result in the rapid growth of ozone and sharp reduction of water vapor content respectively above the transition zone between the two regions. There exists possessing the characteristics of tropospheric air and stratospheric air called TTL (Tropical transition Layer) (fig. 1.2 in red). Aerosols do not exhibit consistent behavior in the TTL since source and sink mechanisms coexist.

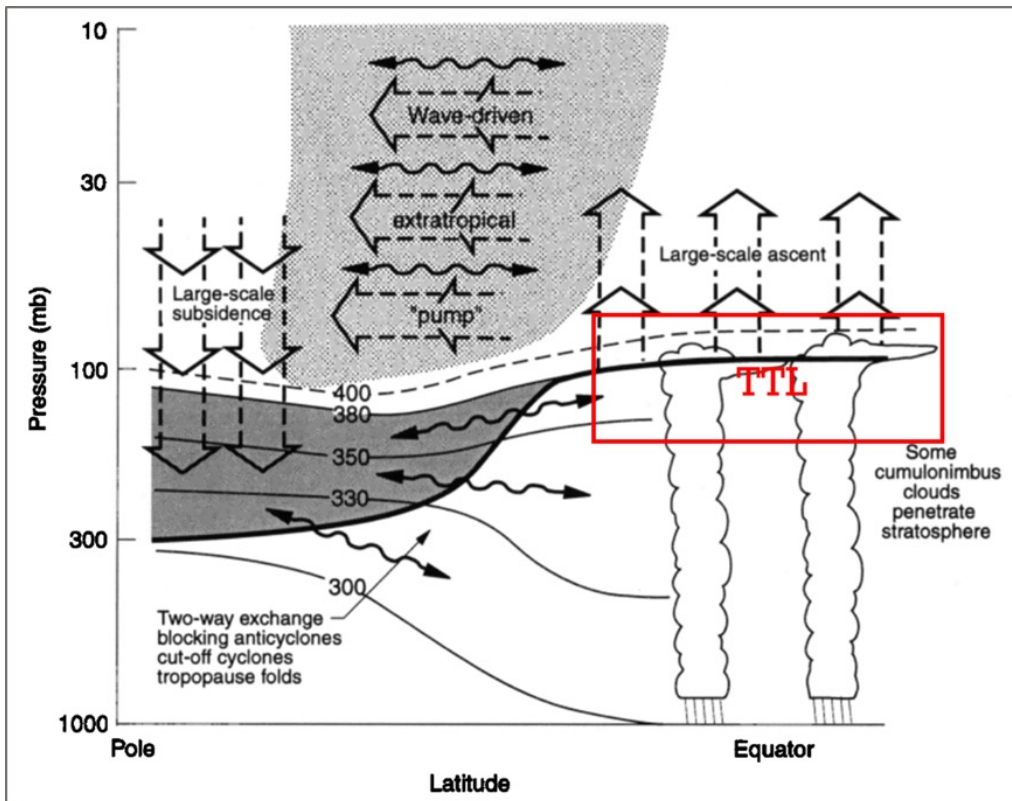


Figure 1.2: Brewer-Dobson circulation. Vertical ascent in the tropics in cumulonimbus clouds relayed by a slow ascent on a large scale. Transport to mid-latitudes in the middle stratosphere induced by planetary waves acting as a pump in tropical regions The TTL has been added in red.(Holton et al., 1995)

1.2.3 A wave-driven mechanism

The BDC is a complex and interesting mechanism that results from wave motions described in section 1.2.3. Rossby wave is an example of this type of wave formed on account of meridional temperature gradients and the planet's rotation (producing Coriolis force) extending thousands of km vertically and horizontally.

Topographical features like the Rocky Mountains, Himalayas, and the Tibetan plateau in addition to meridional temperature gradients and Coriolis deflection, create standing planetary waves, a variation of the Rossby waves in very long wavelengths (10,000 km) eventually propagating into the stratosphere. Once here, it unloads its easterly momentum decelerating the westerly wintertime stratospheric jet stream a mechanism termed "wave breaking" that produces the phenomenon of stratospheric sudden warming causing thermodynamical imbalance consequently leading to wintertime radiational cooling. The colder

air being dense starts sinking and is balanced by a poleward transport of air from the tropics. The BDC is established as tropical air moving poleward to replace the sinking polar air and is itself replaced by rising air in the tropics (Cordero et al.,).

1.2.4 Transport in the upper troposphere lower Stratosphere

The UTLS plays a key role in general circulation as it is the place of entry of tropospheric air masses into the stratosphere (Holton et al. 1995). This transport to the tropics is responsible for transporting a large number of chemical species emitted at ground level into the stratosphere.

However, the importance of one in relation to the other continues to be an open debate since limited observations are available in the altitude range between 15 and 20 km above the tropical continental regions. (Cairo et al., 2009; Vernier et al., 2011) explored this area using balloons and aircraft.

This chapter will continue to explore general circulation in the atmosphere with a particular focus on tropical UTLS focusing on the transition zone, located in the UTLS, between the troposphere and the stratosphere called the TTL (Tropical Transition Layer). This will follow the examination of the different vertical transport mechanisms in the TTL that are proposed today, to finally conclude on the means that will be used in this thesis to try to provide elements of answer to the debate.

1.2.5 Need for troposphere stratosphere differentiation

The troposphere and stratosphere are two regions of the atmosphere enriched with different dynamical, chemical, and radiative properties. The troposphere at mid-latitudes lies between the ground and 12 km (Fig. 1.1) while its summit can reach 15-17 km in tropical regions. It is characterized by a negative thermal gradient favoring instability and vertical transport. The stratosphere begins approximately between 12-17 km and extends up to 50 km having a positive temperature gradient thereby making it, as its name suggests, the altitude that delimits these two regions. However, it is now established that this transition is not punctual but that there is a layer where we find the characteristics of the two regions, a transition zone called the TTL. Knowledge of the properties of this layer is fundamental since it is the "gateway" to the stratosphere through which all chemical species travel leading to a change in its balance. Transport in the stratosphere is then controlled by the Brewer-Dobson circulation (BDC).

1.2.6 The tropical Tropopause layer (TTL)

The TTL is indicated by the transition zone between the troposphere and stratosphere in the tropics between 14 and 18.5 km (Fueglistaler et al., 2009). It is an area where the dynamic, chemical, and radiative properties of the troposphere and stratosphere exist.

Fig. 1.3 describes the processes that occur and influence the balance of TTL. Tropospheric air masses transported in tropical convective systems reach about 14 km (200 hPa), zero buoyancy level (symbolized by the letter (a) in fig. 1.3. This level is close to that of Zero Radiative Heating (LZRH), above which the heater becomes positive (Corti et al., 2005). It is characterized by a minimum thermal gradient from which the static stability of the air increases, with however deep injections possible at higher altitudes beyond the thermal tropopause (minimum temperature) (h). The air then rises slowly by radiative heating (d) into the stratosphere where the Brewer-Dobson circulation takes over. The tropical stratosphere is limited at altitude by subtropical jets that act as a barrier defining a containment region called the "tropical pipe" (Plumb et al. 1996) (f), whereas exchanges are possible in TTL between the tropics and mid-latitudes.

However, there are still uncertainties in this view of the TTL. Among these, the vertical transport layer through this subject has been debated. Indeed, even if recent observations have shown the existence of rapid injections at high altitudes by overshoot (Nielsen et al., 2007; Khaykin et al., 2009; Corti et al., 2008), the contribution of this mechanism on a global scale compared to the slow rise by radiative heating is still subject of intense debate.

1.3 Vertical Transport in the TTL

As discussed above, rapid vertical transport in tropical convective systems followed by the slow ascent due to the "extratropical pump" leads to the transport of air from the troposphere to the stratosphere.

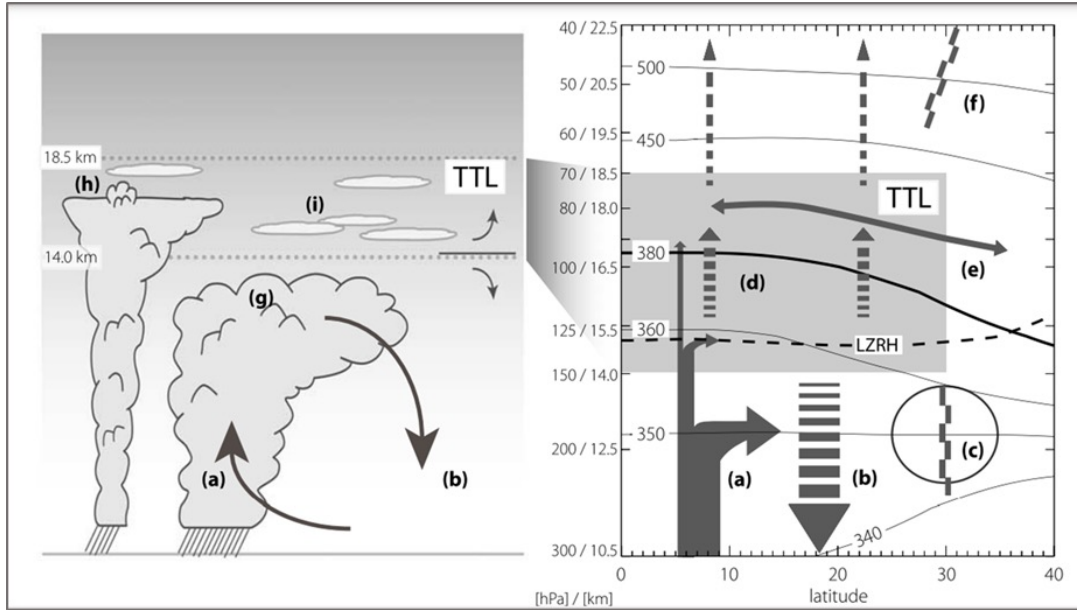


Figure 1.3: Schematic of cloud processes (left) and zonal mean circulation (right). Arrows denote circulation, the dashed line indicates a clear sky level of net zero radiative heating (LZRH). Black solid lines denote isentropes in K. Letters are associated with transport processes. (Fueglistaler et al., 2009).

However, even if global measures are available in this region (e.g. MLS, CO, N₂O), their vertical resolution, limited to ± 2 km does not allow one to conclude as to the dominant mechanism of vertical transport in the TTL (Richaud et al., 2007; Schoeberl et al., 2006). Two schemes compete with slow transport in several months by radiative heating and/or rapid transport by overshoots in a few hours.

1.3.1 Radiative heating

Radiative transfer is a branch of physics concerned with the interaction between radiation and matter. We speak of radiative heating when the material absorbs radiation to transform it into thermal energy. In the atmosphere, water, O₃, and CO₂ that are gases interact with the solar radiation incident in the ultraviolet and telluric infrared emission, producing cooling (e.g. emission in the IR of H₂O in the stratosphere) or warming (absorption of UV by stratospheric ozone).

The balance of these interactions leads to the establishment of a zero-heating level ($Q = 0$) under which the air tends to descend and above which it tends to rise. In the tropics and clear skies, this level is around 14 km or 360 K (Gettleman et al., 2004). The most common pattern today is that air is transported by convection up to 360 K or radiative heating takes over to lift it into the stratosphere.

In the TTL, the presence of fine clouds, shown in fig. 1.4 changes the radiative balance and induces additional heating. The effect is twofold due to global warming of the layer by absorption of IR radiation. Thus, radiative calculations show that the influence of thin cirrus clouds around 370 K (16 km) leads to an ascent of 0.2K/day (Corti et al., 2008). It could be the key element in transporting air at the mean level of convection around 14 km to the lower stratosphere. Another transport mechanism, leading to rapid ascent from the troposphere on account of strong convective overshoots was revealed by Danielsen et al. (1982, 1993).

1.3.2 Convective overshoot

Overshooting convective currents inject hydrated tropospheric air into the TTL, a process occurring only in limited regions. Strong updrafts associated with deep convection carry significant ice into the UTLS.

Evaporation of ice deposited in the UTLS results in saturation of the region, resulting in a moistening effect of the stratosphere. Air is lifted into the tropical upper troposphere from the surface by convection (Fig. 1.4) on account of the release of latent heat. This release alone can result in deep convection reaching a potential temperature of less than 360 K (Folkins et al., 2006). The transport of air from the

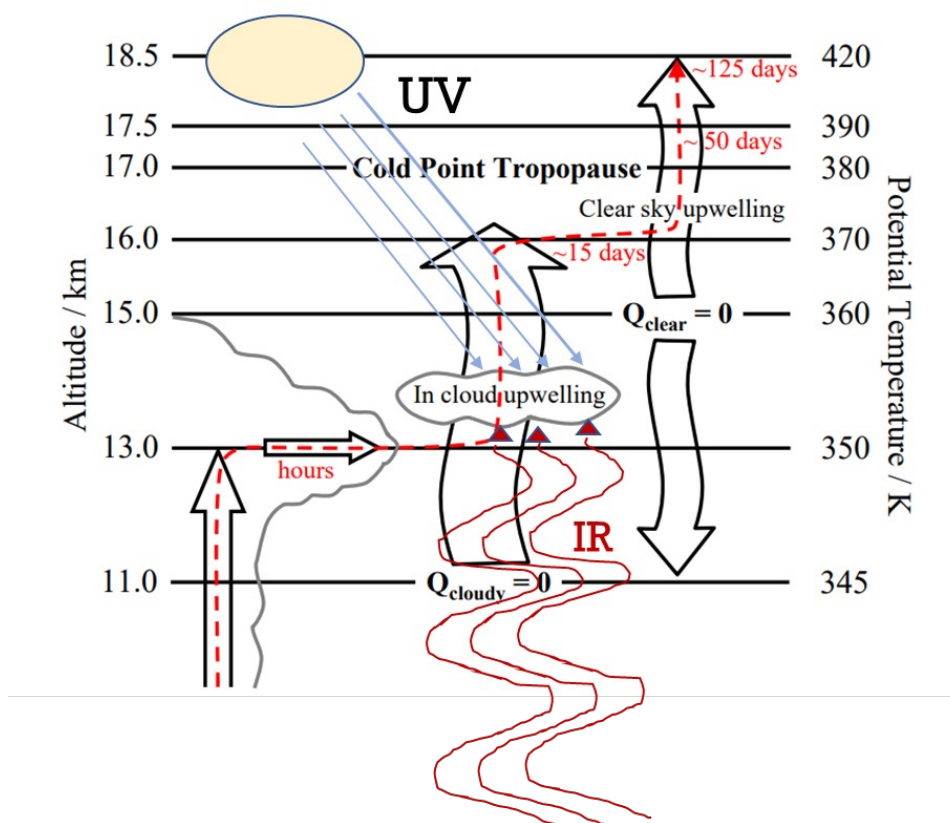


Figure 1.4: The above figure portrays the troposphere-stratosphere transport. On the left convection carries air up to 13-14 km. In the center, the radiative heating amplifies by the presence of cirrus clouds and lifts the air to the tropopause's cold point, supplemented by the slow ascent in the clear sky. The average transport time of the boundary layer is indicated in red. (Corti et al., 2005).

boundary layer to 13 km (350 K) occurs within minutes to hours. While some of this outflow stays within the cirrus clouds the rest is radiatively heated and lifted further. If it stays in the cirrus cloud for most of the time, after about 15 days it reaches 370 K potential temperature assuming typical mean heating rates of 1.5 K d^{-1} . At this altitude, it encounters upwelling thereby ascending at a slower rate. The mean full sky heating rate between 370 and 390 K amounts to 0.6 K d^{-1} , decreasing to 0.4 K d^{-1} at 420 K. The total transport times of 50 and 125 days are estimated from this starting from the boundary layer to 390 and 420 K. This transport mechanism generates a mass flux large enough to nourish the BDC thereby eliminating the need for the frequent occurrence of convective overshooting (Corti et al., 2005).

1.4 The Earth's radiation budget

1.4.1 Global Earth radiation budget

A substantially larger fraction of atmospheric shortwave radiation (5.2%) is reflected corresponding to increased aerosol loadings and clouds. On the contrary, a slightly smaller fraction of atmospheric shortwave absorption of 0.6% has been observed due to lower contents of water vapor. The outgoing longwave radiation (OLR) is balanced by the incoming and reflected solar radiation at the top of the atmosphere (TOA) to maintain climate equilibrium. However, the incoming solar radiation is either scattered by clouds and aerosols or absorbed by the buffering atmosphere (Trenberth et al., 2009; Wild et al., 2013a). The Earth's energy balance is the key driver of atmospheric and oceanic circulation, hydrological cycles, and different surface processes (Wild et al., 2008; Mercado et al., 2009; Wild et al., 2013a; L'Ecuyer et al., 2015). The variation of the atmospheric composition of greenhouse gases and aerosols as well as aerosol-cloud interaction agitate the forcings leading to uneven distribution of the TOA net radiation

thereby causing an impact on the anthropogenic influences on climate change (Trenberth et al., 2014; L Ecuver et al., 2015; Wild et al., 2019).

Figure 1.5 shows the contribution of the different elements involved in the daily energy flux in the Earth's atmosphere in W m^{-2} . The solar flux at the top of the atmosphere is about 1365 W m^{-2} on a plane facing the Sun at the mean Sun-Earth distance; the amount averaged over the entire planet is a quarter of this value (334 W m^{-2}). Part of the solar energy received (about 30%) constitutes albedo: it is directly reflected into space by molecules, clouds, and aerosols in the atmosphere (118 W m^{-2} in all-clear sky and 72 W m^{-2} in the clear sky) and by the earth's surface (35 W m^{-2} on all sky and 44 W m^{-2} on the clear sky). The rest of the radiation is absorbed by the atmosphere (77 W m^{-2} in all-sky and 72 W m^{-2} in the clear sky) and by the oceans and continents at the surface (39 W m^{-2} in all-sky and 190 W m^{-2} in the clear sky). The share of radiation not reflected and absorbed on the surface of the Earth constitutes an energy input for the oceans and continents which, at equilibrium, is compensated by an equivalent energy loss. This loss occurs either in the radiative form in the infrared or in the form of heat transfers related to conduction (sensible heat) or related phase changes of water (latent heat). The infrared radiation emitted is partly absorbed and then re-emitted by greenhouse gases and clouds. At equilibrium, the share transmitted to space must exactly compensate for the net solar radiation at the top of the atmosphere, allowing to have a zero balance between the incident radiation and the radiation reflexive.

Natural greenhouse gases play a major role in regulating the temperature, making life possible on Earth. But anthropogenic emissions disrupt this natural balance by causing global warming. Aerosols (section 1.1) also disturb this natural radiative balance. However, it is difficult to estimate their direct or indirect impact. Aerosols can incident solar radiation as well as thermal infrared flux.

1.4.2 Radiative impacts after a volcanic eruption.

Volcanic eruptions have the potential to cause a significant disturbance to the Earth's atmosphere by releasing material into the stratosphere, where it may persist for several years, depending on the magnitude and altitude of the eruption. The injected material can include ash, which typically remains in the atmosphere for a few months, and gaseous components such as water vapor, SO_2 , and HCl (Mc Cormick et al., 1995). Aerosols are formed when sulfur dioxide is transformed into sulfuric acid, which quickly condenses into aerosols due to its low saturation vapor pressure. These aerosols increase the Earth's albedo by reflecting solar radiation back into space, which results in the cooling of the Earth's surface (Fig. 1.6). The aerosols can also warm the stratosphere by absorbing upwelling infrared radiation. Eventually, the aerosols are transported into the troposphere, where they may modify cloud optical properties and further impact the Earth's radiative processes. Additionally, the eruption can lead to increased efficiency of heterogenous chemical processes, which can modify the chemistry of reactive chlorine and nitrogen, leading to ozone destruction. This process is similar to what produces the Antarctic ozone hole, except that in the case of volcanic eruptions, the surface is provided by the aerosols. The magnitude and duration of the cooling effect depend on the amount of SO_2 released, the altitude of the eruption, and the latitude of the eruption. Large volcanic eruptions can have significant radiative impacts on the Earth's climate, as seen in the cases of Mount Pinatubo in 1991 and Tambora in 1815. The eruption of Mount Pinatubo had a long-term significant impact on the climate as a result of the release of SO_2 gas leading to the formation of sulfate aerosols that persisted in the stratosphere for several years. As a result, sunlight was reflected into space causing a cooling effect on the surface of the Earth. The cooling effect of the Tambora eruption, for example, led to the "year without a summer" in 1816, which had widespread impacts on agriculture and human health in much of the Northern Hemisphere (Robock, 2000).

Resumé du chapitre 1 sur les aerosols et leurs transports a l'échelle globale

Les débats sur le changement climatique durent depuis près de sept décennies. Les changements climatiques sont attribués aux émissions anthropiques et naturelles qui contribuent aux modifications du climat de la Terre. Les gaz à effet de serre comme le CO_2 et le CH_4 jouent un rôle prépondérant dans l'interférence avec le bilan radiatif de la Terre. Cependant, un autre facteur important est la présence d'aérosols, tant anthropiques que naturels, dans l'atmosphère. Ces aérosols peuvent avoir un impact sur les conditions météorologiques en absorbant ou en diffusant le rayonnement solaire, ainsi qu'en influençant la formation des nuages et les régimes de précipitations. Les effets directs et indirects des aérosols sur l'équilibre radiatif de la Terre et la distribution des nuages sont sources d'incertitude pour les modèles climatiques, comme le souligne le rapport AR5 du GIEC. Une compréhension approfondie des aérosols est cruciale pour comprendre leur impact sur le climat et prévoir avec précision les épisodes de pollution atmosphérique. Ce chapitre se concentre sur la structure et la dynamique de l'atmosphère terrestre, en particulier la haute troposphère et la basse stratosphère (UTLS), et fournira des informations générales sur les propriétés optiques des aérosols ainsi que leurs impacts sur le climat.

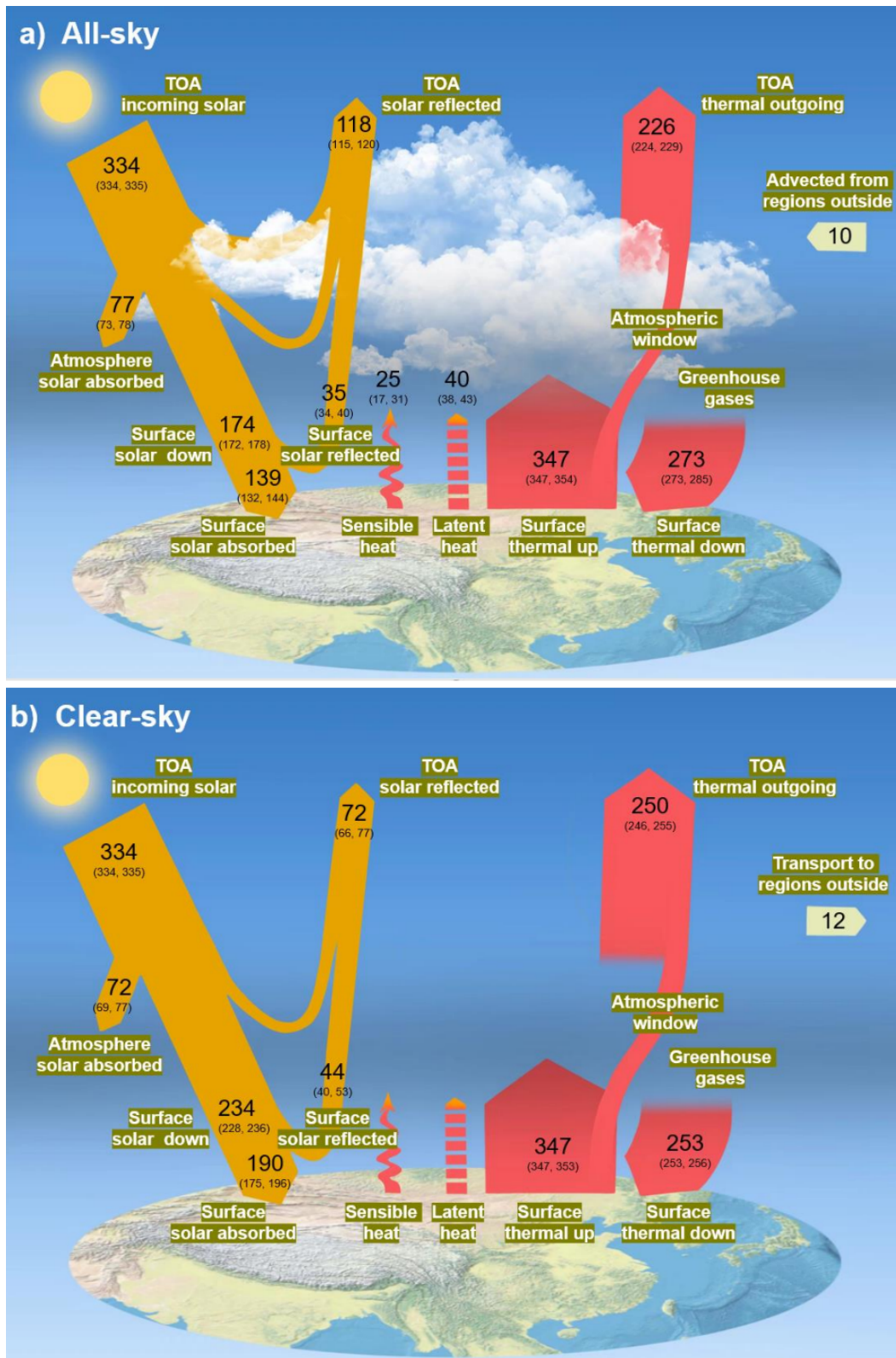


Figure 1.5: Diagrams of the annual land mean energy balance (Units: W m^{-2}) over East Asia under (a) all sky and (b) clear-sky conditions for the present-day climate. The uncertainty ranges are also given in parentheses. (Qiuyan Wang¹ et al., 2022).

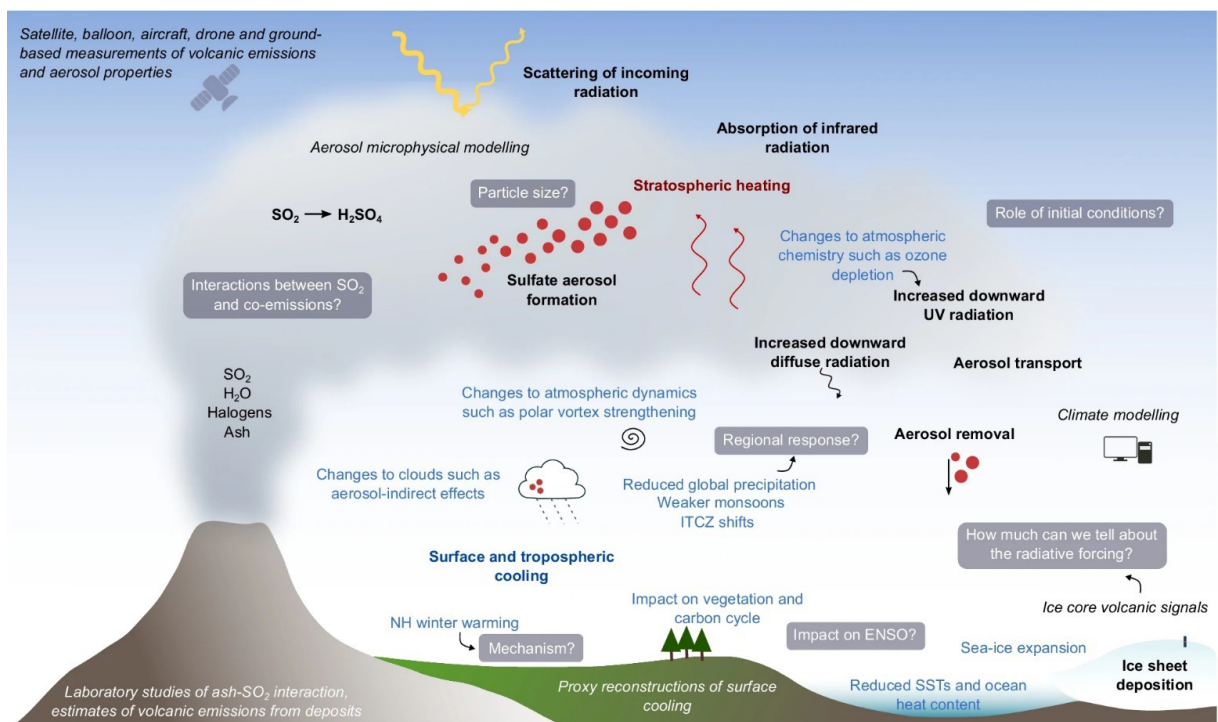


Figure 1.6: The Figure provides an updated summary of the major climate impacts resulting from a large-magnitude volcanic eruption and the processes that lead to them. These impacts are highlighted in blue, while the relevant processes are in bold. The methods used to study the effects of volcanic eruptions on climate, such as observations, proxy reconstructions, and modeling, are described in italic text. Key research questions that remain unanswered are presented in boxes (Marshall et al., 2022).

Chapter 2

Stratospheric aerosols- Observations, processes, and climatic impact



2.1 General introduction on aerosols

A complex mixture of chemical species and individual particles with varying shapes and morphologies define atmospheric aerosols. They are believed to form a major part of the atmospheric air originating from a variety of natural and anthropogenic processes. The morphology in addition to the chemical composition and physicochemical state of the surfaces reveal the “history” to a great extent, thus permitting us to reconstruct not only their origin but also predict their effects on the environment and ultimately, human health. Often denoted as suspended solid or liquid particles, this population plays a key role in several processes governing the atmosphere’s physics and chemistry. They are responsible for the absorption and scattering of solar radiation (Ravishankara et al., 2015), thereby altering the atmosphere’s and climate’s large-scale dynamics (Bellouin et al., 2005). In addition, they also serve as nuclei for cloud droplets and ice crystals (Andrae and Rosenfeld, 2008; De mott et al., 2015, 2010; Farmer et al., 2015), thus impacting radiative transfer (Penner et al., 2004). The fifth IPCC report released in 2013 states that aerosols derived from anthropogenic sources possess an average cooling effect of -0.82 W m^{-2} in contrast to 3.00 W m^{-2} which corresponds to the warming effect of well-mixed greenhouse gases.

2.2 Stratospheric Aerosol Discovery

Earlier measurements showed that a distinct layer of aerosols occurs in the stratosphere between 15-25 km altitude peaking at 20 km (Junge et al., 1961), and extending over a broader range of latitudes (Hofmann et al., 1975). The particles were believed to be formed from the chemical transformation of carbonyl sulfide (OCS) and sulfur dioxide (SO_2) which are in turn tropospheric sulfur-containing compounds, through processes like nucleation, coagulation, and condensational growth. Junge et al. claimed the existence of some stratospheric aerosols in the liquid state. According to their analysis, the particles in addition to containing sulfur were hygroscopic in nature. This was confirmed with balloon-borne measurements by Bigg (1975), and Farlow et al., (1977) and further validated by lidar measurements distinguishing spherical (probably liquid), from aspherical particles (Browell et al., 1990; Beyerle et al., 1994). Stratospheric aerosols are known to be sulfated liquid particles originating from the oxidation of sulfur injected during violent volcanic eruptions (e.g. Mt. Pinatubo in June 1991). However, early balloon measurements in these regions also noted that they were present even in periods without eruption (Junge et al., 1961). In this chapter, we will name stratospheric aerosols all particles that are not ice crystals or polar stratospheric clouds (PSC) between 15 and 40 km.

2.3 Processes controlling the stratospheric layer: overview

Processes like sedimentation and evaporation govern the top of the stratospheric aerosol (Hofmann et al., 1985), while the base of the aerosol layer is linked with the tropopause. The aerosol layer in the stratosphere without being influenced by major volcanic eruptions is often referred to as the “Junge layer”. The processes controlling the stratospheric aerosol layer formation and residence times have been closely associated with the processes controlling the sulfur in the stratosphere. The aerosol lifetime and distribution in the stratosphere are subject to intricate networking of (a) atmospheric transport as a consequence of direct injection like volcanic eruption resulting in troposphere-to-stratosphere exchange, in addition to the transport of tropospheric precursor gases past the TTL, together with stratospheric transportation account for the large-scale Brewer-Dobson circulation (BDC) and, (b) aerosol, formation, growth, and removal by sedimentation in the air crossing the extratropical tropopause thereby altering aerosol chemistry and microphysics. Fig. 2.1 depicts the pertinent processes that control the distribution and lifetime of aerosols in the stratosphere.

1. Surface emission of primary aerosols and aerosol precursor gases from natural and anthropogenic sources.
2. The conversion of trace gases into sulfuric acid (H_2SO_4) and oxidized organic compounds in the tropical upper troposphere.
3. Nucleation of these compounds to new aerosol particles or condensation to existing particles, thus increasing the aerosol mass. The aerosols and trace gases from the TTL layer are transported into the stratosphere.

4. Large-scale vertical advection.
5. Oxidation of trace gases leads to the formation of additional aerosols (largely carbonyl sulfide, OCS).
6. Transportation into the stratosphere. Aerosols and trace gases formed on account of volcanic eruptions in addition to pyro-convective systems potentially injected into the stratosphere thereby enhancing the aerosol population.
7. Meteoritic smoke particles plunge from the mesosphere constitutes condensation nuclei for H_2SO_4 in the upper stratosphere impacting the stratospheric aerosol size distribution.
8. Processes like sedimentation and stratosphere-troposphere exchange lead to the purging of aerosols from the stratosphere in addition to the descent into the troposphere in the downwelling current of the BDC at middle to high latitudes.
9. Finally, in the upper stratosphere, evaporation processes occur.

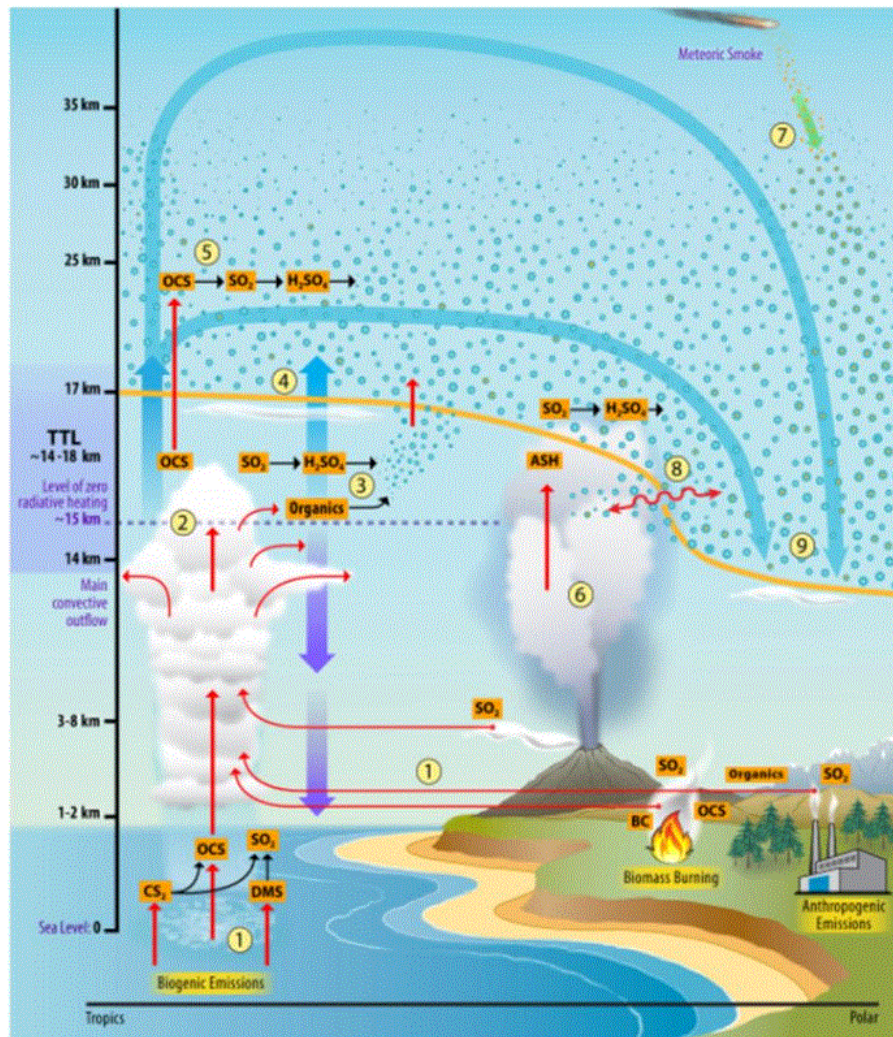


Figure 2.1: (Adapted from Thornberry et al., 2021) shows the processes contributing to the formation, transport, and removal of stratospheric aerosols.

2.4 The Junge Layer

Volcanic eruptions have been known to be one of the main sources of aerosols in the stratosphere. The first observation of an apocalyptic twilight following an eruption was observed in the tropical regions as a result of the eruption of the Krakatoa volcano in 1883 transporting volcanic particles into the stratosphere (Russell et al., 1888). The persistence of aerosols in the stratosphere during non-volcanic periods was observed at dusk in the early twentieth century. However, it was not until the 1950s that the use of balloon impactors confirmed their presence. These first observations revealed an increased number of large particles ($r > 0.15 \mu\text{m}$) around 20 km whose chemical composition was determined by studying their vaporization temperature corresponding to a mixture of 75% sulphuric acid (H_2SO_4) and 25% water vapor (Rosen et al., 1964). These particles were termed to be large enough to scatter sunlight, and their effect was observed from the ground from where they were first partially identified. From these first observations, optical instruments were developed onboard balloons or aircraft for in situ measurements subsequently global from satellites, to understand their origin. The Junge layer (Fig. 2.2) around 25 km is a permanent layer composed of mainly liquid sulfate aerosols



Figure 2.2: A view of Earth from space, visualizing the stratospheric aerosol layer (Junge Layer in red) Credit: Timothy Marvel, NASA/SSAI, Hampton, Va.

2.5 Microphysical properties

Several microphysical processes govern aerosol composition, size distribution, population, and residence time. Stratospheric aerosols are influenced by five major processes: nucleation, coagulation, condensational growth, evaporation, and sedimentation. Only a brief description is provided below.

2.5.1 Nucleation

In the stratosphere, gaseous H_2SO_4 undergoes rapid condensation due to the supersaturation of its partial vapor pressure. The preferred process in new aerosol formation involves the co-condensation of H_2SO_4 and water via binary homogenous nucleation (Hamill et al., 1990; Curtius et al., 2005) at low temperatures, low particle surface areas, and high relative humidity. The beginning of gas-to-liquid heterogeneous nucleation is believed to occur in the presence of condensation nuclei like ions or meteoritic smoke particles at much lower saturation ratios (Merikanto et al., 2007). Until now there's limited information on the impact of non-sulfate material on stratospheric aerosol formation on a global scale (Brock et al., 1995). The TTL is the main nucleation region for stratospheric aerosols (Weigel et al., 20101) and the polar middle stratosphere (Campbell et al., 2014).

2.5.2 Coagulation and Condensation

Newly formed aerosols can continue growing through the process of coagulation, and condensation. The process of collision and the combination of aerosols varying in size and composition to form a single large particle defines coagulation. It depends on the aerosol number concentration. The condensational growth through the uptake of water and H_2SO_4 is chiefly controlled by H_2SO_4 uptake together with

its concentration in addition to its thermodynamic properties and ambient temperature. Nucleation of new particles and coagulation occurs at short time intervals (Deshler, 2008), and higher number concentrations. Condensational growth and evaporation are known to occur during the aerosol lifetime in the stratosphere. The growth rate of freshly nucleated particles is considerably slow (Jacob, 1999).

2.5.3 Evaporation and Sedimentation

The microphysical processes of evaporation and sedimentation are partly responsible for the spatially distributed distinct aerosol layer. In the stratosphere, while evaporation redistributes sulfur between the particulate and the gas phase, sedimentation redistributes sulfur irreversibly downward thereby leading to its transport accompanied by a loss in the troposphere. In the tropical stratosphere, aerosols are transported upward by the BDC. This elevation involves size segregation since larger aerosols move slowly upward or downward depending on their size. Hence, stratospheric aerosols are believed to be small particles (radius $< 0.2 \mu\text{m}$) during a volcanic-free period (SPARC, 2006). The aerosol undergoes evaporation on moving to a warmer environment. Therefore, all sulfur dwells in the gas phase in this region (17 km). The aerosol concentration is said to decrease rapidly near this altitude. The gas phase sulfur is transported to higher latitudes eventually where it encounters lower temperatures favorable for condensation to sulfate aerosols. As they grow, stratospheric aerosols are then removed during transport to mid and high latitudes by sedimentation. The extensive transport and diabatic mixing of aerosols together with the above processes result in a quasi-steady relative maximum in particle number concentration at the Junge layer (Deshler, 2008).

2.6 Sources of Stratospheric aerosols

The stratospheric aerosol layer originates from the input of aerosol and precursor gases (fig. 7), mainly like OCS (Crutzen, 1976) in addition to nonvolcanic SO_2 (Thomason et al., 2006) together with tropospheric sulfate particles (Brock et al., 1995). As the air masses ascend through the TTL (Fueglistaler et al., 2009), they witness the removal of a considerable amount of aerosol and soluble precursors on account of uptake by ice particles following sedimentation. On the other hand, OCS and other insoluble sulfur-containing gases tend to reach the stratosphere depending on their residence time during transport, dehydration, and washout processes (Sinnhuber and Folkins, 2006; Aschmann et al., 2011; Dinh and Fueglistaler, 2014). Volcanic emissions are the main sources of direct injection of SO_2 into the stratosphere thereby resulting in enhanced aerosol concentration residing for many years.

2.6.1 Sulfate aerosols

The oxidation of the sulfur precursor gases results in the formation of gaseous H_2SO_4 . This process is followed by the combination of sulfuric acid with water molecules forming water droplets of sulfuric acid. Figure 2.3 shows the longest available series of stratospheric aerosol measurements from the Garmish lidar station in Germany (47.5°N). The evolution of the backscatter coefficient at 694.3 nm shows the alternation between periods called "background aerosols" indicating a permanent flow and volcanic injections. The main eruptions were those of El Chichon (17°N , April 1982, Mexico) and Mt Pinatubo (15°N , June 1991, Philippines). Outside volcanic periods, there is no indication of an increase in stratospheric aerosol loading due to anthropogenic emissions. However, the discovery of the ATAL in the early 2010's suggests that pollution in Asia contributes significantly to UTLS aerosols in the absence of volcanic eruptions.

2.6.2 Carbon oxysulfide

Carbon oxysulfide (OCS) is emitted from anoxic surfaces, oceans, and volcanoes, and is known to be the most abundant of all gases leading to SO_2 formation in the stratosphere. OCS is formed from the oxidation of dimethyl sulfate (DMS) produced by ocean plankton and carbon sulfide (CS_2) emitted by industry and the marine environment. Its long lifespan of several years and low solubility allows it to be transported to the stratosphere where a fraction of OCS is oxidized to SO_2 and then H_2SO_4 , while the rest returns to the troposphere following the general circulation (Crutzen et al., 1976). It is therefore responsible for maintaining the stratospheric sulfate aerosol layer in the non-volcanic period. The capture of OCS by plants and soils as well as its oxidation by OH radicals are the main wells. The OCS cycle shows

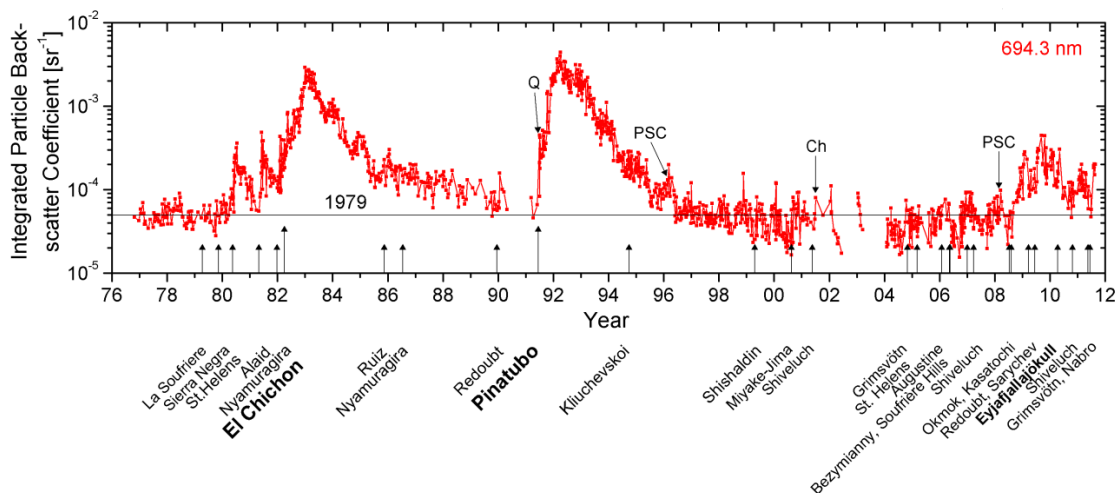


Figure 2.3: Integrated backscatter coefficient of at 694.3 nm measured by lidar in Garmish (Germany) from 1 km above the tropopause to the moment of layering. The position at the time of the main eruptions is indicated by arrows ([http:// www. Imkifu.kit.edu/331.php](http://www.Imkifu.kit.edu/331.php)).

seasonal variation with a maximum in summer when production from marine plankton is maximum. This simplified pattern is complicated by interference with the geographical distribution of sources and sinks and transport, which implies that the OCS cycle is not fully understood (Irion et al., 2002).

2.6.3 Sulfur Dioxide

Sulfur dioxide is believed to originate naturally from either, volcanic emissions or associated with pollution. Anthropogenic SO_2 comes from the combustion of wood and carbon by urban heating (e.g. sulfurous fog, London smog at the end of the 19th and early 20th century), thermal power plants, and forest fires. The transport of sulfur residue in petroleum products through sea, air, and land is also among the sources. Air quality monitoring stations have been measuring ground-level emissions of SO_2 for many years. Its maximum concentration during the 1980s in the United States and Europe, since then shows an estimated reduction of 85-95%. A decrease was also observed in SO_2 levels emitted by air traffic. However, levels in emerging countries such as China, India, and Brazil have increased markedly in recent years (Notholt et al., 2006). Since tropical regions are the preferred areas for transport from the troposphere to the stratosphere, one of the questions is whether these emissions have an influence on the stratospheric aerosol layer. The geographical distribution of SO_2 depends on the places of production and its presence in the TTL of the mode of transport owing to the fact that it has a short lifespan of a few months. SO_2 observations from the upper troposphere have been rare. The NASA PEM and ACE 1 campaigns on the Pacific Ocean revealed interhemispheric differences of an order of magnitude, with a decrease of 100-200 pptv in the altitude range of 4-12 km. The contribution of sulfur transport by convection to the TTL is still uncertain since the transport mechanisms themselves in this region are subject to debate. The total column of sulfur dioxide in the atmosphere is currently measured from space using spectroscopic, infrared (IASI/METOP) and microwave (MLS/Aura), and UV-visible scattering (OMI/Aura or Tropomi) techniques. The latter uses a spectrometer looking at the light scattered at Nadir with a sensitivity to detect both weak volcanic eruptions and anthropogenic SO_2 emissions in Asia and the West (<http://so2.umbc.edu/omi/>).

2.6.4 Dimethyl sulfur, carbon disulfide,, and hydrogen sulfide

Among other gases, dimethyl sulfur (DMS) is produced mainly by seaweed. In the lower troposphere, its lifespan is only a few hours because it oxidizes very quickly to SO_2 . Its presence at high altitudes is therefore only possible by rapid transportation. PEM-West A & B campaigns have shown that DMS can be injected into the upper troposphere and sometimes even into the tropopause during intense convective events (Thornton et al., 1997). Carbon disulfide (CS_2) is observed over continents and originates in volca-

noes and swampy areas. Anthropogenic emissions of CS₂ come from the textile industry. Pollutants such as carbon monoxide (e.g. CO) from northern China show a strong correlation with this compound (Blake et al., 2004). Hydrogen sulfide (H₂S) measurements are quite rare, leading to significant uncertainties relating to its life cycle. The few observations on board aircraft and ships seem to favor the anthropogenic origin of this gas, the maximum of which is observed on the continents.

2.7 Sulfur balance and flux

Anthropogenic and natural emissions (volcanoes) are the 2 major sources of sulfate gases in the atmosphere with a total flux between 89 – 102 Tg S/year (Tg: 1 million tons sulfur) between 1980 and 1990. Today, anthropogenic SO₂ would represent about 70 to 80% of total emissions (Thomason et al., 2006). The other gases, OCS, CS₂, DMS, (CH₃)₂CO, and H₂S emitted in smaller quantities can be separated into two main families: OCS (and its precursors CS₂ and DMS) with a lifespan of several years and the rest of the sulfated species that remain only a few hours in the atmosphere. Fig. 2.4 represents a flow balance of precursor gases in the atmosphere. OCS emissions are of the order of 0.7 Tg S/year. Although weaker than other sulfated species, its long residence makes it an important precursor gas that contributes to increased aerosol loading in the stratosphere (Crutzen, et al., 1976). An imbalance in the OCS budget was highlighted by Chin and Davis 1993. It has made it possible to review the effect of soils that act not as a source but as a sink. On average, erupting volcanoes release approximately 11.9 Tg of SO₂ per year, accounting for 6% of the total flux. This estimated annual SO₂ output is about 23% higher than the most recent estimate derived from direct measurements but its impact on the stratosphere is important because it is injected directly at high altitudes where its lifetime increases. The stability of SO₂ depends on the concentration of OH radicals and its mode of transport. The other reduced gases, H₂S, and (CH₃)₂SH have a secondary influence on the sulfated species content of the atmosphere because they have short lifetimes and their flux does not exceed 3 – 7 Tg S/year. Because of its very long lifespan, OCS is therefore the majority precursor gas in the middle and upper stratosphere. On the contrary, even though anthropogenic SO₂ is abundantly produced at ground level, its presence at higher altitudes requires that it be injected into the TTL or higher by deep convection.

Knowledge of vertical transport processes are therefore essential to assess the quantities of SO₂ capable of reaching the stratosphere. The other major uncertainty lies in the concentrations of OH and HO_x that lead to the oxidation of sulfate species and whose estimates have been revised upwards by a factor of 4 (Thomason and Peter., 2006).

2.8 Volcanic eruptions

Volcanic eruptions have historically been the primary natural cause of climate change, and studying their impact is crucial for understanding climate responses and predicting future volcanic influences on society. The effects of eruptions on climate are well-established: sulfur dioxide (SO₂) emitted during eruptions forms sulfate aerosols that scatter solar radiation, resulting in negative radiative forcing. When injected into the stratosphere, where the aerosols can persist for years, eruptions can cause significant surface cooling by reducing insolation. Sulfate aerosols also absorb infrared radiation, leading to stratospheric heating. These cooling and heating effects have cascading impacts, including changes in precipitation, ocean heat content, atmospheric circulation, and even ozone depletion. The introductory figure in Chapter 1 provides a summary of climate impacts resulting from large-magnitude eruptions (defined as explosive eruptions injecting more than 5 Tg of SO₂ into the stratosphere). However, understanding the intricate details of these broader impacts is challenging due to limited observations following such eruptions. The majority of our knowledge stems from studying the 1991 eruption of Mt. Pinatubo, the most recent large-magnitude eruption. Discrepancies between climate model results and observed/reconstructed responses highlight that our understanding is still incomplete. Further research is needed to improve our comprehension of volcanic impacts on climate. Significant progress has been made in the field of volcanic effects on climate over the past two decades, even in the absence of large-magnitude eruptions. Comprehensive datasets now exist for volcanic sulfur dioxide (SO₂), sulfate aerosols, and aerosol extinction, collected through ground-based, balloon, and satellite measurements ((e.g. Carn et al. 2016; Kremser et al. 2016; von Savigny et al., 2020). These datasets provide better constraints on volcanic emissions, offering daily and near-global observations of SO₂ and aerosol dispersion (Carn 2021; Fisher et al. 2019). Advancements in satellite

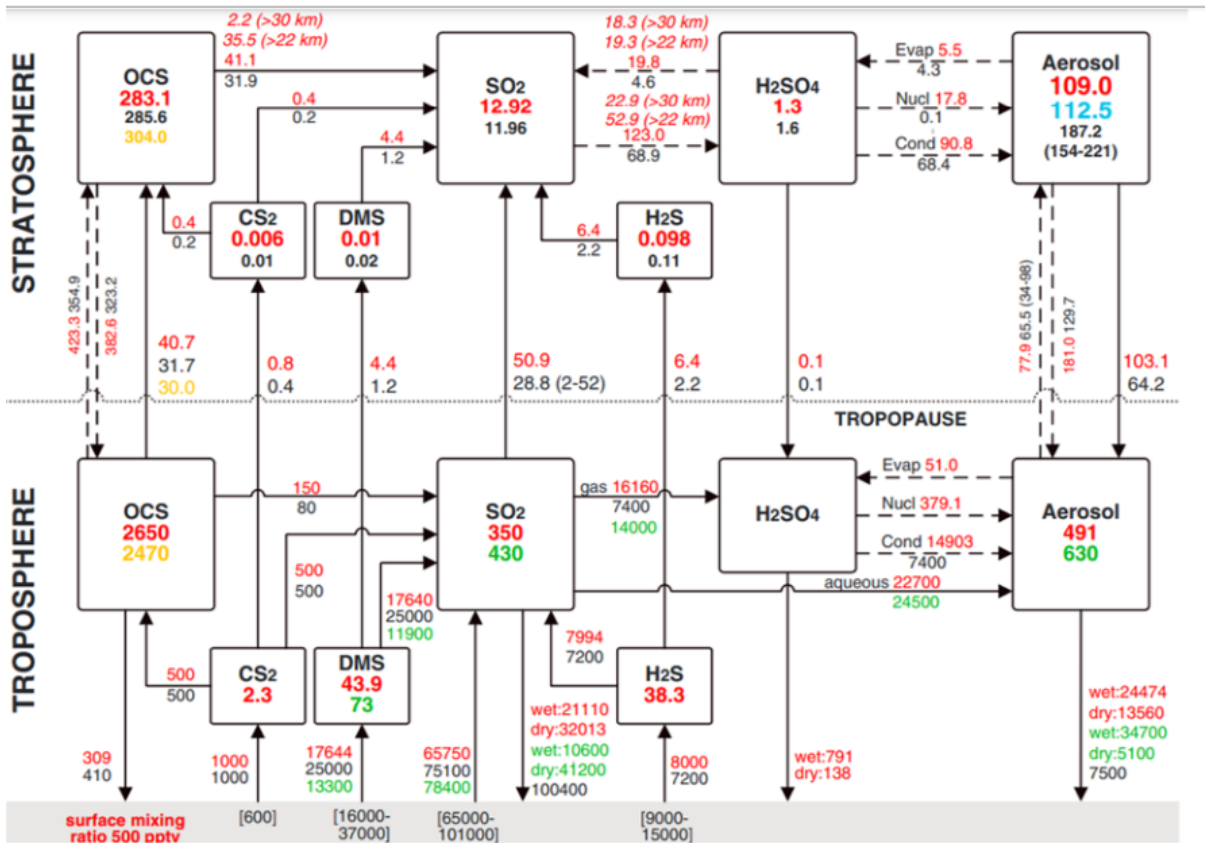


Figure 2.4: Sheng et al. [2015] presented a global balance of atmospheric sulfur (above), where solid arrows indicate net surface emission fluxes, tropopause, sinks, physicochemical sources, and microphysical transformations in Gg of sulfur per year. Dotted arrows indicate the flow in one direction and provide details of microphysical and chemical conversions. Boxes represent tanks of compounds expressed in Gigagrams of sulfur. Red data are from the Socol-ARE model, black data from SPARC (2006), green data from the GOCART model, and orange data from Chin and Davis [1995]. Finally, blue data represent measurements from SAGE II

retrieval algorithms have also allowed for improved estimates of past eruption emissions, such as the 1991 Mt. Pinatubo eruption. The development of the Global Space-based Stratospheric Aerosol Climatology (Glossac) has provided a continuous record of stratospheric aerosol optical properties ((Kovilakam et al. 2020; Thomason et al. 2018)). It has been observed that the variability of stratospheric aerosols since 1998 has been primarily influenced by small-magnitude eruptions (<5 Tg SO_2) ((Solomon et al. 2011; Vernier et al. 2011)), which have also offset some anthropogenic greenhouse gas forcing. This recognition marks a shift from the traditional understanding that only large stratospheric-injecting events have a significant climate impact, although large eruptions still have more substantial impacts per event. Observations and aerosol modeling, particularly following the 2014-2015 Holuhraun eruption in Iceland, have revealed that eruptions releasing gases primarily into the troposphere can increase cloud reflectivity through an aerosol interaction known as the aerosol-indirect effect, leading to additional radiative forcing ((e.g. Gettelman et al. 2015; Malavelle et al. 2017; McCoy and Hartmann 2015; Schmidt et al. 2010; 2012)). Reconstructions of past temperature variability and volcanic radiative forcing have also improved, providing more details about past volcanic eruptions and their potential impacts. Ice core sulfate concentrations have long been used to identify eruption occurrences and estimate their impact on climate. New reconstructions based on ice core records have provided updates on stratospheric SO_2 emissions, eruption latitudes, and stratospheric aerosol optical depth over the last 2,500 to 10,000 years, improving upon previous reconstructions with large uncertainties and discrepancies. These reconstructions are crucial for climate model simulations and for comparison with temperature reconstructions. Additionally, new large-scale tree-ring reconstructions of Northern Hemisphere surface temperature have highlighted

the dominant role of volcanic eruptions in preindustrial climate variability, capturing rapid temperature changes more accurately and reducing long-term memory effects.

2.9 Other sources of aerosols

2.9.1 Smoke aerosols from wildfires

Biomass burning is considered to be one of the important nonvolcanic contributors to the stratospheric aerosol load (Cammass et al., 2009). The influence of wildfire-induced thunderstorms on the Earth’s stratosphere has generally been considered insignificant. However, the North American wildfires in August 2017 presented a notable change in this understanding. The formation of pyro-cumulonimbus (pyroCb) clouds during this event resulted in substantial perturbations within the stratosphere. These perturbations surpassed the magnitudes observed in previous extreme pyroCb activities by an order of magnitude and approached the impact typically associated with a moderate volcanic eruption (khaykin et al., 2018; Peterson et al., 2018). During July-August 2017, severe forest wildfires occurred in northwest Canada and the United States, specifically near Lake Athabasca (NASA Earth Observatory, 2017). The resulting smoke from these fires moved north and northeast, forming a thick plume that broke records. On August 15, the aerosol index (AI) value recorded by the Ozone Mapping and Profiling Suite (OMPS) on the Suomi NPP satellite reached 49.7 (Seftor, 2017), which was approximately 30% higher than previous record values observed after the Australian Black Saturday fires in 2006 (Fromm et al., 2006) and Canadian Chisholm fires in 2001 (Fromm, Torres, et al., 2008). It is important to note that AI values are influenced by both the optical thickness and altitude of the plume (Torres et al., 1998). The exceptionally high AI values suggest that the smoke plume was lifted above the tropopause, allowing it to be carried and dispersed laterally by the polar jet stream. Various methods, including satellite instruments with nadir and limb viewing capabilities, as well as ground-based, airborne, and balloon-borne sensors have been used to assess the stratospheric consequences of intense (PyroCb) events. Several studies have examined the fire plume above western and Central Europe using lidar observations. Model calculations have shown that a significant portion of the fire plume in the stratosphere was rapidly transported toward the poles, influenced by the computed black carbon (BC) content (Ditas et al., 2018). The impact of aerosol plumes from wildfires in the lowermost stratosphere on the radiative balance and climate has been discussed, with a global average direct radiative forcing at the top of the atmosphere (TOA) from biomass burning aerosols estimated to reach -0.20 W m^{-2} . This estimate includes biomass-burning plumes, the affected background atmosphere, and both absorbing and scattering aerosol components (Ditas et al., 2018). Kloss et al., 2019 investigated the transport of the Canadian fire plume in the Asian monsoon area. Two sub-regions were distinguished: (1) the main Asian monsoon region ($15^\circ - 45^\circ\text{N}$, $40^\circ - 110^\circ\text{E}$) and (2) the Asian Monsoon Anticyclone (AMA) box in 2017 ($25^\circ - 38^\circ\text{N}$, $40^\circ - 95^\circ\text{E}$). The AMA center was identified using a maximum in the potential vorticity (PV) gradient on the 380 K isentrope. The circumpolar vortex associated with the AMA was strongest in July and gradually weakened by the end of September. Aerosol extinction values from the SAGE III data set revealed a significant increase in aerosol signatures above 40°N in the middle to end of August, following the major fire event in Canada. This finding aligns with previous studies that also observed heightened aerosol signatures in the Northern Hemisphere at higher latitudes during this time period. The aerosol signature gradually descended at an approximate rate of 0.64 mm/sec in altitude between November 2017 and March 2018, similar to the expected rate of the downwelling Brewer-Dobson circulation. Enhanced aerosols persisted in the lower stratosphere until mid-April 2018. Within the inner AMA region, the first appearance of the fire plume signature was observed on August 30, 2017, at altitudes of approximately 17 km suggesting that the fire plume reached the Tropical Tropopause Layer (TTL) region in the Asian monsoon area, potentially bypassing the AMA on its upper part due to the transport barrier. The fire plume signal remained visible in April 2018, indicating its long-lasting presence even after the breakdown of the AMA confinement. Figure 2.5 shows the enhanced aerosols due to the fire originating from the plume ((Kloss et al., 2019).

2.9.2 Asian Summer Monsoon Transport

The largest source of stratospheric aerosol transport in the absence of volcanic injections is the transport from the tropical upper troposphere (Brock et al., 1995). Studies have shown that the Asian summer monsoon anticyclone (ASMA) creates a “bubble” of tropospheric air above the zonal mean tropopause (Pan et

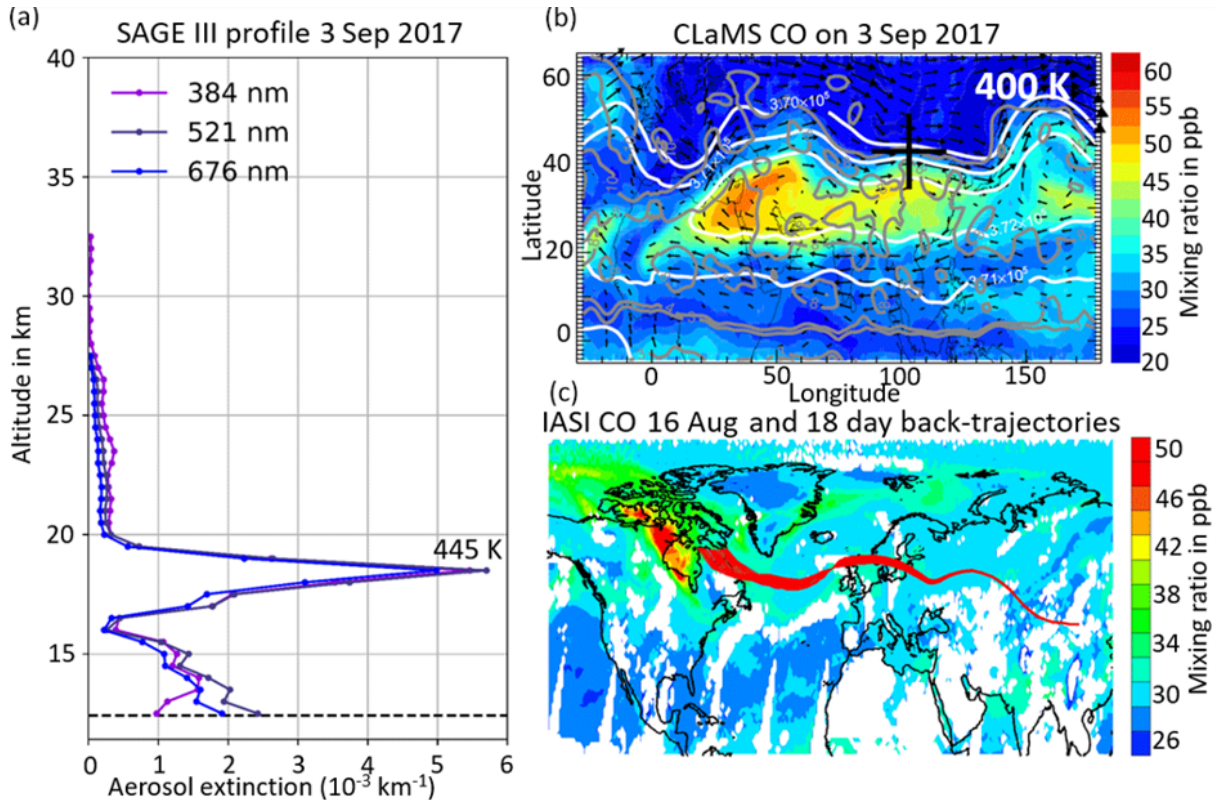


Figure 2.5: Profile showing an enhanced aerosol layer due to the fire, originating from the plume. at 42.94°N and 103.8°E . (a) The given tropopause height by the SAGE III data set is represented by the dotted line. (b) CLaMS CO map at 400 K on 3 September 2017. (c) IASI CO map, integrated over 12 h at 85.18 hPa, 18 d before the SAGE III profile measurement in (a). Superimposed: every fifth of the 1000 18 d TRACZILLA kinematic back-trajectories initialized at the geographical position and altitude of the fire plume peak in (a).

al., 2016) and may adequately transfer tropospheric air into the stratosphere (Randel and Park2006; Park et al., 2007). Deep convection in the ASM is known to serve as a conduit for the transport of boundary layer pollutants (CO , HCN , CH_4) to the UTLS, as revealed by researchers using satellite observations and modeling studies (Bergman et al., 2013; Park et al., 2007; Randel and Park 2006; Randel et al., 2010). Within the ASM, the pollutants are believed to accumulate in closed anticyclonic aberrations of low potential vorticity. This accumulation is fueled by strong gradients in potential vorticity along the subtropical jet in the northern flank and tropical easterlies on the southern side, limiting the exchange of air between the inside and outside area of anticyclonic flow forming the Asian Summer Monsoon Anticyclone (ASMA) (Fairlie et al., 2020). The Rossby wave breaking at the subtropical jet is responsible for the dispersion of air masses eastwards in addition to the enduring exchange of air with the extratropical lower stratosphere (Vogel et al., 2016). Simultaneously, descent into the easterly flow in the tropical upper tropopause results in the scattered air masses westward and consequent ascent into the lower stratosphere (Garny and Randel, 2016). An accompanying aerosol peak between 13 – 18 km in the ASMA was revealed by satellite measurements. Vernier et al (2011) used CALIOP lidar observations and SAGE II satellite data from the late 1990s to unveil the occurrence of the Asian Tropopause Aerosol Layer (ATAL) (Thomason and Vernier, 2013).

2.9.3 The ATAL

An enhanced aerosol layer was observed every year during the Asian summer monsoon (June-August) extending from the eastern Mediterranean across India to western China and vertically at about 13-18 km altitude. Ground-based Lidar measurements and optical particle counters revealed the optical and geometrical properties of the layer implying that the layer is comprised of very low depolarizing and small

particles. In addition, the layer is believed to also contain minute dust particles, together with soot, new particles formed in situ, growing of particles on pre-existing aerosols (Vernier et al., 2011). Since the ATAL was observed during the Asian monsoon, deep convection is believed to be the source of conduit for transporting primary aerosols and their precursors into the UTLS. The horizontal movement of aerosols within the anticyclone in addition to the vertical transport pathways in the troposphere is responsible for balancing the intensity of the ATAL during the ASM season. As seen in Figure 2.6(a), deep convection over the Bay of Bengal (BoB) plays a leading role in transporting carbon monoxide vertically from the polluted boundary layer to the UTLS within the anticyclone where the equatorial easterly jet further transports them westwards. The aerosol particles and precursor gases might be partly removed from the UTLS at approximately 70°E by the large descending motion thereby reducing the concentration in the western part of the ASMA. Researchers observed that together with the large-scale ascending circulation within the eddy shedding at proximities within the anticyclone, (Park et al., 2007; Garny and Randel 2013, 2016), the downward descent of the anticyclone contributes towards an aerosol sink in the UTLS responsible for maintaining a balance in the intensity of the ATAL. In addition, the Northeastern part of the anticyclone is another location of wave breaking and escape toward the Pacific Ocean. Fig. 2.6 (b) shows an intense uplifting of CO fueled by the intersection of the tropopause with 100 hPa level in addition to the tropical easterly jet and subtropical westerly jet which confines the CO enhancement to the south and north respectively (Pan et al., 2016).

2.9.4 Chemical composition of the ATAL and stratospheric aerosols

The concentration of aerosol particles is higher in the lower stratosphere compared to both higher and lower altitudes. Initial measurements conducted using balloon-borne impactors and U2 aircraft flights provided valuable insights into the composition of stratospheric particles. These studies, carried out by Junge et al. (1961), Junge (1963), and Mossop (1963), revealed that sulphur was a major component of the particles, and they were predominantly water-soluble. Following the eruption of Mount Agung, Mossop (1964) detected the presence of mineral-rich ash particles in addition to sulphate. However, the precise chemical form of the sulphate remained unknown initially (Toon and Farlow, 1981). Various possibilities, including ammonium sulphate (Junge and Manson, 1961), sulphuric acid, and other sulphur compounds, were considered by researchers (Bigg et al., 1970). Murphy et al. (2014) explored the stratospheric aerosol layer using the Particle Analysis by Laser Mass Spectrometry (PALMS) instrument on the NASA WB-57F. They concluded that almost all the stratospheric aerosol particles measured by PALMS can be classified into three primary categories: (1) sulphuric acid particles accompanied by metals resulting from meteoroid ablation, (2) predominantly pure sulphuric acid particles with associated water, and (3) organic-sulphate particles originating in the troposphere (Murphy et al., 2007). In addition, the majority of accumulation mode particles in the troposphere were found to consist of mixtures of carbonaceous compounds and sulphates, originating from various sources like biomass burning, industrial and combustion engine emissions, as well as the secondary accumulation of oxidation products from CH_4 and volatile organic compounds. Dust, sea salt, and other particle types constitute less than 10% of accumulation and coarse mode particles in the upper troposphere. Schwarz et al. (2006) conducted measurements of black carbon in the Northern Hemisphere midlatitude stratosphere using a single-particle soot photometer (SP2) in November 2004. Vertical profiles were obtained from the tropopause to nearly 19 km. The results showed black carbon mixing ratios ranging from approximately 1 to 3 ng kg^{-1} of air, accounting for about 0.2 – 0.4% of the aerosol mass. In the tropical region, black carbon constituted around 0.1 – 0.3% of the aerosol mass 2 km above the tropopause (Schwarz et al., 2008). The mixing state of black carbon in the tropical data indicated that nearly 80% of the particles at approximately 19 km altitude near Costa Rica were internally mixed with non-black carbon material. Additionally, the ratio of non-refractory to total particle mass averaged close to 0.9, suggesting that black carbon was a minor component of the entering stratospheric particles. The PALMS instrument, capable of identifying large, uncoated black carbon particles, confirmed that such particles constituted less than 1% of the analyzed stratospheric particles, consistent with the SP2 estimates that uncoated black carbon particles are rare in the stratosphere. Soot particles, identified through morphology, were measured using electron microscopy of the conventional impactor and wire impactor samples. Sheridan et al. (1994) found that among 1778 stratospheric particles, only one was identified as soot, primarily sampled near 20 km. In contrast, Strawa et al. (1999) inferred that soot concentrations were approximately 1% of the concentration of sulfate-rich particles around 20 km in the mid-latitudes. However, there were corrections needed due to the bounce

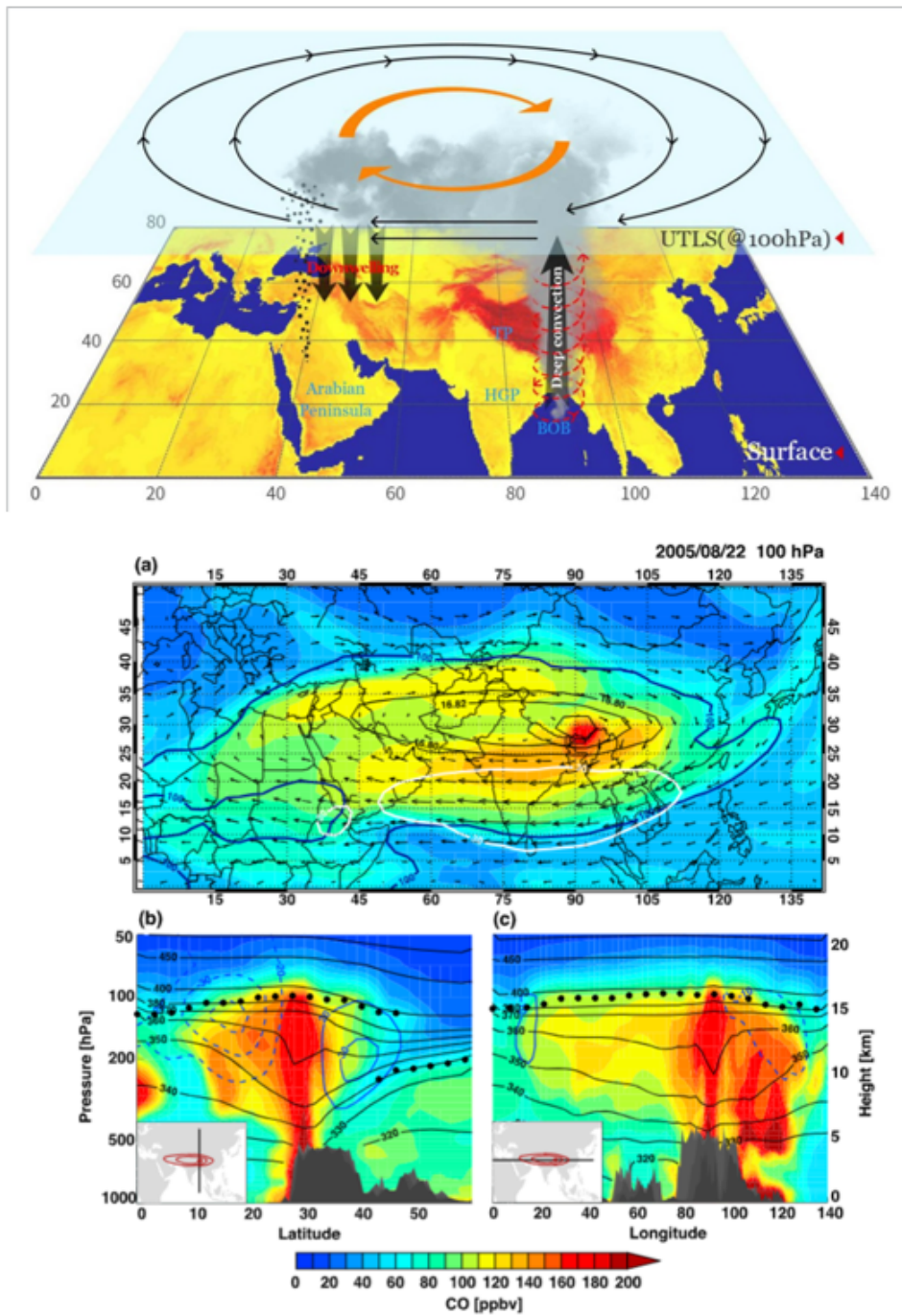


Figure 2.6: (a) Schematic of the transport processes indicating the formation and dissipation dynamics of the ATAL during the ASM (Q He et al., 2021). (b) CO mixing ratio (ppbv) at 100 hPa, in addition to the interception of the tropopause at 100 hPa pressure surface, and the easterly and westerly jets (Pan et al., 2016).

and impaction efficiency of non-spherical soot particles (Strawa et al., 1999). It is worth noting that heavily coated black carbon particles may not be identified as soot based on morphology alone, which could explain the discrepancy between the wire impactor samples (1% fraction of soot particles) and the lower percentages observed in the SP2 data. It is possible that the wire impactor samples were collected in an unusually soot-rich stratospheric environment. The claim made by Renard et al. (2008) of large

concentrations of soot-laden particles based on scattering phase functions was considered not credible due to potential influences from effloresced or glassy organic material. The halogen content of stratospheric aerosol particles has received limited attention compared to the extensive study of gas-phase halogen reactions (Solomon, 1999; Heckendorn et al., 2009). Early measurements in the 1970s using filter samples confirmed that most of the chlorine from chlorofluorocarbons remained in the gas phase (Lazarus et al., 1975). Mass spectrometer measurements of single particles also detected halogens (Murphy and Thomson, 2000). Halogen uptake in stratospheric particles could lead to faster removal through sedimentation. The fluorine content in stratospheric aerosols at 15-20 km altitude was found to be negligible (Mroz et al., 1977; Murphy and Thomson, 2000). The chlorine content in the midlatitude lower stratosphere was also very low, estimated at around 17 ppt (molar) using filters or less than 10 ppt using mass spectrometry (Lazrus et al., 1975; Murphy and Thomson, 2000). However, high values of aerosol chlorine measured on filters may have been influenced by adsorption (Turco et al., 1982). Perchlorate, a form of chlorine, was found in only a small fraction of sulphuric acid particles, and the reasons for this are not well understood (Murphy and Thomson, 2000). The chloride content of sulphate particles at the tropical tropopause increased at extremely low temperatures, around 188 K, which was below the temperature at which nitrate increased. The lack of simultaneous gas-phase chlorine measurements makes it difficult to assess the partitioning, but this chlorine uptake in a dehydrated region could potentially prevent tropospheric chloride from entering the stratosphere. Bromine and iodine were found in more stratospheric particles compared to chlorine or fluorine, including particles originating from the troposphere (Murphy and Thomson, 2000). Bromine and iodine showed correlations with organics and mercury in the particles and exhibited higher concentrations near the tropopause. The presence of bromine and iodine in tropospheric aerosols suggests that halogen products do not readily evaporate. The bromine content in aerosols in the lowermost stratosphere is likely a small but significant fraction of the overall stratospheric bromine, while a considerable portion of stratospheric iodine may exist in aerosols (Murphy and Thomson, 2000). Gas-phase iodine in the tropical lowermost stratosphere was found to be less than 0.16 pptv (Butz et al., 2009). The partitioning of iodine is crucial as gas-phase iodine can participate in catalytic cycles that efficiently deplete ozone (Solomon et al., 1994). More precise measurements of aerosol iodine are necessary to further understand this issue. Nitric acid condenses in polar stratospheric clouds as hydrates and as a ternary solution with water and sulfuric acid (Carslaw et al., 1994, 1997; Solomon, 1999). In addition, smaller amounts of nitric acid have been observed at the cold tropical tropopause on aerosols (Murphy and Thomson, 2000), as larger nitric acid trihydrate crystals (Popp et al., 2006; Voigt et al., 2008), and in ice crystals (Karcher and Voigt, 2006). At temperatures above approximately 195 K, nitrate is present in very small quantities, primarily on mineral dust particles. Measurements from the PALMS instrument indicate an absence of nitrate-rich particles in the stratosphere, unlike the sodium nitrate particles commonly found in polluted air at lower altitudes near the ocean. The chemical composition of stratospheric aerosol particles plays a crucial role in understanding their sources, phase characteristics, and potential for heterogeneous chemistry and ice nucleation. The primary focus lies in determining the sources of these particles. Tropospheric particles contribute significantly to the lower part of the stratosphere, but their importance diminishes as altitude increases. Sulfuric acid particles exhibit either a minimal or negligible presence of meteoritic material. Ablated and recondensed meteoritic material originating from the mesosphere serves as a condensation nucleus for sulfuric acid, with the process being most prominent during polar winters. Additionally, sulfuric acid particles can also form independently through new particle formation, likely near the tropical tropopause. Black carbon, on the other hand, is a minor component in the stratosphere, constituting a trace fraction compared to mineral dust. While extensive studies have been conducted on the mass concentration, number, and optical properties of stratospheric aerosols (Cadle and Grams (1975), Toon and Farlow (1981), Turco et al., (1982), Thomason and Peter (2006) and Deshler (2008), there was limited information on the chemical composition of the aerosols in the ATAL and the stratosphere. A recurring summertime maximum of CO was seen by satellite observation and model simulations over the Asian monsoon region (Lawrence and Lelieveld, 2010; Kar et al., 2004; Park et al., 2007). Deep convection and horizontal advection in the anticyclonic circulation prevail in the UTLS over Asia during summer and are responsible for lifting CO in this region (Vernier et al., 2015). Plumes of HCN, CH₄, and H₂O extend from southeast Asia to the eastern Mediterranean Sea during the ASM (Park et al., 2007; Li et al., 2005; Randel, and Park 2006; Randel et al., 2010). Moreover, observations of cloud and aerosol layers in the UTLS from the Cloud-Aerosol Lidar with Orthogonal Polarization (CALIOP) lidar (Winker et al., 2010) demonstrated a non-volcanic aerosol maximum near the tropopause during the ASM validated by the Stratospheric Aerosol and Gas Experiment (SAGE) II observations (Vernier et al., 2011; Thomason,

and Vernier 2013). The next chapter will provide a detailed analysis of samples collected within the ATAL using a balloon-borne impactor. Together with trajectory modeling and simulations using the GEOS-Chem transport models, this chapter was successfully published during the course of my PhD.

Resumé du chapitre 2 sur les aérosols stratosphériques, observations, processus et impacts climatiques

Des mesures antérieures ont révélé la présence d'une couche d'aérosols dans la stratosphère, en particulier entre 15 et 25 km d'altitude avec une concentration maximale à 20 km. On a constaté que ces aérosols s'étendaient sur une grande gamme de latitudes. Ces particules sont formées par la transformation chimique de sulfure de carbone (OCS) et dioxyde de soufre (SO₂). Des études de Junge et al. (1961) ont suggéré que certains des aérosols stratosphériques existaient à l'état liquide et étaient hygroscopiques, ayant la capacité d'absorber l'humidité de l'environnement environnant. Cette constatation a été appuyée par des mesures effectuées par Bigg (1975) et Farlow et al. (1977), ainsi que des mesures lidar qui distinguent les particules sphériques (probablement liquides) de sphériques (Browell et coll., 1990; Beyerle et coll., 1994). Les aérosols stratosphériques sont principalement composés de particules liquides sulfatées résultant de l'oxydation du soufre injecté dans la stratosphère lors d'éruptions volcaniques majeures, comme l'éruption du mont Pinatubo en juin 1991. Les mesures dans ces régions ont également indiqué la présence d'aérosols stratosphériques pendant les périodes sans éruptions volcaniques. Des processus tels que la sédimentation et l'évaporation jouent un rôle important dans la dynamique des aérosols stratosphériques. Le sommet de la couche d'aérosols dans la stratosphère est régi par des processus de sédimentation et d'évaporation, tels qu'étudiés par Hofmann et al. (1985). La base de la couche d'aérosols est étroitement liée au processus de formation d'aérosols vers la tropopause, la frontière entre la troposphère et la stratosphère. En l'absence d'éruptions volcaniques majeures, la couche d'aérosols stratosphériques est appelée la couche de "Junge layer". Le cycle de vie de cette couche est étroitement lié aux processus qui contrôlent le soufre dans la stratosphère. La durée de vie et la distribution des aérosols dans la stratosphère sont influencées par divers facteurs, y compris le transport atmosphérique et la présence de gaz précurseurs qui ont pour origine la troposphère. La circulation de Brewer-Dobson (BDC) contribue à la distribution des aérosols dans la stratosphère. De plus, les processus de formation, de croissance et d'élimination des aérosols sont influencés par la sédimentation lorsque l'air traverse la tropopause extratropicale. Ce mouvement à travers la tropopause modifie la chimie et la microphysique des aérosols, jouant un rôle dans leur distribution et comportement globaux dans la stratosphère. L'interaction entre le transport atmosphérique, la formation et la croissance d'aérosols et les mécanismes d'élimination façonne la dynamique complexe des aérosols stratosphériques.

Chapter 3

Exploring the ionic composition of the Asian tropopause aerosol layer using medium-duration balloon flights



3.1 Introduction

3.1.1 Why is the ATAL an important research criterion?

The ATAL (Asian Tropopause Aerosol Layer) constitutes one of the most important sources of UTLS aerosols in the absence of volcanic eruptions (Vernier et al., 2011). It has the potential to affect the Earth's radiative balance (Vernier et al., 2015), stratospheric ozone chemistry, and the properties of cirrus clouds. For example, an increase in the solid-particle concentration relative to the liquid background aerosol levels could trigger heterogeneous freezing and the formation of cirrus clouds at a lower relative humidity with respect to ice (Zawadowicz et al., 2015; Wang et al., 2020). Model simulations suggest that the ATAL represents 20% of the total column surface area density in the stratosphere of the Northern Hemisphere (Yu et al., 2018) with potential halogen heterogeneous chemistry on aerosols that can affect ozone trends (Solomon et al., 2016). The types of aerosols populating the ATAL could affect those chemical processes. Finally, the presence of absorbing aerosols (e.g., soot) in the UTLS could shift the level of zero net radiative heating upward and enhance troposphere-to-stratosphere transport (Yu et al., 2015).

3.1.2 What is the ATAL comprised of

Ever since its discovery, researchers have been trying to explore the chemical composition of the ATAL. Results from Energy-dispersive X-ray (EDX) analysis of aerosols sampled nearly 10-12 km aboard commercial aircraft as part of the Civil Aircraft for the Regular Investigation of the atmosphere Based on an Instrument Container (CARIBIC) program, at the bottom part of the ATAL, suggest a ratio of carbon to sulfur in the range of 2-10 (Vernier et al., 2015). Aircraft limb infrared measurements carried out during the StratoClim (Stratospheric and upper tropospheric processes for better climate predictions) campaign in Nepal and India in summer 2017 show the presence of ammonium nitrate in aerosol particles, validating satellite observations from the Cryogenic Infrared Spectrometers and Telescopes for the Atmosphere (CRISTA) and Michelson Interferometer for Passive Atmospheric Sounding (MIPAS) instruments (Höpfner et al., 2019). Balloon-borne measurements carried in 2017 during the BATAL campaign (Vernier et al., 2018) using heated and non-heated inlets connected to two OPCs showed that the ATAL was comprised of volatile particles (volatility fraction > 90%). More recent results using single-particle analysis from laser desorption and ionization mass spectrometry during StratoClim revealed that ATAL particles mainly consisted of an internal mixture of nitrate, ammonium, sulfate, and organics, with a significant particle fraction (up to 70% by number) resulting from the conversion of inorganic and organic gas-phase precursors rather than from the uplift of primary particles from below (Appel et al., 2021). A combination of community models and aerosol-climate-chemistry models indicate that, along with surface-emitted and secondary organic aerosols, the ATAL could be comprised of a significant amount of mineral dust either as a major component (Fadnavis et al., 2013; Lau et al., 2018; Ma et al., 2019; Bossolasco et al., 2021) or minor component (Yu et al., 2015, 2017; Gu et al., 2016; Fairlie et al., 2020). However, model simulations largely overestimate dust fraction within the ATAL probably due to their inability to represent accurately scavenging processes. The aerosol particles in the ATAL are looked upon as an insignia of the presence of pollution in the monsoon circulation from large SO₂ organic compounds and NO_x emissions in South and Southeastern Asia. Human-induced biomass burning (Van der A et al., 2008), fossil fuel combustion (Ghude et al., 2009), wildfires (Goode et al., 2000; Andreae and Merlet, 2001), and lightning (Martin et al., 2007; Yuan et al., 2019) are the significant anthropogenic and natural sources of NO_x. Soil biogenic emission of NO_x represents a large fraction of total NO_x (Jalié et al., 2004). Reactive nitrogen is emitted from tropical soils by microbial processes such as NO (Yienger and Levy, 1995; Conrad, 1996). Investigations of the composition of the aerosol particles in the ATAL are exiguous, although preliminary data from balloon-borne measurements indicate the presence of nitrate aerosol particles (Vernier et al., 2018). Recent in situ aerosol mass spectrometric measurements also reveal the presence of nitrate, ammonium, and sulfate within the ATAL (Höpfner et al., 2019; Yuan et al., 2019). Here, we investigate the inorganic composition of the ATAL over India during the summer monsoon and in winter using a balloon-borne aerosol impactor system with offline ion chromatography (IC) analysis. Section 3.3 describes the concept of the balloon experiment and the impactor system. The results of the IC analysis of the samples collected on the ground (GRND), during the two balloon flights (ZF2 and ZF3) in the summer of 2017, and during the flight (ZFW) in the winter of 2018 are described in Section 3.3.4. Section 3.4 compares the results obtained from balloon-borne measurements and satellite observations. Section 3.5 describes the influence of the Canadian wildfire event on the Balloon-borne

measurement campaigns of the Asian Tropopause Aerosol Layer (BATAL) winter flight. The origin of the air masses sampled during those flights is assessed in Section 3.6 using back-trajectory analysis combined with convective proxies. Section 3.7 addresses the formation of nitrite and its measurements. The GEOS-Chem model simulations are presented in Section 3.8 to put the measurements in the context of regional aerosol transport and distribution; this is followed by a summary and conclusions in Section 3.9.

3.2 Balloon flights, instrumentation, and chemical analysis

3.2.1 Rationale for the experiment

Contingent on measurements during the 2015 BATAL campaign, a concentration of about 20 particles cm^{-3} was found near the tropopause for aerosols with a size greater than $0.15 \mu\text{m}$ (Vernier et al., 2018). This translates into a mass concentration of 40 ng m^{-3} at STP (standard temperature and pressure; hereafter STP is assumed when mass concentrations are given), assuming that the aerosols were liquid sulfate droplets. During that time, the lower detection limit for the IC instrument at NASA Langley Research Center was around 20 ng m^{-3} . To reach the detection limit of sulfate aerosols, one would need to sample at least 0.5 m^3 , assuming the sulfate concentration above. Based on those results and weight limitations, we decided to use an impactor with a flow rate of 7 L min^{-1} which would need to float in the UTLS region for several hours to sample a sufficient air volume (2 h of sampling results in 0.84 m^3).

3.2.2 Zero-pressure balloon experiment

We used zero-pressure plastic balloons to achieve a float near the tropopause and sample enough aerosols to reach the detection limit of the IC. The infrastructure for conducting the experiment was provided by the Tata Institute of Fundamental Research Balloon Facility (TIFR-BF) in Hyderabad, India. Polyethylene balloons with volumes between 300 and 500 m^3 (manufactured by TIFR) were used for the zero-pressure flights (ZF) to carry a communication/control package (developed by TIFR), a science module (including a meteorological radiosonde), a Compact Optical Backscatter and Aerosol Detector (COBALD) system (Vernier et al., 2015; Yu et al., 2017), an aerosol impactor, and a ballast module at the end of the flight train. The schematic diagram shown in Fig. 1a describes a typical balloon flight. During the ascent, the atmospheric pressure decreases allowing gas inside the balloon to occupy a large space (stage 2 in Fig. 1a). The equilibrium point is reached when the hydrogen escapes from the side escape tubes attached at the bottom of the balloon until the inside pressure equals the outside pressure (stage 3 in Fig. 1a), leading to a pressure differential of zero (zero-pressure balloon). The float altitude depends upon the volume of the balloon, the density of the gas, and the total weight of the system following a simple Archimedes principle. Extreme cold temperatures near the tropopause affect the float due to radiative cooling, leading to a reduction in the buoyancy force, which entrains the descent of the system (stage 4 in Fig. 1a). To counterbalance this effect, ballast shots are released from a container to reduce the total weight (stage 5 in Fig. 1a), leading to the ascent of the balloon.

3.2.3 Balloon-borne aerosol impactor

For the ZF flights, a balloon-borne aerosol impactor (BAI) was developed (Figure 3.2). This aerosol sampler consists of a four-stage impactor, a vacuum pump, a volumetric flow controller, and a Raspberry Pi-based controller connected to a meteorological sonde. The mechanical design of the impactor, created by California Measurements, Inc., operates on the principle of inertia, where the flow and instrument dimensions determine the size cutoff at each stage. The size cutoffs for particle radius at the impactor's four stages (S-1, S-2, S-3, and S-4) are 2, 0.5, 0.15, and $0.05 \mu\text{m}$, respectively, at 7 L min^{-1} . The pump is electronically controlled based on pressure measurements from the meteorological sonde. Our objective is to sample aerosols within the ATAL region, so the pump is activated below 150 hPa ($\sim 14 \text{ km}$) and deactivated above 70 hPa ($\sim 18 \text{ km}$). However, due to reduced efficiency at those levels, the flow rates range between 5 and 6 L min^{-1} , causing a slight shift in the size cutoff of up to 18% (e.g., $2.36 \mu\text{m}$ instead of $2 \mu\text{m}$ for a flow of 5 L min^{-1} for S-1). In 2017, a series of balloon flights were conducted using the BAI and a COBALD sonde to measure aerosol backscatter in cloud and aerosol layers encountered by the BAI. The time–height evolution of the three ZFs is shown in Fig. 1c, with flight ZF1 being a test flight to understand and maintain the float altitude using ballast. The maximum flight duration was obtained

during ZF3, which had a float time of nearly 2h 50 min above 150 hPa and below 70 hPa. The oscillation observed in the trajectories of the balloons can be attributed to the cooling of the gas within the balloon and the subsequent release of ballast to regain higher altitudes. To ensure the preservation of the sampled aerosols, the BAI was carefully packed in a foam box containing dry ice during transportation to TIFR. Upon arrival, the filters were promptly unloaded and stored in 47 mm Petri dishes that were frozen at -24 °C until further analysis at the Physical Research Laboratory, Ahmedabad, India. Figure 3.3 represents the time evolution of altitude, temperature, and relative humidity inside the box containing the impactor and also outlines the different phases of the experiment.

3.3 Balloon flights, instrumentation, and chemical analysis

3.3.1 Rationale for the experiment

Based on the measurements conducted during the 2015 BATAL campaign, an aerosol concentration of approximately 20 particles cm^{-3} was observed in the vicinity of the tropopause for aerosols with a radius exceeding 75 nm (Vernier et al., 2018). This translates into a mass concentration of 40 ng m^{-3} at STP (standard temperature and pressure; hereafter STP is assumed when mass concentrations are given), assuming that the aerosols were liquid sulfate droplets. During that period, the lower detection limit for the IC (Ion Chromatography) instrument at NASA Langley Research Center was approximately 20 ng m^{-3} . To achieve the detection limit for sulfate aerosols, a minimum air volume of 0.5 m^3 , would need to be sampled, assuming the given sulfate concentration. Considering the results obtained and the constraints of weight limitations, we decided to employ an impactor with a flow rate of 7 L min^{-1} . This choice required the impactor to remain suspended in the UTLS region for several hours to sample a sufficient air volume. Specifically, 2 hours of sampling would yield approximately 0.84 m^3 of air volume.

We used zero-pressure plastic balloons to achieve a float near the tropopause and sample enough aerosols to reach the detection limit of the IC. The Tata Institute of Fundamental Research Balloon Facility (TIFR-BF) in Hyderabad, India, provided the infrastructure to conduct the experiment. Polyethylene balloons with volumes between 300 and 500 m^3 (manufactured by TIFR) were used for the zero-pressure flights (ZF) to carry a communication/control package (developed by TIFR), a science module (including a meteorological radiosonde), a Compact Optical Backscatter and Aerosol Detector (COBALD) system (Vernier et al., 2015; Yu et al., 2017), an aerosol impactor, and a ballast module at the end of the flight train. The schematic diagram shown in figure 3.1a describes a typical balloon flight. During the ascent of the balloon, the atmospheric pressure gradually decreases, allowing the gas inside the balloon to expand and occupy a larger space (stage 2 in figure 3.1a). The equilibrium point is reached when the hydrogen gas escapes from the side escape tubes located at the bottom of the balloon. This process continues until the pressure inside the balloon matches the pressure outside (stage 3 in figure 3.1a), resulting in a zero-pressure balloon with no pressure differential. The floating altitude of the balloon depends on several factors, including the volume of the balloon, the density of the gas used, and the total weight of the system, as governed by the principles of Archimedes. However, the extremely cold temperatures near the tropopause can impact the float of the balloon due to radiative cooling. This cooling effect reduces the buoyancy force, causing the system to descend (stage 4 in Figure 3.1a). To counterbalance this descent and enable the balloon to ascend, ballast shots are released from a dedicated container (stage 5 in 3.1a). This intentional reduction in the total weight of the system allows the balloon to regain buoyancy and resume its ascent.

3.3.2 Balloon-borne aerosol impactor

A balloon-borne aerosol impactor (BAI) was specifically developed for the ZF flights, as depicted in (Figure 3.2). This aerosol sampling device consists of a four-stage impactor, a vacuum pump, a volumetric flow controller, and a Raspberry Pi-based controller connected to a meteorological sonde. The mechanical design of the impactor was provided by California Measurements, Inc. and operates based on the principle of inertia, where the flow rate and instrument dimensions determine the size cutoff at each stage. The impactor's four stages (S-1, S-2, S-3, and S-4) have size cutoffs with respect to the particle radius of 2 , 0.5 , 0.15 , and 0.05 μm , respectively, at a flow rate of 7 L min^{-1} . The vacuum pump is electronically controlled based on pressure measurements from the meteorological sonde. Our objective was to sample aerosols within the ATAL region. To achieve this, the pump was activated below 150 hPa (~ 14 km) and

deactivated above 70 hPa (~ 18 km). However, due to a decrease in pump efficiency at these altitudes, the flow rates ranged from 5 and 6 L min⁻¹, resulting in a slight shift in the size cutoff of up to 18% (e.g., 2.36 μm instead of 2 μm for a flow of 5 L min⁻¹ for S-1). In 2017, we conducted a series of balloon flights using the BAI and a COBALD sonde for aerosol backscatter measurements of cloud and aerosol layers encountered by the BAI. The time–height evolution of the three ZFs is shown in Figure 3.1c, with flight ZF1 being a test flight to understand and maintain the float altitude using ballast. The maximum flight duration was obtained during ZF3, which had a float time of nearly 2h 50 min above 150 hPa and below 70 hPa. The oscillation of the balloon trajectories is due to the cooling of the gas inside the balloon and the subsequent release of ballast to regain higher altitudes. The BAI was preserved in a foam box containing dry ice during transportation to TIFR; once there, the filters were immediately unloaded and stored in 44 mm Petri dishes that were frozen at -24 °C until further analysis at the Physical Research Laboratory, Ahmedabad, India. Figure 3.3 represents the time evolution of altitude, temperature, and relative humidity inside the box containing the impactor and also outlines the different phases of the experiment.

3.3.3 IC analysis of major ions in aerosol samples

Aerosol samples were extracted in deionized (MiliQ, specific resistance ≥ 18.2 M Ω cm) in sterile polypropylene vials for 30 min (three intervals of 10 min each) using ultrasonication. The extract was further analyzed for water-soluble inorganic species (WSIS, such as Na⁺, K⁺, Mg²⁺, Ca²⁺, NH₄⁺, Cl⁻, NO₂⁻, NO₃⁻, SO₄²⁻ using an ion chromatograph (Dionex ICS-5000 DC-5, Thermo Scientific). For calibration, 1000 mg L⁻¹ stock solution of each cation (using Merck high-purity analytical-grade NaNO₂, (NH₄)₂SO₄, KNO₃, CaCl₂, 2H₂O, and Mg metal) were prepared. In addition, mixed standards were prepared by diluting stock solutions in polypropylene vials, thereby satisfying the primary requirement of instrument calibration for cations. Similarly, anion Multi-element standard II (1000 mg L⁻¹ in H₂O, reference no. HC 409399, Merck) was diluted subsequently as instrument calibration for anions. Post extraction, the extract of each sample was then separated and eluted in the cation column (Dionex IonPacTM CS16, 5mm \times 250mm) and anion column (Dionex IonPacTM AS23, 4mm \times 250mm) via the interaction with the mobile phases, i.e., 30mmol methyl sulfonic acid (MSA) for cations and a mixture of 4.5 mmol carbonate +0.8 mmol bicarbonate solutions for anions. The quantification of each ion was then performed using the conductivity detector. Several blanks were analyzed along with the samples. The ionic concentrations reported here are blank corrected. As the concentrations of different species were too low in UTLS aerosol samples, only those values which were at least 2 times higher than their respective blanks are reported. More than 50% of samples were repeated for reproducibility, and they were found to vary by between 2% and 20% for all of the analyzed ions. To validate the analysis, Dionex Six Cation-I Standard (product code 040187) and Dionex Combined Seven Anion Standard II (product code 57590) were diluted and checked in the respective cation and anion calibration curves which were found within $\pm 10\%$ relative standard deviation (RSD).

3.3.4 Results of the IC analysis

Figure 3.4 shows the ionic concentration of ground samples (GRND) as well as those of airborne samples (ZF2 and ZF3) collected aboard zero-pressure flights on 15 and 21 August 2017. Additionally, the figure also shows the ionic concentration of the flight held during the winter 2018 campaign denoted as (ZFW). In GRND samples, Na⁺ and Ca²⁺ cations are seen on S-1 and S-2 with corresponding anions (NO₃⁻, SO₄²⁻, and NO₂⁻) coexisting at the same stage. High NH₄⁺ is observed only on S-3, with a concentration of 212 ng m⁻³ at STP. K⁺ was also seen on S-3, with a concentration of 26 ng m⁻³ at STP (fine mode), and could have originated from biomass burning. City pollution from Hyderabad is likely the source of those aerosols observed on the GRND filters. Flights ZF2 and ZF3 show significant amounts of NO₃ and NO₂ (87–343 ng m⁻³ at STP) with trace amounts of mineral dust proxies (Ca²⁺). Biomass burning (K⁺) was observed in the results of flight ZF2 only. The presence of non-sea-salt Ca²⁺ in aerosols is often used as a proxy for mineral dust (Schüpbach et al., 2013), whereas non-sea-salt K⁺ in aerosols is often used as a proxy for biomass burning (Li et al., 2003). Although their concentrations were too low (close to the detection limit), their presence indicates the possibility of trace contributions from mineral dust and biomass burning.

Other species were below 5 (for cations) to 10 (for anions) ng m⁻³ at STP, the detection limit of

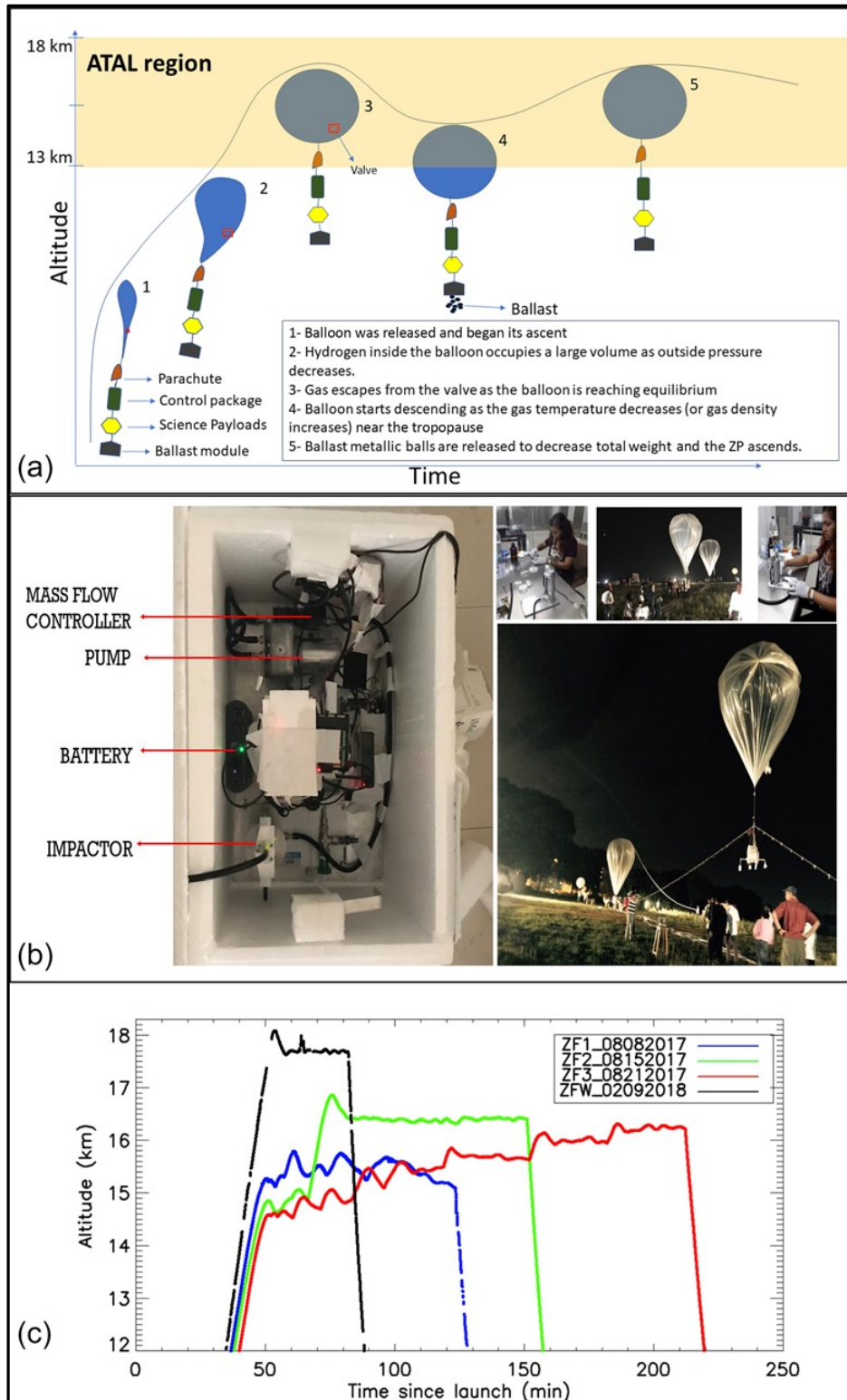


Figure 3.1: (a) Schematic diagram of the zero-pressure flight (ZP) concept. (b) Picture of the science payload, impactor preparation, and balloon flight launch. (c) Time–height curves of the GPS altitudes of the three zero-pressure flights during summer 2017, in comparison with that of winter 2018, launched from TIFR-BF, Hyderabad, India.

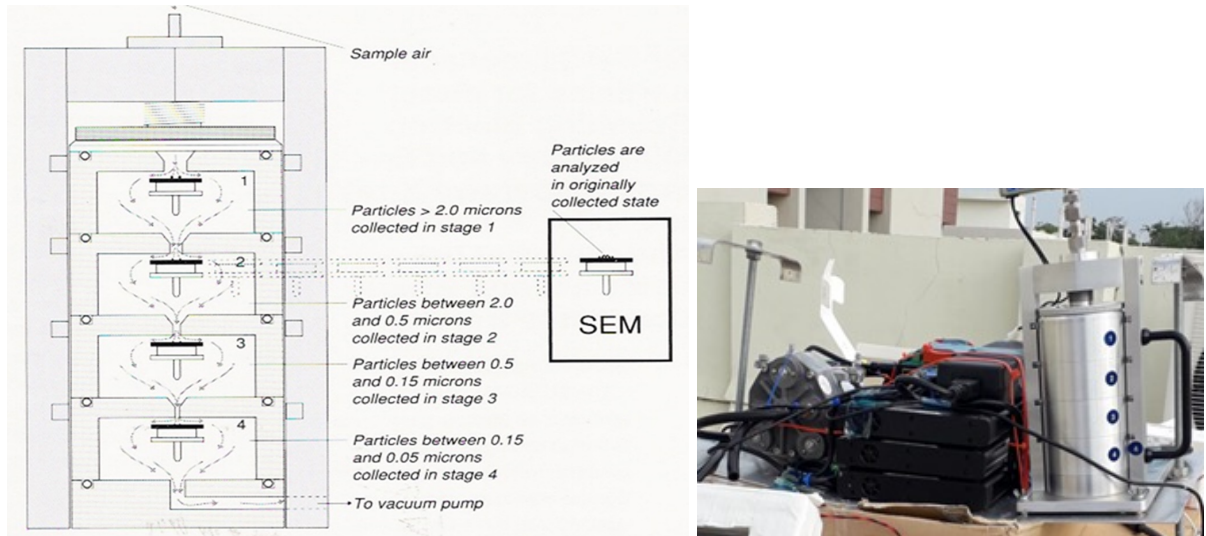


Figure 3.2: Schematic of the balloon-borne impactor used for sampling aerosols. Stages S1, S2, S3, & S4 collect aerosol particles of sizes greater than and between $2 \mu\text{m}$ to $0.05 \mu\text{m}$ in descending order.

the IC instrument for our analytical setup. Charge balance was not achieved due to a higher negative charge, mainly from NO_3^- and NO_2^- , than a positive charge, mainly from NH_4^+ , Ca^{2+} , and K^+ (Fig. 1.3), implying the existence of NO_3^- and NO_2^- in forms other than salt. For instance, nitric acid trihydrate (NAT, $\text{HNO}_3 \cdot 3\text{H}_2\text{O}$) could be another aerosol cluster in which NO_3^- may be present in the tropical UTLS (Voigt et al., 2000). We did not find a significant amount of ammonium in our ZF flight samples during the summer. Overall, the concentration of nitrate ($80 - 100 \text{ ng m}^{-3}$ at STP) found on both flights seems to be lower than the levels observed during StratoClim (Höpfner et al., 2019). In the only flight during the winter of 2018, Na^+ and K^+ were almost nonexistent. In comparison, the mineral dust proxy (Ca^{2+}) was present in trace amounts in all four impactor stages and could be associated with SO_4^{2-} , which was also found in all four stages (Fig. 3.3b). Balloon-borne and aircraft sampling techniques have been used since the early 1970s to study the composition of aerosols in the UTLS region (Lazarus et al., 1970). Höpfner et al. (2016) reported the presence of enhanced amounts of NO_3 between 12 and 15 km within the Asian summer monsoon region. While sulfate tends to be stable enough to be collected and further analyzed without major chemical transformation, other nitrate-containing particles can be more unstable. NO_3 salts apart from NH_4NO_3 is not significantly volatile after sampling (Newman, 1993). The dissociation of NH_4NO_3 into gas-phase HNO_3 and NH_3 increases sharply with increasing temperature and relative humidity (Stelson and Steinfield, 1982; Lightstone et al., 2000), leading to a significant loss of particulate nitrate (PN). The slight retention of HNO_3 (gas) on the PTFE (polytetrafluoroethylene) filter could represent a significant source of particulate nitrate on filters at low concentrations and has been used in the past to estimate stratospheric HNO_3 (Lazarus et al., 1970) Additional information available during ZF2 will be discussed to assess the presence of ice clouds.

3.4 Presence of ice clouds during flight ZF2

Flight ZF2, included a COBALD backscatter sonde launched to be collocated in space and time (within 20 km and 1 h, respectively) with satellite observations from the CALIOP lidar aboard the CALIPSO satellite. Figures 3.4a and 3.4b show the scattering ratio (SR) and color index (CI) profiles from COBALD (470nm and 940 nm) as well as CALIOP SR and volume depolarization profiles at 532 nm. Both balloon and satellite observations show a layer between 13.5 and 16 km with high depolarization (CALIOP) and a high color ratio (COBALD), likely made of aspherical particles. The derived particulate depolarization ratio from CALIOP Level 2v4.1 within the layer was 0.47 ± 0.06 (Fig. 3.5) and was associated with an optical depth of 0.03 ± 0.02 , indicating the presence of a subvisible cirrus cloud.

Flight ZF2 floated nearly 14.5–17 km for more than 2 h (Fig. 3.1c). The time series (Fig. 3.1c) indicate that the measurements took place within two different air masses: first within an ice cloud, as

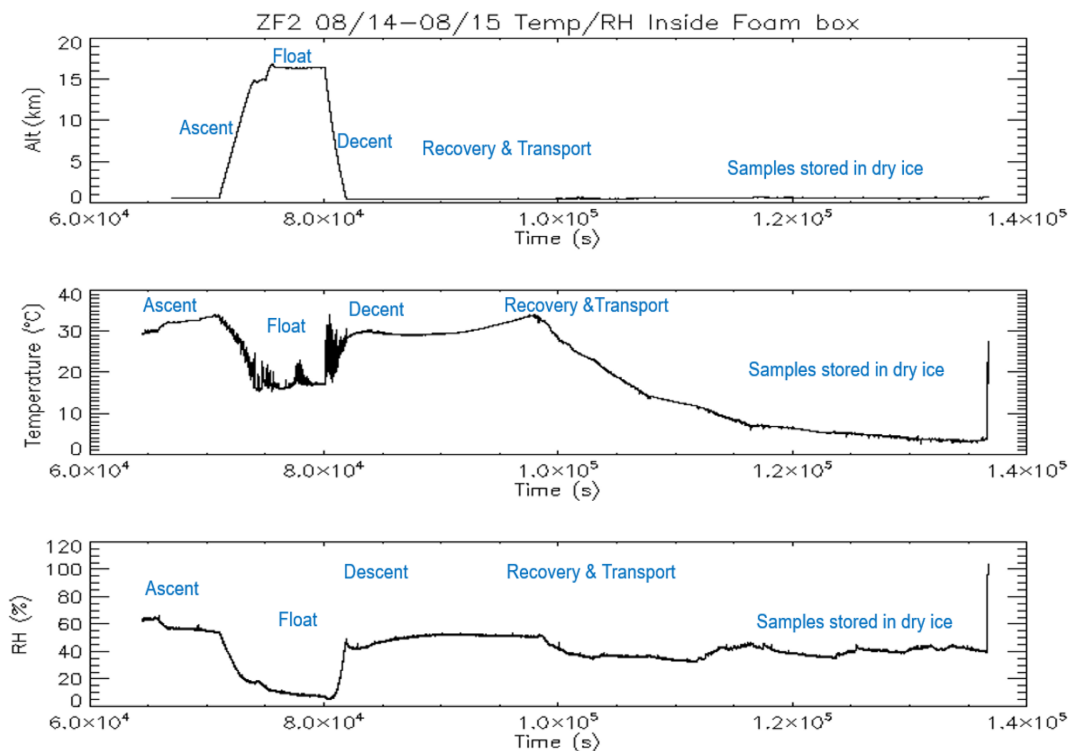


Figure 3.3: Time series of the altitude, temperature, and relative humidity profiles of the samples inside the foam box during the ZF2 flight.

discussed above, followed by in a cloud-free region. The pump connected to the impactor was switched on below 150 hPa and run for ~ 16 min within the cloud and for ~ 1 h 30 min in a cloud-free region.

3.4.1 Nitrate particles in-cloud

The sampling within an ice cloud (Fig. 3.6) during ZF2 could, therefore, indicate the presence of in-cloud $\text{NO}_3^- \cdot \text{HNO}_3$, (an oxidation product of NO_x) and NH_3 (released from agricultural sources) are said to be absorbed into cloud droplets which then aid in the conversion of HNO_3 to aerosol NO_3^- (Hayden et al., 2007). HNO_3 , being readily soluble, tends to completely dissolve in cloud water (Steinfeld and Pandis, 1998). Bela et al. (2016) found an almost 90% scavenging efficiency for HNO_3 by sampling the inflow and outflow of convective storms over the United States during the Deep Convective Clouds and Chemistry (DC3) field campaign. However, we found that ZF2 sampled 90 ng m^{-3} at STP of NO_3^- for particle sizes between 2 and $0.5 \mu\text{m}$ on stage 2 and 11 ng m^{-3} at STP of NO_3^- on stage 3, corresponding to particle sizes between 0.5 and $0.15 \mu\text{m}$; this indicates that other mechanisms might be taking place for HNO_3 and nitrate to survive convection. Our measurements were conducted at higher altitudes (16–17 km instead of 10–12 km) and much colder temperatures (-70°C to -80°C) than DC3, which may explain this apparent contrast between DC3 and our measurements. Bela et al. (2016) found that ice retention had little impact on scavenging efficiency in the Weather Research and Forecasting (WRF) model coupled with Chemistry, suggesting that HNO_3 formation in ice clouds via lightning-induced NO_x could be a more efficient source than convective transport. The GEOS-Chem chemical transport model (CTM) showed the presence of inorganic nitrate aerosol to be dominant in the ATAL (Gu et al., 2016), with a significant fraction from lightning-induced NO_x (Fairlie et al., 2020). The authors concluded that gas-aerosol conversion of HNO_3 was the driving factor behind this dominance, via the processes discussed above.

3.4.2 NAT particles

Another candidate for the presence of nitrate on the filters could be NAT particles. They have been reported in tropical ice clouds by Voigt et al. (2008) with sizes ($D < 6 \mu\text{m}$) consistent with their sampling

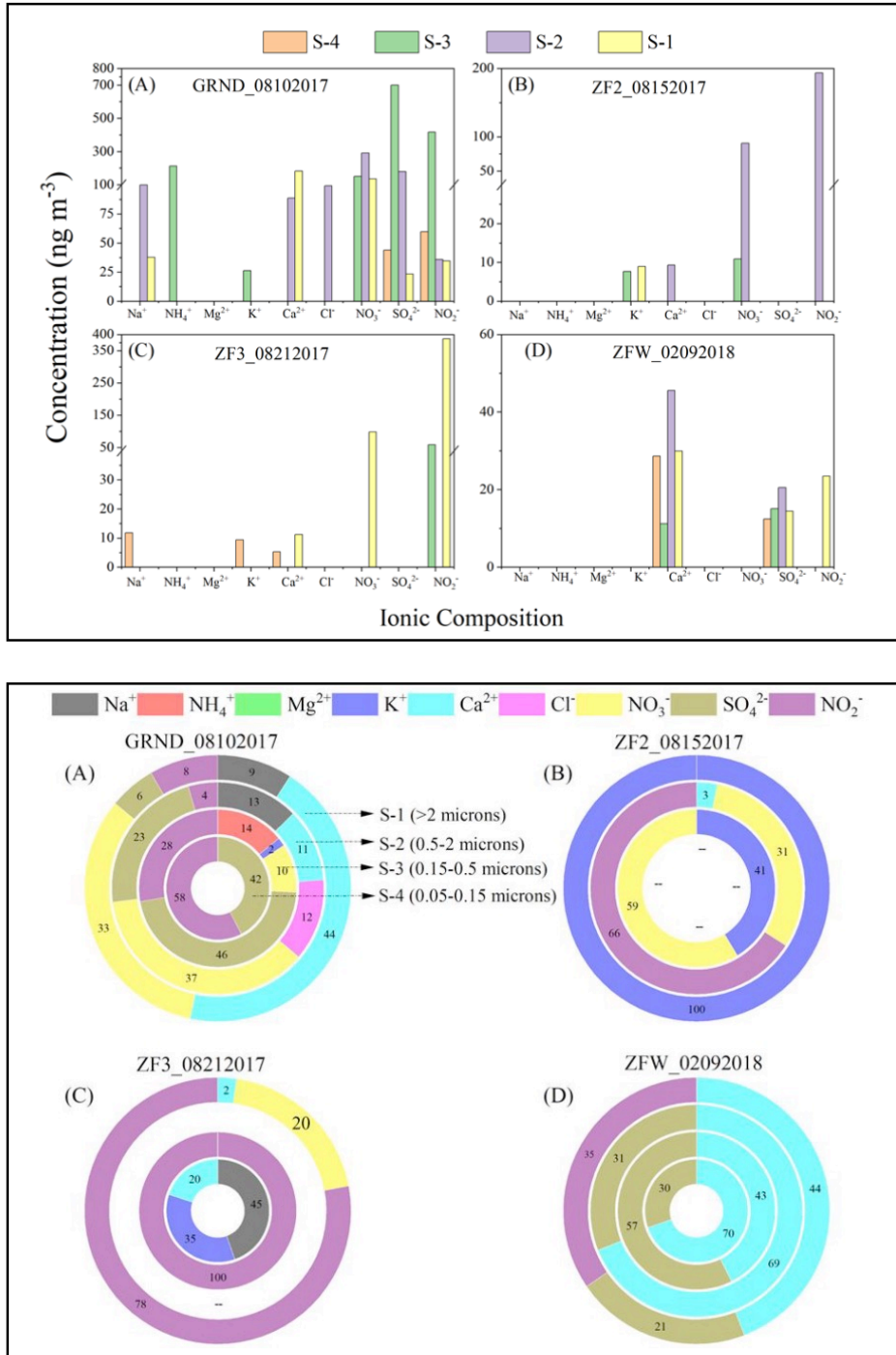


Figure 3.4: (a) Results from the analysis of inorganic aerosol for the aerosol ionic composition of the filters collected (i) on the ground (ii) during ZF2, (iii) during ZF3 in summer 2017, and (iv) during ZFW in winter 2018. (b) The percentage distribution of individual ions. S-1 to S-4 indicate the four stages of the impactor. The size cutoffs are > 2, 0.5, 0.15, and 0.05 microm for S-1, S-2, S-3, and S-4, respectively.

on stages 1 (> 2 μm) and 2 (0.5– 2 μm) of the impactor. In addition, NAT nucleation seems to be more efficient in subvisible ice clouds at higher ambient temperatures than the temperature associated with NAT formation at $-78\text{ }^\circ\text{C}$ (Voigt et al., 2008). The sampling within the ice cloud at temperatures between -65 and $-75\text{ }^\circ\text{C}$ would allow the presence of NAT. However, in the process of sampling, transport, and extraction, there is a strong possibility of NAT particle losses (if they were collected). In addition, if

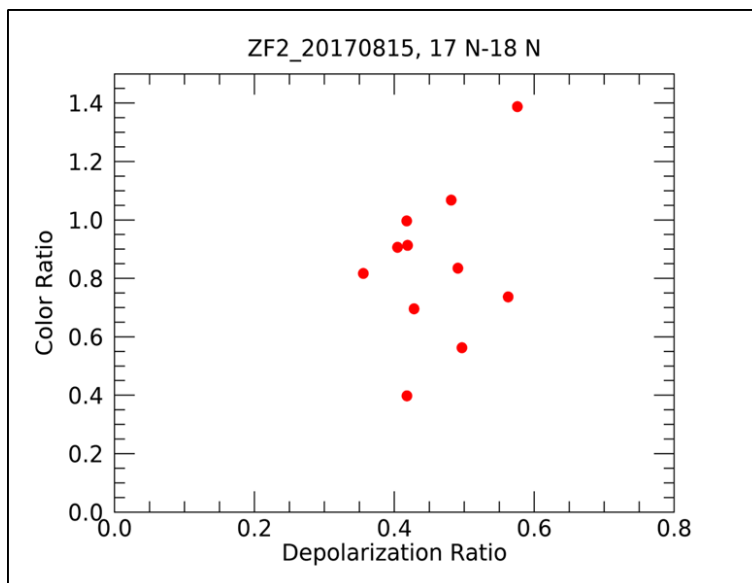


Figure 3.5: Cirrus cloud layer properties using CALIOP L2V4.2 Cloud Layer product for August 15th, 2017 between 17.12°N and 17.92°N corresponding to the profiles shown in Fig.1.4. Depolarization ratio versus color ratio plot for these layers which indicates the presence of aspherical large particles consistent with the properties of sub-visible cirrus clouds (mean AOD $\sim 0.03 \pm 0.02$).

NO_3^-) was present in another form (refractory nitrate), it would remain relatively stable during the above-mentioned processes. Observed cations were close to or below the detection limit compared with the significant concentrations of NO_2 and NO_3 . This observation along with the higher abundance of NO_2^- allowed us to suggest the presence of NAT particles. However, the reported NAT concentrations should be considered as the lower limit, presuming some losses (unquantifiable) during the sampling, transport, and extraction processes.

3.4.3 In-cloud calcium and its Implication

The IC results of flight ZF2 showed the presence of particles of Ca_2^+ (9 ng m^{-3} at STP) on stage 2 of the impactor ($0.5\text{--}2 \mu\text{m}$). The erosion of calcareous soils followed by strong convective vertical transport during summer results in cloud water calcium (Issac et al., 1990). Cloud water experiments have shown the formation of $\text{Ca}(\text{NO}_3)_2$ in the presence of NH_3 . Hill et al. (2007) and Leaitch et al. (1986) found a positive correlation between Ca^+ and NO_3^- . In addition to Ca_2^+ , ZF2 also showed the presence of NO_3^- (90 ng m^{-3} at STP) on the same stage of the impactor (large particles $< 2 \mu\text{m}$), further implying the possibility of $\text{Ca}(\text{NO}_3)_2$ formation in the presence of the acid HNO_3 . Lastly, a high concentration of nitrite (193 ng m^{-3} at STP) was also found on stage 2 of the impactor. The presence of nitrite in clouds is further discussed in section 3.7.

3.5 The influence of Canadian wildfire plumes during the winter flight

For the only flight during the winter of 2018, Na^+ and K^+ were almost nonexistent. In comparison, the mineral dust proxy (Ca^{2+}) was present on all four impactor stages: 30 ng m^{-3} on stage 1 (particle sizes $> 2 \mu\text{m}$), 46 ng m^{-3} on stage 2 (particle sizes between 0.5 and $2 \mu\text{m}$), 11 ng m^{-3} on stage 3 (particle sizes between 0.15 and $0.5 \mu\text{m}$), and 29 ng m^{-3} on stage 4 (particle sizes between 0.05 and $0.15 \mu\text{m}$). Interestingly, SO_4^{2-} was also found in all four stages (Fig. 3.4): 14 ng m^{-3} on stage 1, 21 ng m^{-3} on stage 2, 15 ng m^{-3} on stage 3, and 12 ng m^{-3} on stage 4. Satellite analysis of aerosol extinction at 1020 nm from the Stratospheric Aerosol and Gas Experiment III (SAGE III) was conducted to understand the origin of those particles. We found high aerosol extinction values in the Northern Hemisphere from August 2017

to February 2018, consistent with the presence of smoke from the 2017 Canadian fire (Fig.3.7). Fires that intensify towering thunderstorms have the tendency to inject aerosols into the lower stratosphere that were otherwise thought to have originated from volcanic plumes (Fromm et al., 2010). The 2017 Canadian wildfire event led to the formation of multiple pyrocumulonimbus (PyroCb) episodes, resulting in a vast aerosol cloud. Within a few weeks, a portion of this initial plume was transported by the polar jet streams across the Atlantic Ocean in the Northern Hemisphere (Peterson et al., 2018), causing a strong perturbation of the stratospheric aerosol loads (Stocker et al., 2021). The quantity of smoke injected was enormous – so much so that it was observed for more than 8 months (Yu et al., 2019). The presence of the resultant aerosol layer was pointed out by high ultraviolet aerosol index values and confirmed with CALIOP lidar observations in the UTLS (Torres et al., 2020). The aerosol mass increase and subsequent adiabatic aerosol self-lofting as a result of absorption of solar radiation were also observed by the Earth Polychromatic Imaging Camera (EPIC) sensor aboard the Deep Space Climate Observatory (DSCOVR) satellite. Kloss et al. (2019) used SAGE III aerosol extinction values to show that the fire plume was transported within the AMA circulation in August 2017. Our analysis suggests that the smoke plume was still present at 18 km above Hyderabad between January and February 2018, indicating that aerosols sampled during the winter flight were influenced by this smoke plume.

3.6 Convective influence

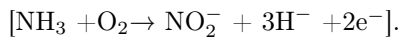
Deep convection, emanating from Southeast Asia, and maritime convection over surrounding seas serve as a conduit for the transport of boundary layer (BL) pollutants (CO, HCN, CH₄) to the UTLS (Belikov et al., 2013; Park et al., 2007, 2006; Randel et al., 2010). Wind-driven physical processes lead to the accumulation of pollutants due to the limited exchanges of air between the interior and exterior of the Asian monsoon anticyclone (Fairlie et al., 2014, 2020; Ploeger et al., 2015). To study the impact of convection on our measurements, we calculate back trajectories from ZF2 and ZF3 using the Langley Trajectory Model (LaTM; Fairlie et al., 2014) driven by winds from the NASA Global Modelling and Assimilation Office (GMAO) Goddard Earth Observing System, Version 5, Forward Processing (GEOS-5 FP) product (Lucchesi, 2018). We locate the intersection with anvils and deep convective clouds observed through cloud-top brightness temperature from the Himawari-8 satellite (Vernier et al., 2018).

Figure 3.8 shows the position of those 5-day back trajectories (colored lines) and deep convective influences (black dots). Air sampled during ZF2 on 15 August 2017 traveled along two branches influenced by convection over southern/eastern China and western China, respectively. Air masses sampled by ZF3 originated from convection over Laos, Myanmar, the Bay of Bengal, and possibly local convection over the Indian eastern shore close to the measurement location.

3.7 Nitrite measurements

The role of clouds in nitrite formation is further discussed in this section. To date, only a few nitrite measurements have been reported, mainly because of their low concentrations and the fact that nitrite ions are easily oxidized (Lammel and Cape, 1996). The first quantitative information on nitrite in cloud water was detected at Mt Tsukuba, Japan: values of 400 – 1050 µg/liter with pH levels of 5.7 – 6.5 were reported. In contrast, acidic cloud water samples (pH of 3.4 – 4.3) collected at significantly higher altitudes showed low nitrite values (15 – 104 µg/liter) (Okita, 1968). Nitrite and nitrous acid are short-lived intermediates of reactive oxidized nitrogen in the atmosphere. There is limited information on nitrite measurements in the atmosphere (Lammel and Cape, 1996). Nitrite was also measured in fog water samples in a polluted region in Germany (Lammel and Metzger, 1998). Moreover, Bachmann et al. (1989) directly measured nitrite in rain and fog water samples using ion chromatography; respective values of 1.8 and 16 µmolL⁻¹ were found. Photolysis of particulate nitrate, hydrolysis of NO₂, and uptake of HNO₂ by particles are the sources of particulate nitrite in the atmosphere (Chen et al., 2019). HNO₂ is an important precursor for nitrite formation, but there are challenges involved with making reliable HNO₂ measurements at desired concentrations, leading to a lack of information about HNO₂ in the troposphere. Firstly, due to its short lifetime (because of photolysis) and subsequent very low concentration from sources, HNO₂ is a challenging species to observe. Secondly, HNO₂, being sticky in nature, may be lost to the walls of sampling tubes or absorbed on filters. Thus, nitrite is present

in very low concentrations and is easily oxidized. Intensive agricultural activities have led to the Indo-Gangetic Plain having the highest ammonia (NH_3) loading worldwide (Wang et al., 2020), as revealed by satellite observations (Van Damme et al., 2018; Warner et al., 2016) and ground-based measurements (Carmichael et al., 2003). Dentener and Crutzen (1994) reported ammonia (NH_3) emissions related to DMS (dimethylsulfide). Höpfner et al. (2016) reported the first detection of ammonia in the ATAL. Nitrite and nitrate are formed by the oxidation of NH_3 through the process of nitrification



In addition, the existence of NH_3 in the presence of nitrate leads to the formation of ammonium nitrate which could neutralize aerosol particles and favor the persistence of nitrite, as revealed by a few existing measurements in the polluted region (Lammel and Metzger, 1998). The StratoClim campaign also revealed the presence of ammonium nitrate in the UTLS which would confirm that the neutralization of nitrate is effective at high altitudes and may explain the persistence of nitrite found with our balloon measurements.

3.8 Comparison with GEOS-Chem simulations

We (through a collaboration with Hongyu Liu from NIA/NASA LaRC) conducted GEOS-Chem model simulations to put our observations in the context of the large-scale transport and distribution of atmospheric composition. GEOS-Chem is a state-of-the-art global 3-D chemical transport model that includes fully coupled ozone- NO_x -volatile organic compound-aerosol chemistry for both the troposphere and stratosphere (Bey et al., 2001; Park et al., 2004; Eastham et al., 2014). Here, we use model version 11-01 (http://wiki.seas.harvard.edu/geos-chem/index.php/GEOS-Chem_v11-01, last access: 29 July 2022). A previous version of the model was used to study the origins of aerosols in the ATAL by Gu et al. (2016) and Fairlie et al. (2020). The model simulates black carbon (Park et al., 2003), primary and secondary organic aerosols (POAs and SOAs, respectively; Pye et al., 2010), sulfate-nitrate-ammonium-aerosol thermodynamics coupled to ozone- NO_x -hydrocarbon-aerosol chemistry (Park et al., 2004), mineral dust (Fairlie et al., 2007; Ridley et al., 2014), and sea salt (Jaeglé et al., 2011), treated as an external mixture. SOA simulation uses the volatility-based scheme (VBS) of Pye et al. (2010). Sulfate-nitrate-ammonium thermodynamics is computed using the ISORROPIA II thermodynamic equilibrium model of Fountoukis and Nenes (2007). ISORROPIA has been evaluated with in situ measurements during several campaigns in the United States (Guo et al., 2016, 2020) and, more recently, in Korea (Ibikunle et al., 2020). Aerosol wet deposition includes rainout and washout due to large-scale precipitation as well as scavenging in convective updrafts (Liu et al., 2001). Scavenging of aerosols by snow and mixed precipitation is described by Wang et al. (2011) and Q. Wang et al. (2014).

Dry deposition of dust and sea-salt aerosols uses the size-dependent scheme of Zhang et al. (2011). Dry deposition for other aerosols follows the resistance-in-series scheme of Wesely (1989). Anthropogenic emissions use the Emissions Database for Global Atmospheric Research (EDGAR; Olivier and Berdowski, 2001) with regional options, including the MIX inventory over East Asia (Li et al., 2014) and the EPA/NEI 2011 inventory over North America (Travis et al., 2016). Biofuel emissions are from Yevich and Logan (2003). Carbonaceous aerosol emissions are provided by Bond et al. (2007). Biogenic emissions are calculated by the Model of Emissions of Gases and Aerosols from Nature (MEGAN; Guenther et al., 2012). Biomass burning emissions use the Quick Fire Emissions Dataset (QFED; Darmerov and da Silva, 2015). Lightning NO_x emissions (LNO_x) are as described by Murray et al. (2012) and match the Lightning Imaging Sensor and the Optical Transient Detector (LIS/OTD) climatological observations of lightning flashes. Volcanic O_2 emissions are provided by the AeroCom project (data available from [http://wiki.seas.harvard.edu/geos-chem/index.php/Volcanic SO₂ emission](http://wiki.seas.harvard.edu/geos-chem/index.php/Volcanic_SO2_emission), last access: 29 July 2022). The model simulations are driven by the Modern-Era Retrospective analysis for Research and Applications (MERRA-2) reanalysis from the NASA GMAO (Gelaro et al., 2017) or computational efficiency, MERRA-2 fields have been mapped from the native grid to a $2.5^\circ \times 2^\circ$ (longitude \times latitude) horizontal resolution for input to GEOS-Chem. Further, we used the simulations with and without lightning NO_x emissions to understand the contribution of lightning to the formation of nitrate aerosol. In situ, chemical analyses are compared with GEOS-Chem simulations. Figure 3.9 shows the maps of CO , nitrate, sulfate, ammonium, black carbon (BC), and dust aerosol concentrations averaged over 100–150 hPa at 22:00 UTC for 15 and 21 August during the ZF2 and ZF3 flights, respectively (white circle

on the map). On 15 August, CO, BC, nitrate, ammonium, and dust aerosol concentrations are enhanced over West China, Nepal, and northeastern India, with the center of the anticyclone positioned over West China. On the contrary, on 21 August during ZF3, the position of the anticyclone was shifted to the east, and the flight apparently sampled air at the edge of the anticyclone.

The simulation shows a 20% and a 50% increase in CO and BC on 21 August, respectively, compared with 15 August (Fig3.9). Additionally, the ammonium concentration was decreased by 50% and dust was reduced by 60% on 21 August compared with the first flight on 15 August. However, the SO_4^{2-} concentration is seen to be stable at $\sim 80 \text{ ng m}^{-3}$ for both 15 and 21 August above Hyderabad. The simulated NO_3 concentrations near the location of ZF2 and ZF3 are spatially inhomogeneous, with variations between 30 and 2700 ng m^{-3} across South India. Figure 3.10 shows the time series of model 3-hourly CO, sulfate, and nitrate concentrations averaged over 100–150 hPa within the model grid point where Hyderabad is located during August 2017.

3.9 Conclusions

The chemical composition of the ATAL has been investigated using offline IC analysis of aerosol-impacted samples collected aboard zero-pressure balloon flights as part of the BATAL campaigns. The measurements of the 2017 summer campaign indicate the dominant presence of nitrate and nitrite aerosols with concentrations between 88 and 374 ng m^{-3} at STP. Our first flight (ZF2) on 15 August 2017 occurred within the AMA and, thus, sampled air masses therein. In situ measurements revealed the presence of NO_3^- , and NO_2 aerosols (60–200 ng m^{-3} at STP) with sizes ranging from 0.05 to 2 μm . The second flight (ZF3) on 21 August 2017, however, occurred at the edge of the anticyclone, and subsequent in situ measurements revealed the presence of larger-particle-size NO_3 and NO_2 aerosols at higher concentrations (87.3–343 ng m^{-3} at STP). Throughout the flights during the 2017 summer campaign, sulfate aerosol remained below the detection limit of the system (10 ng m^{-3} at STP) and was much lower than the results from the GEOS-Chem model simulation (80–120 ng m^{-3} at STP). The higher model sulfate levels compared with the values from IC are believed to be due to relatively weak scavenging of SO_2 and/or SO_4^{2-} in the model. Unlike the summer, Ca^{2+} and SO_4^{2-} were found on all four stages (sizes ranging between 0.2 and 0.05 μm) along with traces of NH_4^+ , which could not be quantified in the winter campaign. The winter flight sampled residuals from the 2017 Canadian wildfires that affected stratospheric aerosol loadings for several months. We study the influence of convection on those measurements using back-trajectory calculations co-located with geostationary satellite observations. We show that ZF2 and ZF3 were influenced by convection over Western China, the Bay of Bengal, Myanmar, Thailand, and Laos. The model was able to reproduce the convective transport from the mid-troposphere (9–12 km) to the upper troposphere (14–15 km). There was no indication of the transport of these air parcels from the boundary layer. Although Himawari-8 observations showed the convective transport reproduced in MERRA-2, the mixture between horizontal and vertical transport was not visible in trajectory calculations. Tropical convection could explain the rapid ascent of the air parcels to higher altitudes because other mechanisms, namely radiative heating, would delay the transport of air parcels from the middle to the upper troposphere. While the model seems to represent convection in the upper troposphere (14–15 km), with the rapid ascension of air parcels, the model’s ability to simulate convective influence at higher altitudes seems to be limited.

We used the GEOS-Chem model simulations with and without lightning, $\text{NO}_2 = x$ emissions to understand the contribution of lightning to nitrate aerosol. Flights ZF2 (15 August) and ZF3 (21 August) occurred during a period when the levels of nitrate were relatively small ($< 100 \text{ ng m}^{-3}$ at STP) with minimal influence of lightning NO_x , in contrast with other periods largely affected by nitrate produced by LNO_x . As shown by trajectory calculations in Fig. 3.8, flights ZF2 and ZF3 sampled air masses localized at the border of the Asian anticyclone. Fairlie et al. (2020) showed that the eastern part of the ATAL anticyclone depicts a peak in ammonium contribution from Chinese emissions. The western core of the ATAL, on the other hand, is seen to be enriched with 80% of anthropogenic sources from India, with the southern and eastern flanks of the anticyclone showing peaks of Chinese contribution wherein nitrate concentrations were found to be the highest. As the ASM (Asian summer monsoon) varies with respect to spatial dimensions and methodology, inconsistencies in the seasonal and interannual contribution to the ATAL are expected. Mineral dust is considered to be the most abundant type in the troposphere, with its main emission source being from arid and semiarid regions (Huneeus et al., 2011). CaCO_3 is considered

to be one of the most important components of mineral dust, and about 1.3 Tg of CaCO_3 is loaded in the troposphere, corresponding to approximately 8% of the total loading of mineral dust (Scanza et al., 2015). During atmospheric transport, heterogeneous reactions occur with trace gases, forming more soluble species and resulting in the increased CCN (cloud condensation nuclei) activity of mineral dust particles. Flight ZF2 sampled air masses within a cloud showing the presence of Ca^{2+} and NO_3^- on the same stage (particle size $< 0.15 \mu\text{m}$). This implies the formation of $\text{Ca}(\text{NO}_3)_2$ in the presence of HNO_3 . Indeed, the atmosphere is an amalgamated den in which gaseous species, particulates, and liquid droplets coexist at the same time. Through our balloon campaigns during the ASM with simultaneous offline measurements of inorganic species and, subsequently, comparing these results with model simulations, we were able to understand if not fully answer, the many unanswered questions regarding the existence and behavioral patterns of these ionic species of interest. We will continue to research this area with improved techniques and additional experimentation.

Résumé du chapitre 3 : Composition ionique de la couche d'aérosols de la tropopause asiatique à l'aide de mesures transportées par ballonnet et de données satellitaires

Ce chapitre se concentre sur la couche asiatique d'aérosols présente vers la tropopause (ATAL) et ses implications importantes pour le climat et les processus atmosphériques. L'ATAL est une source importante d'aérosols dans la haute troposphère et la basse stratosphère, influençant l'équilibre radiatif, la chimie de l'ozone et la formation de cirrus vers la tropopause. Les simulations numériques indiquent que l'ATAL contribue de manière significative à la densité totale de la surface des aérosols dans la stratosphère de l'hémisphère Nord, ce qui pourrait affecter les tendances de l'ozone et la chimie des composés halogènes. La composition chimique de l'ATAL a fait l'objet de recherches approfondies. Des études ont utilisé diverses techniques pour analyser les aérosols et ont fourni des informations sur leur composition. Par exemple, Vernier et al. (2015) ont trouvé un rapport carbone/soufre entre 2 et 10 dans la partie inférieure de la couche en utilisant l'analyse par rayons X à dispersion d'énergie. Les mesures infrarouges des membres au cours de la campagne StratoClim ont confirmé la présence de nitrate d'ammonium dans les particules d'aérosols ATAL, validant les observations satellitaires. En combinant des modèles et des mesures, les chercheurs suggèrent que l'ATAL peut contenir des quantités importantes de poussière minérale, d'aérosols organiques émis en surface et des aérosols secondaires, cependant ces simulations n'ont pas été confirmées par les observations. La présence de particules d'aérosols dans l'ATAL est probablement associée à la pollution due aux activités anthropiques en Asie du Sud et du Sud-Est, telles que la combustion de biomasse, la combustion de combustibles fossiles, les incendies de forêt et la foudre. Pour étudier la composition inorganique de l'ATAL, une campagne de mesure de ballons a été menée en Inde pendant la mousson d'été et en hiver à des fins de comparaison. Des ballons en plastique à pression nulle avec divers instruments et modules ont été utilisés pour prélever des échantillons d'aérosols près de la tropopause. Les aérosols échantillonnés ont été analysés par chromatographie ionique et les résultats ont été comparés aux observations satellitaires. Les origines des masses d'air ont été évaluées à l'aide d'une analyse de rétro-trajectoire, et les mesures ont été contextualisées avec des simulations régionales de transport et de distribution d'aérosols à l'aide du modèle GEOS-Chem. Le chapitre fournit des détails sur le système d'impaction d'aérosol transporté en ballon utilisé pendant la campagne BATAL. L'impacteur se compose de quatre étages avec des seuils de taille spécifiques pour échantillonner les aérosols dans la région de l'UTLS aux altitudes de l'ATAL. Des vols en ballon ont été effectués et l'altitude, la température et l'humidité relative à l'intérieur de l'impacteur ont été surveillées tout au long de l'expérience. Des échantillons d'aérosols ont été recueillis, extraits et analysés pour détecter la présence d'espèces inorganiques solubles dans l'eau à l'aide de la chromatographie ionique. Les échantillons au sol analysés dans l'étude ont montré la présence de divers cations et anions, tels que Na^+ , Ca^{2+} , NO_2^- , NO_3^- , SO_4^{2-} . Le solde de charge n'a pas été atteint en raison d'une charge négative plus élevée du NO_3^- et du NO_2^- . La présence de nitrate sous des formes autres que le sel a été suggérée, et la concentration de nitrate était plus faible que dans les études précédentes. L'instabilité des particules contenant des nitrates et la dissociation de $(\text{NH}_4)_2\text{NO}_3$ en HNO_3 et NH_3 ont été notées. D'autre part, la campagne hivernale a montré la présence de Ca^{2+} et de SO_4^{2-} probablement influencés par les feux de forêt canadiens. L'influence de la convection sur les mesures a été étudiée à l'aide de calculs de rétro-trajectoire et d'observations satellitaires. Le chapitre se termine en soulignant les contributions des émissions chinoises et indiennes à l'anticyclone asiatique et l'abondance de poussière minérale dans la troposphère. Les principales conclusions concernant la composition chimique de l'ATAL lors de la campagne de mesure en ballon sont les suivantes :

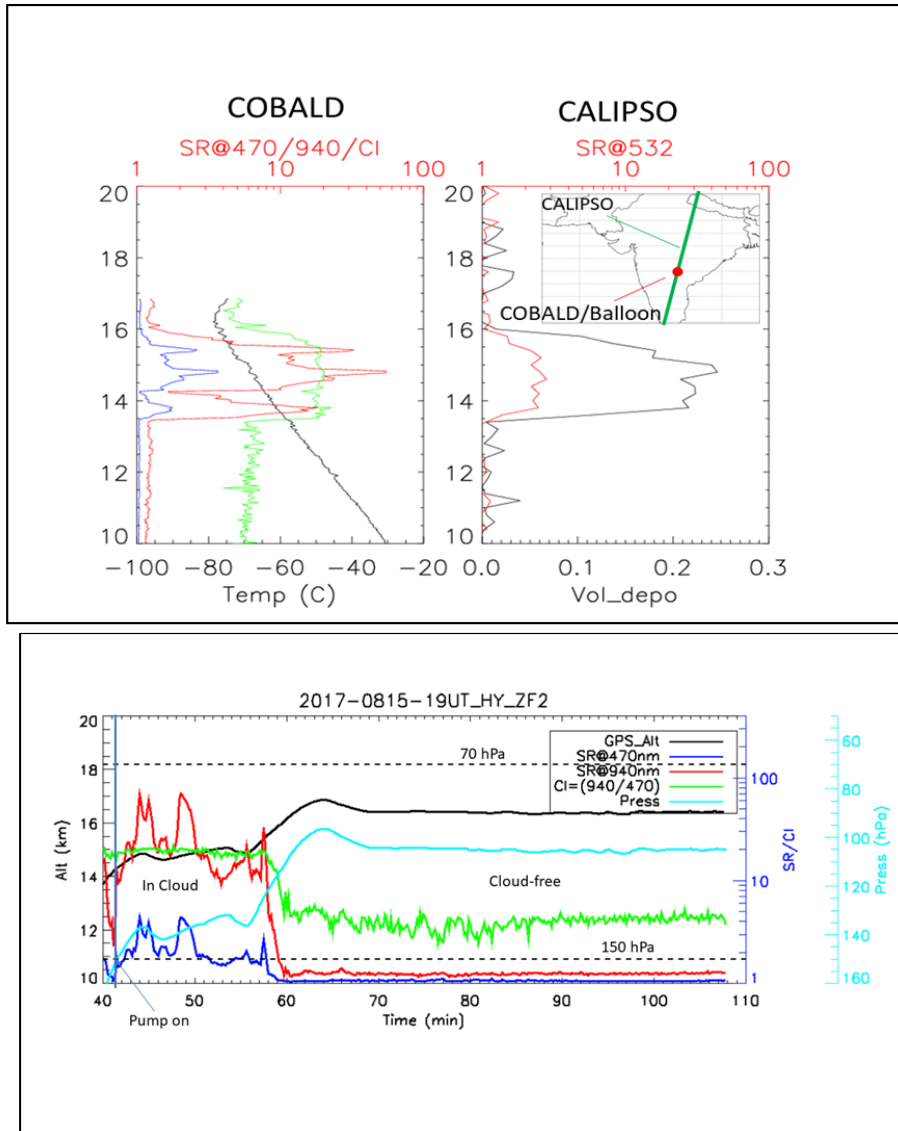


Figure 3.6: (a) COBALD in situ scattering ratio (SR) and color index (CI) profiles and (b) CALIOP satellite SR and volume depolarization profiles co-located in time and space (within 20 km and 1 h, respectively) on 15 August at 19:00 UT. (c) Time series along ZF2 of SRs at 940 and 470 nm from COBALD as well as the GPS altitude and measured pressure from the iMet radiosonde.

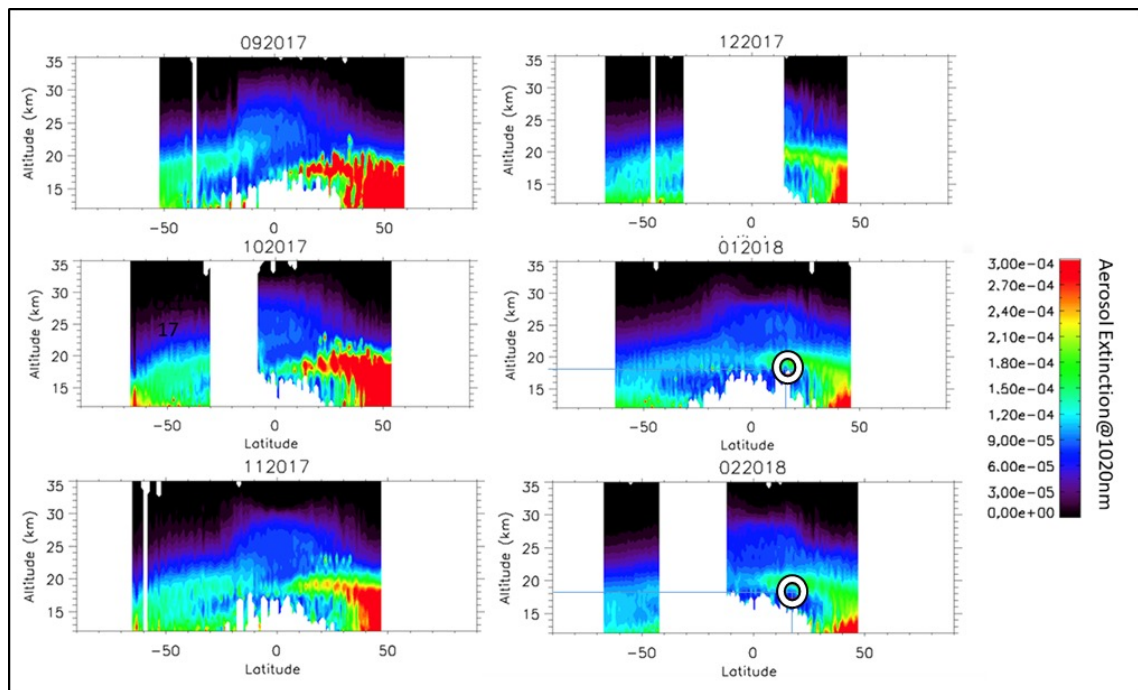


Figure 3.7: Zonal mean aerosol extinction at 1020 nm derived from the SAGE III/ISS V051 data products between September 2017 and February 2018. Ice clouds in the troposphere have been removed using a threshold of color ratio (521nm/1020nm) below 2 (Vernier et al., 2015). An increase in aerosol extinction between 10-50°N and 13-21 km is observed from September 2017 to the end of 2017 due to the Pacific Northwest Canadian PyroCbs which injected smoke in the Upper Troposphere and Lower Stratosphere in August 2017. A residual of the smoke plume is still detected up to February 2018. The white rings show the location of the balloon flight at the bottom of the aged smoke plume.

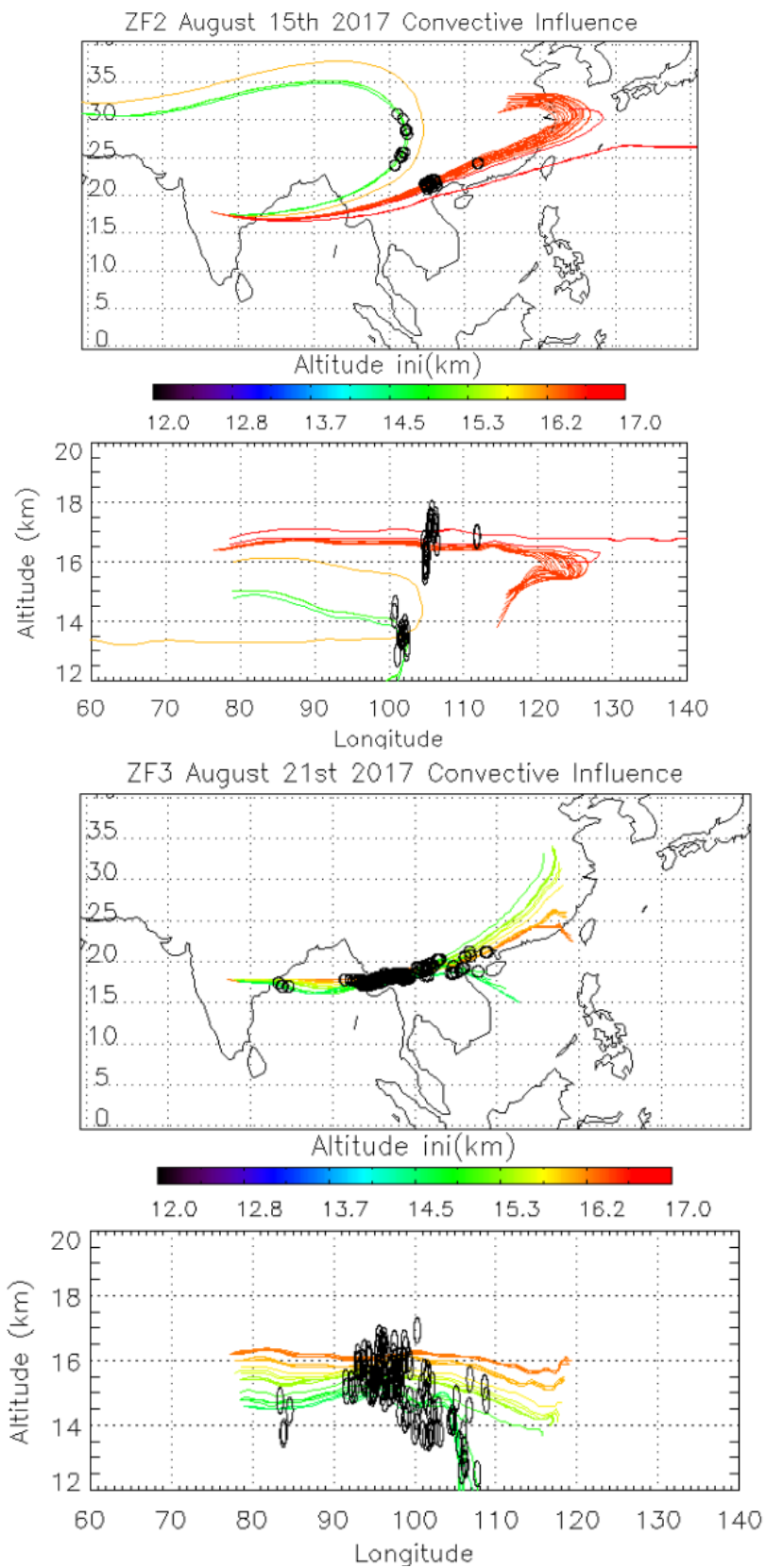
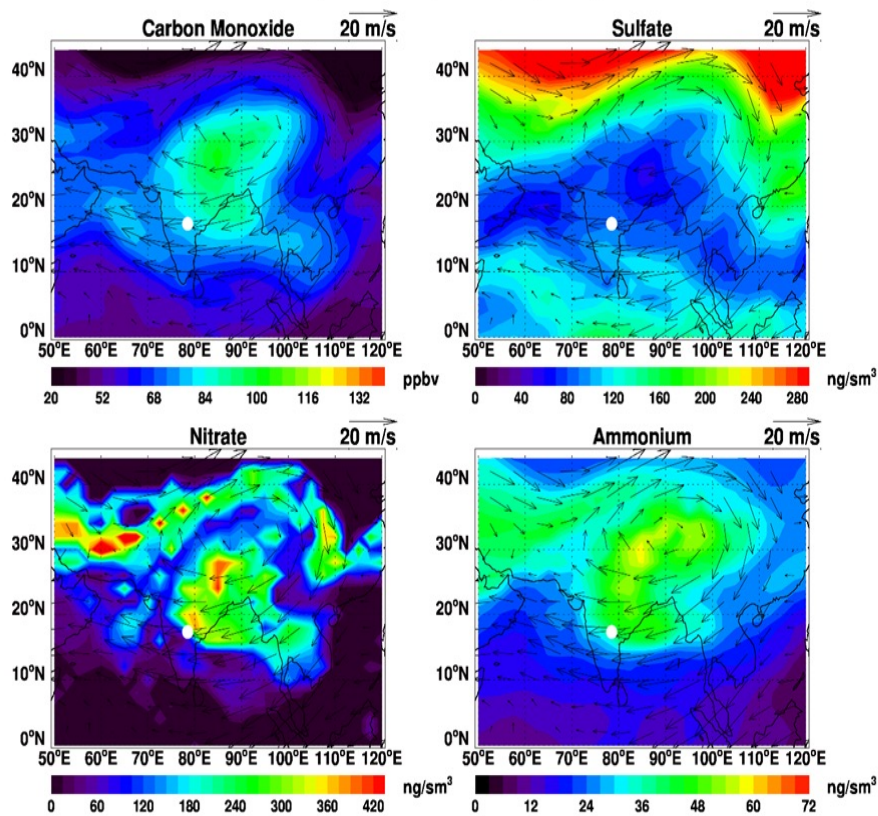
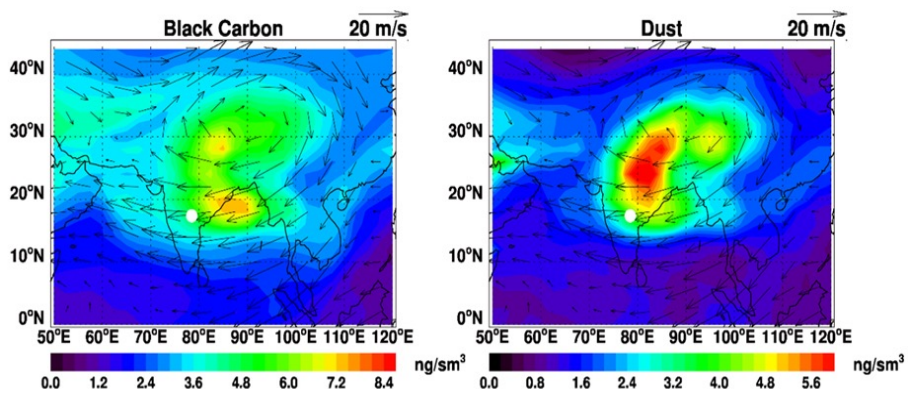


Figure 3.8: Back trajectories initialized from ZF2 (15/08) and ZF3 (21/08) measurements between 150 and 70 hPa. Black dots along the trajectories are the position of convective systems intersecting air masses sampled during the balloon flight.

GC/MERRA2, 100-150hPa, 22UTC, August 15, 2017



GC/MERRA2, 100-150hPa, 22UTC, August 15, 2017



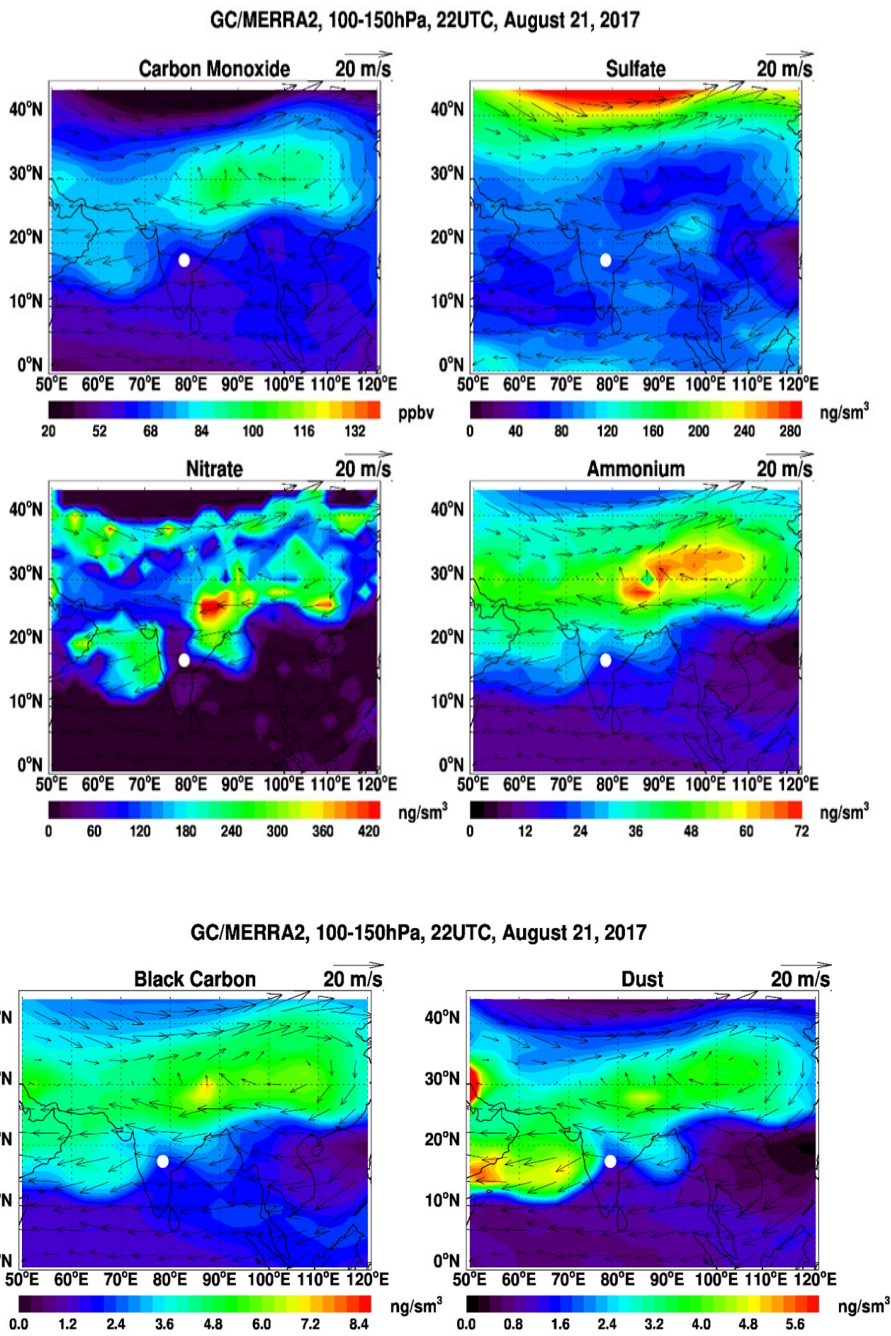


Figure 3.9: The two sets of six panels show the respective GEOS-Chem model-simulated carbon monoxide (CO , ppbv), sulfate (SO_4^{2-} , ng m^{-3} at STP), nitrate (NO_3^- , ng m^{-3} at STP), ammonium (NH_4^+ , ng m^{-3} at STP), black carbon (BC, ng m^{-3} at STP), and dust (Ca_2^+ , ng m^{-3} at STP) concentrations averaged over 100–150 hPa at 22:00UTC on 15 August 2017 (top six panels) and 21 August 2017 (bottom six panels). Standard temperature and pressure are 298 K and 1013.25 hPa, respectively. Arrows denote the wind direction, and the white circle indicates the sampling location in Hyderabad, India.

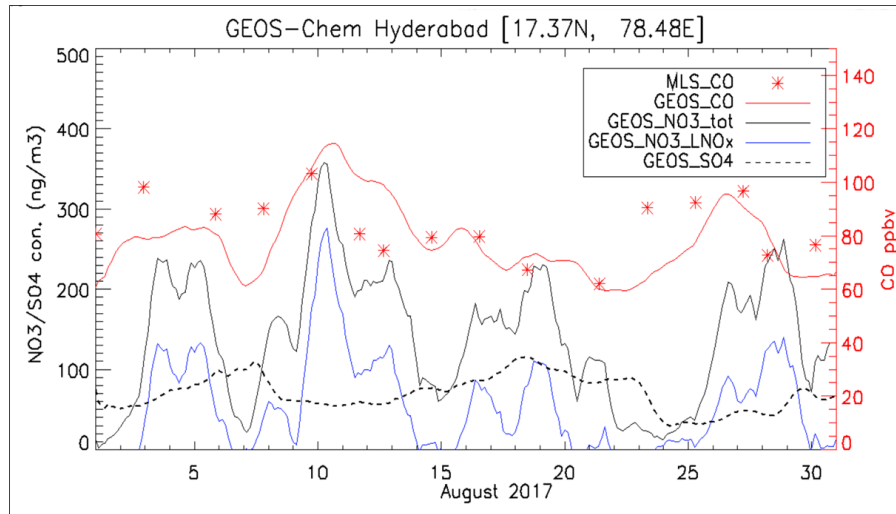


Figure 3.10: BTime series of simulated 3-hourly CO, SO_4^{2-} , and NO_3^- concentrations averaged over 100–150 hPa at Hyderabad during the ZF2 and ZF3 flights on 15 and 21 August 2017. Also shown are concentrations of NO_3^- due to lightning NO_x emissions (NO_3^- , LNO_x). See the text for details.

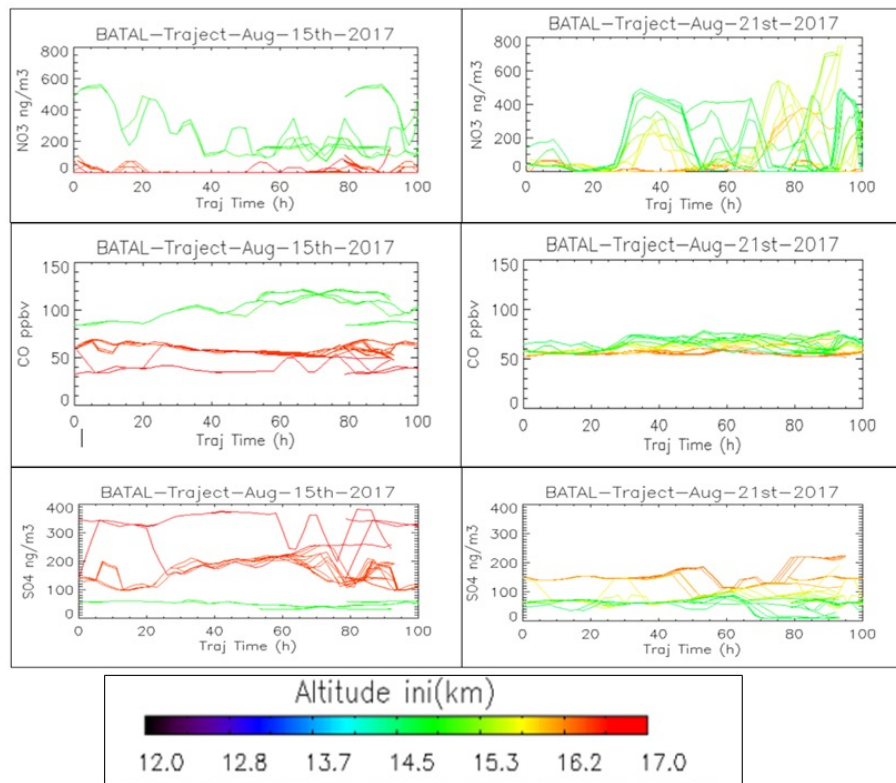


Figure 3.11: GEOS-Chem model-simulated NO_3^- , CO, and SO_4^{2-} concentrations (at STP) extracted along the trajectory lines during flights ZF2 and ZF3 (as shown in Fig. 1.5).

Chapter 4

An ocean of stratospheric aerosols after the Hunga Tonga Hunga-Ha'apai Volcanic eruption



4.1 Introduction

The stratospheric aerosol layer has witnessed several perturbations in the last couple of years. From intense wildfires in North America and Australia to explosive eruptions like Ambae, in July 2018, Raikoke, in June 2019, and finally the Hunga-Tonga Ha’apai (HTHH) in January 2022. The 2022 HTHH eruption was a major volcanic event with atmospheric gravity waves circumnavigating the world several times and a tsunami felt much across the Pacific Ocean. The HTHH submarine eruption led to the direct injection of a massive amount of materials into the stratosphere at an altitude of ~ 58 km (Zhu et al., 2022), never observed in the satellite era (Khaykin et al., 2022, Proud et al., 2022). Major volcanic eruptions are known to produce long-lasting stratospheric sulfate aerosols from SO_2 emissions which can last for years and cool surface temperatures as observed after Mt Pinatubo (Parker et al., 1996). However, in contrast to the large SO_2 injection of ~ 20 Tg by Mt Pinatubo, HTHH emitted a modest $0.6 - 0.7$ Tg of SO_2 (Carn et al., 2022) but a massive amount of water vapor. Satellite observations from the Aura Microwave Limb Sounder (MLS) showed the unprecedented injection of H_2O estimated to be 146 ± 5 Tg, 10% of the total stratosphere water vapor burden (Millán et al., 2022). H_2O vapor is known to be a very efficient greenhouse gas contributing towards climate warming in contrast to sulfate produced by the oxidation of SO_2 known to reduce surface temperatures due to an “umbrella” effect (Charlson et al., 1992). Early studies showed that the injected H_2O vapor may have reduced SO_2 lifetime by 50% through the rapid conversion of SO_2 to H_2SO_4 (Zhu et al., 2022). Months after the eruption, a mid-stratospheric volcanic H_2O vapor layer were found slightly above the volcanic aerosol layer at 26 km (Schoeberl et al., 2022). The H_2O vapor layer was found to ascend slowly (~ 0.44 km/day) by diabatic circulation generating tropical trace gas tape recorders (Schoeberl et al., 2018) whereas the aerosol layer descended on account of the gravitational settling of particles estimated to $1.2 \mu\text{m}$ (Legras et al., 2022). The large H_2O perturbation by the HTHH may increase by 7% the likelihood of exceeding the Earth’s average temperature of 1.5°C above industrial area within the next 5 years, a threshold set to be avoided as a part of climate negotiation of the Paris Agreement. In contrast, it’s believed that the modest SO_2 injected and the resulting sulfate would lead to a minor global cooling of 0.004°C (Zuo et al., 2022).

Simple climate prediction used in Zuo et al. 2022 based on the relationship between SO_2 injected, expected Stratospheric Aerosol Optical Depth (SAOD), and associated radiative forcing and climate impacts (Aubry et al., 2012) are likely not applicable to HTHH, a submarine eruption with such a large amount of water injected. In the next section, we will look at the discrepancies between SO_2 and SAOD.

4.2 Modest injection of Sulfur Dioxide and the large resulting AOD

The SO_2 injected into the stratosphere because of explosive volcanic events undergoes oxidation and nucleation thereby converting to long-lasting sulfate aerosols. These aerosols are known to reduce the surface downward shortwave radiation and absorb the near-infrared and outgoing longwave radiation causing a decrease in surface temperature and an increase in stratospheric temperature (Robock, 2000). The Earth’s radiative budget alterations further influence the climate through processes associated with suppressed global water cycle (Robock et al., 2000; Timmreck et al., 2012) anomalous winter Eurasian warming (Robock, 2000; Stenchikov et al., 2002), El Niño-like sea surface temperature response (Zuo et al., 2018; Sun et al., 2019) in addition to weakened monsoon circulation (Man et al., 2014, Fadvanis et al., 2018).

We used the Global Space-based Stratospheric Aerosol Climatology (GloSSAC) database to investigate the relationship between injected SO_2 and impacts on the stratospheric aerosol burden over the last four decades. GloSSAC was created to produce homogenous, consistent, and continuous data to build robust and consensual observational records of stratospheric aerosol observations (Kovilakam, and Thomason, 2022). Figure 4.1 (left) shows the time series of the global zonal mean Stratospheric Aerosol Optical Depth (SAOD) between 60°N and 60°S between 1979 and 2023. Sulfate produced by volcanic SO_2 is considered to be the major contributor to SAOD and subsequent radiative and climate impacts (Robock, 2000; Aubry, et al., 2022). Thus, we also show a scatter diagram (right) of mean semi-annual SAOD (sSAOD) following each eruption as a function of the volcanic SO_2 . We choose a semi-annual average instead of yearly to avoid averaging the impacts of multiple events together such as the Raikoke eruption in June 2019 which was still affecting the stratospheric during the Australian bushfires in December

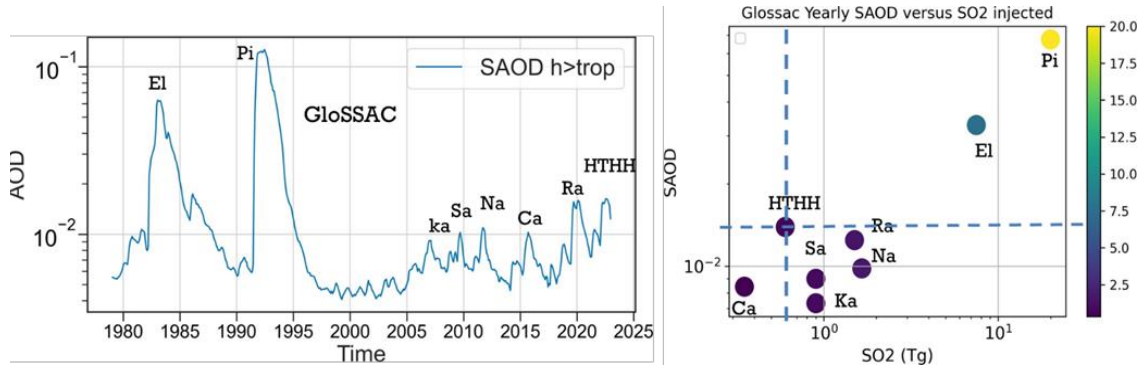


Figure 4.1: GloSSAC time series zonal mean [60N-60S] Stratospheric Aerosol Optical Depth (SAOD) was calculated with a combination of satellite observations above the tropopause (left). Scatter plot (right) of volcanic SO_2 and semi-annual mean SAOD from the date of each eruption [the first two letters of each volcanic eruption are annotated]. El: El Chinchon, Pi: Mt Pinatubo, Ka: Kasatochi, Sa: Sarychev, Na: Nabro, Ca: Calbuco, Ra: Raikoke, HTHH: Hunga Tonga Hunga Ha'apai.

2009/January 2020. With a modest 0.65 Tg of SO_2 injected (Carn et al., 2022), the HTHH eruption produced a significantly higher sSAOD as compared to moderate volcanic eruption observed since the late 2000s. For example, the Raikoke eruption in 2019 injected around 1.5 Tg of SO_2 and resulted in a sSAOD of 0.012 while the modest 0.65 Tg SO_2 injected by HTHH resulted in a sSAOD of 16% higher. Comparing HTHH with other eruptions yield to conclude that the expected SAOD produced by HTHH should have been a factor 3-4 smaller owing to the small levels of SO_2 injected.

Thus, we conclude that either estimate of SO_2 from satellites might have been strongly underestimated or an alternative source of aerosols could contribute to the SAOD observed after this eruption. We cannot rule out the first hypothesis since a signature of sulfate was found within a day after the HTHH eruption by IASI observations (Clerbaux et al., 2023, HTHH workshop) and additional analysis would be required to understand the sulfate chemistry within the HTHH early plume.

In order to investigate the apparent discrepancy between the large sSAOD and the SO_2 injected, we mounted a field experiment to study the chemical, optical, and microphysical properties of the HTHH plume.

4.3 BraVo campaign

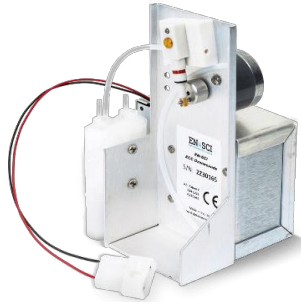
NASA, LPC2E-CNRS, France, and several research institutes in Brazil mounted a field campaign from May to August 2022 to study HTHH known as the Brazil Volcano (BraVo) project. We successfully deployed a suite of sensors to Brazil to investigate the physical, chemical, optical, and microphysical nature of the HTHH plume from Bauru (22.36°S, 49.03°W) in Sao Paulo state. We provide herein below a quick description of the payloads used for the campaign (see figure 4.2):

The CFH measures water vapor concentration through the chilled-mirror principle using a cryogenic liquid as a coolant. A small mirror attached at the end of the cold finger piece is electrically heated and cryogenically cooled to maintain a constant thin layer of frost that is optically detected. The mirror temperature is then equal to the ambient dewpoint or frost-point temperature and is measured by a small thermistor embedded in the surface of the mirror. The frost-point temperature is used to calculate the partial pressure of water vapor in air and determine the water vapor mixing ratio (WVMR) with an uncertainty of about 4% in the lower tropical troposphere to about 10% in the middle stratosphere and tropical tropopause (Vömel et al. 2007). Table 4.1 provides a summary of the balloon flights that took place during the BraVo campaign between May and November 2022.

Throughout the campaign and when the weather allowed, ground-based lidar measurements were carried out in Sao Paulo as well as in Bauru (400 km west of Sao Paulo). Figure 4.3 shows lidar data from Bauru (right) on 29 May 2022. The HTHH aerosol visible using raw backscatter signal at 532 nm shows the plume centered near 22.5 km within ± 2 km. The mean latitudinal cross-section of Scattering Ratio (SR: Total/molecular backscatter) at 532 nm using CALIPSO data between 23 May 2022 and 2 June



(a) We used iMet RS-41 radiosondes. These instruments measure temperatures from -90°C to 50°C with a resolution of 0.1°C and an accuracy of 0.5°C . Wind speed resolution is 0.1 m s^{-1} with an accuracy of 0.2 m s^{-1} .



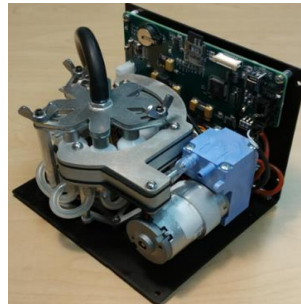
(b) We launched electrochemical concentration cell (ECC) ozonesondes (Komhyr et al. 1995) to measure the vertical distribution of ozone from the surface to balloon-burst altitude. The measurement is based on the electrochemical oxidation of potassium iodide by ozone in an aqueous solution. The accuracy of the ECC ozonesonde is $\sim 5\% - 10\%$.



(c) A small balloon-borne OPC payload was deployed based upon the adaptation of the Particle Plus 8306 OPC profiler to make aerosol concentration measurement at eight radii between 0.15 to $5\text{ }\mu\text{m}$ up to the middle stratosphere (POPC). The New POPC is a similar instrument (9301 series) with 30 channels between 0.15 to $5\text{ }\mu\text{m}$.



(d) Compact Optical Backscatter Aerosol Detector (COBALD). COBALD is a lightweight (540 g) instrument that consists of two high-power light-emitting diodes (LEDs) that emit about 500 mW of optical power, at wavelengths of 470 and 940 nm , respectively. The backscattered light from the molecules, aerosols, or ice particles is recorded by a silicon photodiode using phase-sensitive detection. Absolute error interval of 5% , while precision along the profile is better than 1% in the UTLS region (Vernier et al. 2015).



(e) The aerosol CHEM sampler is a simple device that captures aerosol particles on filters for later chemical analysis (Brechtel filter sampler). The sampler has eight filter cartridges that hold the individual filters. Further details about the sampler are provided in the next section.



(f) Cryogenic Frost point Hygrometer (CFH). See text for detailed description.

Figure 4.2: Payloads used for the campaign.

2022 shows the presence of the plume extending between $20\text{-}26\text{ km}$ consistent with lidar observations. However, we note here that CALIPSO data around South America were not used due to high noise associated with the geomagnetic South Atlantic anomaly.

We further study the microphysical properties of the plume using POPC data made during the BraVo project. Figure 4.4 shows the number concentration profiles for aerosol radius greater than a given size. We show selected sizes between $0.15\text{ }\mu\text{m}$ and $5\text{ }\mu\text{m}$ for two flights 82 days apart on 05/25 and 08/12. Noticeable features include a separation of around 2.5 km between the peaks of aerosol for $r > 0.4\text{ }\mu\text{m}$ observed in May and August that could be translated into a descent rate of the plume of $\sim 30\text{ m d}^{-1}$.

Date and Flight#	Launch time LT	Imet	CFH	ECC	POPC	NPOPC	Sampler	COBALD	Rs-41
20220524_BRU_BraVo_01	7.30pm	x			x	x		x	x
20220525_BRU_BraVo_02	10.30am	xx				x	x		x
20220527_BRU_BraV_03	7.30pm	x			x	x		x	x
20220529_BRU_BraVo_04	10.30am	x				x	x		x
20220530_BRU_BraVo_05	10.30am	x				x	x		x
20220601_BRU_BraVo_06	10.30am	x				x	x		x
20220630_BRU_BraVo_07	2am	x				x		x	x
20220807_BRU_BraVo_08	3.30am	xx	x	x		x		x	x
20220812_BRU_BraVo_09	3.30am	xx	x	x		x		x	x
20220816_BRU_BraVo_10	3:00pm	x					x		x
20220820_BRU_BraVo_11	3:30am	x	x	x		x		x	x
20221103_BRU_BraVo_12	3:30am	xx	x			x		x	x

Table 4.1: Balloon flights from Bauru (-22.36, -49.03), Brazil during the BraVo campaign.

Early observations suggest the presence of volcanic aerosols up to 30 km while the profile in August shows their absence. The maximum concentration for $r > 0.15 \mu\text{m}$ is seen to decrease from $15 \text{ \#}/\text{cm}^3$ to $7 \text{ \#}/\text{cm}^3$ suggesting that the plume was dispersed during its transport.

Low-cost and lightweight balloon flights were used to study the HTHH plume in the mid-stratosphere which was too high for most aircraft measurements. While several balloon campaigns were conducted in Reunion Island (France) (Kloss et al., 2022), and Lauder (New Zealand), none of those campaigns attempted to study the chemical properties of the plume. Among the science payloads used during this campaign, the most relevant to this study is the lightweight aerosol sampler coupled with a radio-controlled valve. We will further analyze the only successful flight that incorporated both systems.

In the next section, we will describe the radio-controlled valve, the aerosol sampler and the IC analysis used to study volcanic aerosol ionic composition. The valve, attached to the neck of the balloon, was opened to release gas and decrease the ascent of the balloon to extend the sampling duration inside the HTHH plume (Vernier et al., 2018). The system allowed sampling of the HTHH plume for more than 40 min between 19 and 22 km 3-4 times longer than with a traditional balloon flight. Three sets of samples were collected corresponding to the boundary layer, the free troposphere, and the lower stratosphere within the HTHH plume.

4.4 Materials and methods

4.4.1 Radio-Controlled balloon system:

The radio-controlled balloon system is based on a valve attached to the neck of the balloon which can be opened and closed using commands sent via 433 MHz. The system is also called boomerang and was operated in India during a balloon campaign in 2016. Boomerang is composed of two elements, a valve and a simple ballast system. For the BraVo and to avoid potential contamination, no ballast module was included. Figure 4.5 shows the position of the radio-controlled balloon module connected to the neck of

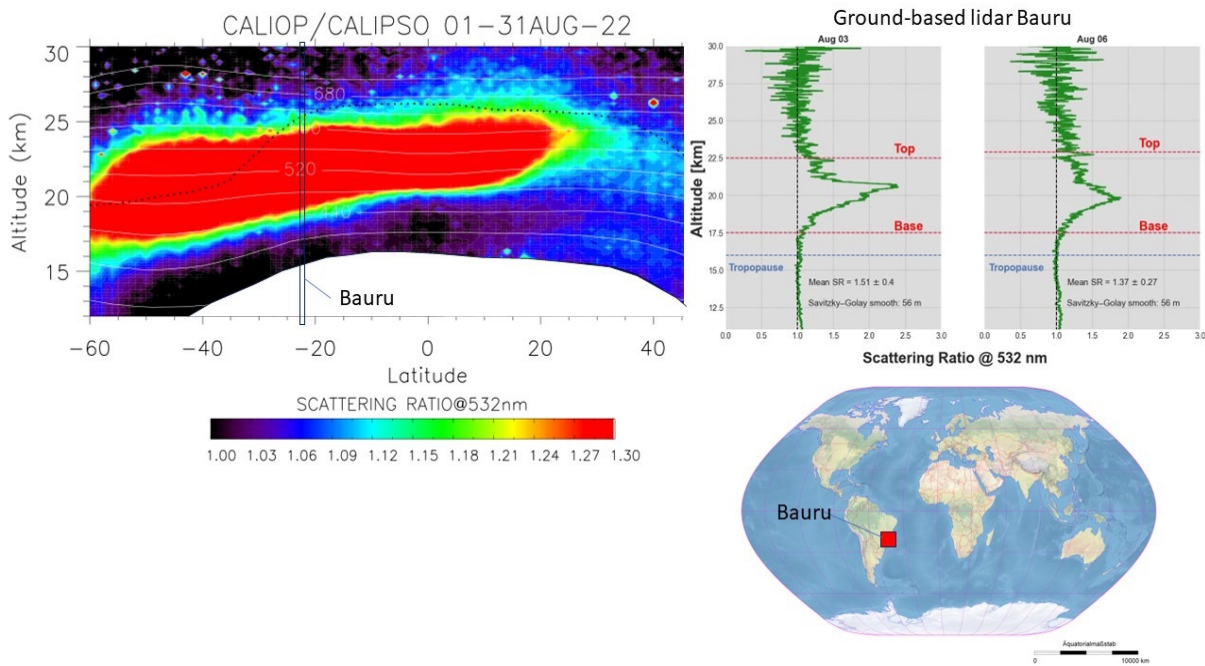


Figure 4.3: (bottom right) world map showing the location of the BraVo campaign in Brazil. (Top right) Ground-based lidar observations Scattering Ratio (SR) at 532 nm from Bauru in August 2022. (Top left) Latitudinal cross-section of the mean SR at 532 nm between 23 May and 2 June 2022 showing the HTHH volcanic plume (in red).

the latex balloon.

The unfavorable weather and logistical constraints permitted us only one flight with the above system. Unfortunately, we couldn't fly the POPC together with the aerosol sampler flight due to weight limitations. However, we obtained particle size measurements using the POPC four days before this flight. Figure 4.6 (left) shows the GPS altitude with respect to sampling time and temperature during the balloon flight while the figure on the right shows the total aerosol concentration for particles measured by the POPC. The concentration is shown for particle diameters greater than a given size. Lidar observations during the campaign showed that the plume was homogeneous between those two flights which took place 8 months after the eruption. The HTHH plume is seen between 18 through 26 km with the larger aerosols ($d > 0.8 \mu\text{m}$) located at the bottom of the plume near 18-20 km while smaller particles are more widely spread up to 25-27 km (figure 4.6). The GPS altitude trajectory of the controlled flight with the aerosol sampler shows a decrease in the ascent rate near 18 km until it reaches a maximum altitude near 21.6 km and descends thereafter. The slow ascent, float, and slow descent permitted the aerosol sampler to stay aloft within the plume layer for 40 min, 3-4 times longer than a traditional balloon flight. In addition, the sampling took place in the main plume containing both large and small particles at temperatures between $-70 \text{ }^\circ\text{C}$ and $-50 \text{ }^\circ\text{C}$.

The aerosol sampler was immediately stored in dry ice upon recovery. The filters bearing the aerosol samples were unloaded in a Laminar air flow unit, placed in individual perti-plates labeled, sealed, and transported to France in dry ice for extraction and analysis.

4.4.2 Lightweight aerosol sampler

We used the commercially available aerosol CHEM filter sampler for aerosol collection, and analysis. CHEM Filter Sampler is designed to collect particles on eight different filters for time-resolved sampling (Bates et al., 2013). The system was adapted for balloon-borne applications and uses a microcontroller. This is connected via serial communication and an InterMet radiosonde that provides information on weather parameters (pressure, temperature, relative humidity) as well as Global Position System locations

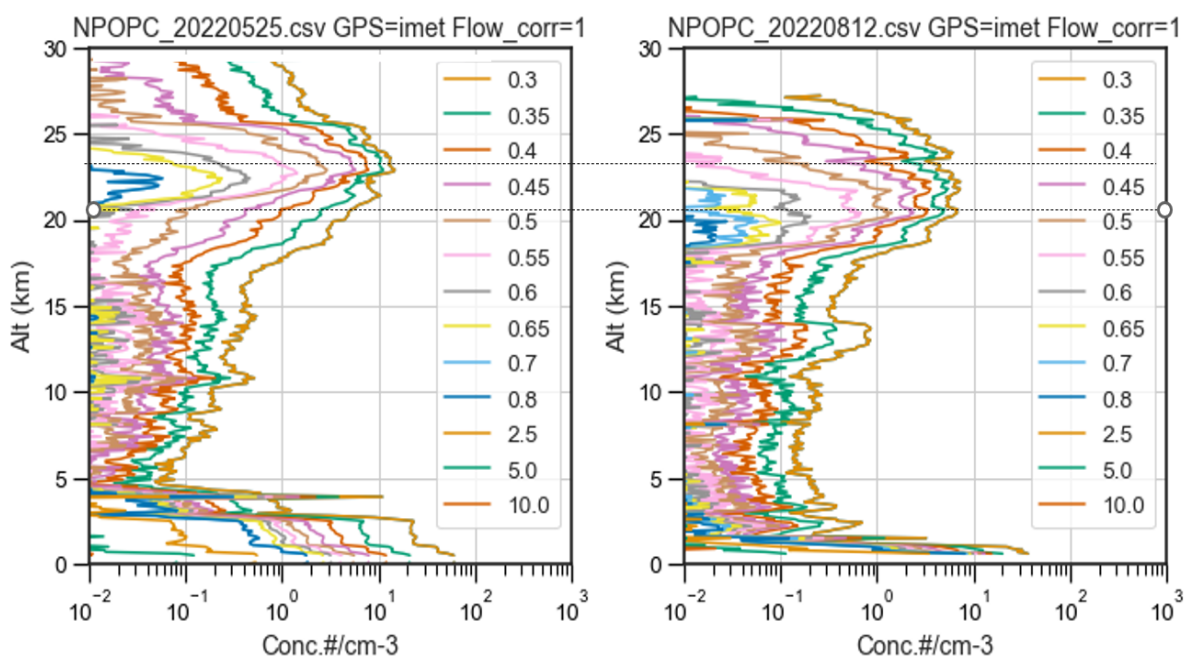


Figure 4.4: Aerosol concentration profiles for aerosol radius greater than 13 size bins between 0.15 μm and 5 μm derived from the Particle Plus Optical Particle Counter

(longitude, latitude, altitude). The sampler consists of eight filter holders that hold the individual filters (Fig. 4.7) and permit time-resolved and/or altitude-based sampling. The interaction between permanent magnets on an external rotating disk and internal valve magnets results in only one valve opening depending on the altitude, as the disk rotates. The rotating disk is located downstream from the filters. The laminar flow element on the inlet measures the sampled flow. The speed of the built-in vacuum pump is adjusted to control the sampled flow. The Imet radiosonde's pressure measurements are used to control the sampler. When activated, the device automatically exposes every filter to the sampled flow within a particular atmospheric layer defined by minimum and maximum pressure limits. When the position is changed, the pump is switched off for 5s. Prior to every flight, the aerosol sampler was meticulously cleaned using isopropyl alcohol.

4.4.3 Ion Chromatography Analysis

A conjugated system of 2 Ion Chromatographs from Dionex (Integrion HPIC, Anions, and Cations) was used to analyze water-soluble inorganic species (WSIS) namely, K^+ , Na^+ , Mg^{2+} , Ca^{2+} , NH_4^+ , Cl^- , F^- , Br^- , NO_2^- , NO_3^- , SO_4^{2-} , and PO_4^{3-} were studied with conductivity detection. AS-18-FAST-4 μm , 2 \times 150 mm was used as the anion column with a KOH gradient as eluent for 25 min: 10 mmol from 0 to 6 min, 10 mmol to 60 mmol from 6min to 15min, and 60 mmol from 15 min to 25 min. Whereas, CS-12A, 4 \times 2500 mm was used as the cation column with Methyl Sulfonic Acid gradient as eluent for 25 minutes: 10 mmol from 0 to 6 min, 10 mmol to 35 mmol from 6 min to 15 min, and 35 mmol from 15 min to 25 min. An EQ7000 Millipore ultra-pure water purification system (Resistivity $\geq 18.2 \text{ M}\Omega \text{ cm}$) was used to generate ultra-pure water used for dilutions, extractions, and preparation of the mobile phase columns. A 5 mg L^{-1} mix was prepared from a 1000 mg L^{-1} stock solution of each cation using a highly pure analytical grade standard solution from Merck (NH_4Cl , CaCO_3 , KNO_3 , MgNO_2 , and NaNO_3) for calibrating each cation. Likewise, Merck's high purity grades of anion standards (NaCl , NaNO_3 , NaBr , NaNO_2 , and NaSO_4) were prepared for calibrating each anion. The cation, and anion mix were diluted, to create a series of working standards with concentrations of 1, 5, 10, 50, 100, and 500 $\mu\text{g L}^{-1}$. These were injected into the instrument (sampling loop of 250 μL) to create a calibration range for the samples. The ultra-pure water was pre-checked for probable cation & anion contamination prior to sample analysis.

Filters on positions 5,6,7 and 8 of the sampler were used as blanks. We followed the extraction



Figure 4.5: Preparation of the aerosol sampler flight (left). Zoom on the radio-controlled valve used to reduce the ascent inside the HTHH plume on 08/12.

procedure that was previously described (Vernier et al., 2022). Following the extraction, each sample was injected three times (Fig.5). The average values of each ionic species were calculated and the data were analyzed using the same method described earlier (Vernier et al., 2022). The analysis was repeated three times and Only values with percentage variability lower than 20% were considered here.

4.4.4 Method to derive mass from POPC

The Particle Plus Optical Counter (POPC) is a commercially available sensor that was adapted for balloon applications with a flow control system and an interface for telemetry through an IMet radiosonde (Vernier et al., 2023, in preparation). It has been used since 2018 on several field campaigns in India and France (Dumelie et al., 2023, in review) with more than 50 flights. Using concentration measurements from 30 channel sizes ranging from 0.3 μm to 10 μm made during a flight on 08/12 (Fig.4.7) and, flow and ascent rate during the sampler flight on 08/16, we derive a theoretical aerosol mass that would have been collected based on OPC data. An aerosol density of 2.16 g m^{-3} , corresponding for sea salt particles, was assumed and the data at Standard Pressure and Temperature (STP) were corrected. We found a total mass concentration in the plume of 3.4 $\mu\text{g m}^{-3}$ STP, a value which will be later on compared with the laboratory analysis.

4.5 Results

During the sampling, and transportation there could have been alterations in the temperature affecting the chemical composition of the filtered aerosol mass. The results reported here primarily focus on what was detected by the IC instrument after following the extraction procedure. The extended flight within the plume resulted in collecting additional aerosol mass on pos#4 [9.3 $\mu\text{g m}^{-3}$]. Pos#4 exhibits an enriched composition of diverse ions, forming a complex mixture that includes Na^+ , K^+ , NH_4^+ , Ca^{2+} , Cl^- , F^- , NO_3^- , and SO_4^{2-} . However, the presence of F^- , NO_3^- , and NH_4^+ in pos#4 remains uncertain due to the large error bars associated with these ions. (Fig. 4.9). In the tropospheric layer, specifically

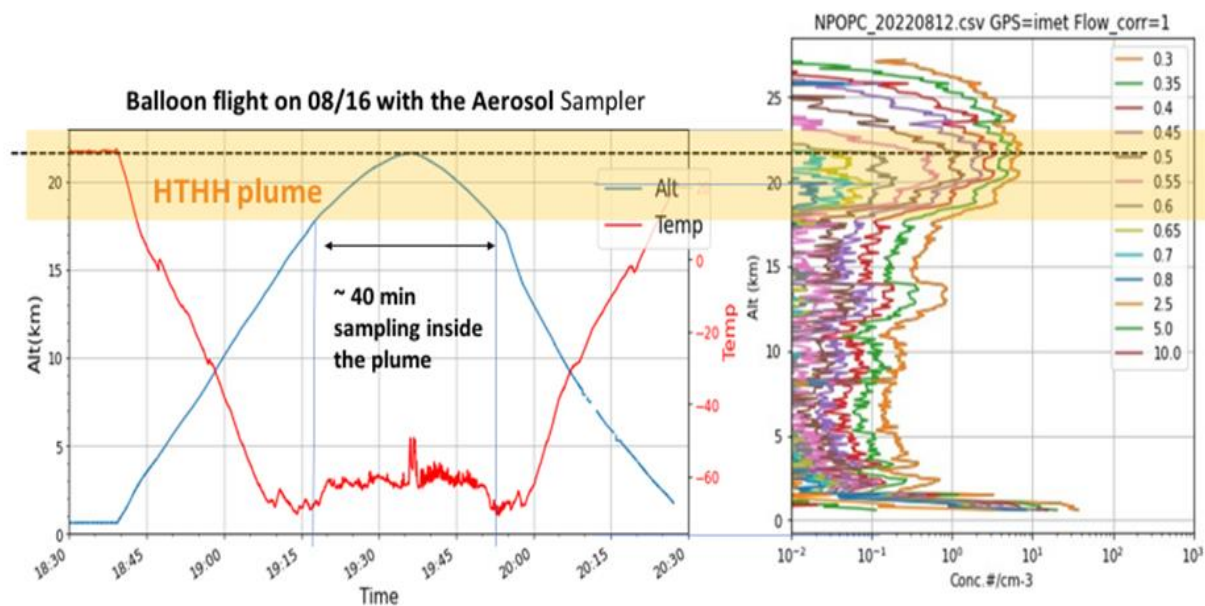


Figure 4.6: (left) Trajectory of the radio-controlled balloon flight showing GPS altitude with respect to time, and temperature. (right) Aerosol concentration profiles from POPC show that the sampling was done within the HTHH plume

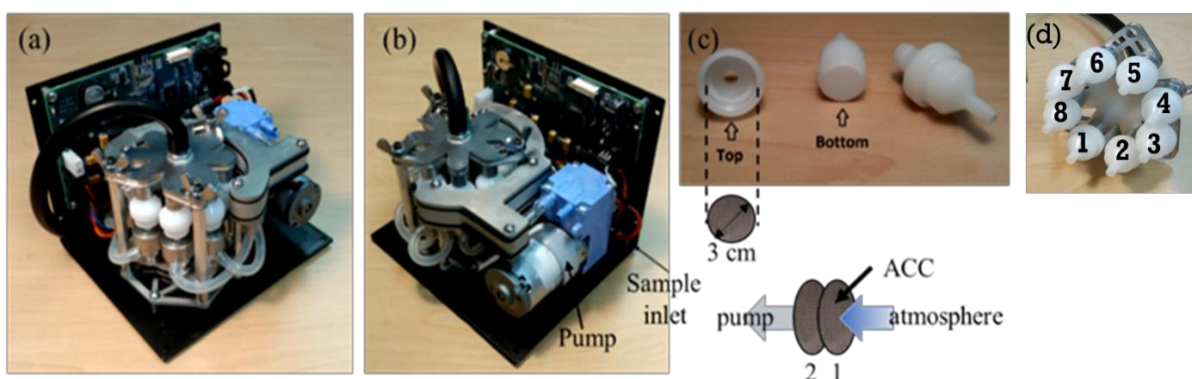


Figure 4.7: (a,b) CHEM lightweight balloon-borne filter sampler.(c,d) filter holders bearing filters.

between 5-17 km, pos# 3 recorded a total ionic concentration of $1.2 \pm 0.6 \mu\text{g m}^{-3}$. Notably, among the ions analyzed, Ca^{2+} was the sole ion detected in noticeable quantities within this layer. In the boundary layer, ranging from 1.6 to 5 km, Pos#2 revealed the presence of Na^+ , K^+ , NH_4^+ , Mg^{2+} , Ca^{2+} , Cl^- , NO_3^- , and SO_4^{2-} . However, it is important to highlight that only Ca^{2+} , Mg^{2+} , NO_3^- , and SO_4^{2-} ions are deemed reportable within this specific context. The Cl^-/Na^+ ratio on position 3 was found to be 1.6, close to the expected sea water chlorinity which is 1.8 (Thamban et al., 2007). Thus, the results suggest the presence of sea salt that would have originated from the HTHH submarine eruption. It is anticipated that around 5 teragrams (Tg) of Cl^- , in the form of NaCl, were transported to the stratosphere as a result of the HTHH eruption out of which only 0.02% equivalent to a small fraction, persisted as active chlorine in the stratosphere (Zhu et al., 2023). In addition, they analyzed the NaCl concentration presented in the results shown here using WACCM model simulations and estimated that a quantity ranging from 0.5 – 1 Tg of NaCl could have been released into the stratosphere and remained suspended. They conclude by saying that beyond the plume area, the prevalence of HCl and ClONO_2 , suggests that the majority of Cl exists in reservoirs. The major ions (Na^+ , K^+ , NH_4^+ , Mg^{2+} , Ca^{2+} , Cl^- , F^- , SO_4^{2-} , and NO_3^-), found in position 4 are consistent with aerosol mass spectroscopy analysis of sea salt (Murphy et al., 2019).

The presence of Cl^- however seems to be inconsistent since H_2SO_4 and other acids are known to displace halogens thereby forming HCl (Chameides, W. L. and Stelson, 1992); Finlayson-Pitts, B. J.

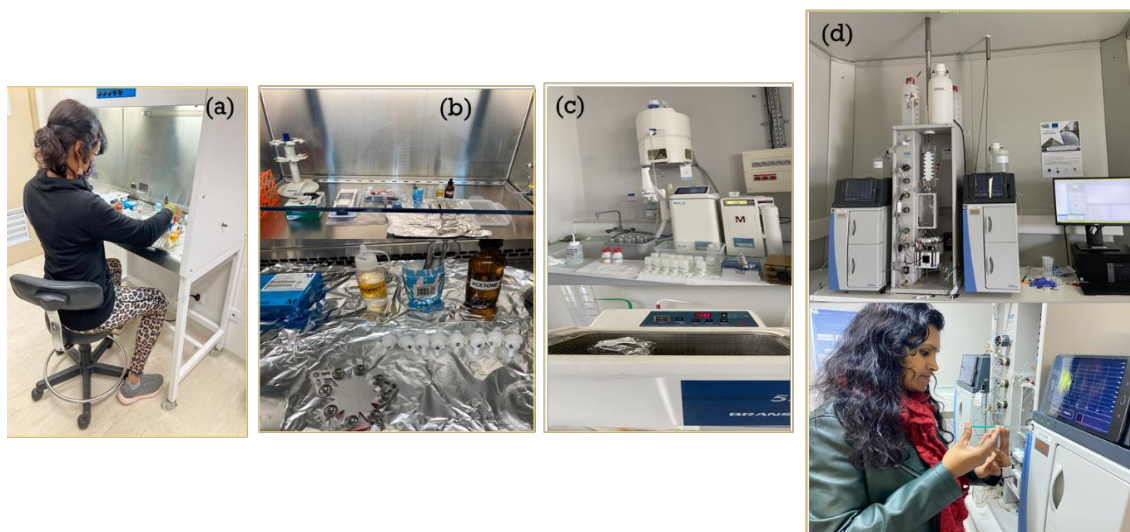


Figure 4.8: (a,b) Loading and unloading of filters in the Laminar air flow chamber. (c) Aerosol extraction. (d) Analysis of extracts using Dionex ion chromatograph instrument.

and Hemminger, J. C, 2000). Halite particles (NaCl) were found to have reacted with H_2SO_4 1 month after the El Chinchón eruption thereby releasing gaseous HCl (Woods et al., 1982; Leu et al., 1995). El Chichon injected salt of volcanic origin but not from the ocean. This would result in a deficit of Cl^- in marine aerosols (Leu et al., 1995). Some volcanoes release trace amounts of NH_3 along with HCl . this could possibly contribute to the formation of NH_4Cl through a series of reactions and in doing so retain the Cl^- .

We further explore the microphysical properties of the HTHH plume using size distribution information from the POPC collected in May, August and November (Fig.4.10). Aerosol measurements from the Optical Particle Counter on 08/07 indicate that aerosols collected on position #4 were associated with elevated number concentration for sizes lower than $1.25 \mu\text{m}$ within the HTHH plume with a multimodal distribution centered near $0.35\text{-}0.4 \mu\text{m}$, $0.45\text{-}0.5 \mu\text{m}$, and $0.7\text{-}0.8 \mu\text{m}$. The larger mode is located at the bottom of the plume between 18-20 km. While in May 2022, no significant enhancement of aerosol was observed above $d > 0.9 \mu\text{m}$, we see the mode of larger particles between 18-20 km appearing in August and November.

We conclude that the presence of three different modes and the sedimentation of the largest suggest that sulfate aerosol is likely not the only type of aerosol present. In addition, the more complex microphysical properties of the plume converge with the idea that the aerosol present in the HTHH is not only sulfate but more chemically diversified.

4.6 GEOS-Chem simulation and conclusion.

We ran (in collaboration with Hongyu Liu from NIA/NASA LaRC) the GEOS-Chem chemical transport model simulations driven by MERRA-2 with and without using 0.42 Tg of SO_2 injected between 19-28 km to study HTHH impacts on sulfate aerosols. A description of GEOS-Chem is provided in chapter 3. We found between $0.5 - 5 \mu\text{g m}^{-3}$ STP of SO_4 values within the sampling region between 17-21 km of the aerosol sampler. This is much lower than the $\sim 0.2 \mu\text{g m}^{-3}$ found in the IC results. Comparing a single-point observed value and a monthly mean value may explain some of the differences observed here. However, we don't expect that the monthly mean sulfate concentration would strongly deviate from a single measurement since the plume should already be well homogeneous 8 months after the eruption.

The removal of SO_4 in the HTHH plume by deep convection may not be accounted for well in the model simulation which could explain these discrepancies. Vernier et al. (2011) found that overshooting convection in winter is a significant driver of clean air injection in the lower stratosphere up to 19-20 km. However, this cleansing mechanism should apply not only for sulfate but for additional aerosol found in the plume and found in position #4. The simulation does not account for the presence of water vapor

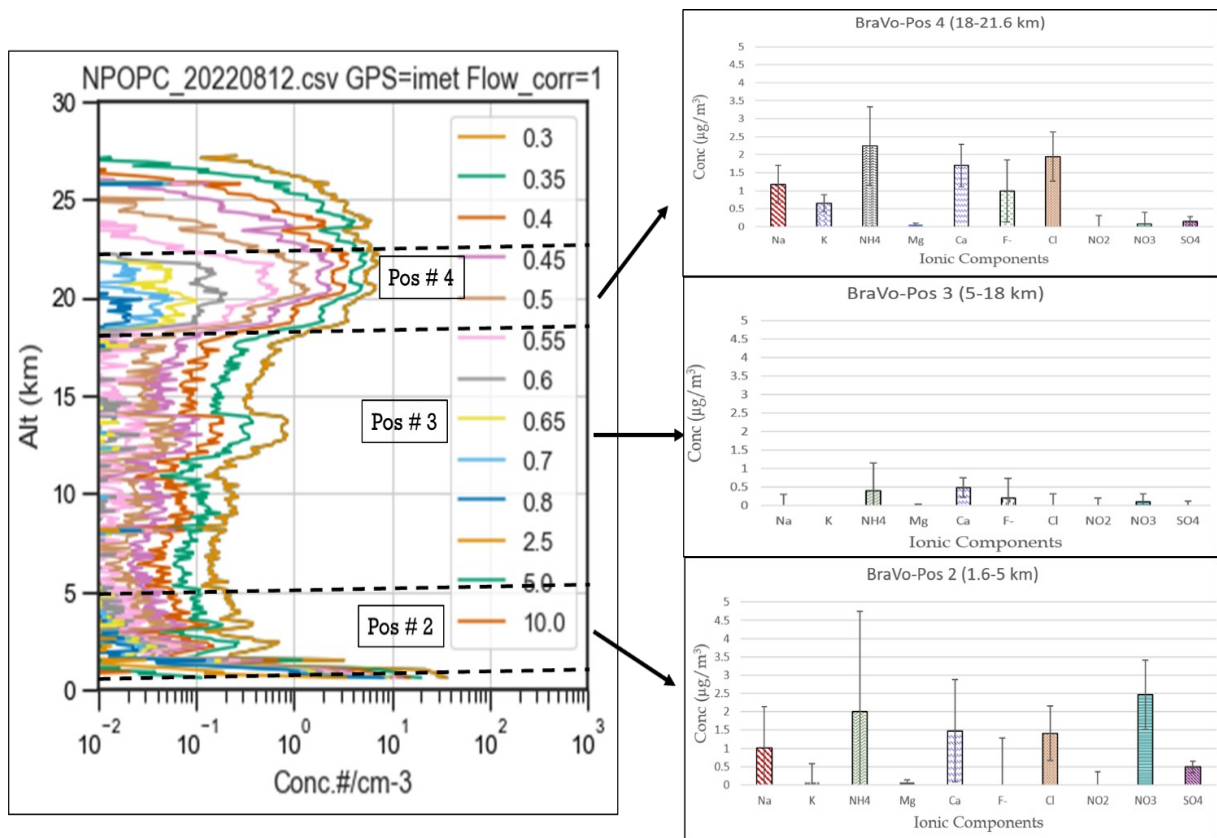


Figure 4.9: The aerosol concentration profile was measured using POPC on August 12th, and on August 18th, the ionic mass concentration was determined through flow rate and IC analysis (right). Aerosol samples were collected on PTFE filters at three distinct positions, enabling the differentiation of aerosols in the boundary layer (Pos #2), the free troposphere (Pos #3), and within the HTHH aerosol layer (Pos #4). The error bars for each species were calculated based on the standard deviation obtained from three repetitions of the IC analysis

that could reduce the lifetime of SO_4 due to particle growth by water uptake and condensation which would lead to a faster removal of particles by sedimentation.

The POPC measurements suggest the settling of aerosols at 18-20 km (Fig.4.10) which would corroborate the idea of particle removal by this mechanism. This might be more efficient for certain types of aerosols such as sulfate since high hydrophilic in nature. Satellite observations often assume that stratospheric volcanic plumes are solely composed of sulfate aerosols alone and implement algorithms to retrieve their physical properties (effective radius) based on this assumption (Travis et al., 2023). However, our results indicate that HTHH may have resulted in the injection of a diversity of marine-related aerosols in the stratosphere which could explain the discrepancy between the large SAOD and the modest SO_2 injected. It is not known how the presence of marine aerosols will affect the radiative, climate, and chemical impacts of the HTHH.

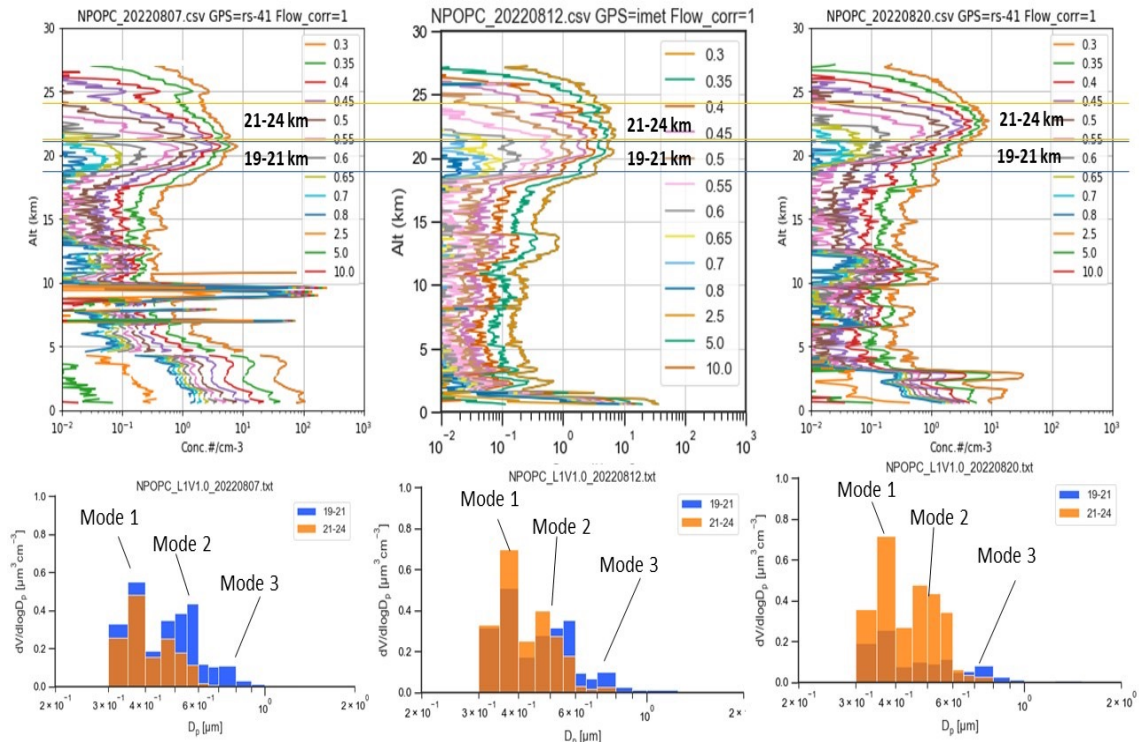


Figure 4.10: Aerosol concentration profiles for selected sizes (0.3 μm to 10 μm) from three flights (08/07, 08/12, and 08/20) in the POPC, along with the corresponding volumetric size distribution between 19-21 km and 21-24 km (dark orange represents the overlapping distribution of the two layers).

Résumé du chapitre 4 : Un océan d'aérosols stratosphériques après l'éruption volcanique Hunga Tonga Hunga-Ha'apai

La couche d'aérosols stratosphériques a connu diverses perturbations au cours des dernières années, notamment des incendies de forêt intenses et des éruptions volcaniques explosives. L'un de ces événements a été l'éruption du Hunga Tonga-Hunga Ha'apai (HTHH) en janvier 2022, qui a injecté une quantité massive de matériaux dans la stratosphère, notamment de la vapeur d'eau et du dioxyde de soufre (SO_2). Alors que les éruptions volcaniques majeures sont connues pour produire des aérosols sulfatés dans la stratosphère qui refroidissent les températures de surface, l'éruption HTHH a émis une quantité modeste de SO_2 mais une quantité importante de vapeur d'eau. Les observations satellitaires ont révélé l'injection sans précédent de vapeur d'eau par HTHH, estimée à 146 ± 5 Tg, soit 10% de la charge totale de vapeur d'eau stratosphérique. La vapeur d'eau est un puissant gaz à effet de serre qui contribue au réchauffement climatique, contrairement aux aérosols sulfatés formés par l'oxydation du SO_2 , qui ont un effet de refroidissement. Les premières études suggèrent que la vapeur d'eau injectée pourrait avoir réduit la durée de vie du SO_2 de 50% grâce à une conversion rapide en sulfate. Des mois après l'éruption, une couche de vapeur d'eau volcanique a été trouvée au-dessus de la couche d'aérosol volcanique. La couche de vapeur d'eau est montée lentement en raison de la circulation diabatique, tandis que la couche d'aérosol est descendue en raison de la sédimentation gravitationnelle des particules. Cette découverte indique la dynamique complexe de la vapeur d'eau et des aérosols dans la stratosphère après les éruptions volcaniques. Dans ce chapitre, nous avons utilisé la base de données "Global Space-based Stratospheric Aerosol Climatology (GloSSAC)" pour étudier la relation entre le dioxyde de soufre injecté (SO_2) et ses répercussions sur la charge des aérosols stratosphériques sur une période de quatre décennies. La base de données GloSSAC, conçue pour l'analyse des observations d'aérosols stratosphériques, offre un ensemble de données cohérent et continu. Un accent mis sur l'épaisseur optique moyenne zonale globale des aérosols

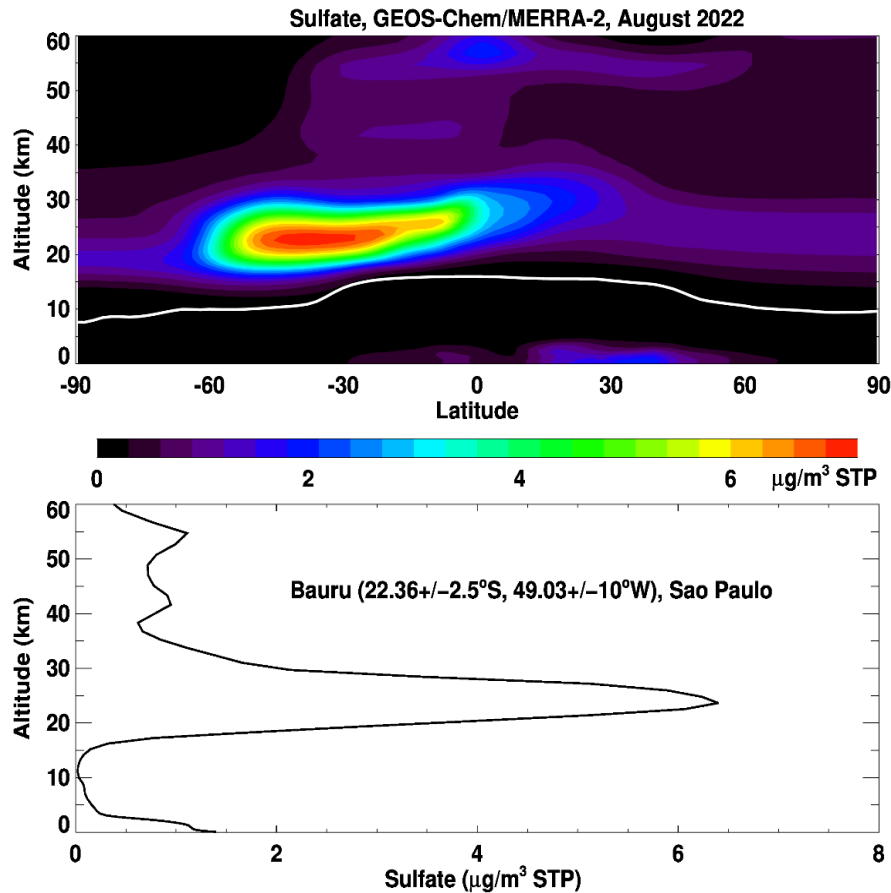


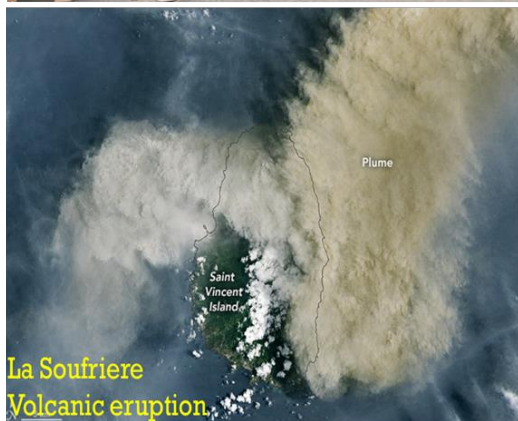
Figure 4.11: (top) Latitudinal cross-section of sulfate concentration in STP in August 2022 derived from GEOS-Chem simulation and (bottom) associated mean sulfate concentration profile within $\pm 2.5^\circ$ latitudes and $\pm 10^\circ$ longitudes from Bauru, Brazil.

stratosphériques (SAOD) entre 60°N et 60°S de 1979 à 2023 a permis d'élucider l'évolution temporelle de ce paramètre. Notamment, la SAOD générée après l'éruption de HTHH est considérablement plus grande (3-4 fois) que celle générée par des éruptions similaires émettant les mêmes quantités de SO_2 . Pour mieux comprendre les disparités observées, la campagne Brazil Volcano (BraVo) a été organisée en mai et août 2022. L'objectif principal était de mesurer les caractéristiques chimiques, optiques et microphysiques du panache de HTHH, en s'efforçant de découvrir les facteurs sous-jacents aux valeurs élevées des profondeurs optiques des aérosols stratosphériques (SAOD) malgré l'injection relativement modeste de SO_2 . Des institutions, dont la NASA, le LPC2E-CNRS en France et plusieurs instituts de recherche brésiliens, ont uni leurs forces pour ce projet Volcan du Brésil (BraVo) mené de mai à août 2022. Cette initiative visait à étudier de manière exhaustive l'éruption Hunga Tonga-Hunga Ha'apai (HTHH). La ville de Bauru au Brésil a été stratégiquement choisie comme site de déploiement d'un ensemble de capteurs, facilitant la collecte de données sur divers aspects des propriétés du panache HTHH. Cette approche globale visait à fournir une caractérisation la nature du panache. La collaboration visait à améliorer les connaissances scientifiques sur les caractéristiques et les impacts de l'éruption de HTHH, faisant ainsi progresser notre compréhension des panaches volcaniques et de leurs interactions avec l'atmosphère et le climat. Dans le cadre du projet BraVo, un examen approfondi des attributs microphysiques du panache HTHH a été effectué. Cette évaluation était principalement centrée sur la distribution granulométrique des aérosols dans le panache, en tirant parti des données recueillies lors des vols en mai, août et novembre. Cette comparaison au fil du temps a révélé des résultats significatifs, tels qu'une séparation notable d'environ 2.5 km entre les pics de concentrations d'aérosols avec des tailles de particules supérieures à $0.4 \mu\text{m}$. Cette divergence de concentration suggérait un taux de descente du panache d'environ 30 mètres par jour. De plus, la présence d'aérosols volcaniques a été initialement détectée jusqu'à une altitude de

30 km, tandis que leur absence dans le profil aérosol d'août a mis en évidence leur dispersion pendant le transport. Pour étudier le panache HTHH dans la stratosphère moyenne, où les mesures des avions conventionnels posent des défis, une approche innovante impliquant des vols en ballon léger a été adoptée. Ces vols transportaient un échantillonneur d'aérosol unique équipé d'une valve radiocommandée. Cette approche a permis la collecte d'échantillons, ce qui a permis de mieux comprendre les caractéristiques et le comportement du panache. Le système de valve a permis une durée d'échantillonnage prolongée de 40 minutes dans la couche du panache. Après le vol, l'échantillonneur d'aérosols a été conservé dans de la glace carbonée et des analyses ultérieures des échantillons d'aérosols ont été effectuées, ce qui a permis d'obtenir des informations précieuses sur leur composition et leurs caractéristiques. Les espèces inorganiques solubles dans l'eau (SMSI) ont été analysées à l'aide d'un chromatographe ionique. Cette analyse a englobé une gamme d'ions, et une procédure méticuleuse a été suivie pour assurer la précision et la pureté. Les données résultantes ont contribué à une meilleure compréhension des attributs chimiques des aérosols. Les résultats indiquent que la présence d'aérosols marins et les propriétés microphysiques complexes du panache pourraient expliquer les écarts entre la profondeur optique élevée des aérosols stratosphériques (SAOD) et le SO₂ injecté relativement faible. En conclusion, ce chapitre met en lumière les caractéristiques des aérosols stratosphériques et la vapeur d'eau, illustrée par l'éruption du HTHH. En utilisant des instruments sophistiqués et des méthodologies innovantes de plafonnement, ces recherches ont permis d'explorer les propriétés microphysiques, chimiques et optiques du panache, contribuant ainsi à une compréhension globale de son comportement et de ses impacts.

Chapter 5

Impacts of wildfires and volcanic eruptions on stratospheric aerosol over the Northern Hemisphere- The REAS project



5.1 Introduction

Medium-to-large volcanic eruptions historically had the greatest impact on stratospheric aerosols. However, in recent years, extreme wildfires have led to stratospheric aerosol enhancement comparable to medium-size volcanic events (Peterson et al., 2018). These new sources of stratospheric particles in the form of carbonaceous aerosols are further lifted into the stratosphere through radiative heating (Khaykin et al., 2021). Smoke from wildfires transported in the polar region could further affect stratospheric ozone and delay its recovery in the future (Solomon et al., 2021).

In 2021, the Northern Hemisphere wildfires and the eruption of La Soufrière volcano (Saint Vincent island) had significant impacts on the stratospheric aerosol layer and several balloon flights were conducted in France the following fall/winter, allowing to better characterize these plumes microphysical and chemical properties.

The stratospheric aerosol layer has been studied for decades through various methods including optical particle counters, lidar observations, and satellite observations. In the past decade, major wildfires, such as the 2017 British Columbia wildfires and the 2019/20 Australian bushfires, have impacted the stratosphere for several months at levels never seen before, resulting in a Stratospheric Aerosol Optical Depth (SAOD) increase comparable to medium volcanic eruptions (Peterson et al., 2018). Volcanic and wildfire plumes have different impacts on chemistry and climate due to their absorbing/reflecting properties. Smoke from wildfires can produce significant heating in the plume, lasting longer and increasing its impact. Stratospheric smoke generates 60% more radiative heating than volcanic sulfate at an aerosol optical depth equivalent (Yu et al., 2023). So, characterizing the stratospheric aerosol layer is essential, but aircraft observations have several limitations due to their associated cost and deployment readiness level, together with altitude restrictions. Thus, rapid balloon deployments of lightweight sensors can provide critical information about plume properties at a manageable cost.

To better understand the impact of volcanic eruptions and extreme wildfires on stratospheric aerosol loadings and properties in the Northern Hemisphere, the Rapid Experiments for Sudden Aerosol Injection in the Stratosphere (REAS) project was launched. The first phase took place between November 2021 and January 2022 and continued under the MAGIC campaign in fall 2022.

17 balloons were launched from Reims, Eastern France, to measure the atmospheric content of trace/greenhouse gases and aerosols from the ground up to stratospheric levels. Instruments such as an Aircore gas collector, Optical Particle Counters (OPC), COBALD backscatter sondes, an aerosol sampler, an aerosol impactor, and ozone sondes were used to make these measurements. The main objective was to investigate the influence of the aged La Soufrière volcanic plume and smoke particles from PyroCb events that occurred in North America during the previous summer/fall. The burden and properties of the observed aerosols were quantified from these in situ observations, in conjunction with satellite data. New instruments were developed to collect aerosol particles using a chemical aerosol sampler and an aerosol impactor. The aerosol impactor was downsized from a similar instrument flown during the BATAL campaign (Chapter 3) under large plastic balloons. This chapter describes the logistics, infrastructure, payloads, and preliminary results of the project.

During my thesis, I was responsible for preparing the two collectors and the subsequent IC analysis performed. The instruments development, deployment and preliminary chemical analysis constituted a central part of my PhD.

Overall, The REAS project offered a unique opportunity to separate natural and anthropogenic sources of stratospheric aerosol and better understand the growing influence of wildfires on the atmosphere under a warming climate. While this effort is challenging, early results obtained during this project constitute a major step to fulfill these objectives.

5.2 Major events before the REAS Campaign

5.2.1 The volcanic eruption of La Soufrière

The La Soufrière volcano on St. Vincent Island in the Caribbean became explosively active from April 9 to April 22, 2021, with 32 explosive sequences and at least 32 injections in the upper troposphere and lower stratosphere (Taylor et al., 2022). The eruption resulted in the emission of 0.57 ± 0.44 Tg of SO_2 and a plume that reached 40° by the end of April (Taylor et al., 2022). The CALIOP level 1 V4.01 product showed multiple volcanic layers produced after the eruption between May 1-16 and between 14

and 21 km. The plume was transported across the upper troposphere and lower stratosphere due to the multiple injections, with the lower part of the plume transported between 380 and 420 K at mid-latitudes from May to August 2021 (Dumelie et al., 2023, in revision). The transport continued until at least 520 K in November, possibly due to the worsening of Rossby waves in winter.

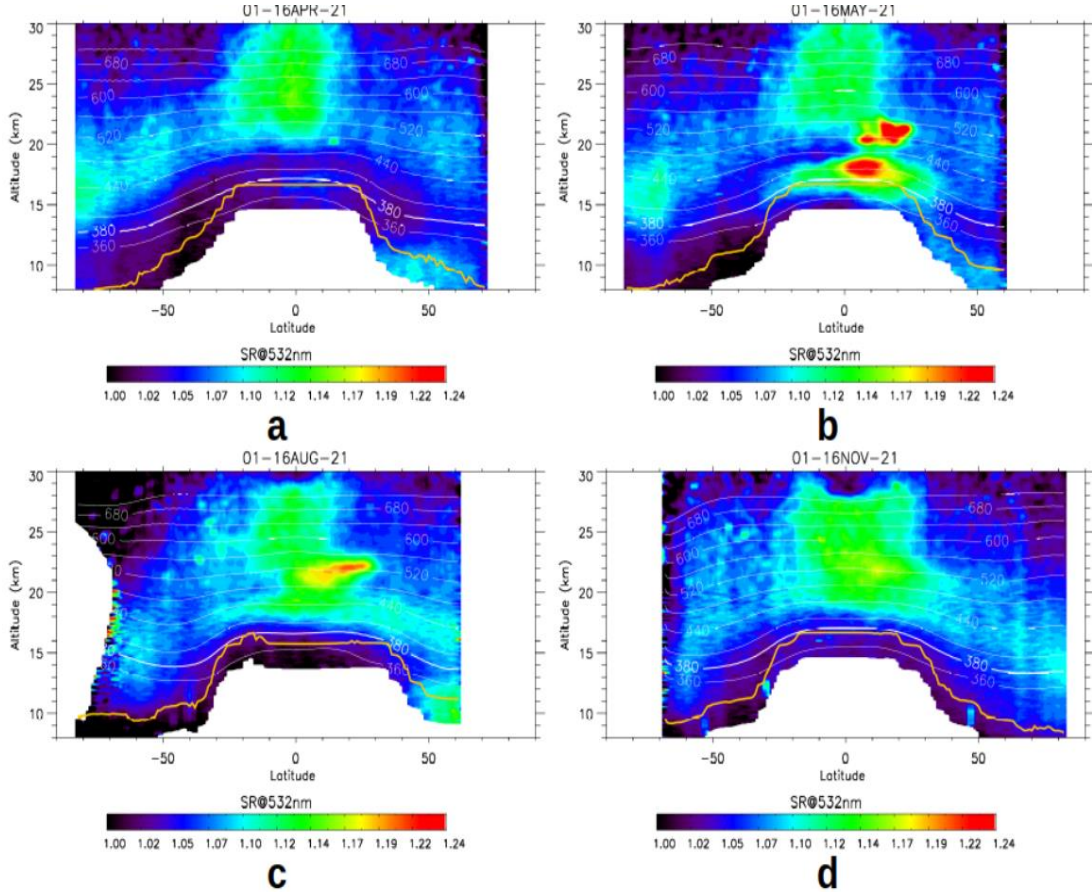


Figure 5.1: Zonal mean cross-section of Scattering Ratio (SR) from CALIOP level 1 V4.01 between 01-16 April 2021 (a), 01-16 May 2021 (b), 01-16 October 2021(c) and 01-16 November 2021 (d). White lines are zonal mean isentropic surfaces, and the tropopause altitude is shown in orange. Data 3 km below the tropopause are discarded for possible contamination by cirrus cloud). Depolarization values $> 5\%$ are used to remove clouds (Vernier et al., 2009). Adapted from Dumelie et al.(2023).

5.2.2 The 2021 Northern Hemisphere wildfires

Several forest fires raged across North America, but the majority of the smoke that reached the eastern U.S. likely originated from a group of fires near the border of the Canadian provinces of Manitoba and Ontario, just north of Minnesota (Dumelie et al., 2023). Fires that were burning farther to the west in British Columbia and the Pacific Northwest of the United States may have contributed a small amount of smoke as well (Dumelie et al., 2023). Severe drought and warm weather have sustained several major fires in northern California throughout August, triggering air quality alerts in Sacramento and San Francisco. The heat and smoke generated by wildfires result in the formation of pyrocumulonimbus clouds or PyroCbs (Dumelie et al., 2023). They are similar to thunderstorm clouds but are fueled by the heat and moisture released from burning vegetation or volcanic ash. These clouds can grow to great heights, even reaching the stratosphere, and can produce lightning, strong winds, and fire tornadoes. The smoke and ash from pyroCbs can also travel long distances, affecting air quality and climate. In September 2021, the KNP Complex fire burned in California’s Sequoia National Park, generating a massive PyroCbs cloud that rose over 15 kilometers high and released smoke and ash into the stratosphere. These pollutants were then

carried by winds and transported to Europe, as shown by satellite images that revealed the smoke plume reaching as far as the United Kingdom and Scandinavia. Figure 5.2a shows an RGB composite image taken by Sentinel 3A OLCI on October 4th, depicting one of the PyroCb produced by the KNP Complex fire. On October 10th, data from Calipso showed a plume at about 13km high, indicating the transport of smoke from the fire (Fig. 5.2b). Back-trajectories from HYSPLIT also suggest that the smoke could have been transported from the KNP Complex fire to Europe (Fig. 5.2c). The merging of two fires in the same national park resulted in the KNP Complex fire, which also produced a series of PyroCb on October 4th. There is evidence that these clouds may have affected both aerosol and greenhouse gas emissions in Europe, as demonstrated in Figure 5.2.

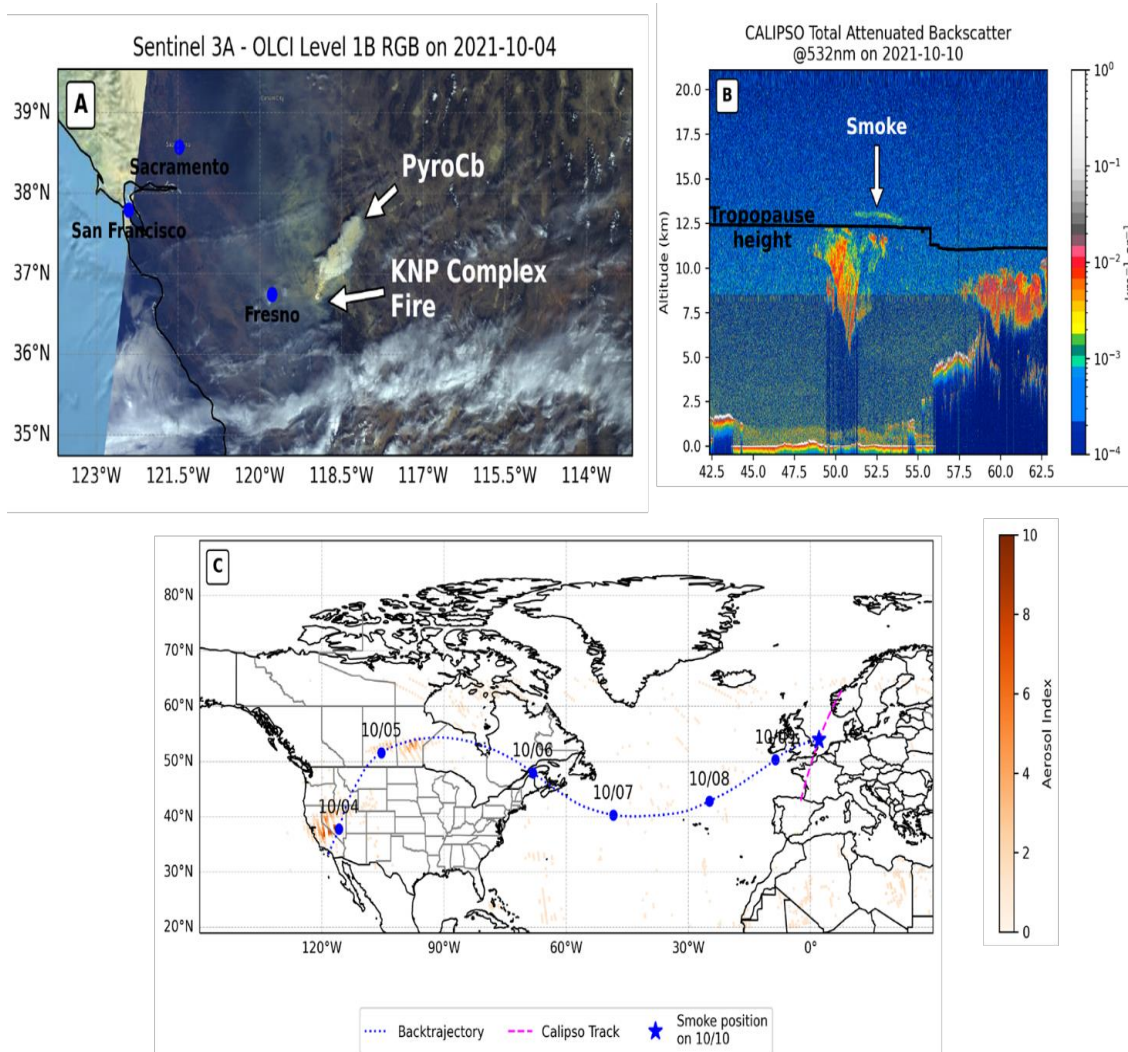


Figure 5.2: displays three different pieces of information. (4a) is a composite image in red, green, and blue (RGB) showing a pyrocumulonimbus cloud on October 4th. (4b) is a graph showing the total attenuated backscatter at 532nm measured by CALIPSO, which indicates the presence of a plume in Europe. Lastly, (4c) is a HYSPLIT back-trajectory associated with the OMPS Aerosol index that was measured on October 4th. Dumelie et al., 2023.

The next section will describe the instruments used during the REAS project focusing on the chemistry part of the experiment. Collecting aerosols in the atmosphere is a very important endeavor since most of the state-of-the-art analysis that can be carried in laboratory cannot be flown on airborne platforms. During the campaign, two different instruments were used for aerosol collection. An impactor that was adapted for medium balloon flight and a lightweight aerosol sampler that could be deployed under lightweight balloons (< 4 kg). Both systems provide a different way for stratospheric aerosol collection.

The impactor uses particle gravity with orifices that allow particles to settle down on a filter while the chemical sampler is a filtering system where air passes through a filter which collect particles in the air. The next chapter will further describe those collection techniques and the associated offline analysis that were employed to derive the inorganic and organic composition of collected matter.

5.3 REAS project

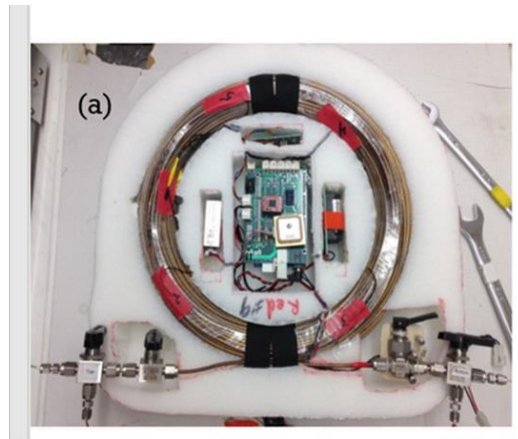
5.3.1 Balloon flights

Unmanned free balloon flights in Europe follow the “Standardized European Rules of the Air” (SERA) Annex 2, which outlines regulations for three different types of balloons. Scientific flights usually fall under the light balloon category, which simplifies the rules and allows for one or more packages to be carried, weighing less than 4 kg combined. Medium balloons, which can carry a combined weight of up to 6 kg, are subject to more constraints, as they are considered potentially hazardous to airline traffic. A flight protocol was developed to launch medium balloons, that included a 24-hour notice before launch, detailed trajectory predictions, and a NOTAM (notice to the airmen) issued by air traffic authorities during the campaign. The first REAS campaign had three main objectives. Firstly, we use several balloon-borne instruments to study the properties of stratospheric aerosols. Secondly, to test new instruments, such as the impactor, that are not typically flown in Europe due to their weight. Lastly, to compare different instruments through in-flight comparisons, made possible by the medium flight capabilities.

The REAS campaign involved the collaborative efforts of NIA/NASA-LARC, LPC2E, and GSMA to study the optical, physical, and chemical properties of the aerosols. A total of 17 balloon flights were launched, out of which four among them were medium balloons carrying multiple instruments. Table 5.1 shows the list of balloon flights with details of time, balloon type, altitude information, and payloads used.

Date UTC	Time UTC	Flight Number	Flight class	Max. altitude	Payloads	Payload weight	Balloon type
2021/11/18	10h09	REAS01	Light	8.2 km	POPS,LOAC,M10	2.5 kg	1200 g
2021/11/24	10h07	REAS02	Light	29 km	Aircore, M20	3.1 kg	1600 g
2021/11/24	19h00	REAS03	Light	27.5 km	POPC,COBALD,iMet	2.6 kg	1200 g
2021/11/25	09h50	REAS04	Light	8.7 km	POPS, LOAC, M10	2.5 kg	1200 g
2021/12/02	19h00	REAS05	Light	29 km	POPC, COBALD, iMet	2.6 kg	1200 g
2021/12/08	13h20	REAS06	Light	16 km	POPC, iMet	2.5 kg	1200 g
2021/12/08	13h25	REAS07	Medium	16.1 km	IMPACOR, iMet	5.6 kg	1600 g
2021/12/16	9h24	REAS08	Medium	27.5 km	LOAC, POPS, Aircore,M10	5.3 kg	1600 g
2021/12/16	9h30	REAS09	Medium	27.1 km	IMPACTOR, iMet	5.6 kg	1600 g
2021/12/16	9h27	REAS10	Light	27 km	SAMPLER, POPC, IMET	3.8 kg	1600 g
2021/12/22	9h28	REAS11	Light	17.5 km	POPC, M20	2.2 kg	1600 g
2022/01/06	9h38	REAS12	Light	23.4 km	POPC, POPCN, O ₃ , IMET, M10	3.1 kg	1200 g
2022/01/06	9h41	REAS13	Light	25 km	SAMPLER, iMet	2.8 kg	1200 g
2022/01/17	19h00	REAS14	Light	26.3 km	POPC, POPCN,, COBALD, iMet	2.8 kg	1200 g
2022/01/18	9h11	REAS15	Light	25.5 km	POPS,LOAC,M10	3.9 kg	1600 g
2022/01/18	9h08	REAS16	Medium	25.6 km	Aircore, Ozone ECC, M10	5.2 kg	1600 g
2022/01/18	14h00	REAS17	Light	20 km	SAMPLER, iMet	2.8 kg	1200 g

Table 5.1: List of balloon flights launched throughout the REAS campaign showing associated details on flight altitude, duration, and payloads used (Dumelie et al., 2023).



The AirCore principle in 5 easy steps

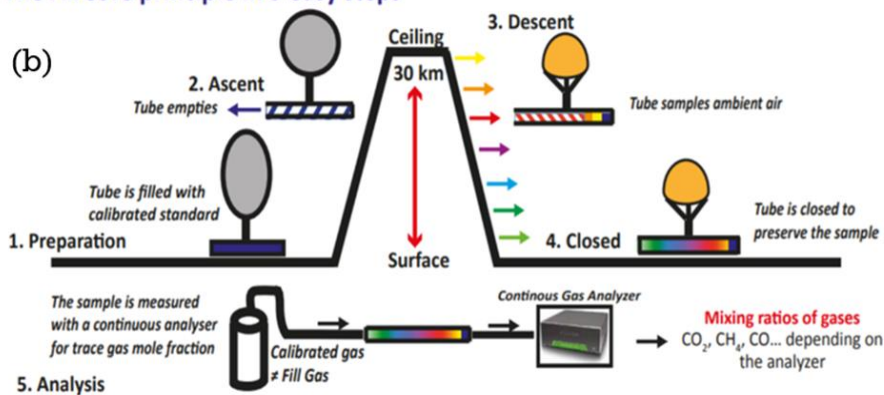


Figure 5.3: (a) Model display of Aircore. (b) Schematic showing the working principle of Aircore. Aircore is a gas collector system that rely on a balloon flight to store air gases into a long coil which is further empty on the ground and pass through a gas analyzer to derive gases concentration such as CO, CO₂ and CH₄.

5.3.2 Instruments used during REAS

Aircore

Aircore is an air sampling technique that was originally developed by NOAA (Karion et al. 2010). The method involves using long-coiled tubing with one open end and one closed end, which is filled with a gas of known concentration before launch. As the balloon ascends, the gas is emptied from the Aircore due to the balancing of internal tubing pressure with external atmospheric pressure, until the balloon reaches its maximum altitude. During descent, the Aircore collects an air sample as it is filled with the surrounding air. The open end is automatically closed upon landing to preserve the air sample, which is then analyzed using a gas analyzer (Picarro G024). By utilizing the temperature and pressure data obtained from a meteorological radiosonde that is flown under the balloon, a vertical profile can be retrieved.

Particle plus Optical Particle Counter (POPC)

The POPC has been described in Chapter 4.

Lightweight aerosol sampler

The lightweight aerosol sampler is described in the previous chapter [4]. It was developed under the REAS project through a partnership with NIA-NASA. The samples that were collected for the IC analysis followed the same collection, storage, and analysis protocol as described in chapters, 3 and 4. Additional

information about the organic chemistry analysis with orbitrap mass spectroscopy technique is provided herein after.

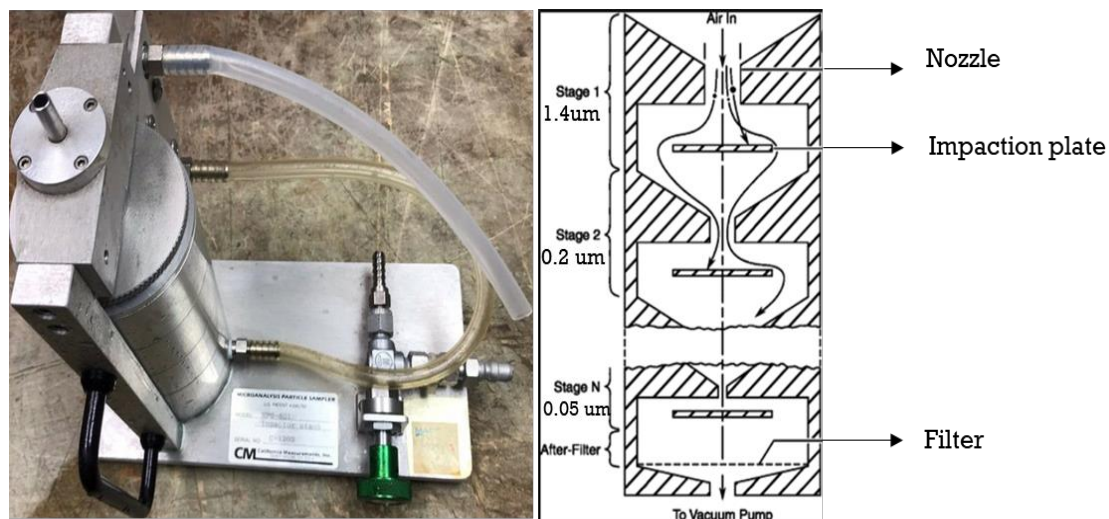


Figure 5.4: (Left) image of the 3-stage particle sampler. (Right) Schematic of their flow within the MPS-3 Particle sampler.

MPS-3 Microanalysis Particle Sampler

The MPS-3 Microanalysis Particle Sampler (Fig. 5.4), a 3-stage impactor, was used to collect aerosol samples. It was connected to a small air pump that delivered a flow rate of 2 L min^{-1} . The sampling device used inertial impaction to collect particles, with each stage of the impactor being associated with a specific particle size diameter cut-point: $1.4 \mu\text{m}$ for Stage-1 (S-1), $0.2 \mu\text{m}$ for Stage-2 (S-2), and down to $0.05 \mu\text{m}$ for Stage-3 (S-3).

5.4 Offline chemical analysis during REAS

5.4.1 Ion Chromatography

A portable clean room was used for preparing the 3-stage impactor, and the lightweight aerosol sampler for aerosol collection. PTFE (Polytetra Fluoro ethylene) filters were used in this experiment. After each impactor/sampler flight, the instruments (impactor/sampler) were transported to the GSMA site in dry ice where the filters were transferred into sterile petri-dishes, sealed, covered to protect from light, and stored in dry ice. After the end of the campaign, the PTFE filters bearing the aerosol samples were shipped to the Physical Research Laboratory (PRL), in India where they were analyzed using the same protocol described in chapter 3.

5.4.2 Orbitrap Q-Exactive, high-resolution mass spectrometry

The Orbitrap analysis was used in conjunction with the aerosol sampler. For aerosol and gas collections during the flight, a set of two Activated Carbon Cloth (ACC) filters of 1.3 cm diameter were cut out and placed in each filter cartridge. ACC made from a viscose precursor was used as an adsorbent to collect volatile organic compounds (VOCs) and organic aerosols (OAs) present in the atmosphere. These materials have a highly developed specific surface area and are recognized for their effectiveness in air pollution control applications (Pui et al., 2019; Wang et al., 2022; Delpeux-Ouldriane et al., 2015). The fabrics used are composed of carbon fibers with hydrophilic properties and a range of porosity covering several orders of magnitude. The fibers have a high oxygen content, are arranged in acidic functionalities, and have a specific surface area of over $1100 \text{ m}^2 \text{ g}^{-1}$ with a total pore volume of $0.75 \text{ cm}^3 \text{ g}^{-1}$. The pore size distribution shows mainly two ranges of pore sizes, around 1.2 and 3.8 nm, able to trap small

gaseous molecules or oligomers and aerosols, respectively. The detailed procedure and filter information is described by Benoit et al., (2023). The filters were labeled and placed in individual aluminum foils after the flight. To prevent chemical transformation, the samples were stored in a desiccator that was repeatedly flushed with nitrogen to eliminate any traces of humidity and oxygen. The samples were stored at room temperature until analysis.

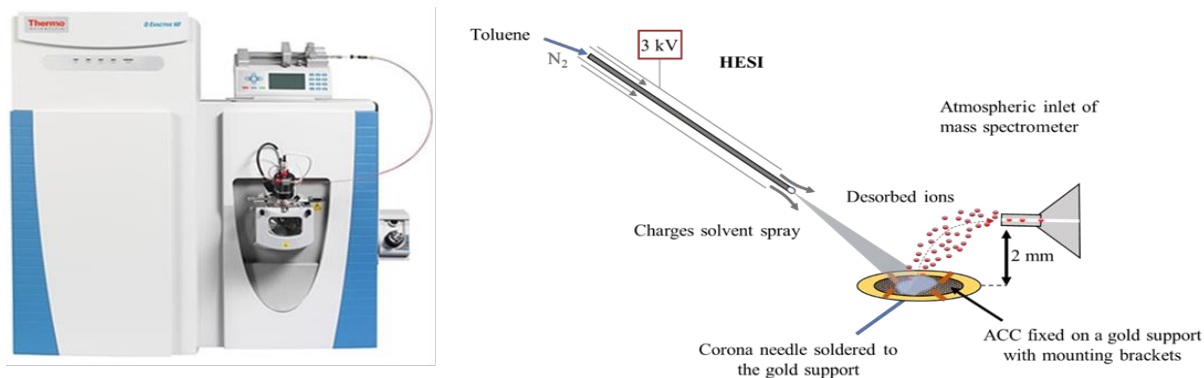


Figure 5.5: (Left) photo of the orbitrap instrument and (right) schematic of desorption technique used for extracting organic matters from the filters.

The Orbitrap Q-Exactive is a type of high-resolution mass spectrometer that uses a combination of quadrupole and Orbitrap technology for accurate mass measurement and high sensitivity. The instrument operates by ionizing analytes in the sample, separating them based on their mass-to-charge ratio (m/Z), and detecting the resulting ions using a mass analyzer. The Orbitrap Q-Exactive employs a quadrupole mass filter to select ions of a specific (m/Z) ratio, which are then accumulated in the Orbitrap for high-resolution analysis. The Orbitrap analyzer works by trapping ions in a high-frequency oscillating electric field, which causes them to spiral around a central electrode. The frequency of this oscillation is then measured to determine the mass-to-charge ratio of the ion.

5.5 Microphysical properties of volcanic aerosol and smoke during REAS

The long-range transport of the La Soufriere Hills volcanic plume mainly affected the balloon measurements during the REAS campaign as revealed by the aerosol extinction profiles from the NASA/NOAA OMPS-Limb Profiler (LP) instrument over Europe.

However, the stratospheric aerosol layer has been perturbed by different plumes both volcanic (e.g. Raikoke, in 2019) and fires (e.g. North America, and Siberia). SAGE III's increased vertical resolution revealed a double peak structure in July 2021 which persisted until January 2022, located at approximately 12.5 and 17.5 km (Fig.5.6).

This pattern indicates possible variations in injection processes or air mass origins in the lower stratosphere, potentially resulting from the long-distance movement of smoke produced by fires. These findings align with the in-situ balloon-borne observations conducted during the REAS campaign. The particle size concentration profiles obtained by POPC and POPS optical particle counters for sizes greater than 0.15 μm are shown in Figure 5.7.

Both instruments show similar concentration values and vertical shapes revealing the Boundary layer below 1.5 km. In addition, a minimum aerosol concentration level is seen in the free troposphere, followed by an increase in the stratosphere, peaking between 12.5 and 20 km, and gradually decreasing in the mid-stratosphere. A peak in aerosol concentration near 14 km and a minimum near 12 km was observed on 17th January 2022. The optical particle counters were launched in collocation with the COBALD (Compact Optical Back-scatter Aerosol Detector) at night. The increased influence of wildfires on the stratosphere in recent years highlights a significant shift in our understanding of the effects of climate change on the stratosphere, according to Fromm et al. (2022). The three-scattering ratio (SR) profiles observed by COBALD in collocation with POPC are seen to be consistent with each other thereby

portraying similar profile shapes as well as fine structures. The peak in SR at 14 km together with a minimum at 12 km are identical. Both POPC and COBALD show a decrease in aerosol concentration/SR from 24th November 2021 to 2nd December 2021, and again on 17th January 2022 as seen in the figure.

5.6 Chemical composition during REAS

Out of the 17 balloon flights throughout the REAS involving scientific payloads to study aerosol microphysics, there were 5 flights that were launched for aerosol collection using the balloon-borne impactor and the aerosol sampler. The table below shows the flow rate, sampling time, and altitude level of the two impactor flights on a medium balloon and three sampler flights on a light balloon.

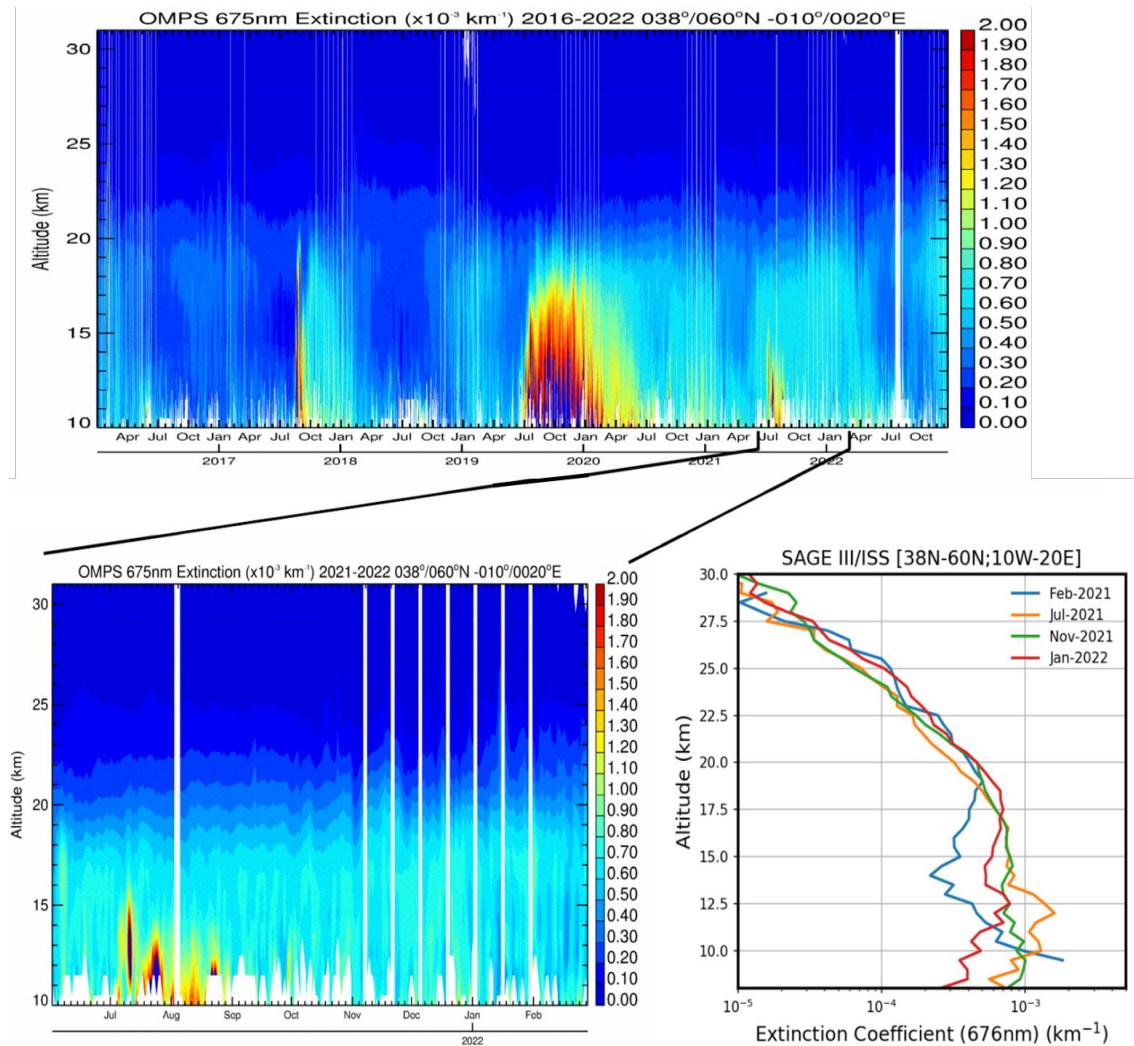


Figure 5.6: OMPS time series of daily mean aerosol extinction at 675nm between January 2020 and November 2022 above the 38°N – 60°N/10°W – 20°E area corresponding to the major part of Europe (Top). Zoom of OMPS extinction time series from June 2021 to February 2022 (Bottom left) for the same area. Vertical profiles of aerosol extinction from the SAGEIII/ISS instrument (Bottom right).

Samples were collected at the ground on 2nd Dec. using the impactor. The filters were loaded in a sterile environment and the impactor was run for 32 minutes with a maximum flow rate of 2 L min^{-1} thereby achieving a total flow of 64 L.

The results of the POPC measurements were compared with that of the backscatter measurements of scattering ratio at 940 and 470 nm with COBALD. There was only one successful flight with the impactor launched on 8th December. The impactor could not be flown during the rest of the campaign

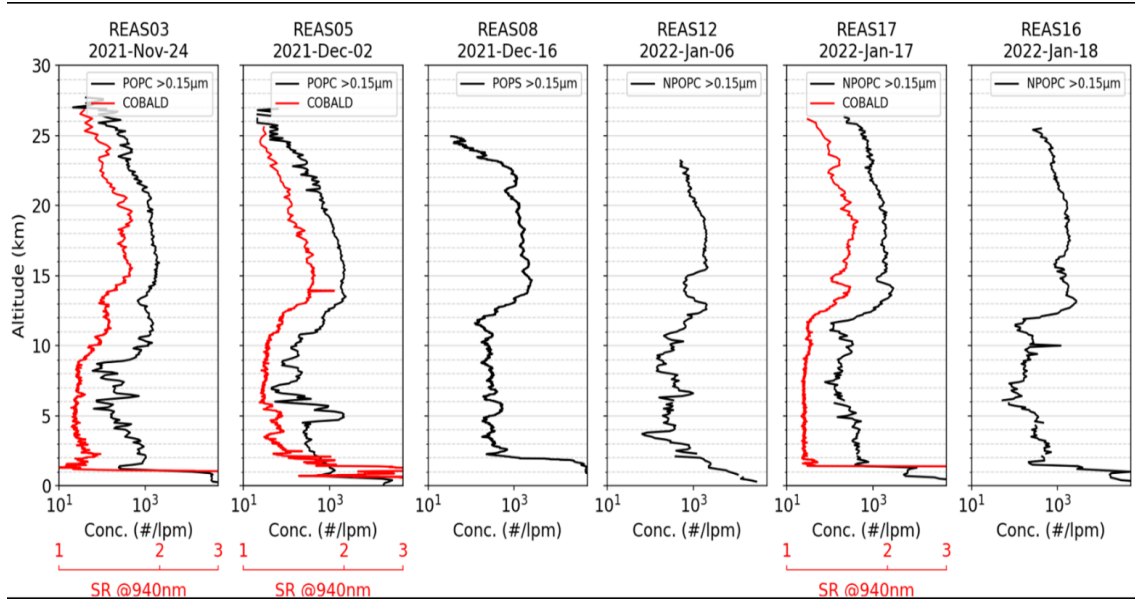


Figure 5.7: Aerosol concentration profiles for sizes greater than $0.15 \mu\text{m}$ obtained with the Particle Plus Optical Particle Counter (POPC) and the Printed Optical Particle Spectrometer (POPS) during 6 balloon flights of the REAS campaign between November 2021 and January 2022 and corresponding Scattering Ratio at 940 nm for 3 flights of the COBALD instrument coincident with POPC on 11/24/2021, 12/02/2021 and 01/17/2022. (Dumelie et al., 2023).

Flight Number	Instrument	Mean Flow	Time running	Volume sampled	Altitude	Comments
R6-2021-12-08 13h20	Impactor 3	2 lpm	29 min	$\sim 58 \text{ L}$	9 – 16 km	Good flight
R9-2021-12-16 9h30	Impactor 3	2 lpm	$\sim 1\text{h}30\text{min}$	$> 100 \text{ L}$	0 – 25 km	Pump still on during descent
R8-2021-12-16 9h27	Sampler	2-3 lpm	Pos 2 (5 min) Pos 3 (22 min)	Pos 2 (13 L) Pos 3 (122 L)	Pos 2(0.5 – 1.8 km) Pos 3(1.8 – 9.5 km)	Only Pos 2/3
R12-2021-01-06 9h40	Sampler	2-3 lpm	Pos 2 (4 min) Pos 3 ($> 1\text{h}$) Pos 4 (20 min) Pos 5 (30 min)	Pos 2 (9 L) Pos 3 (96 L) Pos 4 (60 L) Pos. 5 (50 L)	Pos 2 (0.5 – 1.8 km) Pos 3 (1.8 – 9.5 km) Pos 4 (9.5 – 16.1 km) Pos 5 (16.1 – 27 km)	Remained on Pos 3 (include ground aerosols during descent. Pos 4&5 Strato)
R14-2022-01-18 9h40	Sampler	2-3 lpm	Pos 2 (5 min) Pos 3 (20min) Pos 4 (20 min) Pos 5 (30 min)	Pos 2 (15 L) Pos 3 (101 L) Pos 4 (42 L) Pos 5 (52 L)	Pos 2 (0.5 – 1.8 km) Pos 3 (1.8 – 9.5 km) Pos 4 (9.5 – 16.1 km) Pos 5 (16.1 – 27 km)	Good flight

Table 5.2: Showing the aerosol sampling altitude and time using the balloon-borne impactor and the lightweight aerosol sampler

due to restriction by air traffic control for medium duration flights. The IC results of the aerosol samples collected on the ground and flight using the aerosol impactor are shown in Figure 5.8 below.

IC results of samples collected on the ground revealed the presence of anions, Cl^- , NO_2^- , NO_3^{2-} , and dimethylamine. Cl^- and NO_2^- , were seen in the second stage of the impactor, whereas NO_3^{2-} , and dimethylamine were seen in the second and third stages. Among the cations Na^+ , NH_4^+ , K^+ , Mg^{2+} , and Ca^{2+} are seen. The presence of Ca^{2+} only on stage 2 of the impactor indicates that it could have existed as CaCl_2 and CaNO_2 . Calcium chloride and calcium nitrite can be found in the atmosphere from various natural and anthropogenic sources. Calcium chloride is commonly used as a de-icing agent on roads and can be produced through industrial processes such as the Solvay process for the production of sodium carbonate. It can also be found naturally in marine aerosols (Kawamura and Sakaguchi, 1999). Calcium nitrite can be formed from the reaction of nitric oxide (NO) with calcium hydroxide (Ca(OH)_2) or from the reaction of calcium carbonate (CaCO_3) with nitric acid (HNO_3) (Wang et al., 2016). Calcium nitrite can also be used as a corrosion inhibitor in concrete structures (Andrade et al., 2012).

The results of the IC analysis of aerosol samples collected on 8th Dec. between 9-16 km show the presence of nitrate, and nitrite, only in stages 2, and 3 with Na^+ in stages 1, and 2 implying that sodium could have existed as sodium nitrite and sodium nitrate. Other cations namely NH_4^+ , K^+ , Mg^{2+} , and Ca^{2+} are seen in all three stages of the impactor. Volcanic eruptions are known to release large amounts of sulfur dioxide (SO_2) into the atmosphere, which can in turn react with other atmospheric species to form ammonium nitrate (NH_4NO_3) and ammonium nitrite (NH_4NO_2). Additionally, the reaction of nitrogen oxides with water vapor and oxygen can produce nitric acid (HNO_3), which can react with ammonia (NH_3) to form ammonium nitrate. Similarly, the reaction of nitrogen oxides with hydroxyl radicals (OH) can produce nitric acid, which can also react with ammonia to form ammonium nitrate. These reactions can occur in the volcanic plume or in the surrounding atmosphere, depending on the conditions. Moreover, studies have shown that the concentrations of ammonium nitrate and ammonium nitrite in volcanic plumes can vary depending on the type of volcano, the eruption style, and the composition of the magma (e.g., Rose et al., 2018; Giuffrida et al., 2019). Sulfate (SO_4^{2-}) is a common component of fine particulate matter in the atmosphere, formed by the oxidation of sulfur dioxide (SO_2). However, sulfate is not commonly seen at ground level in its aerosol form due to several factors. Firstly, sulfate aerosols are typically less than 2.5 μm in diameter (PM_{2.5}), which makes them small enough to remain suspended in the air for long periods of time and transported over long distances by winds before settling out of the atmosphere. This is supported by a study by Monks et al. (2015) which found that fine particles, including sulfate, can remain aloft for several days or even weeks, particularly in urban areas with high levels of air pollution.

Secondly, sulfate aerosols are often formed in the upper atmosphere, such as in the stratosphere, where sulfur dioxide reacts with other chemicals in the presence of sunlight to form sulfate aerosols. These aerosols can then be transported downward into the lower atmosphere, but they tend to remain aloft due to their small size and can be transported over long distances by winds before settling out of the atmosphere. This is supported by a study by Zhang et al. (2017) which found that sulfate aerosols in the lower atmosphere were predominantly formed through secondary reactions of sulfur dioxide with other chemicals, rather than being directly emitted into the atmosphere.

Finally, sulfate aerosols can be removed from the atmosphere through precipitation, such as rain, snow, and hail. When these particles come in contact with water vapor, they can dissolve and become part of the precipitation. This is why sulfate is often found in rainwater and snow, but not commonly seen at ground level in its aerosol form. This is supported by a study by Liu et al. (2019) which found that sulfate aerosols were efficiently removed from the atmosphere through wet deposition processes, such as rain.

In summary, sulfate aerosols are not commonly seen at ground level in their aerosol form due to their small size, formation in the upper atmosphere, and efficient removal through precipitation processes.

The formation of ammonium nitrate and ammonium nitrite from volcanic plumes can contribute to the total mass of particulate matter in the atmosphere and can have negative impacts on human health and the environment. These compounds can cause respiratory problems and can also contribute to the acidity of rain and snow, leading to eutrophication and harm to aquatic life. Understanding the formation and behavior of these compounds in volcanic plumes can help improve our understanding of the impacts of volcanic eruptions on the environment. In addition to forming salts in reaction with ammonium, nitrate salts can also form with other cations such as potassium (K^+), magnesium (Mg^{2+}), sodium (Na^+), and calcium (Ca^{2+}). These cations can react with nitric acid (HNO_3) to form potassium nitrate (KNO_3), magnesium nitrate ($\text{Mg(NO}_3)_2$), sodium nitrate (NaNO_3), and calcium nitrate ($\text{Ca(NO}_3)_2$), respectively.

The concentrations of nitrate salts with different cations can vary depending on the location, sea-

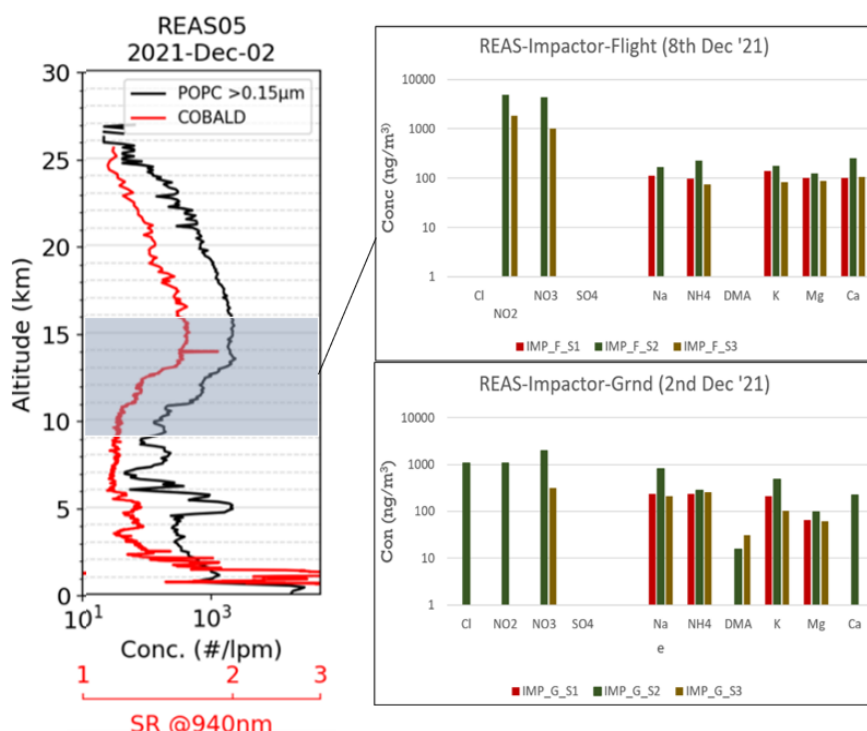


Figure 5.8: (Left panel) Particle size concentration measurements from POPC. (Middle) COBALD backscattering ratio at 940 and 470 nm. (Right) results of the IC analysis using the aerosol impactor: in stage 1 ($r > 1.4 \mu\text{m}$) and stage 2 ($0.2 \mu\text{m} < r < 0.05 \mu\text{m}$). The major difference observed between the two samples is in stage 3 ($r \leq 0.05 \mu\text{m}$)

son, and sources of emissions. For example, in urban areas with high traffic emissions, sodium, and calcium nitrates are often more abundant, while in rural areas with agricultural activities, potassium and ammonium nitrates can be more prevalent (Chang et al., 2016; Sun et al., 2020).

5.7 Combined IC and Orbitrap analysis during the Jan 18th flight

5.7.1 Flight description

On January 18, 2022, three balloon flights were conducted from Reims, France, as part of the REAS campaign. (Fig. 5.9) shows the results of measurements taken during three balloon flights launched from Reims. The left panel displays particle concentrations for nine different size radii between $0.15 \mu\text{m}$ and $0.4 \mu\text{m}$, as measured by the Particle plus Optical Counter (POPC) during the first flight at 9:08 am. The middle panel shows corresponding temperature, ozone, and CO profiles, which were measured by an M20 radiosonde, an Electrochemical Concentration Cell (ECC), and Aircore on a second flight, which took place a few minutes after the first. The right panel displays the flow rate on different filter positions (P1 to P5) that were used to sample aerosols with the aerosol sampler, during a third flight launched at 2:03 pm. = The collected data revealed meteorological and chemical information about the sampled layers, including a positive gradient in aerosol concentration and an increase in ozone concentration at the cold point tropopause (13 km). The lowermost stratosphere (12-16 km) was found to be an active zone of exchanges between the tropics and mid-latitudes, while the lower stratosphere above 16 km was generally influenced by the horizontal and downward motions of the Brewer-Dobson circulation. The sampler flight aimed to collect samples from distinct atmospheric layers with different origins. Higher ozone values indicated a tropical origin associated with volcanic aerosols, while the second peak at lower levels may be associated with smoke from biomass burning. The boundary between the planetary boundary layer and the free troposphere was differentiated at 2 km above sea level. In order to investigate the organic and

inorganic composition of the collected aerosol samples, two different experiments were conducted. One involved the ORBITRAP mass spectra to study the carbonaceous composition, and the other determined the inorganic composition using Ion Chromatography (IC).

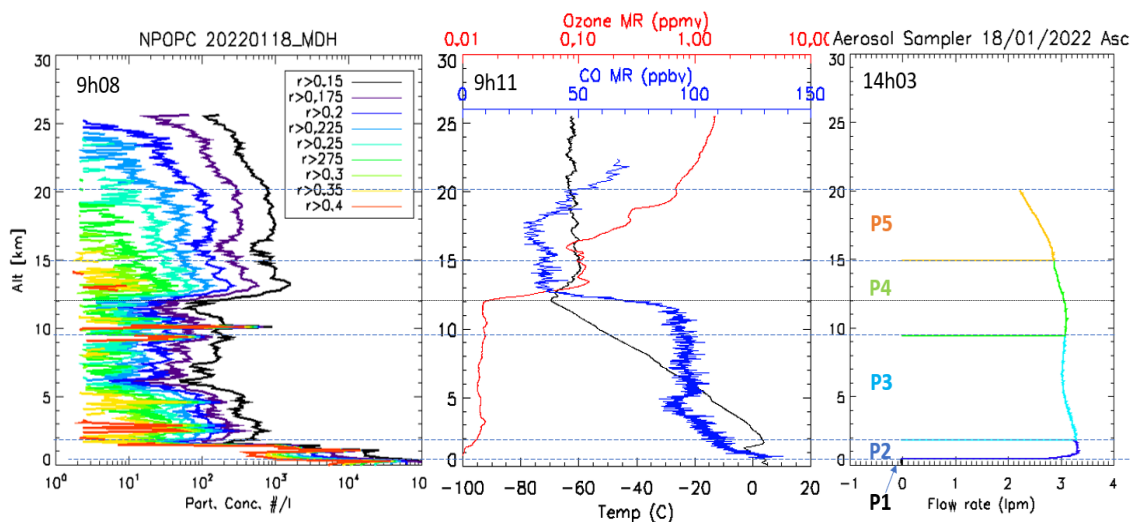


Figure 5.9: (Left panel) Particle size concentration measurements from POPC. (Middle) temperature, ozone, and CO profiles from M20 radiosonde and Electrochemical concentration cell (ECC) and Aircore. (Right) flow rate at different positions of the aerosol sampler corresponding to sampling altitudes

5.7.2 Results of the ORBITRAP analysis

The samples collected for ORBITRAP analysis were transported in the desiccator to the laboratory in ICARE (Institut de Combustion Aérothermique Réactivité Environnement), in Orleans. They were subsequently analyzed by our collaborator, Dr. Roland Benoit. The analysis was conducted using a flow injection analysis system with specific settings for HESI ionization. The Orbitrap® Q-Exactive from Thermo Scientific was used for mass spectrometry, with a mass resolution of 140,000 and mass accuracy < 0.5 ppm RMS. The ionization was performed in both positive and negative ionization modes, and the samples were analyzed three times at three different m/Z ranges to correct for the decrease in trapping efficiency at higher masses. More information about these technical aspects is available in a recent review by Hecht et al. (2019). The data was processed on all filters and provided six sets of chemical formulas as mentioned in detail in Benoit et al., (2023). A search for molecules containing carbon, hydrogen, oxygen, nitrogen, and sulfur atoms was made. Molecular formulas of these molecules were determined with a maximum mass deviation of 3 ppm and an intensity greater than 10^3 . Molecular formulas that were detected only once out of three analyses and had an intensity lower than 5.0×10^3 were not considered. The study centered on volatile organic compounds (VOCs) and oxygenated aerosols (Oas) that are primarily composed of carbon, hydrogen, and oxygen. These types of VOCs and Oas make up the majority of those found in the atmosphere and include hydrocarbons, Oas, oxygenated VOCs, and polycyclic aromatic hydrocarbons (PAHs), Sindelarova et al. (2014). A total of 6589 chemical formulas were identified for the filters which were processed using a Venn diagram.

The six sets of chemical formulas identified on filters 2-5 were correlated to the physical parameters of the flight (atmospheric pressure and gas flow). It was seen that the exposed air volume did not affect the number of chemical formulas detected but a decrease in pressure and temperature had a positive impact on adsorption.

A lower pressure helped remove contamination layers, while a lower temperature, combined with gas flow, increased adsorption. During the balloon's descent, the increase in these two parameters, along with porosity, helped stabilize the adsorbed layers (Benoit et al., 2023). According to Figure 5.10, there are 15 sets (0001-1111) that may indicate similarities in atmospheric conditions across the various sampling areas. Four groups of data were defined according to the following criteria. The data obtained from the four filters were divided into four groups. The first group contained data from the (1111) set that

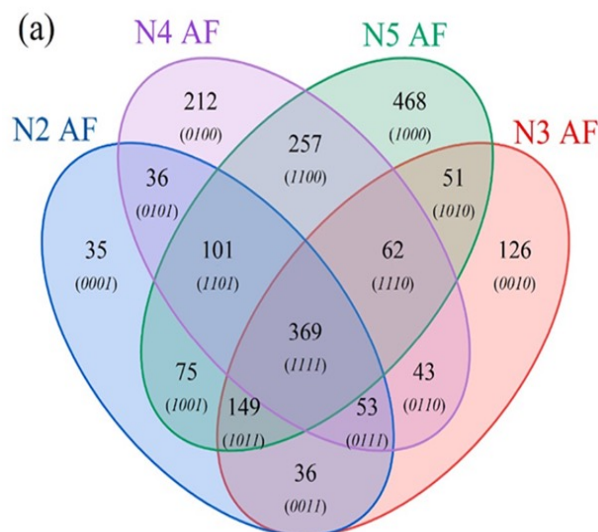


Figure 5.10: Venn diagram showing common chemical formulas detected in samples 2–5 AF

was common to all four filters, comprising 30% of the total population of chemical formulas identified. The second group consisted of sets common to two or three neighboring sampling areas, while the third group consisted of four sets specific to individual sampling zones. The final group contained sets where at least one sampling zone was distant and accounted for only 20% of all chemical formulas. Dr. Benoit did not study the distant groups that shared chemical formulas, which may have resulted from exchanges between different layers, but the absence of information prevented him from confirming this hypothesis. The aim was to determine the origin of a certain group of chemical formulas to determine if they were detected during the flight. The group could have resulted from contamination, residual adsorption, or chemical adsorption during the flight.

To test the above objectives, a comparison was made of the data from reference filters (N1 and Virgin). The N1 filter was subjected to the same conditions as the other four filters, except it was not exposed to a gas flow. Instead, it experienced pressure variations due to theft. As a result, N1 had the highest exposure time without gas flow, which likely reduced adsorption. Meanwhile, the Virgin filter was not flown and did not experience gas flow or pressure variation.

The percentage of chemical formulas common to all four filters was only 10% for the Virgin filter, and the set with complete similarity (1111) was reduced to 1%. Therefore, the number of chemical formulas detected had no quantitative value for the Virgin reference filter. Set 1111 has been identified as a common set of chemical formulas present in the atmosphere.

The study found a unique fingerprint for each sampling zone, characterized by the dispersion of chemical formulas, oxidation level, and amount of unsaturation. These results were most significant for filters 3, 4, and 5, but the low number of specific chemical formulas and dispersion of formulas in filter 2 limited interpretation. Filter 2 was also less exposed to airflow between 0.5 and 1.8 km. Filter 3 had a higher oxidation level with a distribution centered on $O/C = 0.5$, while filters 4 and 5 showed a distribution centered on $O/C = 0.25$. On filter 4, all chemical formulas with a distribution centered on $O/C = 0.25$ and an average double bond equivalent (DBE) of 12 showed unsaturation not linked to the formation of ketones or aldehydes. Similar to filter 3, the growth of molecules increased the DBE number without significantly affecting the O/C ratio, resulting in a multimodal distribution of the carbon number ($CN = 23, 28, \text{ and } 35$), which could indicate oligomerization.

There is a clear and distinctive pattern (Fig. 5.10) for each sampling zone, which is characterized by a clustering of chemical formulas with a specific oxidation level, amount of unsaturation, and number of carbon atoms. These results are particularly significant for filters 3, 4, and 5, and are highly correlated with the number of carbon atoms. However, for filter 2, there are fewer chemical formulas that are specific to this filter and the pattern of chemical formulas is more dispersed, which makes it difficult to interpret the data. It should be noted that filter 2 was exposed to less air flow between 0.5 and 1.8 km compared to the other filters.

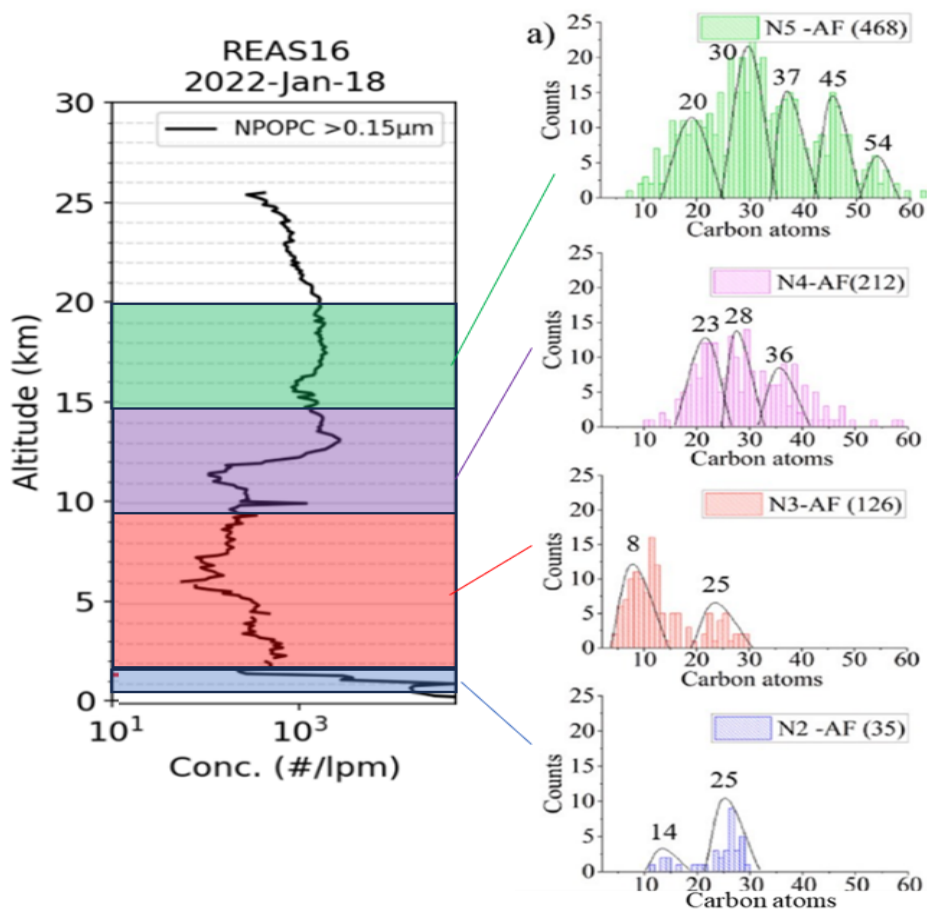


Figure 5.11: The distribution of carbon numbers for filters 2-5. As seen in the figure the number of carbon chains increase with altitude

5.7.3 Results of IC analysis

Figure 5.12 shows the results of the IC analysis of the aerosol samples collected using the lightweight aerosol sampler on 18th January 2022. These results are put in perspective with the POPC measurements of the particle size concentration of the aerosol particles corresponding to the sampling altitudes. As seen in the figure, positions 2, 3, 4, & 5 sampled aerosol particles within the boundary layer (0.5 – 1.8 km), the free troposphere (1.8 – 9.4 km), the UTLS region (9.4 – 14.9 km), and the stratosphere (14.9 – 20 km).

Position 2 shows a high concentration of nitrite (NO_2^-), nitrate (NO_3^{2-}), and sodium (Na^+). Sodium nitrate and sodium nitrite have been known to exist in the boundary layer of the atmosphere, from natural and anthropogenic sources and with varying concentrations (McMurry et al., 1997). This layer also shows the presence of dimethylamine (DMA), and ammonium (NH_4^+), together with biomass-burning potassium (K^+), and magnesium (Mg^{2+}). Mineral dust particles in the atmosphere can adsorb nitrate from heterogeneous reactions with nitrogen oxides including HNO_3 and NO_2 , which can act as a sink for nitrogen oxides in the atmosphere. However, when these dust particles are irradiated with UV light, they have the potential to release gas-phase nitrogen oxides back into the atmosphere (Gankanda, 2014). Position 3 sampled aerosol particles in the free troposphere between 01.8 – 9.4 km. Aerosols of particle size diameter ranging from $r > 0.4$ to $r > 0.15$ were sampled in this layer (Fig.5.9). In addition, this layer was found to consist of nitrate, and nitrite, co-existing with cations, NH_4^+ , K^+ , Mg^{2+} , and Na^+ . There is a likelihood that these aerosols could have existed as nitrate salts in the form of ammonium nitrate (NH_4NO_3), potassium nitrate KNO_3 , and sodium nitrite NaNO_2 . A low concentration of DMA is also seen in this layer.

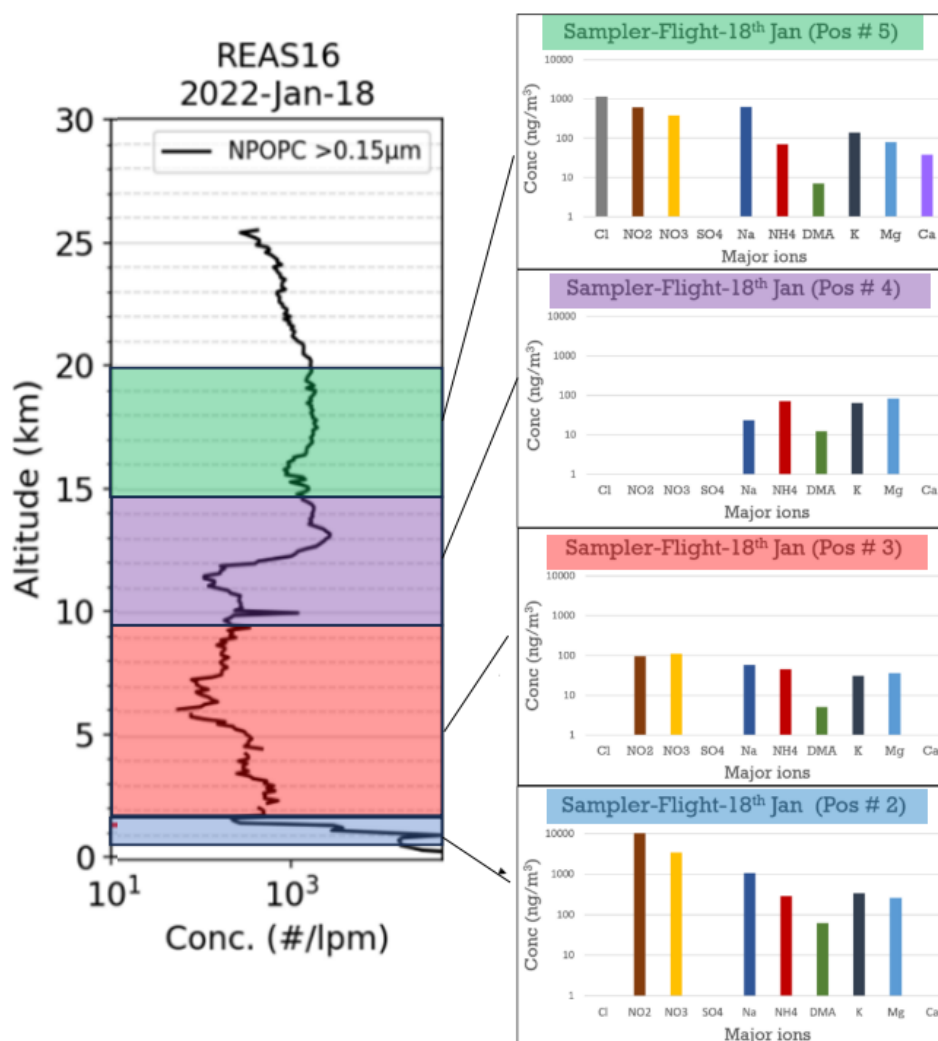


Figure 5.12: (Left). Particle concentration for 9 size radii between 0.15 μm and 0.4 μm measured by the Particle plus Optical Counter (POPC) on a balloon flight on January 18, 2022, from Reims. (Right) results of the ionic composition of aerosol samples collected on the ground and in the UTLS using the balloon-borne impactor and the aerosol sampler.

Position 4 sampled aerosols within the UTLS region between 9.4 – 14.9 km. Here the aerosol particle size radius ranges from $r > 0.4$ (the largest) to $r > 0.15$ (the smallest). This layer comprises a mixture of DMA, salts (NH_4^+ , and Na^+), as well as biomass-burning K^+ , and Mg^{2+} ions. Lastly, position 5 sampled aerosols within the stratospheric layer between 15-25 km altitude. This layer is seen to be enriched with a high concentration of chlorine (Cl^-) ions, in addition to nitrates, nitrites, and DMA. Biomass burning K^+ , Mg^{2+} , and Ca^{2+} also exist in this layer in addition to sodium, and ammonium salts.

The main source of chlorine in the stratosphere is chlorofluorocarbons (CFCs), which are man-made compounds that were widely used in refrigeration, air conditioning, and aerosol sprays. CFCs can persist in the atmosphere for several decades since they're stable compounds (Clarmann, 2013). They are eventually transported to the stratosphere where they are broken down by ultraviolet radiation, releasing chlorine atoms (Cl) that can react with ozone (O_3), leading to the destruction of the ozone layer (Solomon et al., 2014). Ammonium nitrate and ammonium nitrite can undergo photolysis in the presence of UV radiation, and release NO_x sps which could affect ozone (O_3) (Barnes, et al., 2018).

Additionally, ammonium nitrate and ammonium nitrite can react with chlorine (Cl) radicals in the stratosphere forming dichlorine oxide (Cl_2O), which can contribute to the depletion of stratospheric ozone (Saunders et al., 2015).

5.8 Discussion and Conclusion

The lightweight balloon-borne aerosol sampler was used during several consecutive flights to collect atmospheric samples on carbon and PTFE filters from different layers of the atmosphere. The samples were analyzed using DESI coupled with high-resolution mass spectrometry for carbonaceous compounds and inorganic compounds using IC. While 30% of the chemical organic formulas were common across all samples, a significant proportion of chemical formulas were specific to certain samples, indicating distinct sources, chemical processes, or chemical evolution of organic matter from the troposphere to the lower stratosphere. It was found that carbon chains increase from the troposphere to the stratosphere, and there is a reduction in unsaturation in the stratosphere compared to lower layers. The oxidation of organic compounds measured by the O/C ratio remains stable across the layers corresponding to the UTLS and the stratosphere, but the number of oxidized compounds increases with altitude. It was also seen that unsaturated organic compounds above 15 km are strongly influenced by UV light absorption, which can cause unsaturation breakdown and explain the observed multimodal carbon distribution. The connection between quasi-coincident aerosol number concentration and size measurements collected with an optical particle counter and the chemical analysis remains challenging to assess due to different particle sizes. Sample 5 was likely influenced by air masses from the tropics associated with enhanced O₃ and aerosols likely influenced by the La Soufriere eruption. The IC results show that Nitrate and nitrite aerosols are found in the boundary layer, free troposphere, and stratosphere which could account for natural or anthropogenic activities, (Wang et al., 2020) in the presence of ammonia and other atmospheric compounds. Once they're formed, nitrates and nitrites can contribute to the formation of aerosols. They can also participate in chemical reactions that can affect the concentrations of other atmospheric species, such as methane (CH₄) and ozone. Nitrate aerosols can contribute to the formation of cirrus clouds, leading to a significant impact on the radiative balance of the atmosphere (Kärcher et al., 2010). On the other hand, nitrite compounds have been shown to play a role in the depletion of stratospheric ozone (Rex et al., 2014). DMA is one of the most abundant volatile organic compounds emitted in large quantities during wildfires (Yee et al., 2013; Gilman et al., 2015). Youn et al., (1994) found that during wildfires the DMA emitted is further dissolved in cloud water thereby leading to its enhanced levels. In our analysis, the fact of observing the presence of DMA in the boundary, free troposphere, and UTLS layers implies that the NH wildfires could have been its main source. The presence of DMA in the stratosphere highlights the complexity of atmospheric chemistry and the need for further research to understand its sources, transport, and impacts. We did not find any detectable levels of sulfate perhaps due to the lower volume of sample mass filtered or the sensitivity of the ion chromatograph instrument. The results conclude that the origin of the organic compounds detected, especially in the UTLS and the stratosphere, needs further investigation. There is a need for further investigations at other seasons and latitudes to determine whether the results are reproducible and correspond to a steady feature of the atmosphere. This work is scheduled to be continued during the MAGIC-II campaign planned to take place in September.

Résumé du chapitre 5 : Impacts des feux de forêt et des éruptions volcaniques sur les aérosols stratosphériques au-dessus de l'hémisphère Nord - Le projet REAS

Les feux de forêt extrêmes sont devenus un contributeur majeur des aérosols strato-sphériques, comparable aux éruptions volcaniques de moyennes tailles. Ces feux de forêt libèrent des aérosols carbonés dans la stratosphère, qui sont transportés vers le haut par chauffage radiatif. La fumée de ces feux de forêt, lorsqu'elle est transportée vers les régions polaires, peut affecter l'ozone stratosphérique. En 2021, les feux de forêt dans l'hémisphère Nord et l'éruption du volcan La Soufrière ont eu un impact significatif sur la couche d'aérosols stratosphériques. En réponse à ces événements, des vols ballons ont été effectués en France pour mieux comprendre les propriétés microphysiques et chimiques de ces aérosols. L'utilisation de capteurs légers transportés par des ballons offre un moyen rentable de mieux comprendre les propriétés de ces panaches d'aérosols. Le projet REAS (Rapid Balloon Experiments for Sudden Aerosol Injection in the Stratosphere) a été mené en deux phases, de novembre 2021 à janvier 2022 et à l'automne 2022 durant la campagne MAGIC. L'objectif du projet était de comprendre l'impact des éruptions volcaniques et des incendies de forêt sur les aérosols stratosphériques dans l'hémisphère Nord. Dix-sept ballons ont été lancés depuis Reims, en France, équipés d'instruments tels que des compteurs de particules optiques et des échantillonneurs d'aérosols. Le projet a étudié le panache volcanique de La Soufrière et les particules de fumée provenant des feux de forêt en Amérique du Nord. De nouveaux instruments ont été mis au point pour prélever des échantillons d'aérosols, et ces échantillons ont été utilisés conjointement avec des observations satellitaires. La collaboration a impliqué des organisations telles que NIA/NASA-LARC, LPC2E et GSMA. Les vols en ballon, dont quatre de taille moyenne, visaient à explorer diverses propriétés des aérosols. Sur les 17 vols en ballon du projet REAS, cinq vols ont été consacrés à la collecte d'aérosols à l'aide d'un impacteur et d'un échantillonneur d'aérosols. Ces vols comprenaient deux vols d'impacteurs sur un ballon moyen et trois vols d'échantillonneur sur un ballon lumineux. Les échantillons prélevés ont été comparés à des mesures de rétrodiffusion utilisant des sondes optiques de rétrodiffusion. Un seul vol d'impacteur qui a été réussi a eu lieu le 8 décembre, tandis que d'autres tentatives ont été entravées par les restrictions du contrôle de la circulation aérienne. L'échantillonneur d'aérosols léger transporté par ballon a été utilisé pour prélever des échantillons atmosphériques de différentes couches atmosphériques. Ces échantillons ont été analysés à l'aide de DESI (Desorption Electrospray Ionization) couplé à la spectrométrie de masse (MS) et à la chromatographie ionique (IC) à haute résolution. Le DESI offrait une sensibilité accrue pour les faibles concentrations, tandis que HESI (Heated Electrospray Ionization) convenait à la détection de particules d'aérosol plus grosses. Le spectromètre de masse Orbitrap Q-Exactive, connu pour sa haute résolution et sa précision, a été utilisé pour les analyses DESI et HESI. L'étude a révélé que les chaînes carbonées augmentaient de la troposphère à la stratosphère, indiquant potentiellement l'existence de mécanisme d'oligomérisation. De plus, on a observé la réduction de l'insaturation dans la stratosphère par rapport aux couches inférieures. L'oxydation des composés organiques, mesurée par le rapport O/C, est restée stable dans toutes les couches étudiées, mais le nombre de composés oxydés a augmenté avec l'altitude.

La chromatographie ionique d'échantillons d'aérosols troposphériques a révélé la présence d'anions tels que Cl^- , NO_2^- , NO_3^- et diméthylamine (DMA), ainsi que de cations comme Na^+ , NH_4^+ , K^+ , Mg^{2+} et Ca^{2+} . La présence de chlorure de calcium et de nitrite de calcium indiquait des sources naturelles et humaines telles que des aérosols marins, des agents de dégivrage et des procédés industriels. Le 18 janvier 2022, trois vols en ballon ont été effectués dans le cadre de la campagne REAS. Ces vols ont permis de recueillir des informations météorologiques et chimiques sur les couches échantillonnées, y compris les concentrations de particules, la température, l'ozone et les profils de CO. L'échantillonneur d'aérosols a prélevé des échantillons de différentes couches atmosphériques d'origines distinctes. L'analyse des échantillons d'aérosols a révélé la présence de divers composés, notamment du nitrate de sodium, du nitrite de sodium, de la diméthylamine, de l'ammonium, du potassium, du magnésium et des ions chlore. Ces composés ont des implications pour la chimie atmosphérique et peuvent contribuer à l'appauvrissement de l'ozone stratosphérique. L'étude souligne la complexité de la chimie atmosphérique et la nécessité de poursuivre les recherches pour comprendre les sources, le transport et les impacts des aérosols. Les résultats suggèrent l'importance d'étudier les composés organiques dans la région de la stratosphère et de l'UTLS (Upper Troposphere-Lower Stratosphere) pour mieux comprendre le rôle des feux de forêt et des éruptions volcaniques dans la composition des aérosols et leur impact sur le climat et l'appauvrissement

de la couche d'ozone.

Chapter 6

Summary, and Conclusion

Atmospheric aerosols are a complex mixture of chemical species and individual particles originating from natural and anthropogenic processes. They are known to play a key role in several processes governing the atmosphere's physics and chemistry, including the absorption and scattering of solar radiation, altering the atmosphere's and climate's large-scale dynamics, and impacting radiative transfer. Aerosols also serve as nuclei for cloud droplets and ice crystals. The fifth IPCC report released in 2013 states that aerosols derived from anthropogenic sources have an average cooling effect of -0.82 W m^{-2} , in contrast to the warming effect of well-mixed greenhouse gases, which is 3.00 W m^{-2} . The morphology, chemical composition, and physicochemical state of aerosol surfaces reveal their "history," allowing us to reconstruct their origin and predict their effects on the environment and human health.

The stratosphere is an important component of the Earth's climate system that has undergone significant changes in recent decades, leading to challenges in research activities. Processes namely atmospheric pollution, ozone depletion, and alterations in the Brewer-Dobson circulation affect the radiative budget and atmospheric circulation, and hence understanding the dynamic, chemical, and radiative coupling between the stratosphere and troposphere is essential to predict the evolution of our climate. Researchers have been exploring the transport of trace chemical species between the stratosphere and troposphere, with anthropogenic constituents from the troposphere contributing to ozone depletion chemistry in the stratosphere and downward transfer from the stratosphere introducing ozone and other reactive species into the tropical chemical system. The stratosphere contains an aerosol layer that is largely enhanced after major volcanic eruptions and is also influenced by anthropogenic emissions in Asia, resulting in the formation of the Asian Tropopause Aerosol Layer (ATAL). Extreme wildfires can also impact the stratosphere through the direct injection of smoke via PyroCbs. Due to the variety of sources in the stratosphere, its composition is uncertain but crucial to predict its radiative, climate, and chemical impacts. This Ph.D. dissertation focused on assessing the composition of stratospheric aerosols using offline analysis of balloon-borne samples collected in the stratosphere.

ATAL's composition using a balloon-borne impactor

The ATAL is observed annually during the Asian summer monsoon, extending from the eastern Mediterranean across India to western China and at about 13 – 18 km altitude. The layer is comprised of low depolarizing and small particles likely originating from new particles formed in situ or growing on pre-existing aerosols. Deep convection is believed to be the source of conduit for transporting primary aerosols and their precursors into the upper troposphere and lower stratosphere (UTLS), with horizontal movement within the anticyclone and vertical transport pathways in the troposphere contributing to balancing the intensity of the Asian Tropopause Aerosol Layer (ATAL) during the Asian summer monsoon season. Since the discovery of the ATAL, researchers have been studying its chemical composition. Previous studies have used various methods such as Energy-dispersive X-ray analysis (EDX) and aircraft limb infrared measurements to identify the presence of carbon, sulfur, and ammonium nitrate in aerosol particles. Models suggest that the ATAL may contain a significant amount of mineral dust, as well as surface-emitted and secondary organic aerosols. Although there have been extensive studies on the mass concentration, number, and optical properties of stratospheric aerosols, there has been limited information on their chemical composition in the ATAL and the stratosphere. An extensive analysis of

ATAL aerosols in India using a balloon-borne impactor system with offline Ion Chromatography analysis. The study aimed to understand the physical, chemical, and optical properties of aerosols using a unique strategy of balloon-borne measurements over the UTLS region in India. The goal was to shed light on the convective transport and distribution of aerosols on a regional scale while comparing satellite data and chemistry models with balloon observations.

The chemical composition of the ATAL was studied by collecting aerosol samples aboard zero-pressure balloon flights, using an aerosol impactor. The ion chromatography results of the collected samples revealed the dominant presence of nitrate and nitrite aerosols during the 2017 summer campaign. Winter flights sampled residuals from the 2017 Canadian wildfires, and the influence of convection on these measurements was studied using back-trajectory calculations. The GEOS-Chem model simulations were used to understand the contribution of lightning to nitrate aerosol. Flights ZF2 and ZF3 sampled air masses localized at the border of the Asian anticyclone, with the eastern part depicting a peak in ammonium contribution from Chinese emissions and the western core seen to be enriched with anthropogenic sources from India. Flight ZF2 also showed the presence of Ca^{2+} and NO_3^- in a cloud, implying the formation of $\text{Ca}(\text{NO}_3)_2$ in the presence of HNO_3 . The study provides insights into the existence and behavioral patterns of these ionic species of interest in the atmosphere. This area will continue to be investigated with improved techniques and additional information.

An ocean of stratospheric aerosols after the Hunga-Tonga Hunga-Ha'apai eruption

Chapter 4 investigates the impact of the Hunga-Tonga undersea eruption on the stratospheric aerosol population using balloon measurements, satellite data, and model simulations. The eruption injected the equivalent of 10% of the total stratospheric water vapor content into the stratosphere. While injecting a modest 0.4 Tg of SO_2 , the subsequent stratospheric aerosol optical depth was 3-4 times larger than expected. To understand the source of these discrepancies and assess the optical, microphysical, and chemical properties of the plume, the Brazil Volcano (BraVo) campaign was mounted. This chapter is centered around the analysis of the inorganic composition of the volcanic plume, which was achieved through the examination of aerosol samples collected within the plume. Notably, the presence of NaCl at a ratio consistent with sea salt (1.6) indicates that marine-influenced aerosols had a significant impact on the plume's chemical properties. In addition, the presence of Ca^{2+} may indicate residual ash particles. The presence of marine species was externally confirmed by ACE-FTS which showed the presence of H_2O isotopes consistent with sea water (Khaykin et al., 2022) as well as the early depletion observed in the HTHH plume related to HOCl chemistry from released HCl likely from NaCl (Zhu et al., 2023). However, our study found the presence of other compounds such as ammonia (NH_3) and (F^-), not representative of volcanic aerosol for which we do not fully understand the origin. Finally, the GOESGEOS-chem simulation performed for the first 8 months after the eruption suggests that the level of sulfate found on the samples was significantly lower than expected pointing out an unknown sink mechanism for sulfate, a loss of sulfate between collection and analysis, or a limitation of the IC techniques for measuring accurately sulfate. Additional analysis needs to be performed to improve the error characterization associated with the analysis that I plan to carry on in the future.

Impacts of wildfires and volcanic eruptions on stratospheric aerosol over the Northern Hemisphere- The REAS project

Volcanic eruptions of medium-to-large scale have had a considerable impact on stratospheric aerosols in the past decade. However, in recent years, carbonaceous aerosols from extreme wildfires have emerged as a new source of stratospheric particles, causing significant effects on climate and may delay expected ozone recovery. The Rapid Experiments for Sudden Aerosol Injection in the Stratosphere (REAS) project was launched to gain a better understanding of the impact of such events on stratospheric aerosol loadings in the Northern Hemisphere. My Ph.D. relied on two deployments during which new sampling techniques were developed and tested in partnership with other institutions. The REAS initiative aims to quickly respond to sudden events that influence the composition of stratospheric aerosols. Between November 2021 and January 2022, 17 balloons were deployed from Reims, Eastern France to measure the atmospheric composition of trace/greenhouse gases and aerosols from the ground up to stratospheric levels. The instruments used for the measurements included an Aircore gas collector, optical particle

counters, ozone sondes, COBALD backscatter sondes, an aerosol sampler, and an aerosol impactor. Even though there were no extreme events that affected the stratosphere during the campaign, observations within the aged volcanic plume from La Soufrière volcano (Saint Vincent island) and smoke particles from PyroCb events in North America were made. The properties and burden of the observed aerosols were determined by analyzing these in situ measurements alongside satellite data. Chapter 5 of the dissertation discusses an extensive study on the organic and inorganic composition of stratospheric aerosols to unveil the signature of a mixed plume of volcano and wildfire using a lightweight aerosol sampler. The study focused on analytical techniques in sample analysis using high-resolution mass spectrometry (operated by ICARE, Orleans) and ion chromatography (which I operated myself at PRL, India). The lightweight balloon-borne aerosol sampler was used to collect atmospheric samples from different layers of the atmosphere, which were analyzed using DESI coupled with high-resolution Mass spectrometry (MS) and IC. DESI offers heightened sensitivity for low concentrations, while HESI is suitable for detecting larger aerosol particles. The sensitivity of DESI was well-suited for the observed concentrations in the study. On the other hand, HESI utilizes a heated electrospray ionization source and employs toluene for chemical ionization. It enables the detection of larger aerosol particles and requires specific settings for gas flows, temperatures, and voltages. Both DESI and HESI analyses were performed using the Orbitrap Q-Exactive mass spectrometer, renowned for its exceptional resolution and accuracy. Different mass-to-charge ratio ranges were utilized to encompass a wide array of molecules. The MS study found that carbon chains increase from the troposphere to the stratosphere which could be consistent with the oligomerization mechanism. In addition, we found a reduction in unsaturation in the stratosphere compared to lower layers. The oxidation of organic compounds measured by the O/C ratio was seen to remain stable across the layers corresponding to the UTLS and the stratosphere, but the number of oxidized compounds increased with altitude. IC results of the samples collected at ground level using the aerosol impactor revealed the presence of anions including Cl^- , NO_2^- , NO_3^{2-} , and dimethylamine (DMA), with Cl^- and NO_2^- detected in the second stage of the impactor, and NO_3^{2-} and DMA detected in the second and third stages with sizes ranging from 0.2 μm to 0.05 μm . Additionally, cations including Na^+ , NH_4^+ , K^+ , Mg^{2+} , and Ca^{2+} were found, with Ca^{2+} only present in the second stage of the impactor, indicating it may have existed as CaCl_2 and $(\text{CaNO})_2$. Calcium chloride and calcium nitrite can be present in the atmosphere from various natural and anthropogenic sources, including marine aerosols, de-icing agents, industrial processes, and corrosion inhibitors in concrete structures. Results of the IC analysis of aerosol samples collected between 9-16 km detected nitrate and nitrite in stages 2 and 3, with Na^+ present in stages 1 and 2, indicating the possible presence of sodium nitrite and sodium nitrate. Other cations including NH_4^+ , K^+ , Mg^{2+} , and Ca^{2+} were found in all three stages. Volcanic eruptions release large amounts of SO_2 , which on reaction with oxygen forms can react with other atmospheric species to form SO_3 which in the presence of water vapor and 3 ammonium nitrate and ammonium nitrate. The concentrations of these compounds in volcanic plumes can vary based on the type of volcano, eruption style, and magma composition. Sulfate is a common component of fine particulate matter in the atmosphere, but is not commonly seen at ground level in aerosol form due to its small size, formation in the upper atmosphere, and efficient removal through precipitation processes. The formation of ammonium nitrate and ammonium nitrite can have negative impacts on human health and the environment, and the concentrations of nitrate salts with different cations can vary depending on location, season, and emission sources. The balloon flights on January 18th combining ORBITRAP MS and IC On January 18, 2022, three balloon flights were conducted from Reims, France, as part of the REAS campaign. The flights gathered meteorological and chemical information about sampled layers, with particle concentrations measured during the first flight and temperature, ozone, and CO profiles measured during the second flight. The third flight launched an aerosol sampler to collect samples from different atmospheric layers with distinct origins. The lowermost stratosphere (12-16 km) was an active zone of exchanges between the tropics and mid-latitudes, while the lower stratosphere above 16 km was generally influenced by the Brewer-Dobson circulation. Higher ozone values indicated a tropical origin associated with volcanic aerosols, while lower levels may be associated with smoke from biomass burning. The boundary between the planetary boundary layer and the free troposphere was differentiated at 2 km above sea level. The collected aerosol samples were analyzed for their organic and inorganic composition using ORBITRAP mass spectra and IC, respectively. Results and Discussion Atmospheric samples were collected and analyzed using a flow injection analysis system with specific settings for HESI ionization. A search was made for molecules containing carbon, hydrogen, oxygen, nitrogen, and sulfur atoms, and their molecular formulas were determined. Only VOCs and Oas primarily composed of carbon, hydrogen, and oxygen

were studied, and molecular formulas with low intensity or detected less than twice were excluded. The study identified 6589 chemical formulas for the filters and correlated them with flight parameters such as atmospheric pressure and gas flow. Lower pressure and temperature had a positive impact on adsorption, while exposed air volume did not affect the number of chemical formulas. The study identified 15 sets of chemical formulas that may indicate similarities in atmospheric conditions across various sampling areas. The study found a unique fingerprint for each sampling zone characterized by the dispersion of chemical formulas, oxidation level, and amount of unsaturation. Filters 3, 4, and 5 showed significant results, while interpretation was limited for filter 2 due to the low number of specific chemical formulas and dispersion of formulas. The ionic composition results of aerosol particles collected on January 18th, 2022 using a lightweight aerosol sampler were compared with the particle size concentration obtained from POPC measurements at corresponding sampling altitudes. The analysis revealed that positions 2-5 collected aerosol particles from the boundary layer, free troposphere, UTLS region, and stratosphere. Position 2 exhibited a high concentration of sodium nitrate, sodium nitrite, dimethylamine, ammonium, biomass-burning potassium, and magnesium. Nitrate adsorption onto mineral dust particles in the atmosphere can act as a sink for nitrogen oxides, but when exposed to UV light, dust particles can release gas-phase nitrogen oxides. Position 3 showed the presence of nitrate, nitrite, ammonium, potassium, magnesium, and sodium, which could have existed as nitrate salts. Position 4 contained a mixture of DMA, salts, and biomass-burning ions, while position 5 was enriched with chlorine ions, nitrates, nitrites, DMA, and biomass-burning ions. Chlorofluorocarbons were identified as the main source of chlorine in the stratosphere, which can react with ozone and lead to its depletion. Ammonium nitrate and ammonium nitrite can also affect ozone through photolysis and reaction with chlorine radicals, which can contribute to the depletion of stratospheric ozone. The study highlights the complexity of atmospheric chemistry and the need for further research to understand its sources, transport, and impacts. The results conclude that the origin of the organic compounds detected, especially in the UTLS and the stratosphere, needs further investigation. There is a need for investigations of additional measurements at other seasons and latitudes to determine whether the results are reproducible and correspond to a steady feature of the atmosphere. The lightweight balloon-borne aerosol sampler was used in multiple flights to collect atmospheric samples, which were analyzed using DESI coupled with high-resolution mass spectrometry and IC. The results revealed that while some chemical organic formulas were common across all samples, others were specific to certain samples, indicating distinct sources or chemical processes. Carbon chains increased from the troposphere to the stratosphere, and there was a reduction in unsaturation in the stratosphere compared to lower layers. Nitrate and nitrite aerosols were found in the boundary layer, free troposphere, and stratosphere, and their formation can contribute to the formation of aerosols and affect the concentrations of other atmospheric species. DMA was detected in all layers, suggesting that wildfires could be a significant source. Sulfate was not detected. Further investigations are necessary to determine the origin of organic compounds detected and whether the results are reproducible throughout different seasons and latitudes. The study will continue during the MAGIC-II campaign scheduled for September 2023.

Participation

Field Campaigns

BATAL-Balloon measurements of the Asian Tropopause Aerosol Layer (2017-1019)

REAS- Rapid Experiments for sudden aerosol loading in the Stratosphere on account of volcanic eruptions and wildfires (2021-2022)

BraVo- Brazil Volcano Project to study the effect of the undersea Hunga Tonga Hunga-Ha'apai volcanic eruption on stratospheric aerosol chemistry (May, and August 2022)

MAGIC- (Oct-Jan 2023)

International Conferences

Hazel Vernier, Neeraj Rastogi, Duncan Fairlie, Hongyu Liu, Amit Pandit, Kristopher Bedka, Anil Patel, Venkat Ratham, Jean-Paul Vernier, and Suneel Kumar. "Chemical composition of the Upper Troposphere and Lower Stratosphere during the Asian summer monsoon." (2021).

Oral presentation at the EGU General Assembly 2021.

Hazel Vernier, Demilson Quintão, Bruno Biazon, Eduardo Landulfo, Giovanni Souza, Fabio JS Lopes, Neeraj Rastogi, Rohit Meena, Hongyu Liu, Suvarna Fadnavis, Mahesh Kovilakam, Gwenaël Berthet, Jean-Paul Vernier. “Understanding the impact of Hunga-Tonga undersea eruption on the stratospheric aerosol population using Balloon measurements, Satellite data, and model simulations”

Oral presentation at the EGU General Assembly 2023.

Hazel Vernier, Demilson Quintão, Bruno Biazon, Eduardo Landulfo, Giovanni Souza, Fabio JS Lopes, Neeraj Rastogi, Rohit Meena, Hongyu Liu, Suvarna Fadnavis, Mahesh Kovilakam, Gwenaël Berthet, Jean-Paul Vernier. “An ocean of stratospheric aerosols after the Hunga Tonga–Hunga Ha’apai eruption volcanic eruption”

Oral presentation at the SPARC Hunga Tonga open science workshop 2023.

International Publications

Hazel Vernier, Neeraj Rastogi, Hongyu Liu, Amit Kumar Pandit, Kris Bedka, Anil Patel , Madineni Venkat Ratnam , Buduru Suneel Kumar, Bo Zhang, Harish Gadhavi, Frank Wienhold, Gwenaël Berthet, Jean-Paul Vernier. “Exploring the inorganic composition of the Asian Tropopause Aerosol Layer using medium-duration balloon flights”. *Atmospheric Chemistry and Physics*, 2022, 22, pp.12675-12694. <10.5194/acp-22-12675-2022>. <insu-03839027>

Benoit Roland, Vernier Hazel, Vernier Jean-Paul, Joly Lilian, Dumelié Nicolas, Wienhold Frank G, Crevoisier Cyril, Delpoux Sandrine, Bernard François, Dagaut Philippe, Berthet Gwenaël. “The first balloon-borne sample analysis of atmospheric carbonaceous components reveals new insights into formation processes. *Chemosphere*. 2023 Jun;326:138421. doi: 10.1016/j.chemosphere.2023.138421. Epub 2023 Mar 17. PMID: 36935062.

Hazel Vernier, Demilson Quintão, Bruno Biazon, Eduardo Landulfo, Giovanni Souza, Benoit Grosslin, Neeraj Rastogi, Amanda V. Santos, Fabio J. S. Lopes, Alex C. P. Mendes, José A. S. da Matta, Damaris K. Pinheiro, Maria P.M. P. Jorge, Maria de Fátima Andrade, Hongyu Liu, Suvarna Fadnavis, Akhil Raj, Mahesh Kovilakam, Rohit Meena, Gwenaël Berthet, and Jean-Paul Vernier. “An ocean of stratospheric aerosols after the Hunga Tonga–Hunga Ha’apai eruption volcanic eruption” (*Nature-Communications Earth and Environ.* - Under Review)

My ongoing projects with international collaborators involve advancements in analytical techniques, and I will be presenting the results of the Batal 2019 and the REAS campaigns at the upcoming AGU meeting. I am excited about the opportunity to connect with other researchers, showcase my work, and establish new collaborations as I embark on my postdoctoral career.

Despite the challenges posed by the COVID pandemic and my personal struggles with surviving a brain hemorrhage, I persevered and succeeded in expanding my collaborations and conducting fieldwork.

I am grateful for this opportunity to set an example and inspire others to pursue their passions regardless of the obstacles they face. Research is my passion, and I am committed to contributing to the field whenever I am given the chance.

Resumé du chapitre 6 et conclusion en Français

Les aérosols atmosphériques sont un mélange complexe d'espèces chimiques et de particules individuelles provenant de processus naturels et anthropiques. Ils sont connus pour jouer un rôle fondamental dans plusieurs processus régissant la physique et la chimie de l'atmosphère, y compris l'absorption et la diffusion du rayonnement solaire, la modification de la dynamique à grande échelle de l'atmosphère et du climat et l'impact sur le transfert radiatif. Les aérosols servent également de noyaux de condensation de nuages. Le cinquième rapport du GIEC publié en 2013 indique que les aérosols dérivés de sources anthropiques ont un impact radiatif moyen de $-0,82 \text{ W m}^{-2}$, contrairement à l'impact des gaz à effet de serre, qui est de $3,00 \text{ W m}^{-2}$. La morphologie, la composition chimique et l'état physico-chimique des surfaces des aérosols révèlent leur histoire, ce qui nous permet de reconstituer leur origine et de prédire leurs effets sur l'environnement et la santé humaine. La stratosphère est une composante importante du système climatique terrestre qui a subi des changements importants au cours des dernières décennies. Les processus, à savoir la pollution atmosphérique, l'appauvrissement de la couche d'ozone et les altérations de la circulation de Brewer-Dobson, affectent le bilan radiatif. La compréhension du couplage dynamique, chimique et radiatif entre la stratosphère et la troposphère est essentielle pour prédire l'évolution de notre climat. Les chercheurs ont exploré le transport d'espèces chimiques mineurs entre la stratosphère et la troposphère, les constituants anthropiques de la troposphère contribuant à la chimie de l'appauvrissement de la couche d'ozone dans la stratosphère et au transfert vers le bas de la stratosphère introduisant de l'ozone et d'autres espèces réactives dans le système chimique tropical. La stratosphère contient une couche d'aérosol qui est largement influencé par des éruptions volcaniques majeures ainsi que par les émissions anthropiques en Asie, entraînant la formation de la couche asiatique d'aérosols vers la tropopause (ATAL). Les feux de forêt extrêmes peuvent également avoir un impact sur la stratosphère par l'injection directe de suies via les processus de Pyroconvection. En raison de la variété des sources dans la stratosphère, sa composition est incertaine mais cruciale pour prédire ses impacts radiatifs, climatiques et chimiques. Cette thèse de doctorat porte principalement sur l'évaluation de la composition des aérosols stratosphériques à l'aide de l'analyse en laboratoire d'échantillons collectés dans la stratosphère mais aussi sur les propriétés microphysiques et optiques de ces aérosols.

Composition de l'ATAL à l'aide d'un impacteur sous ballon

L'ATAL est observé chaque année pendant la mousson d'été asiatique, s'étendant de la Méditerranée orientale à travers l'Inde et jusqu'à l'ouest de la Chine entre 13-18 km d'altitude. La couche est composée de petites particules faiblement dépolarisantes et probablement provenant de nouvelles particules formées in situ ou se développant sur des aérosols préexistants. On pense que la convection profonde transporte pendant la saison de la mousson d'été asiatique des aérosols primaires et leurs précurseurs dans la haute troposphère et la basse stratosphère (UTLS), avec un mouvement horizontal à l'intérieur de l'anticyclone. Depuis la découverte de l'ATAL, les chercheurs étudient sa composition chimique. Des études antérieures ont utilisé diverses méthodes telles que l'analyse par rayons X à dispersion d'énergie (EDX) et les mesures infrarouges pour identifier la présence de carbone, de soufre et de nitrate d'ammonium dans les particules d'aérosol. Les modèles suggèrent que l'ATAL peut contenir une quantité importante de poussière minérale, ainsi que des aérosols organiques secondaires émis en surface. Bien qu'il y ait eu des études approfondies sur la concentration, le nombre et les propriétés optiques des aérosols stratosphériques, il y a eu peu d'informations sur leur composition chimique dans l'ATAL. Une analyse approfondie des aérosols de l'ATAL en Inde à l'aide d'un système d'impactin transportés sous ballon suivit d'une analyse chromatographie ionique en laboratoire a fait l'objet de cette thèse. L'étude visait à comprendre les propriétés physiques, chimiques et optiques des aérosols en utilisant une stratégie unique de mesures sous ballons au-dessus de la région UTLS en Inde. L'objectif était de faire la lumière sur le transport convectif et la distribution des aérosols à l'échelle régionale tout en comparant les données satellitaires et les modèles chimiques avec les observations de ballons. La composition chimique de l'ATAL a été étudiée en recueillant des échantillons d'aérosols à bord de ballons plafonnant, à l'aide d'un impacteur d'aérosols. Les résultats de la chromatographie ionique des échantillons prélevés ont révélé la présence dominante de nitrate et de nitrite au cours de la campagne estivale 2017. Les vols hivernaux ont échantillonné les résidus des feux de forêt canadiens de 2017. L'influence de la convection sur ces mesures a été étudiée à l'aide de calculs de trajectoire. Les simulations du modèle GEOS-Chem ont été utilisées pour comprendre la contribution des éclairs générant des Nox et conduisant à la formation de nitrate. Le vol ZF2 a égale-

ment montré la présence de Ca^{2+} , et NO_3^- dans un nuage, ce qui implique la formation de $\text{Ca}(\text{NO}_3)_2$ en présence de HNO_3 . L'étude donne un aperçu de l'existence et des modèles comportementaux de ces espèces ioniques d'intérêt dans l'atmosphère. Ce domaine continuera d'être étudié avec des techniques améliorées et des informations supplémentaires.

Un océan d'aérosols stratosphériques après l'éruption Hunga-Tonga Hunga-Ha'apai (HTHH)

Le chapitre 4 est consacré à l'étude de l'impact de l'éruption sous-marine HTHH sur la population d'aérosols stratosphériques à l'aide de mesures sous ballons, de données satellitaires et de simulations numérique. L'éruption a injecté l'équivalent de 10% de la teneur totale en vapeur d'eau de la stratosphère. Cependant l'injection de 0.4 Tg de SO_2 a généré des épaisseurs optiques de d'aérosol stratosphérique beaucoup plus importante que prévu (3 à 4 fois supérieure aux valeurs attendues). Pour comprendre ces divergences et évaluer les propriétés optiques, microphysiques et chimiques du panache, la projet « Brazil Volcano » (BraVo) a été montée. Ce chapitre est centré sur l'analyse de la composition inorganique du panache volcanique qui a été réalisée grâce à l'examen d'échantillons d'aérosols collectés dans le panache. Notamment, la présence de NaCl à un rapport compatible au le sel marin (1,6) indique que les aérosols d'influence marine ont pu avoir un impact significatif sur les propriétés chimiques du panache. De plus, la présence de Ca^{2+} peut indiquer des particules de cendres résiduelles. La présence d'eau provenant de l'océan dans la stratosphère a été montré par la présence d'isotopes H_2O compatibles avec l'eau de mer (Khaykin et al., 2022). Les faibles concentrations d'ozone observées dans le panache HTHH semble être lié à la chimie de HOCl provenant de HCl libéré probablement par les sels NaCl (Zhu et al., 2023). Cependant, notre étude a révélé la présence d'autres composés tels que l'ammoniac (NH_3) et (F^-), qui ne semble pas représentatifs des aérosols volcaniques ou marins dont nous ne comprenons pas complètement l'origine. Enfin, la simulation GEOS-chem réalisée pendant les 8 premiers mois après l'éruption suggère que le niveau de sulfate trouvé sur les échantillons était significativement plus faible que prévu, indiquant un mécanisme de puits inconnu pour le sulfate, ou bien une perte de sulfate entre la collecte et l'analyse qui semble improbable puisque les sulfates sont des composés stables. On ne peut pas non plus exclure une limitation des techniques IC pour mesurer avec précision le sulfate. Des analyses supplémentaires doivent être effectuées pour améliorer la caractérisation des erreurs associées à l'analyse que je prévois poursuivre à l'avenir.

Impacts des feux de forêt et des éruptions volcaniques sur les aérosols stratosphériques au-dessus de l'hémisphère Nord - Le projet REAS

Les éruptions volcaniques de moyenne à grande échelle ont eu un impact considérable sur les aérosols stratosphériques au cours de la dernière décennie. Cependant, ces dernières années, les aérosols carbonés provenant d'incendies de forêt extrêmes sont apparus comme une nouvelle source de particules stratosphériques, entraînant des effets importants sur le climat et pouvant retarder la régénération prévue de l'ozone. Le projet REAS (Rapid Experiments for Sudden Aerosol Injection in the Stratosphere) a été lancé pour mieux comprendre l'impact de tels événements sur les charges d'aérosols stratosphériques dans l'hémisphère Nord. Ma thèse s'est appuyée sur deux déploiements au cours desquels de nouvelles techniques d'échantillonnage ont été développées et testées en partenariat avec d'autres institutions. L'initiative REAS vise à réagir rapidement aux événements soudains qui influencent la composition des aérosols stratosphériques. Entre novembre 2021 et janvier 2022, 17 ballons ont été déployés depuis Reims, dans l'est de la France, pour mesurer la composition atmosphérique des gaz à effet de serre et des aérosols depuis le sol jusqu'aux niveaux stratosphériques. Les instruments utilisés pour les mesures comprenaient un collecteur de gaz Aircore, des compteurs de particules optiques, des sondes d'ozone, des sondes à rétrodiffusion COBALD, un échantillonneur d'aérosols et un impacteur d'aérosol. Même s'il n'y a pas eu d'événements extrêmes qui ont affecté la stratosphère pendant la campagne en 2021-2022, des observations dans le panache volcanique ancien de La Soufrière (île Saint-Vincent) et probablement des suies provenant d'événements de pyroconvection en Amérique du Nord ont été réalisés. Les propriétés et la charge des aérosols observés ont été déterminées en analysant ces mesures in situ parallèlement aux données satellitaires. Le chapitre 5 de la thèse traite d'une étude approfondie sur la composition organique et inorganique des aérosols stratosphériques qui dévoile probablement la signature de panaches d'aérosols volcaniques et de feu de forêt à l'aide d'un échantillonneur d'aérosols. L'étude s'est concen-

trée sur les techniques analytiques d'échantillons utilisant la spectrométrie de masse à haute résolution (opérée par ICARE, Orléans) et la chromatographie ionique (que j'ai moi-même opérée à PRL, en Inde). L'échantillonneur d'aérosols léger transporté par ballon a été utilisé pour prélever des échantillons atmosphériques de différentes couches de l'atmosphère, qui ont été analysés à l'aide de DESI couplé à la spectrométrie de masse (MS) et à la CI à haute résolution. DESI offre une sensibilité accrue pour les faibles concentrations, tandis que HESI convient à la détection de particules plus grosses. La sensibilité du DESI était bien adaptée aux concentrations observées dans l'étude. D'autre part, HESI utilise une source d'ionisation électro-pulvérisation chauffée et utilise du toluène pour l'ionisation chimique. Il permet la détection de particules d'aérosol plus grosses et nécessite des réglages spécifiques pour les débits de gaz, les températures et les tensions. Les analyses DESI et HESI ont été réalisées à l'aide du spectromètre de masse Orbitrap Q-Exactive, réputé pour sa résolution et sa précision exceptionnelles. Différentes plages de rapport masse/charge ont été utilisées pour englober un large éventail de molécules. L'étude MS a révélé que les chaînes carbonées augmentent de la troposphère à la stratosphère, ce qui pourrait être compatible avec le mécanisme d'oligomérisation. De plus, nous avons constaté une réduction de l'insaturation dans la stratosphère par rapport aux couches inférieures. L'oxydation des composés organiques mesurée par le rapport O/C est restée stable à travers les couches correspondant à l'UTLS et à la stratosphère, mais le nombre de composés oxydés a augmenté avec l'altitude. Les résultats de la chromatographie ionique des échantillons prélevés au niveau du sol à l'aide de l'impacteur d'aérosol ont révélé la présence d'anions, notamment Cl^- , NO_2^- , NO_3^- , et diméthylamine (DMA), avec Cl^- , et NO_2^- , détectés dans le deuxième étage de l'élément de l'impacteur, et NO_3^- , et DMA détectés dans les deuxième et troisième étages avec des tailles allant de 0.2 μm à 0.05 μm . De plus, des cations comprenant Na^+ , NH_4^+ , K^+ , Mg^{2+} , et Ca^{2+} ont été trouvés, le Ca^{2+} n'étant présent que dans le deuxième étage de l'élément de frappe, ce qui indique qu'il pourrait avoir existé sous forme de $\text{Ca}(\text{Cl}_2)$ et $\text{Ca}(\text{NO}_2)$. Le chlorure de calcium et le nitrite de calcium peuvent être présents dans l'atmosphère à partir de diverses sources naturelles et anthropiques, y compris les aérosols marins, les agents de dégivrage, les procédés industriels et les inhibiteurs de corrosion dans les structures en béton. Les résultats de l'analyse IC d'échantillons d'aérosols prélevés entre 9 et 16 km ont révélé la présence de nitrate et de nitrite aux stades 2 et 3, avec Na^+ présent aux stades 1 et 2, indiquant la présence possible de nitrite de sodium et de nitrate de sodium. D'autres cations, y compris NH_4^+ , K^+ , Mg^{2+} et Ca^{2+} , ont été trouvés dans les trois stades. Les éruptions volcaniques libèrent de grandes quantités de SO_2 qui, en réaction avec l'oxygène, peut réagir avec d'autres espèces atmosphériques pour former du SO_3 qui, en présence de vapeur d'eau forme du nitrate d'ammonium. Les concentrations de ces composés dans les panaches volcaniques peuvent varier en fonction du type de volcan, du style d'éruption et de la composition du magma. Les vols en ballon du 18 janvier ont combiné ORBITRAP MS et IC Le 18 janvier 2022, trois vols en ballon ont été effectués depuis Reims, en France, dans le cadre de la campagne REAS. Les vols ont permis de recueillir des informations météorologiques et chimiques sur les couches échantillonnées, avec des concentrations de particules mesurées lors du premier vol et des profils de température, d'ozone et de CO mesurés lors du deuxième vol. Le troisième vol a lancé un échantillonneur d'aérosols pour collecter des échantillons de différentes couches atmosphériques d'origines distinctes. La stratosphère la plus basse (12-16 km) était une zone active d'échanges entre les tropiques et les latitudes moyennes, tandis que la stratosphère inférieure au-dessus de 16 km était généralement influencée par la circulation de Brewer-Dobson. Des valeurs d'ozone plus élevées indiquent une origine tropicale associée aux aérosols volcaniques, tandis que des niveaux plus faibles peuvent être associés à la fumée provenant de suies émis pendant l'été et l'automne qui a précédé la campagne. Les échantillons d'aérosols prélevés ont été analysés pour leur composition organique et inorganique à l'aide des spectres de masse ORBITRAP et IC, respectivement. L'étude a trouvé une empreinte digitale unique pour chaque zone d'échantillonnage caractérisée par la dispersion des formules chimiques, le niveau d'oxydation et la quantité d'insaturation. Les filtres 3, 4 et 5 ont donné des résultats significatifs, tandis que l'interprétation a été limitée pour le filtre 2 en raison du faible nombre de formules chimiques spécifiques et de la dispersion de formules. Les résultats de la composition ionique des particules d'aérosol recueillies le 18 janvier 2022 à l'aide d'un échantillonneur d'aérosols léger ont été comparés à la concentration granulométrique obtenue à partir de mesures POPC aux altitudes d'échantillonnage correspondantes. L'analyse a révélé que les positions 2 à 5 collectaient des particules d'aérosol de la couche limite, de la troposphère libre, de la région UTLS et de la stratosphère. La position 2 présentait une concentration élevée de nitrate de sodium, de nitrite de sodium, de diméthylamine, d'ammonium, de potassium brûlant de la biomasse et de magnésium. L'adsorption des nitrates sur les particules de poussière minérale dans l'atmosphère peut agir comme un puits pour les oxydes d'azote, mais lorsqu'elles

sont exposées à la lumière UV, les particules de poussière peuvent libérer des oxydes d'azote en phase gazeuse. La position 3 montrait la présence de nitrate, de nitrite, d'ammonium, de potassium, de magnésium et de sodium, qui auraient pu exister sous forme de sels de nitrate. La position 4 contenait un mélange de DMA, de sels et d'ions brûlant la biomasse, tandis que la position 5 était enrichie en ions chlore, nitrates, nitrites, DMA et ions brûlant la biomasse. Les chlorofluorocarbures ont été identifiés comme la principale source de chlore dans la stratosphère, qui peut réagir avec l'ozone et conduire à son appauvrissement. Le nitrate d'ammonium et le nitrite d'ammonium peuvent également affecter l'ozone par photolyse et réaction avec les radicaux chlorés, ce qui peut contribuer à l'appauvrissement de l'ozone stratosphérique. L'étude souligne la complexité de la chimie atmosphérique et la nécessité de poursuivre les recherches pour comprendre ses sources, son transport et ses impacts. Les résultats concluent que l'origine des composés organiques détectés, en particulier dans l'UTLS et la stratosphère, nécessite une enquête plus approfondie. Il est nécessaire d'étudier des mesures supplémentaires à d'autres saisons et latitudes pour déterminer si les résultats sont reproductibles et correspondent à une caractéristique stable de l'atmosphère. D'autres recherches sont nécessaires pour déterminer l'origine des composés organiques détectés et si les résultats sont reproductibles au cours des différentes saisons et latitudes. L'étude se poursuivra pendant la campagne MAGIC-II prévue en septembre 2023.

References

- Andreae, M. O., & Rosenfeld, D. (2008). Aerosol–cloud–precipitation interactions. Part 1. The nature and sources of cloud-active aerosols. *Earth-Science Reviews*, *89*(1), 13–41. <https://doi.org/https://doi.org/10.1016/j.earscirev.2008.03.001>
- Appel, O., Köllner, F., Dragoneas, A., Hünig, A., Molleker, S., Schlager, H., Mahnke, C., Weigel, R., Port, M., Schulz, C., Drewnick, F., Vogel, B., Stroh, F., & Borrmann, S. (2022). Chemical analysis of the Asian tropopause aerosol layer (ATAL) with emphasis on secondary aerosol particles using aircraft-based in situ aerosol mass spectrometry. *Atmospheric Chemistry and Physics*, *22*(20), 13607–13630. <https://doi.org/10.5194/acp-22-13607-2022>
- Arias, P. A., Bellouin, N., Coppola, E., Jones, R. G., Krinner, G., Marotzke, J., Naik, V., Palmer, M. D., Plattner, G.-K., Rogelj, J., Rojas, M., Sillmann, J., Storelvmo, T., Thorne, P. W., Trewin, B., Achuta Rao, K., Adhikary, B., Allan, R. P., Armour, K., ... Zickfeld, K. (2021). Technical Summary. In V. Masson-Delmotte, P. Zhai, A. Pirani, S. L. Connors, C. Péan, S. Berger, N. Caud, Y. Chen, L. Goldfarb, M. I. Gomis, M. Huang, K. Leitzell, E. Lonnoy, J. B. R. Matthews, T. K. Maycock, T. Waterfield, O. Yelekçi, R. Yu, & B. Zhou (Eds.), *Climate Change 2021: The Physical Science Basis. Contribution of Working Group I to the Sixth Assessment Report of the Intergovernmental Panel on Climate Change* (p. 33–144). Cambridge University Press. <https://doi.org/10.1017/9781009157896.002>
- Aschmann, J., Sinnhuber, B.-M., Chipperfield, M. P., & Hossaini, R. (2011). Impact of deep convection and dehydration on bromine loading in the upper troposphere and lower stratosphere. *Atmospheric Chemistry and Physics*, *11*(6), 2671–2687. <https://doi.org/10.5194/acp-11-2671-2011>
- Bellouin, N., Boucher, O., Haywood, J., & Reddy, M. S. (2005). Global estimate of aerosol direct radiative forcing from satellite measurements. *Nature*, *438*(7071), 1138–1141. <https://doi.org/10.1038/nature04348>
- Benoit, R., Vernier, H., Vernier, J.-P., Joly, L., Dumelié, N., Wienhold, F. G., Crevoisier, C., Delpeux, S., Bernard, F., Dagaut, P., & Berthet, G. (2023). The first balloon-borne sample analysis of atmospheric carbonaceous components reveals new insights into formation processes. *Chemosphere*, *326*, 138421. <https://doi.org/https://doi.org/10.1016/j.chemosphere.2023.138421>
- Bergman, J. W., Fierli, F., Jensen, E. J., Honomichl, S., & Pan, L. L. (2013). Boundary layer sources for the Asian anticyclone: Regional contributions to a vertical conduit. *Journal of Geophysical Research: Atmospheres*, *118*(6), 2560–2575. <https://doi.org/https://doi.org/10.1002/jgrd.50142>
- Bey, I., Jacob, D. J., Yantosca, R. M., Logan, J. A., Field, B. D., Fiore, A. M., Li, Q., Liu, H. Y., Mickley, L. J., & Schultz, M. G. (2001). Global modeling of tropospheric chemistry with assimilated meteorology: Model description and evaluation. *Journal of Geophysical Research: Atmospheres*, *106*(D19), 23073–23095. <https://doi.org/10.1029/2001JD000807>
- Beyerle, G., & Neuber, R. (1994). The stratospheric aerosol content above Spitzbergen during winter 1991/92. *Geophysical Research Letters*, *21*(13), 1291–1294.

<https://doi.org/https://doi.org/10.1029/93GL03292>

- Bigg, E. K. (1975). Stratospheric Particles. *Journal of Atmospheric Sciences*, 32(5), 910–917. [https://doi.org/https://doi.org/10.1175/1520-0469\(1975\)032<0910:SP>2.0.CO;2](https://doi.org/https://doi.org/10.1175/1520-0469(1975)032<0910:SP>2.0.CO;2)
- BIGG, E. K., ONO, A., & THOMPSON, W. J. (1970). Aerosols at altitudes between 20 and 37 km. *Tellus*, 22(5), 550–563. <https://doi.org/https://doi.org/10.1111/j.2153-3490.1970.tb00522.x>
- Bond, T. C., Bhardwaj, E., Dong, R., Jogani, R., Jung, S., Roden, C., Streets, D. G., & Trautmann, N. M. (2007). Historical emissions of black and organic carbon aerosol from energy-related combustion, 1850–2000. *Global Biogeochemical Cycles*, 21(2). <https://doi.org/10.1029/2006GB002840>
- Bossolasco, A., Jegou, F., Sellitto, P., Berthet, G., Kloss, C., & Legras, B. (2021). Global modeling studies of composition and decadal trends of the Asian Tropopause Aerosol Layer. *Atmospheric Chemistry and Physics*, 21(4), 2745–2764. <https://doi.org/10.5194/acp-21-2745-2021>
- Brewer, A. W. (1949). Evidence for a world circulation provided by the measurements of helium and water vapour distribution in the stratosphere. *Quarterly Journal of the Royal Meteorological Society*, 75(326), 351–363. <https://doi.org/https://doi.org/10.1002/qj.49707532603>
- Brock, C. A., Hamill, P., Wilson, J. C., Jonsson, H. H., & Chan, K. R. (1995). Particle Formation in the Upper Tropical Troposphere: A Source of Nuclei for the Stratospheric Aerosol. *Science*, 270(5242), 1650 LP – 1653. <https://doi.org/10.1126/science.270.5242.1650>
- Browell, E. V., Butler, C. F., Ismail, S., Robinette, P. A., Carter, A. F., Higdon, N. S., Toon, O. B., Schoeberl, M. R., & Tuck, A. F. (1990). Airborne lidar observations in the wintertime Arctic stratosphere: Polar stratospheric clouds. *Geophysical Research Letters*, 17(4), 385–388. <https://doi.org/https://doi.org/10.1029/GL017i004p00385>
- Butz, A., Bösch, H., Camy-Peyret, C., Chipperfield, M. P., Dorf, M., Kreygy, S., Kritten, L., Prados-Román, C., Schwärzle, J., & Pfeilsticker, K. (2009). Constraints on inorganic gaseous iodine in the tropical upper troposphere and stratosphere inferred from balloon-borne solar occultation observations. *Atmospheric Chemistry and Physics*, 9(18), 7229–7242. <https://doi.org/10.5194/acp-9-7229-2009>
- Cairo, F., Pommereau, J. P., Law, K. S., Schlager, H., Garnier, A., Fierli, F., Ern, M., Streibel, M., Arabas, S., Borrmann, S., Berthelot, J. J., Blom, C., Christensen, T., D'Amato, F., Di Donfrancesco, G., Deshler, T., Diedhiou, A., Durr, G., Engelsen, O., ... Yushkov, V. (2010). An introduction to the SCOUT-AMMA stratospheric aircraft, balloons and sondes campaign in West Africa, August 2006: Rationale and roadmap. *Atmospheric Chemistry and Physics*, 10(5). <https://doi.org/10.5194/acp-10-2237-2010>
- Campbell, P., Mills, M., & Deshler, T. (2014). The global extent of the mid stratospheric CN layer: A three-dimensional modeling study. *Journal of Geophysical Research: Atmospheres*,

119(2), 1015–1030. <https://doi.org/https://doi.org/10.1002/2013JD020503>

- Carn, S. A., Clarisse, L., & Prata, A. J. (2016). Multi-decadal satellite measurements of global volcanic degassing. *Journal of Volcanology and Geothermal Research*, 311, 99–134. <https://doi.org/https://doi.org/10.1016/j.jvolgeores.2016.01.002>
- Carn, S. A., Krotkov, N. A., Fisher, B. L., & Li, C. (2022). Out of the blue: Volcanic SO₂ emissions during the 2021–2022 eruptions of Hunga Tonga—Hunga Ha’apai (Tonga). *Frontiers in Earth Science*, 10. <https://doi.org/10.3389/feart.2022.976962>
- Carslaw, K S, Luo, B. P., Clegg, S. L., Peter, T., Brimblecombe, P., & Crutzen, P. J. (1994). Stratospheric aerosol growth and HNO₃ gas phase depletion from coupled HNO₃ and water uptake by liquid particles. *Geophysical Research Letters*, 21(23), 2479–2482. <https://doi.org/https://doi.org/10.1029/94GL02799>
- Carslaw, Kenneth S, Peter, T., & Clegg, S. L. (1997). Modeling the composition of liquid stratospheric aerosols. *Reviews of Geophysics*, 35(2), 125–154. <https://doi.org/https://doi.org/10.1029/97RG00078>
- Chameides, W. L., & Stelson, A. W. (1992). Aqueous-phase chemical processes in deliquescent sea-salt aerosols: A mechanism that couples the atmospheric cycles of S and sea salt. *Journal of Geophysical Research: Atmospheres*, 97(D18), 20565–20580. <https://doi.org/https://doi.org/10.1029/92JD01923>
- Charlson, R. J., Schwartz, S. E., Hales, J. M., Cess, R. D., Coakley, J. A. J., Hansen, J. E., & Hofmann, D. J. (1992). Climate forcing by anthropogenic aerosols. *Science (New York, N.Y.)*, 255(5043), 423–430. <https://doi.org/10.1126/science.255.5043.423>
- Chin, M., & Davis, D. D. (1993). Global sources and sinks of OCS and CS₂ and their distributions. *Global Biogeochemical Cycles*, 7(2), 321–337. <https://doi.org/https://doi.org/10.1029/93GB00568>
- Corti, T., Luo, B. P., de Reus, M., Brunner, D., Cairo, F., Mahoney, M. J., Martucci, G., Matthey, R., Mitev, V., dos Santos, F. H., Schiller, C., Shur, G., Sitnikov, N. M., Spelten, N., Vössing, H. J., Borrmann, S., & Peter, T. (2008). Unprecedented evidence for deep convection hydrating the tropical stratosphere. *Geophysical Research Letters*, 35(10). <https://doi.org/https://doi.org/10.1029/2008GL033641>
- Corti, T., Luo, B. P., Fu, Q., Vömel, H., & Peter, T. (2006). The impact of cirrus clouds on tropical troposphere-to-stratosphere transport. *Atmospheric Chemistry and Physics*, 6(9), 2539–2547. <https://doi.org/10.5194/acp-6-2539-2006>
- Crutzen, P. J. (1976). The possible importance of CSO for the sulfate layer of the stratosphere. *Geophysical Research Letters*, 3(2), 73–76. <https://doi.org/https://doi.org/10.1029/GL003i002p00073>
- Curtius, J., Weigel, R., Vössing, H.-J., Wernli, H., Werner, A., Volk, C.-M., Konopka, P., Krebsbach, M., Schiller, C., Roiger, A., Schlager, H., Dreiling, V., & Borrmann, S. (2005). Observations of meteoric material and implications for aerosol nucleation in the winter Arctic lower

- stratosphere derived from in situ particle measurements. *Atmospheric Chemistry and Physics*, 5(11), 3053–3069. <https://doi.org/10.5194/acp-5-3053-2005>
- Danielsen, E. F. (1982). A dehydration mechanism for the stratosphere. *Geophysical Research Letters*, 9(6), 605–608. <https://doi.org/https://doi.org/10.1029/GL009i006p00605>
- Danielsen, E. F. (1993). In situ evidence of rapid, vertical, irreversible transport of lower tropospheric air into the lower tropical stratosphere by convective cloud turrets and by larger-scale upwelling in tropical cyclones. *Journal of Geophysical Research: Atmospheres*, 98(D5), 8665–8681. <https://doi.org/https://doi.org/10.1029/92JD02954>
- de Laat, A. T. J., Stein Zweers, D. C., Boers, R., & Tuinder, O. N. E. (2012). A solar escalator: Observational evidence of the self-lifting of smoke and aerosols by absorption of solar radiation in the February 2009 Australian Black Saturday plume. *Journal of Geophysical Research: Atmospheres*, 117(D4). <https://doi.org/https://doi.org/10.1029/2011JD017016>
- Delpoux-Ouldriane, S., Gineys, M., Cohaut, N., & Béguin, F. (2015). The role played by local pH and pore size distribution in the electrochemical regeneration of carbon fabrics loaded with bentazon. *Carbon*, 94, 816–825. <https://doi.org/https://doi.org/10.1016/j.carbon.2015.07.010>
- DeMott, P. J., Prenni, A. J., Liu, X., Kreidenweis, S. M., Petters, M. D., Twohy, C. H., Richardson, M. S., Eidhammer, T., & Rogers, D. C. (2010). Predicting global atmospheric ice nuclei distributions and their impacts on climate. *Proceedings of the National Academy of Sciences*, 107(25), 11217–11222. <https://doi.org/10.1073/pnas.0910818107>
- DeMott, Paul J., Hill, T. C. J., McCluskey, C. S., Prather, K. A., Collins, D. B., Sullivan, R. C., Ruppel, M. J., Mason, R. H., Irish, V. E., Lee, T., Hwang, C. Y., Rhee, T. S., Snider, J. R., McMeeking, G. R., Dhaniyala, S., Lewis, E. R., Wentzell, J. J. B., Abbatt, J., Lee, C., ... Franc, G. D. (2016). Sea spray aerosol as a unique source of ice nucleating particles. *Proceedings of the National Academy of Sciences*, 113(21), 5797–5803. <https://doi.org/10.1073/pnas.1514034112>
- Deshler, T. (2008). A review of global stratospheric aerosol: Measurements, importance, life cycle, and local stratospheric aerosol. *Atmospheric Research*, 90(2), 223–232. <https://doi.org/https://doi.org/10.1016/j.atmosres.2008.03.016>
- Dinh, T., & Fueglistaler, S. (2014). Microphysical, radiative, and dynamical impacts of thin cirrus clouds on humidity in the tropical tropopause layer and lower stratosphere. *Geophysical Research Letters*, 41(19), 6949–6955. <https://doi.org/https://doi.org/10.1002/2014GL061289>
- Douville, H., Raghavan, K., Renwick, J., Allan, R. P., Arias, P. A., Barlow, M., Cerezo-Mota, R., Cherchi, A., Gan, T. Y., Gergis, J., Jiang, D., Khan, A., Pokam Mba, W., Rosenfeld, D., Tierney, J., & Zolina, O. (2021). Water Cycle Changes Supplementary Material. In V. Masson-Delmotte, P. Zhai, A. Pirani, S. L. Connors, C. Péan, S. Berger, N. Caud, Y. Chen, L. Goldfarb, M. I. Gomis, M. Huang, K. Leitzell, E. Lonnoy, J. B. R. Matthews, T. K. Maycock, T. Waterfield, O. Yelekçi, R. Yu, & B. Zhou (Eds.), *Climate Change 2021: The Physical Science*

Basis. Contribution of Working Group I to the Sixth Assessment Report of the Intergovernmental Panel on Climate Change. Available

- Duncan Fairlie, T., Jacob, D. J., & Park, R. J. (2007). The impact of transpacific transport of mineral dust in the United States. *Atmospheric Environment*, *41*(6), 1251–1266. <https://doi.org/https://doi.org/10.1016/j.atmosenv.2006.09.048>
- Eastham, S. D., Long, M. S., Keller, C. A., Lundgren, E., Yantosca, R. M., Zhuang, J., Li, C., Lee, C. J., Yannetti, M., Auer, B. M., Clune, T. L., Kouatchou, J., Putman, W. M., Thompson, M. A., Trayanov, A. L., Molod, A. M., Martin, R. V., & Jacob, D. J. (2018). GEOS-Chem High Performance (GCHP v11-02c): a next-generation implementation of the GEOS-Chem chemical transport model for massively parallel applications. *Geosci. Model Dev.*, *11*(7), 2941–2953. <https://doi.org/10.5194/gmd-11-2941-2018>
- Fadnavis, S., Semeniuk, K., Pozzoli, L., Schultz, M. G., Ghude, S. D., Das, S., & Kakatkar, R. (2013). Transport of aerosols into the UTLS and their impact on the Asian monsoon region as seen in a global model simulation. *Atmospheric Chemistry and Physics*, *13*(17), 8771–8786. <https://doi.org/10.5194/acp-13-8771-2013>
- Fairlie, T.D., Vernier, J.-P., Natarajan, M., & Bedka, K. M. (2014). Dispersion of the Nabro volcanic plume and its relation to the Asian summer monsoon. *Atmospheric Chemistry and Physics*, *14*(13). <https://doi.org/10.5194/acp-14-7045-2014>
- Fairlie, T Duncan, Liu, H., Vernier, J.-P., Campuzano-Jost, P., Jimenez, J. L., Jo, D. S., Zhang, B., Natarajan, M., Avery, M. A., & Huey, G. (2020). Estimates of Regional Source Contributions to the Asian Tropopause Aerosol Layer Using a Chemical Transport Model. *Journal of Geophysical Research: Atmospheres*, *125*(4), e2019JD031506. <https://doi.org/10.1029/2019JD031506>
- Farlow, N. H., & Lem, H. Y. (1973). X ray analysis of balloon-collected particles erroneously considered as an October influx into the lower stratosphere. *Journal of Geophysical Research (1896-1977)*, *78*(33), 7923–7927. <https://doi.org/https://doi.org/10.1029/JC078i033p07923>
- Finlayson-Pitts, B. J., & Hemminger, J. C. (2000). Physical Chemistry of Airborne Sea Salt Particles and Their Components. *The Journal of Physical Chemistry A*, *104*(49), 11463–11477. <https://doi.org/10.1021/jp002968n>
- Fisher, B. L., Krotkov, N. A., Bhartia, P. K., Li, C., Carn, S. A., Hughes, E., & Leonard, P. J. T. (2019). A new discrete wavelength backscattered ultraviolet algorithm for consistent volcanic SO_2 retrievals from multiple satellite missions. *Atmospheric Measurement Techniques*, *12*(9), 5137–5153. <https://doi.org/10.5194/amt-12-5137-2019>
- Folkens, I., Bernath, P., Boone, C., Donner, L. J., Eldering, A., Lesins, G., Martin, R. V., Sinnhuber, B.-M., & Walker, K. (2006). Testing convective parameterizations with tropical measurements of HNO₃, CO, H₂O, and O₃: Implications for the water vapor budget. *Journal of Geophysical Research: Atmospheres*, *111*(D23). <https://doi.org/https://doi.org/10.1029/2006JD007325>

- Fountoukis, C., & Nenes, A. (2007). ISORROPIA II: a computationally efficient thermodynamic equilibrium model for K^+ – Ca^{2+} – Mg^{2+} – NH_4^+ – Na^+ – SO_4^{2-} – NO_3^- – Cl^- – H_2SO_4 aerosols. *Atmospheric Chemistry and Physics*, 7(17), 4639–4659. <https://doi.org/10.5194/acp-7-4639-2007>
- Fromm, M., Lindsey, D. T., Servranckx, R., Yue, G., Trickl, T., Sica, R., Doucet, P., & Godin-Beekmann, S. (n.d.). The Untold Story of Pyrocumulonimbus. *Bulletin of the American Meteorological Society*, 91(9), 1193–1210. <https://doi.org/10.1175/2010BAMS3004.1>
- Fromm, M., Servranckx, R., Stocks, B. J., & Peterson, D. A. (2022). Understanding the critical elements of the pyrocumulonimbus storm sparked by high-intensity wildland fire. *Communications Earth & Environment*, 3(1), 243. <https://doi.org/10.1038/s43247-022-00566-8>
- Fromm, M., Tupper, A., Rosenfeld, D., Servranckx, R., & McRae, R. (2006). Violent pyroconvective storm devastates Australia's capital and pollutes the stratosphere. *Geophysical Research Letters*, 33(5). <https://doi.org/10.1029/2005GL025161>
- Fueglistaler, S., Dessler, A. E., Dunkerton, T. J., Folkins, I., Fu, Q., & Mote, P. W. (2009). Tropical tropopause layer. *Reviews of Geophysics*, 47(1). <https://doi.org/10.1029/2008RG000267>
- Garny, H., & Randel, W. J. (2016). Transport pathways from the Asian monsoon anticyclone to the stratosphere. *Atmos. Chem. Phys.*, 16(4), 2703–2718. <https://doi.org/10.5194/acp-16-2703-2016>
- Gelaro, R., McCarty, W., Suárez, M. J., Todling, R., Molod, A., Takacs, L., Randles, C. A., Darmenov, A., Bosilovich, M. G., Reichle, R., Wargan, K., Coy, L., Cullather, R., Draper, C., Akella, S., Buchard, V., Conaty, A., da Silva, A. M., Gu, W., ... Zhao, B. (2017). The Modern-Era Retrospective Analysis for Research and Applications, Version 2 (MERRA-2). *Journal of Climate*, 30(14), 5419–5454. <https://doi.org/10.1175/JCLI-D-16-0758.1>
- Gettelman, A., Forster, P. M. de F., Fujiwara, M., Fu, Q., Vömel, H., Gohar, L. K., Johanson, C., & Ammerman, M. (2004). Radiation balance of the tropical tropopause layer. *Journal of Geophysical Research: Atmospheres*, 109(D7). <https://doi.org/10.1029/2003JD004190>
- Giuffrida, M., Viccaro, M., & Ottolini, L. (2018). Ultrafast syn-eruptive degassing and ascent trigger high-energy basic eruptions. *Scientific Reports*, 8(1), 147. <https://doi.org/10.1038/s41598-017-18580-8>
- Goode, J. G., Yokelson, R. J., Ward, D. E., Susott, R. A., Babbitt, R. E., Davies, M. A., & Hao, W. M. (2000). Measurements of excess O₃, CO₂, CO, CH₄, C₂H₄, C₂H₂, HCN, NO, NH₃, HCOOH, CH₃COOH, HCHO, and CH₃OH in 1997 Alaskan biomass burning plumes by airborne Fourier transform infrared spectroscopy (AFTIR). *Journal of Geophysical Research: Atmospheres*, 105(D17), 22147–22166.

<https://doi.org/https://doi.org/10.1029/2000JD900287>

- Gu, Y., Liao, H., & Bian, J. (2016). Summertime nitrate aerosol in the upper troposphere and lower stratosphere over the Tibetan Plateau and the South Asian summer monsoon region. *Atmos. Chem. Phys.*, *16*(11), 6641–6663. <https://doi.org/10.5194/acp-16-6641-2016>
- Gutiérrez, J. M., Jones, R. G., Narisma, G. T., Alves, L. M., Amjad, M., Gorodetskaya, I. V., Grose, M., Klutse, N. A. B., Krakovska, S., Li, J., Martínez-Castro, D., Mearns, L. O., Mernild, S. H., Ngo-Duc, T., van den Hurk, B., & Yoon, J.-H. (2021). Atlas. In V. Masson-Delmotte, P. Zhai, A. Pirani, S. L. Connors, C. Péan, S. Berger, N. Caud, Y. Chen, L. Goldfarb, M. I. Gomis, M. Huang, K. Leitzell, E. Lonnoy, J. B. R. Matthews, T. K. Maycock, T. Waterfield, O. Yelekçi, R. Yu, & B. Zhou (Eds.), *Climate Change 2021: The Physical Science Basis. Contribution of Working Group I to the Sixth Assessment Report of the Intergovernmental Panel on Climate Change*. Available
- Hamill, P., Jensen, E. J., Russell, P. B., & Bauman, J. J. (1997). The Life Cycle of Stratospheric Aerosol Particles. *Bulletin of the American Meteorological Society*, *78*(7), 1395–1410. [https://doi.org/10.1175/1520-0477\(1997\)078<1395:TLCOSA>2.0.CO;2](https://doi.org/10.1175/1520-0477(1997)078<1395:TLCOSA>2.0.CO;2)
- Hecht, E. S., Scigelova, M., Eliuk, S., & Makarov, A. (2019). Fundamentals and Advances of Orbitrap Mass Spectrometry. In *Encyclopedia of Analytical Chemistry* (pp. 1–40). John Wiley & Sons, Ltd. <https://doi.org/https://doi.org/10.1002/9780470027318.a9309.pub2>
- Heckendorn, P., Weisenstein, D., Fueglistaler, S., Luo, B. P., Rozanov, E., Schraner, M., Thomason, L. W., & Peter, T. (2009). The impact of geoengineering aerosols on stratospheric temperature and ozone. *Environmental Research Letters*, *4*(4), 45108. <https://doi.org/10.1088/1748-9326/4/4/045108>
- Hill, K. A., Shepson, P. B., Galbavy, E. S., Anastasio, C., Kourtev, P. S., Konopka, A., & Stirm, B. H. (2007). Processing of atmospheric nitrogen by clouds above a forest environment. *Journal of Geophysical Research: Atmospheres*, *112*(D11). <https://doi.org/https://doi.org/10.1029/2006JD008002>
- Hofmann, D. J., Rosen, J. M., Pepin, T. J., & Pinnick, R. G. (1975). Stratospheric Aerosol Measurements I: Time Variations at Northern Midlatitudes. *Journal of Atmospheric Sciences*, *32*(7), 1446–1456. [https://doi.org/https://doi.org/10.1175/1520-0469\(1975\)032<1446:SAMITV>2.0.CO;2](https://doi.org/https://doi.org/10.1175/1520-0469(1975)032<1446:SAMITV>2.0.CO;2)
- Holton, J. R., Haynes, P. H., McIntyre, M. E., Douglass, A. R., Rood, R. B., & Pfister, L. (1995). Stratosphere-troposphere exchange. *Reviews of Geophysics*, *33*(4), 403–439. <https://doi.org/https://doi.org/10.1029/95RG02097>
- Höpfner, M., Ungermann, J., Borrmann, S., Wagner, R., Spang, R., Riese, M., Stiller, G., Appel, O., Batenburg, A. M., Bucci, S., Cairo, F., Dragoneas, A., Friedl-Vallon, F., Hünig, A., Johansson, S., Krasauskas, L., Legras, B., Leisner, T., Mahnke, C., ... Wohltmann, I. (2019). Ammonium nitrate particles formed in upper troposphere from ground ammonia sources during Asian monsoons. *Nature Geoscience*, *12*(8), 608–612.

<https://doi.org/10.1038/s41561-019-0385-8>

- Ianniello, A., Spataro, F., Esposito, G., Allegrini, I., Hu, M., & Zhu, T. (2011). Chemical characteristics of inorganic ammonium salts in PM_{2.5} in the atmosphere of Beijing (China). *Atmospheric Chemistry and Physics*, *11*(21), 10803–10822. <https://doi.org/10.5194/acp-11-10803-2011>
- Irion, F. W., Gunson, M. R., Toon, G. C., Chang, A. Y., Eldering, A., Mahieu, E., Manney, G. L., Michelsen, H. A., Moyer, E. J., Newchurch, M. J., Osterman, G. B., Rinsland, C. P., Salawitch, R. J., Sen, B., Yung, Y. L., & Zander, R. (2002). Atmospheric Trace Molecule Spectroscopy (ATMOS) Experiment Version 3 data retrievals. *Appl. Opt.*, *41*(33), 6968–6979. <https://doi.org/10.1364/AO.41.006968>
- Jaeglé, L., Quinn, P. K., Bates, T. S., Alexander, B., & Lin, J.-T. (2011). Global distribution of sea salt aerosols: new constraints from in situ and remote sensing observations. *Atmos. Chem. Phys.*, *11*(7), 3137–3157. <https://doi.org/10.5194/acp-11-3137-2011>
- Jones, A. C., Hill, A., Remy, S., Abraham, N. L., Dalvi, M., Hardacre, C., Hewitt, A. J., Johnson, B., Mulcahy, J. P., & Turnock, S. T. (2021). Exploring the sensitivity of atmospheric nitrate concentrations to nitric acid uptake rate using the Met Office's Unified Model. *Atmospheric Chemistry and Physics*, *21*(20), 15901–15927. <https://doi.org/10.5194/acp-21-15901-2021>
- Junge, C. E., & Manson, J. E. (1961). Stratospheric aerosol studies. *Journal of Geophysical Research (1896-1977)*, *66*(7), 2163–2182. <https://doi.org/https://doi.org/10.1029/JZ066i007p02163>
- Kablick III, G. P., Allen, D. R., Fromm, M. D., & Nedoluha, G. E. (2020). Australian PyroCb Smoke Generates Synoptic-Scale Stratospheric Anticyclones. *Geophysical Research Letters*, *47*(13), e2020GL088101. <https://doi.org/10.1029/2020GL088101>
- Kar, J., Bremer, H., Drummond, J. R., Rochon, Y. J., Jones, D. B. A., Nichitiu, F., Zou, J., Liu, J., Gille, J. C., Edwards, D. P., Deeter, M. N., Francis, G., Ziskin, D., & Warner, J. (2004). Evidence of vertical transport of carbon monoxide from Measurements of Pollution in the Troposphere (MOPITT). *Geophysical Research Letters*, *31*(23). <https://doi.org/10.1029/2004GL021128>
- Kärcher, B., Kleine, J., Sauer, D., & Voigt, C. (2018). Contrail Formation: Analysis of Sublimation Mechanisms. *Geophysical Research Letters*, *45*(24), 13,513-547,552. <https://doi.org/https://doi.org/10.1029/2018GL079391>
- Kawamura, K., & Sakaguchi, F. (1999). Molecular distributions of water soluble dicarboxylic acids in marine aerosols over the Pacific Ocean including tropics. *Journal of Geophysical Research: Atmospheres*, *104*(D3), 3501–3509. <https://doi.org/https://doi.org/10.1029/1998JD100041>
- Khaykin, S. M., Godin-Beekmann, S., Hauchecorne, A., Pelon, J., Ravetta, F., & Keckhut, P. (2018). Stratospheric Smoke With Unprecedentedly High Backscatter Observed by Lidars

Above Southern France. *Geophysical Research Letters*, 45(3), 1639–1646.
<https://doi.org/10.1002/2017GL076763>

- Khaykin, S., Pommereau, J.-P., Korshunov, L., Yushkov, V., Nielsen, J., Larsen, N., Christensen, T., Garnier, A., Lukyanov, A., & Williams, E. (2009). Hydration of the lower stratosphere by ice crystal geysers over land convective systems. *Atmospheric Chemistry and Physics*, 9(6), 2275–2287. <https://doi.org/10.5194/acp-9-2275-2009>
- Khaykin, Sergey, Legras, B., Bucci, S., Sellitto, P., Isaksen, L., Tencé, F., Bekki, S., Bourassa, A., Rieger, L., Zawada, D., Jumelet, J., & Godin-Beekmann, S. (2020). The 2019/20 Australian wildfires generated a persistent smoke-charged vortex rising up to 35 km altitude. *Communications Earth & Environment*, 1(1), 22. <https://doi.org/10.1038/s43247-020-00022-5>
- Khaykin, Sergey, Podglajen, A., Ploeger, F., Grooß, J.-U., Tence, F., Bekki, S., Khlopenkov, K., Bedka, K., Rieger, L., Baron, A., Godin-Beekmann, S., Legras, B., Sellitto, P., Sakai, T., Barnes, J., Uchino, O., Morino, I., Nagai, T., Wing, R., ... Ravetta, F. (2022). Global perturbation of stratospheric water and aerosol burden by Hunga eruption. *Communications Earth & Environment*, 3(1), 316. <https://doi.org/10.1038/s43247-022-00652-x>
- Kloss, C., Berthet, G., Sellitto, P., Ploeger, F., Bucci, S., Khaykin, S., Jégou, F., Taha, G., Thomason, L. W., Barret, B., Le Flochmoen, E., von Hobe, M., Bossolasco, A., Bègue, N., & Legras, B. (2019). Transport of the 2017 Canadian wildfire plume to the tropics via the Asian monsoon circulation. *Atmos. Chem. Phys.*, 19(21), 13547–13567.
<https://doi.org/10.5194/acp-19-13547-2019>
- Kloss, C., Berthet, G., Sellitto, P., Ploeger, F., Taha, G., Tidiga, M., Eremenko, M., Bossolasco, A., Jégou, F., Renard, J.-B., & Legras, B. (2021). Stratospheric aerosol layer perturbation caused by the 2019 Raikoke and Ulawun eruptions and their radiative forcing. *Atmospheric Chemistry and Physics*, 21(1), 535–560. <https://doi.org/10.5194/acp-21-535-2021>
- Kloss, Corinna, Sellitto, P., Renard, J.-B., Baron, A., Bègue, N., Legras, B., Berthet, G., Briaud, E., Carboni, E., Duchamp, C., DufLOT, V., Jacquet, P., Marquestaut, N., Metzger, J.-M., Payen, G., Ranaivombola, M., Roberts, T., Siddans, R., & Jégou, F. (2022). Aerosol Characterization of the Stratospheric Plume From the Volcanic Eruption at Hunga Tonga 15 January 2022. *Geophysical Research Letters*, 49(16), e2022GL099394.
<https://doi.org/https://doi.org/10.1029/2022GL099394>
- Kovilakam, M., Thomason, L., & Knepp, T. (2023). SAGE III/ISS aerosol/cloud categorization and its impact on GloSSAC. *Atmospheric Measurement Techniques*, 16(10), 2709–2731.
<https://doi.org/10.5194/amt-16-2709-2023>
- Kovilakam, M., Thomason, L. W., Ernest, N., Rieger, L., Bourassa, A., & Millán, L. (2020). The Global Space-based Stratospheric Aerosol Climatology (version 2.0): 1979--2018. *Earth System Science Data*, 12(4), 2607–2634. <https://doi.org/10.5194/essd-12-2607-2020>
- Kremser, S., Thomason, L. W., von Hobe, M., Hermann, M., Deshler, T., Timmreck, C., Toohey,

- M., Stenke, A., Schwarz, J. P., Weigel, R., Fueglistaler, S., Prata, F. J., Vernier, J.-P., Schlager, H., Barnes, J. E., Antuña-Marrero, J.-C., Fairlie, D., Palm, M., Mahieu, E., ... Meland, B. (2016). Stratospheric aerosol—Observations, processes, and impact on climate. *Reviews of Geophysics*, *54*(2). <https://doi.org/10.1002/2015RG000511>
- L'Ecuyer, T. S., Beaudoin, H. K., Rodell, M., Olson, W., Lin, B., Kato, S., Clayson, C. A., Wood, E., Sheffield, J., Adler, R., Huffman, G., Bosilovich, M., Gu, G., Robertson, F., Houser, P. R., Chambers, D., Famiglietti, J. S., Fetzer, E., Liu, W. T., ... Hilburn, K. (2015). The Observed State of the Energy Budget in the Early Twenty-First Century. *Journal of Climate*, *28*(21), 8319–8346. <https://doi.org/https://doi.org/10.1175/JCLI-D-14-00556.1>
- Lau, W. K. M., Yuan, C., & Li, Z. (2018). Origin, Maintenance and Variability of the Asian Tropopause Aerosol Layer (ATAL): The Roles of Monsoon Dynamics. *Scientific Reports*, *8*(1), 3960. <https://doi.org/10.1038/s41598-018-22267-z>
- Lawrence, M. G., & Lelieveld, J. (2010). Atmospheric pollutant outflow from southern Asia: a review. *Atmos. Chem. Phys.*, *10*(22), 11017–11096. <https://doi.org/10.5194/acp-10-11017-2010>
- Lazrus, A. L., Gandrud, B., & Cadle, R. D. (1972). Nitric Acid Vapor in the Stratosphere. *Journal of Applied Meteorology and Climatology*, *11*(2), 389–392. [https://doi.org/https://doi.org/10.1175/1520-0450\(1972\)011<0389:NAVITS>2.0.CO;2](https://doi.org/https://doi.org/10.1175/1520-0450(1972)011<0389:NAVITS>2.0.CO;2)
- Leitch, W. R., Strapp, J. W., Wiebe, H. A., Anlauf, K. G., & Isaac, G. A. (1986). Chemical and microphysical studies of nonprecipitating summer cloud in Ontario, Canada. *Journal of Geophysical Research: Atmospheres*, *91*(D11), 11821–11831. <https://doi.org/https://doi.org/10.1029/JD091iD11p11821>
- Legras, B., Duchamp, C., Sellitto, P., Podglajen, A., Carboni, E., Siddans, R., Grooß, J.-U., Khaykin, S., & Ploeger, F. (2022). The evolution and dynamics of the Hunga Tonga plume in the stratosphere. *EGU sphere*, *2022*, 1–19. <https://doi.org/10.5194/egusphere-2022-517>
- Li, M., Zhang, Q., Streets, D. G., He, K. B., Cheng, Y. F., Emmons, L. K., Huo, H., Kang, S. C., Lu, Z., Shao, M., Su, H., Yu, X., & Zhang, Y. (2014). Mapping Asian anthropogenic emissions of non-methane volatile organic compounds to multiple chemical mechanisms. *Atmos. Chem. Phys.*, *14*(11), 5617–5638. <https://doi.org/10.5194/acp-14-5617-2014>
- Li, Q., Jiang, J. H., Wu, D. L., Read, W. G., Livesey, N. J., Waters, J. W., Zhang, Y., Wang, B., Filipiak, M. J., Davis, C. P., Turquety, S., Wu, S., Park, R. J., Yantosca, R. M., & Jacob, D. J. (2005). Convective outflow of South Asian pollution: A global CTM simulation compared with EOS MLS observations. *Geophysical Research Letters*, *32*(14). <https://doi.org/https://doi.org/10.1029/2005GL022762>
- Lightstone, J. M., Onasch, T. B., Imre, D., & Oatis, S. (2000). Deliquescence, Efflorescence, and Water Activity in Ammonium Nitrate and Mixed Ammonium Nitrate/Succinic Acid Microparticles. *The Journal of Physical Chemistry A*, *104*(41), 9337–9346. <https://doi.org/10.1021/jp002137h>

- Lutgens, F. K., & Tarbuck, E. J. (1998). The atmosphere : an introduction to meteorology. In *TA - TT* - (7th ed). Prentice Hall Upper Saddle River, N.J. <https://doi.org/LK> - <https://worldcat.org/title/36877312>
- Ma, J., Brühl, C., He, Q., Steil, B., Karydis, V. A., Klingmüller, K., Tost, H., Chen, B., Jin, Y., Liu, N., Xu, X., Yan, P., Zhou, X., Abdelrahman, K., Pozzer, A., & Lelieveld, J. (2019). Modeling the aerosol chemical composition of the tropopause over the Tibetan Plateau during the Asian summer monsoon. *Atmospheric Chemistry and Physics*, *19*(17), 11587–11612. <https://doi.org/10.5194/acp-19-11587-2019>
- Man, W., Zhou, T., & Jungclaus, J. H. (2014). Effects of Large Volcanic Eruptions on Global Summer Climate and East Asian Monsoon Changes during the Last Millennium: Analysis of MPI-ESM Simulations. *Journal of Climate*, *27*(19), 7394–7409. <https://doi.org/https://doi.org/10.1175/JCLI-D-13-00739.1>
- Marshall, L. R., Maters, E. C., Schmidt, A., Timmreck, C., Robock, A., & Toohey, M. (2022). Volcanic effects on climate: recent advances and future avenues. *Bulletin of Volcanology*, *84*(5), 54. <https://doi.org/10.1007/s00445-022-01559-3>
- Martin, R. V, Sauvage, B., Folkins, I., Sioris, C. E., Boone, C., Bernath, P., & Ziemke, J. (2007). Space-based constraints on the production of nitric oxide by lightning. *Journal of Geophysical Research: Atmospheres*, *112*(D9). <https://doi.org/https://doi.org/10.1029/2006JD007831>
- McCormick, M. P., Thomason, L. W., & Trepte, C. R. (1995). Atmospheric effects of the Mt Pinatubo eruption. *Nature*, *373*(6513), 399–404. <https://doi.org/10.1038/373399a0>
- Mehta, S. K., Fujiwara, M., Tsuda, T., & Vernier, J.-P. (2015). Effect of recent minor volcanic eruptions on temperatures in the upper troposphere and lower stratosphere. *Journal of Atmospheric and Solar-Terrestrial Physics*, *129*. <https://doi.org/10.1016/j.jastp.2015.04.009>
- Mercado, L. M., Bellouin, N., Sitch, S., Boucher, O., Huntingford, C., Wild, M., & Cox, P. M. (2009). Impact of changes in diffuse radiation on the global land carbon sink. *Nature*, *458*(7241), 1014–1017. <https://doi.org/10.1038/nature07949>
- Millán, L., Santee, M. L., Lambert, A., Livesey, N. J., Werner, F., Schwartz, M. J., Pumphrey, H. C., Manney, G. L., Wang, Y., Su, H., Wu, L., Read, W. G., & Froidevaux, L. (2022). The Hunga Tonga-Hunga Ha'apai Hydration of the Stratosphere. *Geophysical Research Letters*, *49*(13), e2022GL099381. <https://doi.org/https://doi.org/10.1029/2022GL099381>
- MOSSOP, S. C. (1963). Stratospheric Particles At 20 Km. *Nature*, *199*(4891), 325–326. <https://doi.org/10.1038/199325a0>
- Mroz, E. J., Lazrus, A. L., & Bonelli, J. E. (1977). Direct measurements of stratospheric fluoride. *Geophysical Research Letters*, *4*(4), 149–150. <https://doi.org/https://doi.org/10.1029/GL004i004p00149>
- Murphy, D. M., Cziczo, D. J., Hudson, P. K., & Thomson, D. S. (2007). Carbonaceous material in

- aerosol particles in the lower stratosphere and tropopause region. *Journal of Geophysical Research: Atmospheres*, 112(D4). <https://doi.org/10.1029/2006JD007297>
- Murphy, D. M., Froyd, K. D., Schwarz, J. P., & Wilson, J. C. (2014). Observations of the chemical composition of stratospheric aerosol particles. *Quarterly Journal of the Royal Meteorological Society*, 140(681), 1269–1278. <https://doi.org/https://doi.org/10.1002/qj.2213>
- Murphy, D. M., & Thomson, D. S. (2000). Halogen ions and NO₂ in the mass spectra of aerosols in the upper troposphere and lower stratosphere. *Geophysical Research Letters*, 27(19), 3217–3220. <https://doi.org/https://doi.org/10.1029/1999GL011267>
- Murray, L. T., Jacob, D. J., Logan, J. A., Hudman, R. C., & Koshak, W. J. (2012). Optimized regional and interannual variability of lightning in a global chemical transport model constrained by LIS/OTD satellite data. *Journal of Geophysical Research: Atmospheres*, 117(D20). <https://doi.org/https://doi.org/10.1029/2012JD017934>
- Nault, B. A., Laughner, J. L., Wooldridge, P. J., Crouse, J. D., Dibb, J., Diskin, G., Peischl, J., Podolske, J. R., Pollack, I. B., Ryerson, T. B., Scheuer, E., Wennberg, P. O., & Cohen, R. C. (2017). Lightning NO_x Emissions: Reconciling Measured and Modeled Estimates With Updated NO_x Chemistry. *Geophysical Research Letters*, 44(18), 9479–9488. <https://doi.org/https://doi.org/10.1002/2017GL074436>
- Nielsen, J. K., Larsen, N., Cairo, F., Di Donfrancesco, G., Rosen, J. M., Durr, G., Held, G., & Pommerehne, J. P. (2007). Solid particles in the tropical lowest stratosphere. *Atmospheric Chemistry and Physics*, 7(3), 685–695. <https://doi.org/10.5194/acp-7-685-2007>
- Notholt, J., Luo, B., Fueglistaler, S., Weisenstein, D., Rex, M., Lawrence, M., Bingemer, H., Wohltmann, I., Corti, T., Warneke, T., von Kuhlmann, R., & Peter, T. (2005). Influence of tropospheric SO₂ emissions on particle formation and the stratospheric humidity. *Geophysical Research Letters*, 32, L07810. <https://doi.org/10.1029/2004GL022159>
- On the role of iodine in ozone depletion. (1994). *Journal of Geophysical Research: Atmospheres*, 99(D10), 20491–20499. <https://doi.org/https://doi.org/10.1029/94JD02028>
- Pan, L. L., Honomichl, S. B., Kinnison, D. E., Abalos, M., Randel, W. J., Bergman, J. W., & Bian, J. (2016). Transport of chemical tracers from the boundary layer to stratosphere associated with the dynamics of the Asian summer monsoon. *Journal of Geophysical Research: Atmospheres*, 121(23), 14,114–159,174. <https://doi.org/https://doi.org/10.1002/2016JD025616>
- Park, M., Randel, W. J., Gettelman, A., Massie, S. T., & Jiang, J. H. (2007). Transport above the Asian summer monsoon anticyclone inferred from Aura Microwave Limb Sounder tracers. *Journal of Geophysical Research: Atmospheres*, 112(D16). <https://doi.org/10.1029/2006JD008294>
- Park, R. J., Jacob, D. J., Chin, M., & Martin, R. V. (2003). Sources of carbonaceous aerosols over the United States and implications for natural visibility. *Journal of Geophysical Research:*

Atmospheres, 108(D12). <https://doi.org/10.1029/2002JD003190>

- Park, R. J., Jacob, D. J., Field, B. D., Yantosca, R. M., & Chin, M. (2004). Natural and transboundary pollution influences on sulfate-nitrate-ammonium aerosols in the United States: Implications for policy. *Journal of Geophysical Research: Atmospheres*, 109(D15). <https://doi.org/10.1029/2003JD004473>
- PARKER, D. E., WILSON, H., JONES, P. D., CHRISTY, J. R., & FOLLAND, C. K. (1996). THE IMPACT OF MOUNT PINATUBO ON WORLD-WIDE TEMPERATURES. *International Journal of Climatology*, 16(5), 487–497. [https://doi.org/https://doi.org/10.1002/\(SICI\)1097-0088\(199605\)16:5<487::AID-JOC39>3.0.CO;2-J](https://doi.org/https://doi.org/10.1002/(SICI)1097-0088(199605)16:5<487::AID-JOC39>3.0.CO;2-J)
- Penner, J. E., Dong, X., & Chen, Y. (2004). Observational evidence of a change in radiative forcing due to the indirect aerosol effect. *Nature*, 427(6971), 231–234. <https://doi.org/10.1038/nature02234>
- Peterson, D. A., Campbell, J. R., Hyer, E. J., Fromm, M. D., Kablick, G. P., Cossuth, J. H., & DeLand, M. T. (2018). Wildfire-driven thunderstorms cause a volcano-like stratospheric injection of smoke. *Npj Climate and Atmospheric Science*, 1(1), 30. <https://doi.org/10.1038/s41612-018-0039-3>
- Popp, P. J., Marcy, T. P., Watts, L. A., Gao, R. S., Fahey, D. W., Weinstock, E. M., Smith, J. B., Herman, R. L., Troy, R. F., Webster, C. R., Christensen, L. E., Baumgardner, D. G., Voigt, C., Kärcher, B., Wilson, J. C., Mahoney, M. J., Jensen, E. J., & Bui, T. P. (2007). Condensed-phase nitric acid in a tropical subvisible cirrus cloud. *Geophysical Research Letters*, 34(24). <https://doi.org/https://doi.org/10.1029/2007GL031832>
- Proud, S. R., Prata, A. T., & Schmauß, S. (2022). The January 2022 eruption of Hunga Tonga-Hunga Ha'apai volcano reached the mesosphere. *Science*, 378(6619), 554–557. <https://doi.org/10.1126/science.abo4076>
- Pye, H. O. T., Chan, A. W. H., Barkley, M. P., & Seinfeld, J. H. (2010). Global modeling of organic aerosol: the importance of reactive nitrogen (NO_x and NO₃). *Atmospheric Chemistry and Physics*, 10(22), 11261–11276. <https://doi.org/10.5194/acp-10-11261-2010>
- Randel, W. J., & Park, M. (2006). Deep convective influence on the Asian summer monsoon anticyclone and associated tracer variability observed with Atmospheric Infrared Sounder (AIRS). *Journal of Geophysical Research: Atmospheres*, 111(D12). <https://doi.org/https://doi.org/10.1029/2005JD006490>
- Randel, W. J., Park, M., Emmons, L., Kinnison, D., Bernath, P., Walker, K. A., Boone, C., & Pumphrey, H. (2010). Asian Monsoon Transport of Pollution to the Stratosphere. *Science*, 328(5978), 611 LP – 613. <https://doi.org/10.1126/science.1182274>
- Ravishankara, A. R., Rudich, Y., & Wuebbles, D. J. (2015). Physical Chemistry of Climate Metrics. *Chemical Reviews*, 115(10), 3682–3703. <https://doi.org/10.1021/acs.chemrev.5b00010>
- Renard, J.-B., Brogniez, C., Berthet, G., Bourgeois, Q., Gaubicher, B., Chartier, M., Balois, J.-Y., Verwaerde, C., Auriol, F., Francois, P., Daugeron, D., & Engrand, C. (2008). Vertical

distribution of the different types of aerosols in the stratosphere: Detection of solid particles and analysis of their spatial variability. *Journal of Geophysical Research: Atmospheres*, 113(D21). <https://doi.org/https://doi.org/10.1029/2008JD010150>

- Rex, M., Wohltmann, I., Ridder, T., Lehmann, R., Rosenlof, K., Wennberg, P., Weisenstein, D., Notholt, J., Krüger, K., Mohr, V., & Tegtmeier, S. (2014). A tropical West Pacific OH minimum and implications for stratospheric composition. *Atmospheric Chemistry and Physics*, 14(9), 4827–4841. <https://doi.org/10.5194/acp-14-4827-2014>
- Ricaud, P., Barret, B., Attié, J.-L., Motte, E., Le Flochmoën, E., Teysseïdre, H., Peuch, V.-H., Livesey, N., Lambert, A., & Pommereau, J.-P. (2007). Impact of land convection on troposphere-stratosphere exchange in the tropics. *Atmospheric Chemistry and Physics*, 7(21), 5639–5657. <https://doi.org/10.5194/acp-7-5639-2007>
- Ridley, D. A., Heald, C. L., & Prospero, J. M. (2014). What controls the recent changes in African mineral dust aerosol across the Atlantic? *Atmos. Chem. Phys.*, 14(11), 5735–5747. <https://doi.org/10.5194/acp-14-5735-2014>
- Robock, A. (2000). Volcanic eruptions and climate. *Reviews of Geophysics*, 38(2), 191–219. <https://doi.org/10.1029/1998RG000054>
- Rosen, J. M. (1964). The vertical distribution of dust to 30 kilometers. *Journal of Geophysical Research (1896-1977)*, 69(21), 4673–4676. <https://doi.org/https://doi.org/10.1029/JZ069i021p04673>
- Scanza, R. A., Mahowald, N., Ghan, S., Zender, C. S., Kok, J. F., Liu, X., Zhang, Y., & Albani, S. (2015). Modeling dust as component minerals in the Community Atmosphere Model: development of framework and impact on radiative forcing. *Atmospheric Chemistry and Physics*, 15(1), 537–561. <https://doi.org/10.5194/acp-15-537-2015>
- Schoeberl, M. R., Duncan, B. N., Douglass, A. R., Waters, J., Livesey, N., Read, W., & Filipiak, M. (2006). The carbon monoxide tape recorder. *Geophysical Research Letters*, 33(12). <https://doi.org/https://doi.org/10.1029/2006GL026178>
- Schwarz, J. P., Gao, R. S., Fahey, D. W., Thomson, D. S., Watts, L. A., Wilson, J. C., Reeves, J. M., Darbeheshti, M., Baumgardner, D. G., Kok, G. L., Chung, S. H., Schulz, M., Hendricks, J., Lauer, A., Kärcher, B., Slowik, J. G., Rosenlof, K. H., Thompson, T. L., Langford, A. O., ... Aikin, K. C. (2006). Single-particle measurements of midlatitude black carbon and light-scattering aerosols from the boundary layer to the lower stratosphere. *Journal of Geophysical Research: Atmospheres*, 111(D16). <https://doi.org/https://doi.org/10.1029/2006JD007076>
- Schwarz, J. P., Gao, R. S., Spackman, J. R., Watts, L. A., Thomson, D. S., Fahey, D. W., Ryerson, T. B., Peischl, J., Holloway, J. S., Trainer, M., Frost, G. J., Baynard, T., Lack, D. A., de Gouw, J. A., Warneke, C., & Del Negro, L. A. (2008). Measurement of the mixing state, mass, and optical size of individual black carbon particles in urban and biomass burning emissions. *Geophysical Research Letters*, 35(13). <https://doi.org/https://doi.org/10.1029/2008GL033968>

- Sheng, J.-X., Weisenstein, D. K., Luo, B.-P., Rozanov, E., Stenke, A., Anet, J., Bingemer, H., & Peter, T. (2015). Global atmospheric sulfur budget under volcanically quiescent conditions: Aerosol-chemistry-climate model predictions and validation. *Journal of Geophysical Research: Atmospheres*, *120*(1), 256–276. <https://doi.org/https://doi.org/10.1002/2014JD021985>
- Sheridan, P. J., Brock, C. A., & Wilson, J. C. (1994). Aerosol particles in the upper troposphere and lower stratosphere: Elemental composition and morphology of individual particles in northern midlatitudes. *Geophysical Research Letters*, *21*(23), 2587–2590. <https://doi.org/https://doi.org/10.1029/94GL01387>
- Sinnhuber, B.-M., & Folkins, I. (2006). Estimating the contribution of bromoform to stratospheric bromine and its relation to dehydration in the tropical tropopause layer. *Atmospheric Chemistry and Physics*, *6*(12), 4755–4761. <https://doi.org/10.5194/acp-6-4755-2006>
- Solomon, S., Daniel, J. S., Neely III, R. R., Vernier, J.-P., Dutton, E. G., & Thomason, L. W. (2011). The persistently variable “background” stratospheric aerosol layer and global climate change. *Science*, *333*(6044). <https://doi.org/10.1126/science.1206027>
- Solomon, S., Kinnison, D., Garcia, R. R., Bandoro, J., Mills, M., Wilka, C., Neely, R. R., Schmidt, A., Barnes, J. E., Vernier, J.-P., & Höpfner, M. (2016). Monsoon circulations and tropical heterogeneous chlorine chemistry in the stratosphere. *Geophysical Research Letters*, *43*(24). <https://doi.org/10.1002/2016GL071778>
- Solomon, Susan. (1999). Stratospheric ozone depletion: A review of concepts and history. *Reviews of Geophysics*, *37*(3), 275–316. <https://doi.org/10.1029/1999RG900008>
- Solomon, Susan, Dube, K., Stone, K., Yu, P., Kinnison, D., Toon, O. B., Strahan, S. E., Rosenlof, K. H., Portmann, R., Davis, S., Randel, W., Bernath, P., Boone, C., Bardeen, C. G., Bourassa, A., Zawada, D., & Degenstein, D. (2022). On the stratospheric chemistry of midlatitude wildfire smoke. *Proceedings of the National Academy of Sciences*, *119*(10), e2117325119. <https://doi.org/10.1073/pnas.2117325119>
- Solomon, Susan, Haskins, J., Ivy, D. J., & Min, F. (2014). Fundamental differences between Arctic and Antarctic ozone depletion. *Proceedings of the National Academy of Sciences*, *111*(17), 6220–6225. <https://doi.org/10.1073/pnas.1319307111>
- Stelson, A. W., & Seinfeld, J. H. (1982). Relative humidity and temperature dependence of the ammonium nitrate dissociation constant. *Atmospheric Environment (1967)*, *16*(5), 983–992. [https://doi.org/https://doi.org/10.1016/0004-6981\(82\)90184-6](https://doi.org/https://doi.org/10.1016/0004-6981(82)90184-6)
- Strawa, A. W., Drdla, K., Ferry, G. V., Verma, S., Poeschel, R. F., Yasuda, M., Salawitch, R. J., Gao, R. S., Howard, S. D., Bui, P. T., Loewenstein, M., Elkins, J. W., Perkins, K. K., & Cohen, R. (1999). Carbonaceous aerosol (soot) measured in the lower stratosphere during POLARIS and its role in stratospheric photochemistry. *Journal of Geophysical Research: Atmospheres*, *104*(D21), 26753–26766. <https://doi.org/https://doi.org/10.1029/1999JD900453>

- Thomason, L., & Peter, T. (Eds.). (2006). SPARC Assessment of Stratospheric Aerosol Properties (ASAP). In *SPARC Report: Vol. No. 4*. SPARC Office. <http://www.sparc-climate.org/publications/sparc-reports/>
- Thomason, L. W., Ernest, N., Millán, L., Rieger, L., Bourassa, A., Vernier, J.-P., Manney, G., Luo, B., Arfeuille, F., & Peter, T. (2018). A global space-based stratospheric aerosol climatology: 1979-2016. *Earth System Science Data*, *10*(1). <https://doi.org/10.5194/essd-10-469-2018>
- Thomason, L. W., & Vernier, J.-P. (2013). Improved SAGE II cloud/aerosol categorization and observations of the Asian tropopause aerosol layer: 1989-2005. *Atmospheric Chemistry and Physics*, *13*(9). <https://doi.org/10.5194/acp-13-4605-2013>
- Timmreck, C. (2012). Modeling the climatic effects of large explosive volcanic eruptions. *WIREs Climate Change*, *3*(6), 545–564. <https://doi.org/https://doi.org/10.1002/wcc.192>
- Toon, O. B., & Farlow, N. H. (1981). Particles Above the Tropopause: Measurements and Models of Stratospheric Aerosols, Meteoric Debris, Nacreous Clouds, and Noctilucent Clouds. *Annual Review of Earth and Planetary Sciences*, *9*(1), 19–58. <https://doi.org/10.1146/annurev.ea.09.050181.000315>
- Torres, O., Bhartia, P. K., Taha, G., Jethva, H., Das, S., Colarco, P., Krotkov, N., Omar, A., & Ahn, C. (2020). Stratospheric Injection of Massive Smoke Plume From Canadian Boreal Fires in 2017 as Seen by DSCOVR-EPIC, CALIOP, and OMPS-LP Observations. *Journal of Geophysical Research: Atmospheres*, *125*(10), e2020JD032579. <https://doi.org/https://doi.org/10.1029/2020JD032579>
- Travis, K. R., Jacob, D. J., Fisher, J. A., Kim, P. S., Marais, E. A., Zhu, L., Yu, K., Miller, C. C., Yantosca, R. M., Sulprizio, M. P., Thompson, A. M., Wennberg, P. O., Crouse, J. D., St. Clair, J. M., Cohen, R. C., Laughner, J. L., Dibb, J. E., Hall, S. R., Ullmann, K., ... Zhou, X. (2016). Why do models overestimate surface ozone in the Southeast United States? *Atmos. Chem. Phys.*, *16*(21), 13561–13577. <https://doi.org/10.5194/acp-16-13561-2016>
- Trenberth, K. E., Dai, A., van der Schrier, G., Jones, P. D., Barichivich, J., Briffa, K. R., & Sheffield, J. (2014). Global warming and changes in drought. *Nature Climate Change*, *4*(1), 17–22. <https://doi.org/10.1038/nclimate2067>
- Trenberth, K. E., Fasullo, J. T., & Kiehl, J. (2009). Earth's Global Energy Budget. *Bulletin of the American Meteorological Society*, *90*(3), 311–324. <https://doi.org/https://doi.org/10.1175/2008BAMS2634.1>
- Turco, R. P., Toon, O. B., Hamill, P., & Whitten, R. C. (1981). Effects of meteoric debris on stratospheric aerosols and gases. *Journal of Geophysical Research: Oceans*, *86*(C2), 1113–1128. <https://doi.org/https://doi.org/10.1029/JC086iC02p01113>
- Vernier, H., Rastogi, N., Liu, H., Pandit, A. K., Bedka, K., Patel, A., Ratnam, M. V., Kumar, B. S., Zhang, B., Gadhave, H., Wienhold, F., Berthet, G., & Vernier, J. P. (2022). Exploring the inorganic composition of the Asian Tropopause Aerosol Layer using medium-duration balloon flights. *Atmospheric Chemistry and Physics*, *22*(18), 12675–12694.

<https://doi.org/10.5194/acp-22-12675-2022>

- Vernier, J.-P., Fairlie, T. D., Deshler, T., Natarajan, M., Knepp, T., Foster, K., Wienhold, F. G., Bedka, K. M., Thomason, L., & Trepte, C. (2016). In situ and space-based observations of the Kelud volcanic plume: The persistence of ash in the lower stratosphere. *Journal of Geophysical Research*, *121*(18). <https://doi.org/10.1002/2016JD025344>
- Vernier, J.-P., Fairlie, T. D., Deshler, T., Venkat Ratnam, M., Gadhavi, H., Kumar, B. S., Natarajan, M., Pandit, A. K., Akhil Raj, S. T., Hemanth Kumar, A., Jayaraman, A., Singh, A. K., Rastogi, N., Sinha, P. R., Kumar, S., Tiwari, S., Wegner, T., Baker, N., Vignelles, D., ... Renard, J.-B. (2018). BATAL: The balloon measurement campaigns of the Asian tropopause aerosol layer. *Bulletin of the American Meteorological Society*, *99*(5). <https://doi.org/10.1175/BAMS-D-17-0014.1>
- Vernier, J.-P., Fairlie, T. D., Natarajan, M., Wienhold, F. G., Bian, J., Martinsson, B. G., Crumeyrolle, S., Thomason, L. W., & Bedka, K. M. (2015). Increase in upper tropospheric and lower stratospheric aerosol levels and its potential connection with Asian pollution. *Journal of Geophysical Research*, *120*(4). <https://doi.org/10.1002/2014JD022372>
- Vernier, J.-P., Thomason, L. W., & Kar, J. (2011). CALIPSO detection of an Asian tropopause aerosol layer. *Geophysical Research Letters*, *38*(7). <https://doi.org/10.1029/2010GL046614>
- Vernier, J.-P., Thomason, L. W., Pommereau, J.-P., Bourassa, A., Pelon, J., Garnier, A., Hauchecorne, A., Blanot, L., Trepte, C., Degenstein, D., & Vargas, F. (2011). Major influence of tropical volcanic eruptions on the stratospheric aerosol layer during the last decade. *Geophysical Research Letters*, *38*(12). <https://doi.org/10.1029/2011GL047563>
- Vernier, J. P., Pommereau, J. P., Garnier, A., Pelon, J., Larsen, N., Nielsen, J., Christensen, T., Cairo, F., Thomason, L. W., Leblanc, T., & McDermid, I. S. (2009). Tropical Stratospheric aerosol layer from CALIPSO Lidar observations. *Journal of Geophysical Research Atmospheres*, *114*(24). <https://doi.org/10.1029/2009JD011946>
- Vogel, B., Günther, G., Müller, R., Grooß, J.-U., Afchine, A., Bozem, H., Hoor, P., Krämer, M., Müller, S., Riese, M., Rolf, C., Spelten, N., Stiller, G. P., Ungermann, J., & Zahn, A. (2016). Long-range transport pathways of tropospheric source gases originating in Asia into the northern lower stratosphere during the Asian monsoon season 2012. *Atmospheric Chemistry and Physics*, *16*(23), 15301–15325. <https://doi.org/10.5194/acp-16-15301-2016>
- Voigt, C., Schlager, H., Roiger, A., Stenke, A., de Reus, M., Borrmann, S., Jensen, E., Schiller, C., Konopka, P., & Sitnikov, N. (2008). Detection of reactive nitrogen containing particles in the tropopause region – evidence for a tropical nitric acid trihydrate (NAT) belt. *Atmospheric Chemistry and Physics*, *8*(24), 7421–7430. <https://doi.org/10.5194/acp-8-7421-2008>
- Voigt, C., Schlager, H., Ziereis, H., Kärcher, B., Luo, B. P., Schiller, C., Krämer, M., Popp, P. J., Irie, H., & Kondo, Y. (2006). Nitric acid in cirrus clouds. *Geophysical Research Letters*, *33*(5). <https://doi.org/https://doi.org/10.1029/2005GL025159>

- Voigt, Christiane, Schreiner, J., Kohlmann, A., Zink, P., Mauersberger, K., Larsen, N., Deshler, T., Kröger, C., Rosen, J., Adriani, A., Cairo, F., Donfrancesco, G. Di, Viterbini, M., Ovarlez, J., Ovarlez, H., David, C., & Dörnbrack, A. (2000). Nitric Acid Trihydrate (NAT) in Polar Stratospheric Clouds. *Science*, *290*(5497), 1756–1758. <https://doi.org/10.1126/science.290.5497.1756>
- Vömel, H., David, D. E., & Smith, K. (2007). Accuracy of tropospheric and stratospheric water vapor measurements by the cryogenic frost point hygrometer: Instrumental details and observations. *Journal of Geophysical Research: Atmospheres*, *112*(D8). <https://doi.org/https://doi.org/10.1029/2006JD007224>
- Von Clarmann, T. (2013). Chlorine in the stratosphere. *Atmósfera*, *26*(3), 415–458. [https://doi.org/https://doi.org/10.1016/S0187-6236\(13\)71086-5](https://doi.org/https://doi.org/10.1016/S0187-6236(13)71086-5)
- von Savigny, C., & Hoffmann, C. G. (2020). Issues related to the retrieval of stratospheric-aerosol particle size information based on optical measurements. *Atmospheric Measurement Techniques*, *13*(4), 1909–1920. <https://doi.org/10.5194/amt-13-1909-2020>
- Wang, M., Kong, W., Marten, R., He, X.-C., Chen, D., Pfeifer, J., Heitto, A., Kontkanen, J., Dada, L., Kürten, A., Yli-Juuti, T., Manninen, H. E., Amanatidis, S., Amorim, A., Baalbaki, R., Baccarini, A., Bell, D. M., Bertozzi, B., Bräkling, S., ... Donahue, N. M. (2020). Rapid growth of new atmospheric particles by nitric acid and ammonia condensation. *Nature*, *581*(7807), 184–189. <https://doi.org/10.1038/s41586-020-2270-4>
- Wang, Q., Jacob, D. J., Fisher, J. A., Mao, J., Leibensperger, E. M., Carouge, C. C., Le Sager, P., Kondo, Y., Jimenez, J. L., Cubison, M. J., & Doherty, S. J. (2011). Sources of carbonaceous aerosols and deposited black carbon in the Arctic in winter-spring: implications for radiative forcing. *Atmospheric Chemistry and Physics*, *11*(23), 12453–12473. <https://doi.org/10.5194/acp-11-12453-2011>
- Wang, Q., Zhang, H., Yang, S., Chen, Q., Zhou, X., Xie, B., Wang, Y., Shi, G., & Wild, M. (2022). An assessment of land energy balance over East Asia from multiple lines of evidence and the roles of the Tibet Plateau, aerosols, and clouds. *Atmospheric Chemistry and Physics*, *22*(24), 15867–15886. <https://doi.org/10.5194/acp-22-15867-2022>
- Wang, T., Song, Y., Xu, Z., Liu, M., Xu, T., Liao, W., Yin, L., Cai, X., Kang, L., Zhang, H., & Zhu, T. (2020). Why is the Indo-Gangetic Plain the region with the largest NH_3 column in the globe during pre-monsoon and monsoon seasons? *Atmospheric Chemistry and Physics*, *20*(14), 8727–8736. <https://doi.org/10.5194/acp-20-8727-2020>
- Wang, X, Zhang, L., & Moran, M. D. (2014). Development of a new semi-empirical parameterization for below-cloud scavenging of size-resolved aerosol particles by both rain and snow. *Geoscientific Model Development*, *7*(3), 799–819. <https://doi.org/10.5194/gmd-7-799-2014>
- Wang, Xiaohong, Cheng, H., Ye, G., Fan, J., Yao, F., Wang, Y., Jiao, Y., Zhu, W., Huang, H., & Ye, D. (2022). Key factors and primary modification methods of activated carbon and their application in adsorption of carbon-based gases: A review. *Chemosphere*, *287*, 131995.

<https://doi.org/https://doi.org/10.1016/j.chemosphere.2021.131995>

- Weigel, R., Borrmann, S., Kazil, J., Minikin, A., Stohl, A., Wilson, J. C., Reeves, J. M., Kunkel, D., de Reus, M., Frey, W., Lovejoy, E. R., Volk, C. M., Viciani, S., D'Amato, F., Schiller, C., Peter, T., Schlager, H., Cairo, F., Law, K. S., ... Curtius, J. (2011). In situ observations of new particle formation in the tropical upper troposphere: the role of clouds and the nucleation mechanism. *Atmospheric Chemistry and Physics*, *11*(18), 9983–10010.
<https://doi.org/10.5194/acp-11-9983-2011>
- Wild, M., Folini, D., Schär, C., Loeb, N., Dutton, E. G., & König-Langlo, G. (2013). The global energy balance from a surface perspective. *Climate Dynamics*, *40*(11), 3107–3134.
<https://doi.org/10.1007/s00382-012-1569-8>
- Wild, M., Grieser, J., & Schär, C. (2008). Combined surface solar brightening and increasing greenhouse effect support recent intensification of the global land-based hydrological cycle. *Geophysical Research Letters*, *35*(17).
<https://doi.org/https://doi.org/10.1029/2008GL034842>
- Woods, D. C., Chuan, R. L., & Rose, W. I. (1985). Halite Particles Injected into the Stratosphere by the 1982 El Chichón Eruption. *Science*, *230*(4722), 170–172.
<https://doi.org/10.1126/science.230.4722.170>
- Yevich, R., & Logan, J. A. (2003). An assessment of biofuel use and burning of agricultural waste in the developing world. *Global Biogeochemical Cycles*, *17*(4).
<https://doi.org/10.1029/2002GB001952>
- Yienger, J. J., & Levy II, H. (1995). Empirical model of global soil-biogenic NO_x emissions. *Journal of Geophysical Research: Atmospheres*, *100*(D6), 11447–11464.
<https://doi.org/https://doi.org/10.1029/95JD00370>
- Yu, P., Portmann, R. W., Peng, Y., Liu, C.-C., Zhu, Y., Asher, E., Bai, Z., Lu, Y., Bian, J., Mills, M., Schmidt, A., Rosenlof, K. H., & Toon, O. B. (2023). Radiative Forcing From the 2014–2022 Volcanic and Wildfire Injections. *Geophysical Research Letters*, *50*(13), e2023GL103791.
<https://doi.org/https://doi.org/10.1029/2023GL103791>
- Yu, P., Rosenlof, K. H., Liu, S., Telg, H., Thornberry, T. D., Rollins, A. W., Portmann, R. W., Bai, Z., Ray, E. A., Duan, Y., Pan, L. L., Toon, O. B., Bian, J., & Gao, R.-S. (2017). Efficient transport of tropospheric aerosol into the stratosphere via the Asian summer monsoon anticyclone. *Proceedings of the National Academy of Sciences*, *114*(27), 6972–6977.
<https://doi.org/10.1073/PNAS.1701170114>
- Zawadowicz, M. A., Proud, S. R., Seppäläinen, S. S., & Cziczo, D. J. (2015). Hygroscopic and phase separation properties of ammonium sulfate/organics/water ternary solutions. *Atmospheric Chemistry and Physics*, *15*(15), 8975–8986. <https://doi.org/10.5194/acp-15-8975-2015>
- Zhu, Y., Bardeen, C. G., Tilmes, S., Mills, M. J., Wang, X., Harvey, V. L., Taha, G., Kinnison, D., Portmann, R. W., Yu, P., Rosenlof, K. H., Avery, M., Kloss, C., Li, C., Glanville, A. S., Millán,

L., Deshler, T., Krotkov, N., & Toon, O. B. (2022). Perturbations in stratospheric aerosol evolution due to the water-rich plume of the 2022 Hunga-Tonga eruption. *Communications Earth & Environment*, 3(1), 248. <https://doi.org/10.1038/s43247-022-00580-w>

Zuo, M., Man, W., Zhou, T., & Guo, Z. (2018). Different Impacts of Northern, Tropical, and Southern Volcanic Eruptions on the Tropical Pacific SST in the Last Millennium. *Journal of Climate*, 31(17), 6729–6744. <https://doi.org/https://doi.org/10.1175/JCLI-D-17-0571.1>

